Investigation of the cytoplasmic pool of centriolar and centrosomal proteins

Thomas L. Steinacker



Lincoln College, University of Oxford

A thesis submitted for the degree of
Doctor of Philosophy
Trinity Term 2021

Thesis summary

Investigation of the cytoplasmic pool of centriolar and centrosomal proteins

Thomas Steinacker

Lincoln College/Sir William Dunn School of Pathology

A thesis submitted for the degree of Doctor of Philosophy, Trinity 2021

How cells control the size and number of their organelles is largely unclear. In the Raff laboratory, we study centriole and centrosome biogenesis to investigate how their assembly is dynamically regulated. Centrioles are barrel-shaped cell organelles that, in preparation for mitosis, can give rise to the centrosome, an amorphous, protein-dense structure. In *Drosophila*, only a small number of proteins are essential for the formation of both organelles: centrioles require the five core duplication proteins Asl, Plk4, Ana2, Sas-6 and Sas-4, and the underlying centrosomal scaffold is formed by an interplay of Polo, Spd-2, and Cnn. By using the early *Drosophila* embryo as a model system, we can simultaneously observe the incorporation dynamics of fluorescently tagged proteins of interest at a large number of centrioles and centrosomes. Ultimately, we would like to mathematically model both assembly processes, but we lack information regarding how the cytoplasmic pool of their individual building blocks behaves during organelle formation. I therefore optimised and developed novel spectroscopy techniques for the early *Drosophila* embryo, including Fluorescence correlation spectroscopy, Fluorescence cross-correlation spectroscopy, and Peak counting spectroscopy. I then used these techniques to assess the biophysical properties of the embryo's syncytial cytoplasm and conducted a systematic characterisation of the core proteins' cytoplasmic concentration, diffusion dynamic, and average cytoplasmic stoichiometry.

Acknowledgements

First and foremost, I would like to thank Jordan for all his support and guidance. Thank you for creating such an encouraging and great lab atmosphere, I genuinely could not have wished for a better lab to do my PhD in! I really appreciate that you always had an open door for me, both, when you first welcomed me into your lab and throughout the years whenever I popped into your office with a question or an exciting new result.

I would also like to thank all the present and former members of the Raff laboratory. Like Pavlov's dog, I will always think of our daily coffee and tea breaks (which were often accompanied by the most amazing cakes!) whenever I hear a bell ringing. A huge thanks goes to my many lab-internal collaborators, thank you for sharing your ideas, expertise, and exciting projects with me. I also would like to express my gratitude to the Dunn School and my external collaborators, especially Christoffer Lagerholm who guided me through the initial steps of setting up the methodologies. I would like to acknowledge the microscope Zeiss 880, where I spent most of my last four years, and the *Drosophila* flies that make our research possible.

I want to thank my wife Hettie for her constant support and encouragement throughout my PhD, I can't tell you how happy I am that we finally managed to get married on our third attempt. Ich möchte mich auch von ganzem Herzen bei meiner Familie bedanken, meiner Mutter Irmgard, meinem Bruder Stephan und meinen Großeltern Georg und Gertraud.

I dedicate this thesis to my grandparents Rudolf and Herta and my music teacher and friend Cornelia, who sadly passed away during my time in Oxford.

Table of contents

1 Introduction 1

1.1 Centrioles, centrosomes, and cilia 1

1.1.1 Centriole structure and function 2

1.1.2 Centrosome structure and function 6

1.1.3 Cilia structure and function 9

1.1.4 Centrosomes and cilia in human pathology 10

1.2 Centriole duplication 13

1.2.1 Asl 17

1.2.2 Plk4 19

1.2.3 Ana2 21

1.2.4 Sas-6 22

1.2.5 Sas-4 23

1.2.6 Duplication control 24

1.3 Centrosome maturation 26

1.4 The early *Drosophila melanogaster* embryo as a model system for centriole duplication/centrosome maturation 28

1.5 Thesis aims 31

2 Materials and methods 32

2.1 Fly husbandry 32

2.1.1 Fly handling 32

2.1.2 *Drosophila melanogaster* stocks 32

2.1.3 CRISPR/Cas9-mediated fly line generation 35

2.1.4 Transgenic fly line generation 38

2.2 Molecular Biology and biochemistry 38

2.2.1 Purification of genomic DNA from *Drosophila melanogaster* 38

2.2.2 DNA vector design 39

2.2.3 Immunoblotting 46

2.3 Live microscopy and spectroscopy 48

2.3.1 Preparation of *D. melanogaster* embryos 48

2.3.2 Fluorescence correlation spectroscopy (FCS) 48

2.3.3 Fluorescence cross-correlation spectroscopy (FCCS) 57

2.3.4 Peak counting spectroscopy (PeCoS) 60

2.3.5 Spinning-disk confocal microscopy 61

2.4 Data visualisation and statistical analysis 62

3 Developing spectroscopy methods to probe the cytoplasmic properties of centriolar and centrosomal proteins 63

3.1 Introduction 63

3.2 Results 63

3.2.1 Fluorescence correlation spectroscopy (FCS) 63

3.2.2 Fluorescence cross-correlation spectroscopy (FCCS) 71

3.2.3 Peak counting spectroscopy (PeCoS) 75

3.2.4 Characterisation of the biophysical properties of the *Drosophila* embryo during nuclear cycles 11-14 80

3.3 Conclusions 86

4 Investigation of the cytoplasmic pool of centriolar proteins 87

4.1 Introduction 87

4.2 Results 91

4.2.1 Generating CRISPR/Cas-9 mNG knock-ins at the endogenous loci of the core centriole duplication genes 91

4.2.2 The cytoplasmic concentration of the core centriole duplication proteins does not change dramatically during the nuclear cycle 93

4.2.3 The cytoplasmic diffusion rate of Ana2 changes significantly as embryos prepare to enter mitosis 96

4.2.4 The change in Ana2's diffusion speed is largely independent of its ability to homo-oligomerise and to interact with Sas-6 98

4.2.5 The change in Ana2's diffusion speed appears to largely be dependent on phosphorylation by Cdk1 101

4.2.6 eAna2(12A)-mNG is recruited to the centriole until the onset of mitosis 103

4.2.7 Centriole growth dynamics are significantly altered in the presence of Ana2(12A) 106

4.2.8 Mutating two conserved potential Cdk1 phosphorylation sites in Ana2 seems to destabilise the protein 109

4.3 Discussion 111

5 FCS and PeCoS analyses reveal important insights into the regulation of centriole assembly 116

5.1 Introduction 116

5.2 Results 118

5.2.1 A centriolar Plk4 oscillation helps to time and execute centriole biogenesis 118

5.2.2 A simple mathematical model can potentially explain Plk4's oscillatory behaviour 118

5.2.3 Using FCS and PeCoS to test predictions of the mathematical model ... 121

5.2.4 The kinase activity of Plk4 helps to destabilise the protein in *Drosophila* embryos 124

5.2.5 The cytoplasmic concentration of Sas-6 and Ana2 remains relatively constant at the start of nuclear cycles 11-14, but the concentration of Sas-4 falls slightly 126

5.2.6 Sas-6 and Ana2 appear to be largely monomeric and dimeric in the cytoplasm, respectively 128

5.2.7 An attempt to establish Fluorescence cross-correlation spectroscopy (FCCS) in the early *Drosophila* embryo to investigate Sas-6's and Ana2's cytoplasmic stoichiometry 134

5.3 Discussion 135

5.3.1 The cytoplasmic concentration of Plk4 decreases between nuclear cycles 11-14 to slow the centriole growth dynamics 135

5.3.2 The cytoplasmic concentration of all other core centriole duplication proteins remains relatively constant between nuclear cycles 11-14 138

5.3.3 Ana2 and Sas-6 appear to be kept in a lower oligomeric state in the cytoplasm than at the centriole 140

6 Investigation of the cytoplasmic pool of centrosomal proteins 143

6.1 Introduction 143

6.2 Results 145

6.2.1 Centrosome size is homeostatically regulated in the early *Drosophila* embryo 145

6.2.2 The growth rate reduction of the PCM client proteins between nuclear cycles 11-13 is not caused by the depletion of their cytoplasmic pool 147

6.2.3 The PCM scaffold-forming proteins exhibit distinct recruitment dynamics to the client proteins 149

6.2.4 Cnn and Spd-2 show a stepwise drop in cytoplasmic levels between nuclear cycles 11-14 149

6.2.5 The drop in [Cnn] at successive cycles is proportional to the amount of Cnn in the cytoplasm 151

6.2.6 The drop in [Cnn] is correlated with a drop in the centrosomal Cnn incorporation and growth rate 154

6.2.7 Manipulating [Cnn] alters the centrosomal Cnn growth rate 155

6.2.8 [Spd-2] influences its incorporation dynamics at the centrosome 158

6.2.9 The centrosomal sequestration of Cnn and Spd-2 is not responsible for the decrease in their cytoplasmic concentration at successive nuclear cycles 161

6.2.10 The centrosomal recruitment of Cnn and Spd-2 may target them for destruction in the cytoplasm at the end of mitosis 164

6.3 Discussion 166

6.3.1 Centrosome size is homeostatically regulated in the early *Drosophila* embryo 166

6.3.2 [Cnn] and [Spd-2] decrease between nuclear cycles 11-14 and influence their incorporation rate at the centrosome 167

6.3.3 Centrosomal Spd-2 might be limiting for Cnn recruitment 169

6.3.4 Cnn and Spd-2 might be targeted for degradation at the end of mitosis 169

7 Discussion 172

7.1 The cytoplasmic concentration of Plk4, Cnn, and Spd-2 decreases between nuclear cycles 11-14 172

7.2 Centriole duplication and centrosome maturation do not seem to be influenced by a cytoplasmic pool limitation in the *Drosophila* embryo 177

8 References 180

9 Appendices 208

9.1 Appendix A 208

9.2 Appendix B 219

9.3 Appendix C 220

9.4 Appendix D 226

9.5 Appendix E 227

9.6 Appendix F 232

List of abbreviations

3D	Three-dimensional
aa	Amino acid
ACF	Autocorrelation function
Ana1	Anastral spindle 1
Ana2	Anastral spindle 2
Ana3	Anastral spindle 3
APC	Anaphase promoting complex
Asl	Asterless
ASH1	Asp, SPD-2, Hydin domain 1
BIC	Bayesian information criterion
Bld10	Basal body protein 10
CA	Centrosome amplification
Cas9	CRISPR-associated protein 9
CC	Coiled-coil
CCC	Centriole-to-centrosome conversion
CDC20	Cell division cycle protein 20
cDNA	complementary DNA
Cdh1	Cadherin 1
Cdk1/CDK1	Cyclin-dependent kinase 1
Cdk2/CDK2	Cyclin-dependent kinase 2
CM2	Common motif 2
Cnn	Centrosomin
Cep/CEP	Centrosomal protein
CPAP	Centrosomal P4.1-associated protein
CPB	Cryptic polo-box
CPM	Photon-count rate per molecule
CRISPR	Clustered regularly interspaced short palindromic repeats
CS	Centrosome separation
DNA	Deoxyribonucleic acid
dNG	dimeric-NeonGreen
D-TACC	Drosophila-transforming acidic coiled-coil protein
EM	Electron microscopy
FCCS	Fluorescence cross-correlation spectroscopy
FCS	Fluorescence correlation spectroscopy
FRAP	Fluorescence recovery after photobleaching
G0	Gap 0 phase
G1	Gap 1 phase
G2	Gap 2 phase
GFP	Green fluorescent protein
HDR	Homology-directed repair
HG	Headgroup

kDa	Kilodalton
LZ	Leucine zipper motif
MCPH	Autosomal recessive primary microcephaly
mNG	monomeric-NeonGreen
MSPS	Mini spindles protein
MT	Microtubule
MTOC	Microtubule-organising centre
NEB	Nuclear envelope breakdown
PBD	Polo-box domain
PD	Primordial dwarfism
PCM	Pericentriolar material
PCR	Polymerase chain reaction
PeCoS	Peak counting spectroscopy
Plp/PCNT	Pericentrin-like protein
Plk1/PLK1	Polo-like kinase 1
Plk4/PLK4	Polo-like kinase 4
PPP1R35	Protein phosphatase 1 regulatory subunit 35
Rcd4	Reduction in Cnn dots protein 4
RNA	Ribonucleic acid
RNAi	RNA interference
RPKM	Reads per kilobase of feature length per million reads
RT	Room temperature
RTTN	Rotatin
S-phase	Synthesis phase
Sak	Sak kinase
SAP	Sas-6/Ana2 particle
Sas-4	Spindle assembly abnormal protein 4
SAS-5	Spindle assembly abnormal protein 5
Sas-6/SAS6	Spindle assembly abnormal protein 6
SCF	SKP1-Cullin-F-box E3 ligase
SDS-PAGE	Sodium dodecyl sulfate-polyacrylamide gel electrophoresis
sgRNA	Single guide RNA
SIM	Structured illumination microscopy
smFISH	Single molecule fluorescence in situ hybridization
SNR	Signal-to-noise ratio
Spd-2/SPD-2	Spindle defective protein 2
SPD-5	Spindle defective protein 5
STAN	STil/ANa2
STIL	SCL-interrupting locus protein
Ubq	Ubiquitin
V_{eff}	Effective volume
WT	Wild type
ZYG-1	Zygotic defective 1

List of figures

Figure 1-1: Centriole architecture in vertebrates and *Drosophila* embryos 3

Figure 1-2: Centriole ultrastructure 5

Figure 1-3: Centrioles act as the nucleation template for centrosomes and cilia 7

Figure 1-4: The canonical centriole duplication cycle in vertebrate cells and in the early *Drosophila* embryo 14

Figure 1-5: The core centriole duplication and centrosome maturation pathway are conserved in *Drosophila melanogaster, Caenorhabditis elegans,* and *Homo sapiens* 16

Figure 1-6: Illustration of the five core centriole duplication proteins and their known interaction sites in *Drosophila melanogaster* 18

Figure 1-7: The syncytium of the early *Drosophila melanogaster* embryo is composed of individual cytoplasmic domains 29

Figure 2-1: Crossing schemes for the identification and isolation of CRISPR/Cas9-mediated knock-in alleles 36

Figure 2-2: *In silico* construction of the donor plasmid for homology-directed repair (HDR) 42

Figure 2-3: Estimation of the effective volume (V_{eff}) size 50

Figure 3-1: Description of Fluorescence correlation spectroscopy (FCS) 64

Figure 3-2: Characterisation of the spectroscopy setup 66

Figure 3-3: Fluorescence correlation spectroscopy workflow for *in vivo* measurements 68

Figure 3-4: FCS is a suitable method to measure cytoplasmic concentrations, diffusion dynamics, and protein stoichiometry within the *Drosophila* syncytial embryo 70

Figure 3-5: Basis of the FCCS setup, and *in vivo* validation for FCCS measurements of mScarlet-I and mNG 73

Figure 3-6: PeCoS allows relative concentration measurements of very low abundant proteins 77
Figure 3-7: Characterisation of the fluorescence background of the embryonic syncytium between the nuclear cycles 11-14 81
Figure 3-8: Characterising the behaviour of inert fluorescent proteins during nuclear cycles 11-14 83
Figure 3-9: Characterising the behaviour of inert fluorescent proteins during nuclear cycle 12 85
Figure 4-1: Centrioles grow in a linear fashion and plateau when they reach their final size 89
Figure 4-2: Endogenously mNG-tagged centriolar proteins localise to the centriole 90
Figure 4-3: Western blots confirm the successful mNG knock-in at the endogenous loci92
Figure 4-4: The cytoplasmic concentration of all five core centriole duplication proteins does not change dramatically during nuclear cycle 12 94
Figure 4-5: The cytoplasmic diffusion rate of Ana2 changes significantly as embryos prepare to enter mitosis 97
Figure 4-6: Ana2's change in diffusion rate is insensitive to the deletion of either the CC or STAN domain 100
Figure 4-7: Ana2's change in diffusion rate is significantly reduced when it cannot be phosphorylated by Cdk1 102
Figure 4-8: eAna2(12A)-mNG exhibits an abnormal pattern of centriolar recruitment. 105
Figure 4-9: Centrioles grow slower and for longer in the presence of Ana2(12A) 107
Figure 4-10: The two conserved potential Cdk phosphorylation sites S284 and T301 are not responsible for eAna2(12A)-mNG's abnormal recruitment pattern 110

Figure 4-11: A multiple sequence alignment between *Drosophila* species highlights the high conservation of multiple potential Cdk1 sites within Ana2 115

Figure 5-1: Centriole size is regulated by an inverse relationship between growth rate and period in the early *Drosophila* embryo..... 117

Figure 5-2: Plk4 levels oscillate at the base of the mother centriole and initiate and time centriole assembly..... 119

Figure 5-3: A simple mathematical model can recapitulate Plk4's oscillatory recruitment to centrioles..... 120

Figure 5-4: The cytoplasmic concentration of Asl remains relatively constant between nuclear cycles 11-14 while Plk4 exhibits a gradual depletion 123

Figure 5-5: A reduction in Plk4 kinase activity leads to increased Plk4 levels in the cytoplasm and at the centriole..... 125

Figure 5-6: The cytoplasmic concentration of Sas-6 and Ana2 remains relatively constant between nuclear cycles 11-14, but the concentration of Sas-4 falls slightly over successive cycles 127

Figure 5-7: FCS-derived CPM analysis indicates that Ana2 is mostly dimeric and Sas-6 mostly monomeric in the early *Drosophila* syncytium 129

Figure 5-8: FCCS measurements potentially indicate that Sas-6 is monomeric and Ana2 oligomeric in the cytoplasm 136

Figure 6-1: A positive feedback loop between the scaffold proteins Spd-2, Polo, and Cnn drives centrosome maturation..... 144

Figure 6-2: PCM client proteins are recruited to the centrosome in an oscillatory manner and grow to a similar size over successive cycles 11-13..... 146

Figure 6-3: The cytoplasmic concentration of all seven PCM client proteins remains relatively constant between nuclear cycles 11-14 148
Figure 6-4: The recruitment dynamics of the three centrosomal scaffold proteins Cnn, Spd-2, and Polo differ from the recruitment dynamics of the client proteins 151
Figure 6-5: [Cnn] and [Spd-2] exhibit a stepwise drop between nuclear cycles 11-14 while [Polo] remains constant 152
Figure 6-6: The stepwise drop in [Cnn] is insensitive to changes in its expression levels and might be responsible for Cnn's decreased centrosomal growth rate over cycles..... 153
Figure 6-7: The centrosomal Cnn growth dynamics are sensitive to cytoplasmic concentration changes, but saturate at high expression levels 156
Figure 6-8: The stepwise drop in [Spd-2] is insensitive to changes in its expression levels and might be responsible for Spd-2's decreased growth rate over cycles..... 159
Figure 6-9: The centrosomal Spd-2 growth dynamics are sensitive to cytoplasmic concentration changes 160
Figure 6-10: [Spd-2] and [Cnn] increase at the beginning of mitosis, but exhibit a significant drop at the end of mitosis 162
Figure 6-11: Truncated forms of Cnn and Spd-2 that show very little centrosomal localisation do not exhibit a stepwise drop in cytoplasmic concentrations between nuclear cycles 11-14 166
Figure 7-1: Most core centriole and centrosome proteins are actively translated during the early *Drosophila* development 175
Figure 8-1: PeCoS allows the quantification of eAna1-GFP's relative cytoplasmic concentration 219

Figure 8-2: Ana2's cytoplasmic oligomerisation state is insensitive to the expression levels of the other core centriole duplication proteins 221
Figure 8-3: Ana2 needs its CC domain for dimerisation, and the deletion of its STAN domain might allow Ana2 to form higher oligomeric structures in the cytoplasm..... 223
Figure 8-4: N-terminally tagged Sas-6 and Ana2 show an increased cytoplasmic concentration compared to their C-terminal proteins when measured by FCS..... 226
Figure 8-5: The smFISH staining of Ana2, Sas-6, and Plk4 does not show an accumulation of their mRNA around the centriole 231
Figure 8-6: Cnn seems to be mainly monomeric in the cytoplasm 232

List of tables

Table 1: List of centriolar and centrosomal proteins that were linked to human pathology 11

Table 2: Alleles used in this thesis 33

Table 3: Primer combinations for mNG knock-in screening 37

Table 4: List of generated sgRNA plasmids 41

Table 5: List of generated HDR donor plasmids 43

Table 6: List of generated pDONR and DEST plasmids 44

Table 7: Antibodies and substrate concentrations used in this thesis 47

Table 8: Selected model and anomalous subdiffusion parameter α for all proteins measured with FCS 53

Table 9: Fly genotypes used in this thesis 208

Table 10: Primers designed for mNG knock-in screening 212

Table 11: Primers designed for sgRNA and HDR donor plasmid generation 213

Table 12: Primers designed for transformation plasmid generation 217

Table 13: Parameters and target sequence which were used for the smFISH probe design 227

1 Introduction

1.1 Centrioles, centrosomes, and cilia

Centrioles are barrel-shaped, membrane-less cell organelles which function as a nucleation template for two cellular structures in different cell cycle stages. During mitosis, centrioles form centrosomes by recruiting a large protein-dense structure around them called pericentriolar material (PCM), which contains hundreds of proteins and acts as the major microtubule-organising centre (MTOC) of the mitotic spindle. In interphase and quiescence, centrioles can migrate to the cell membrane and act as the basal body of the primary cilium/flagellum (Conduit, Wainman and Raff, 2015). Centrioles are believed to have been present in the last common ancestor (Cavalier-Smith, 2002), and the centriolar structure is conserved in most eukaryotic groups (Carvalho-Santos *et al.*, 2011). However, only some sub-groups of proteins are conserved on the sequence level, while other groups emerged in taxon-specific manner and only show functional homology (Carvalho-Santos *et al.*, 2010).

Mutations in centriolar and centrosomal proteins have been linked to many human pathologies including primordial dwarfism, microcephaly, genome instability in cancer, and various ciliopathies (Nigg and Raff, 2009; Bettencourt-Dias *et al.*, 2011; Nigg and Holland, 2018). This broad spectrum of disease-related phenotypes highlights the importance of both centriole-mediated structures, centrosomes and cilia, for correct cell function. Identifying the molecular basis and assembly dynamics of centrioles, centrosomes, and cilia will therefore be an important step towards understanding the contribution of their dysfunction in human disease.

1.1.1 Centriole structure and function

Centrioles are barrel-shaped, protein-based cell organelles of ~200-250 nm in diameter and 150-500 nm in height, which display a nine-fold symmetry and are composed of an inner cartwheel structure surrounded by microtubule (MT) blades (Winey and O'Toole, 2014) (**Figure 1-1**).

Centriole assembly starts with the formation of the inner cartwheel, which is located at the proximal end of the centriole and is thought to determine the shape of the organelle (Hirono, 2014). Cryotomography studies on centrioles isolated from *Trichonympha* allowed the observation of the centriolar structure with unprecedented resolution and revealed that pairs of cartwheel discs are stacked on top of each other. A small ring of approximately 22 nm diameter is located at the centre of each cartwheel disc from which nine symmetrical spokes point outwards (Guichard *et al.*, 2013) (**Figure 1-2A**). The core centriole duplication protein Sas-6 was identified as the key protein that shapes this inner cartwheel structure. Sas-6 can dimerise through its conserved C-terminal coiled-coil (CC) domain and hydrophobic interactions between the N-terminal globular head domains from nine Sas-6 dimers allow the protein to self-assemble into the nine-fold symmetrical cartwheel (Kitagawa, Vakonakis, *et al.*, 2011; Van Breugel *et al.*, 2011) (**Figure 1-2B**). Sas-6 on its own can form the cartwheel structure *in vitro* (Guichard *et al.*, 2017; Yoshiba *et al.*, 2019), but other proteins like Sak/PLK4 and Ana2/STIL play a crucial role in assisting cartwheel assembly *in vivo* (Cottee *et al.*, 2015; Arquint and Nigg, 2016). Although the structure of Ana2 within the cartwheel has not yet been resolved, super-resolution light microscopy identified the position of Ana2 within the outer cartwheel region (Gartenmann *et al.*, 2017), and Ana2 is known to interact with Sas-6 through its

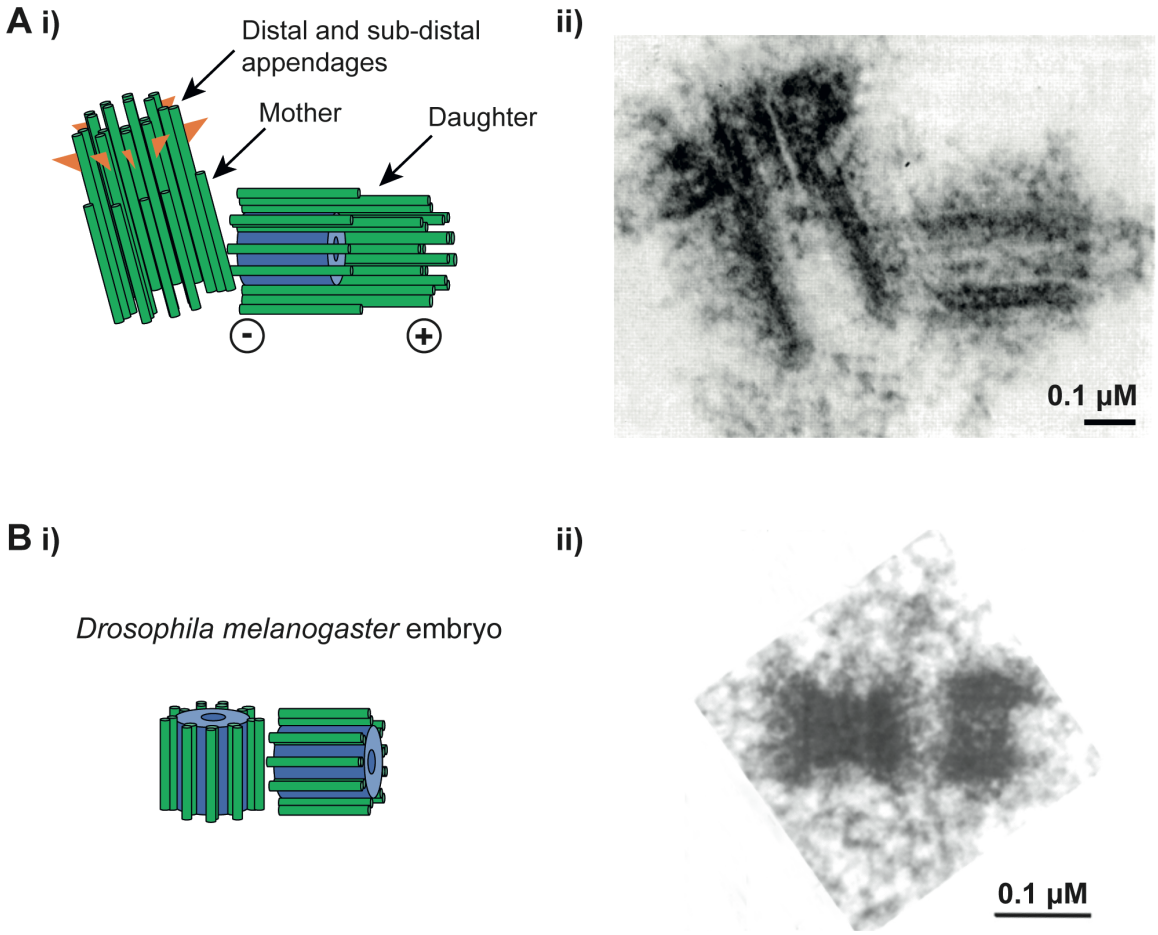


Figure 1-1: Centriole architecture in vertebrates and *Drosophila* embryos
(A) (i) Schematic of a vertebrate centriolar pair. The mother and daughter centriole are perpendicularly oriented to each other. The cartwheel (*blue*) is located at the proximal (-) end, the centriolar microtubules (MTs) (*green*) extend on the distal (+) end. Only the mother centriole is decorated with distal and sub-distal appendages (*orange*). (ii) Electron microscopy (EM) picture of a vertebrate centriolar pair. The mother centriole is on the left, the daughter centriole on the right. Image was modified from Delattre and Gönczy (2004) and originally generated by Paintrand *et al.* (1992). **(B) (i)** Schematic of a centriolar pair in the early *Drosophila melanogaster* embryo. The centriole is shorter in length, and the MTs are present as doublets and do not extend beyond the centriolar cartwheel. **(ii)** EM picture of a centriolar pair within the *Drosophila* blastoderm. Image taken from Vidwans, Wong and O'Farrell (1999).

phosphorylated STAN (STil/ANa2) domain to initiate cartwheel assembly (Dzhindzhev *et al.*, 2014; Ohta *et al.*, 2014; Fatalska *et al.*, 2020).

The C-terminal CC region of Sas-6 dimers forms the base of the radial spokes but is too short to directly link to the MT blades. A pinhead structure that sits at the end of the spoke connects the inner cartwheel to the centriolar MTs (Guichard *et al.*, 2013) (**Figure 1-2A**). Sas-4/CPAP localises to the interspace between the cartwheel and the centriolar MTs (Cottee *et al.*, 2013), and it is essential for centriole assembly (Kirkham *et al.*, 2003; Leidel

and Gönczy, 2003). Sas-4/CPAP can interact with both the centriolar protein Ana2/STIL (Kitagawa, Kohlmaier, *et al.*, 2011; Tang *et al.*, 2011; Cottee *et al.*, 2013) and with tubulin heterodimers (Hung *et al.*, 2004). In *Chlamydomonas* and *Paramecium,* it was shown that also Cep135/Bld10 localizes to the pinhead structure and that it is essential for centriole assembly and stability (Hiraki *et al.*, 2007; Jerka-Dziadosz *et al.*, 2010).

MTs are polymers composed of α- and β-tubulin subunits and play a vital role in many cellular processes including intracellular trafficking and establishing intracellular structure (Brouhard and Rice, 2018). Centriolar MTs are positioned at the tip of the cartwheel spokes and extend away from the cartwheel on the distal end (**Figure 1-1A**). They are polarised structures with their minus end at the proximal end and display an anticlockwise twist (Winey and O'Toole, 2014) (**Figure 1-2Aiii**). Depending on organism and cell type, centriolar MTs can occur as singlets like in *C. elegans* (Pelletier *et al.*, 2006), doublets like in most *Drosophila* cells (Bate, 1993), or triplets, the predominant form in mammals including human cells (Paintrand *et al.*, 1992). Mammalian centrioles are composed of a complete A-MT and two incomplete B- and C-MTs, where A-MTs growth is initiated by the γ-tubulin ring complex (γ-TuRC) and acts as template for B- and C-MT elongation (Guichard *et al.*, 2010). Mammalian centriolar MTs can be grouped into two different domains; at the proximal end, where the cartwheel is located, centriolar triplets are connected by an A-C linker, while at the distal domain MTs look more similar to the ciliary axoneme architecture and form two connections, an inner A-B junction and an outer A-C linker (Greenan *et al.*, 2018). In *Drosophila*, centriolar MTs rather resemble the structure of the mammalian proximal end, but with MT blades linked through their A-MTs (Greenan

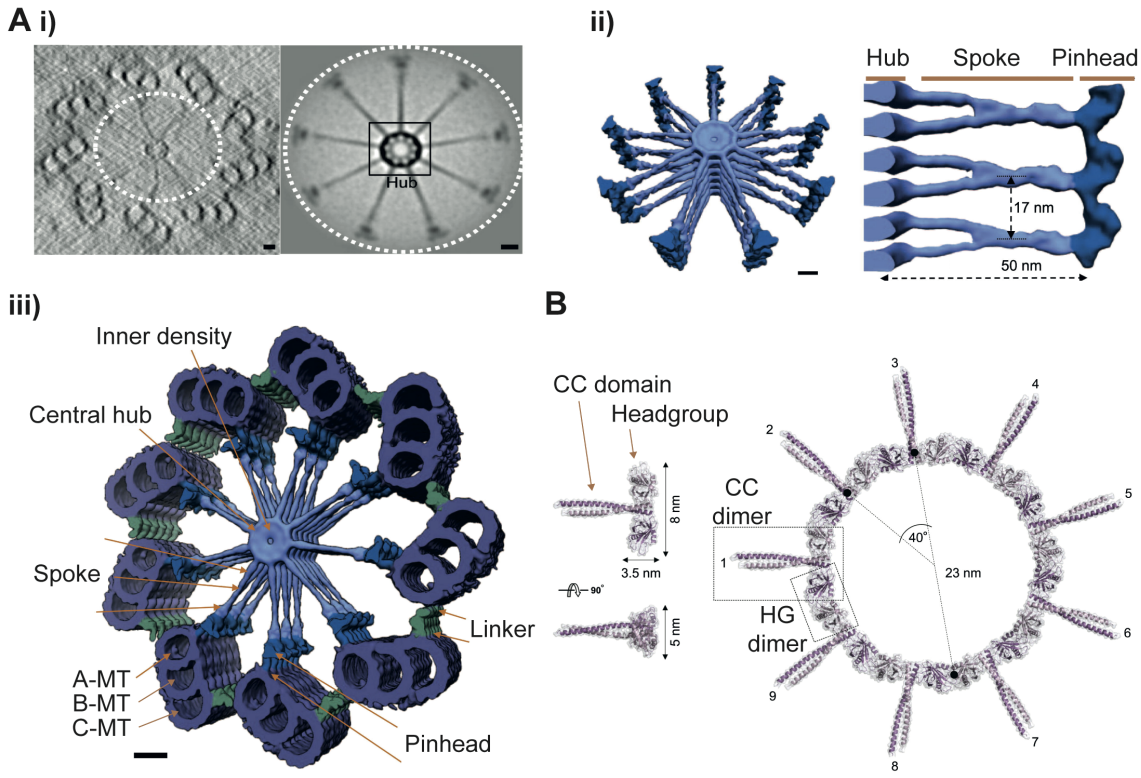


Figure 1-2: Centriole ultrastructure
(A) (i) Cross-section of a *Trichonympha* centriole imaged with cryotomography (*left*) and the projection of the reconstructed cartwheel after subtomogram averaging (*right*). **(ii)** 3D representation (*left*) and longitudinal view (*right*) of the centriolar cartwheel (*light blue*) and the adjacent pinhead (*dark blue*). Two cartwheel discs are stacked on top of each other to form a single spoke. **(iii)** Complete 3D architecture of the proximal end of the *Trichonympha* centriole. The pinhead connects the cartwheel spoke with the A-microtubule (A-MT). MT blades are connected through an A-C linker. The scale bars represent 10 nm in (i) and (ii), and 20 nm in (iii). Illustrations were modified from Guichard *et al.* (2013). **(B)** Structural model of Bld12p (Sas-6 homologue in *Chlamydomonas reinhardtii*) and its oligomerisation into the nine-fold symmetrical centriolar cartwheel structure. Bld12p/Sas-6 homo-dimerises through interactions in its coiled-coil (CC) domain. Dimers can also interact through their N-terminal headgroups (HGs), which induces the ring assembly. Graph was modified from Kitagawa *et al.* (2011).

et al., 2018). In vertebrates, the mother centriole is decorated with distal and sub-distal appendages, which promote membrane docking during cilia formation (Tanos *et al.*, 2013) (**Figure 1-1A**). After mitosis, vertebrate cells seem to lose the cartwheel structure as many cartwheel proteins no longer localise to the centriole (Arquint and Nigg, 2014).

Despite an overall conserved cylindrical shape and nine-fold symmetry, the centriolar architecture can show great variability between organisms and tissue types (Carvalho-Santos *et al.*, 2011; Gupta and Kitagawa, 2018). In the *Drosophila melanogaster* embryo, centrioles display a similar diameter to other model systems (~200 nm), but with a length

of ~120-150 nm are much shorter compared to ~400-500 nm in human cells (Moritz *et al.*, 1995; Debec *et al.*, 1999; Conduit, Wainman and Raff, 2015). The centriolar MTs do not extend significantly on the distal end, so that the inner cartwheel extends throughout essentially the entire centriole (Gonzalez, Tavosanis and Mollinari, 1998; Lattao, Kovács and Glover, 2017) (**Figure 1-1B**). As centrioles in the early *Drosophila* embryo do not display distal or subdistal appendages on the mother centriole (Callaini, Whitfield and Riparbelli, 1997), mother and daughter centrioles can only be distinguished by their orthogonal orientation to each other (Debec *et al.*, 1999), or by fluorescently tagging proteins with asymmetric mother/daughter-recruitment dynamics like the core centriole duplication protein Asterless (Asl) (Novak *et al.*, 2014).

1.1.2 Centrosome structure and function

Centrosomes are membrane-less cell organelles that contain a centriolar pair at their core surrounded by an electron-dense protein matrix termed PCM (Moritz *et al.*, 1995; Conduit, Wainman and Raff, 2015) (**Figure 1-3A**). In *Drosophila melanogaster* and *Caenorhabditis elegans*, an underlying scaffold is formed through the interplay of three essential proteins: Cnn/SPD-5, Spd-2/SPD-2, and Polo/PLK-1 (Conduit, Richens, *et al.*, 2014; Woodruff *et al.*, 2015; Alvarez-Rodrigo *et al.*, 2019). This scaffold then promotes the recruitment of hundreds of client proteins, which allow the centrosome to carry out its cellular functions (Alves-Cruzeiro, Nogales-Cadenas and Pascual-Montano, 2014). Through the localisation of γ-TuRCs within the PCM, centrosomes form the major MTOC of the mitotic bipolar spindle to ensure faithful chromosome segregation (Meraldi, 2016; Prosser and Pelletier, 2017). In addition, centrosomes also concentrate a high number of

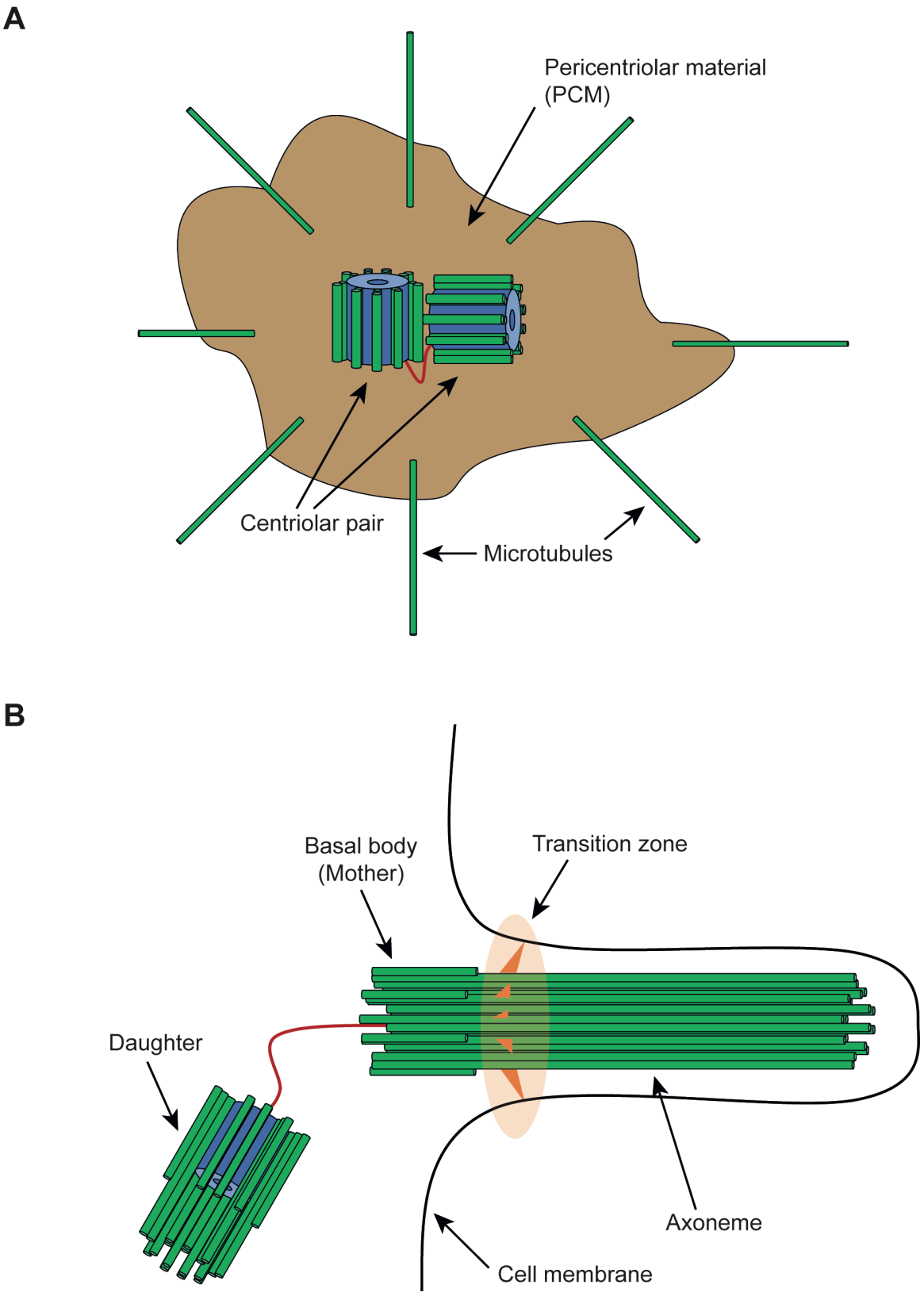


Figure 1-3: Centrioles act as the nucleation template for centrosomes and cilia
A) Schematic of a centrosome. In preparation for mitosis, the mother centriole can nucleate an expanded electron-dense protein structure called the pericentriolar material (PCM), which allows the centrosome to nucleate microtubules to form the major microtubule-organising centre of the mitotic spindle. **(B)** Schematic of a cilium. During interphase/in quiescence, the centriolar pair can migrate to the cell membrane to initiate the formation of the cilium. The mother centriole hereby functions as the basal body from which the axoneme extends into the extracellular space.

signalling molecules including kinases and phosphatases and act as a signalling hub within the cell (Arquint, Gabryjonczyk and Nigg, 2014).

Surprisingly, centrosomes are not always essential for spindle formation and chromosome separation, and alternative spindle assembly pathways have been identified (Prosser and Pelletier, 2017). It was shown that chromatin-coated beads in *Xenopus laevis* egg extract are capable of forming bipolar spindles in the absence of centrosomes (Heald *et al.*, 1996). Also *in vivo* centrosomes are not always required for spindle formation as centrosomes are lost in most animal species during female meiosis (Dumont and Desai, 2012), and fruit flies can proceed through most of their development without centrosomes (Basto *et al.*, 2006). Vertebrate somatic cells, where centrosomes were ablated using laser microsurgery, still formed bipolar spindles and completed mitosis (Khodjakov *et al.*, 2000).

In many systems, however, centrosomes are important for efficient chromosome segregation and cell cycle timing. It was shown that the genetic ablation of centrioles results in a delay in bipolar spindle assembly and in higher rates of chromosomal instability (Sir *et al.*, 2013). Also *Drosophila* development is delayed through the absence of centrosomes, and the very rapid syncytial nuclear cycles of the *Drosophila* blastoderm require the presence of centrosomes (Basto *et al.*, 2006). Further, centrosomes play an important role in defining the orientation of the mitotic spindle, which determines the axis of asymmetric cell division (Knoblich, 2010). *C. elegans* embryos without centrosomes, for example, fail to undergo anteroposterior symmetry breaking (O'Connell, Maxwell and White, 2000; Cowan and Hyman, 2004), and asymmetric cell division of neuroblasts in the *Drosophila* larval brain occurs less efficiently if centrosomes are missing (Basto *et al.*, 2006). In vertebrate cells, but not in *Drosophila*, the loss of centrosomes

triggers apoptosis through the p53-dependent pathway. In mice, centrosome loss therefore results in increased apoptosis and developmental arrest around embryonic day9 (Bazzi and Anderson, 2014; David *et al.*, 2014). Additional depletion of p53 allows near-normal development and chromosome segregation until the mice die presumably due to the lack of cilia (Bazzi and Anderson, 2014). The reason for p53-dependent apoptosis despite near-normal chromosome segregation in centrosome-less vertebrate cells is still unclear and needs further investigation.

1.1.3 Cilia structure and function

Primary (non-motile) cilia are polarised, MT-based cell organelles that assemble on the apical surface of most quiescent human cells and consist of three different regions: the basal body, the transition zone, and the axoneme (**Figure 1-3B**). The basal body is usually formed by the mother centriole and functions as the origin and structural template for the extended MTs of the axoneme. The axoneme itself consists of nine parallel, radially arranged MTs that elongate from the basal body into the extracellular space (Ishikawa and Marshall, 2011). The transition zone is located between the basal body and the axoneme of the cilium, anchors the basal body to the cell membrane, and acts as a selective barrier (Craige *et al.*, 2010; Gonçalves and Pelletier, 2017). The protein and lipid composition of the ciliary membrane differs to the cell membrane to allow for proper cilia function (Garcia, Raleigh and Reiter, 2018). The mother centriole is decorated with distal and sub-distal protein appendages that allow the docking of the mother centriole, but not the daughter, to the cell membrane (Tanos *et al.*, 2013).

Cilia can in general be separated into two classes: motile cilia/flagella, and immotile/primary cilia. Motile cilia are composed of nine MT outer doublets and two

additional MT singlets in their centre (9+2), and function primarily in cell motility and generation of motion (Gilpin, Bull and Prakash, 2020). The inner MTs are linked to the outer MT doublets via spokes and break the symmetry of the cilium/flagellum to define the bending axis. Beating motions are generated through the collective effects of dynein motors sliding between the outer MT doublets (Ishikawa, 2017). Primary cilia, in comparison, lack the inner MT singlets (9+0), and have a crucial role as cellular sensory organs and signalling hubs. They were shown to control key developmental processes like the establishment of left-right asymmetry in mammals (Hirokawa *et al.*, 2006) and the regulation of Hedgehog and Wnt signalling (Huangfu *et al.*, 2003; Jacob *et al.*, 2011). Cilia can—depending on the cellular context—sense and respond to mechanical stimulation (Spasic and Jacobs, 2018), chemosensation (Singla and Reiter, 2006), temperature (Kuhara *et al.*, 2008), light (Insinna and Besharse, 2008), or gravity (Moorman and Shorr, 2008). Due to the involvement of motile and primary cilia in many important cellular processes, mutations in cilia-related genes have been linked to a variety of diseases collectively termed ciliopathies (Bisgrove and Yost, 2006).

1.1.4 Centrosomes and cilia in human pathology

Due to the wide range of processes through which centrioles contribute to cell function—both as centrosomes and cilia—mutations in many centriolar genes have been linked to developmental disorders and human pathologies (**Table 1**). Over the last decades many efforts were directed towards understanding the dynamics of centrosome and cilia biogenesis, but rather little is known about the molecular mechanisms of how mutations in individual genes result in such a variety of diseases (Nigg and Raff, 2009).

Table 1: List of centriolar and centrosomal proteins that were linked to human pathology
MCPH (Microcephaly), MT (Microtubule), PCM (Pericentriolar material), PD (Primordial dwarfism). Modified from Chavali, Pütz and Gergely, 2014.

Human gene	Pathology	*Drosophila* homologue	Protein function
ASPM	MCPH, cognitive impairment, PD, seizures	Asp	Mitotic spindle orientation
CDK5RAP2	MCPH, PD	Cnn	PCM assembly and maturation, MT organisation
CEP135	MCPH	Cep135	Centriole biogenesis, MT organisation
CEP152	MCPH, cognitive impairment, PD, mental retardation	Asl	Centriole biogenesis; PCM assembly
CPAP/CENPJ	MCPH, cognitive impairment, facial dysmorphism, skeletal anomalies	Sas-4	Centriole biogenesis; PCM assembly
MCPH1	MCPH, cognitive impairment, PD	MCPH1	DNA damage response and repair, cell cycle checkpoints
ORC1	MCPH, PD, skeletal abnormalities	Orc1	DNA replication, centriole copy number regulation
PCNT	MCPH, PD, bone abnormalities	Plp	PCM assembly, mitotic spindle organisation
STIL	MCPH, PD	Ana2	Centriole biogenesis
PLK4	MCPH, PD, genome instability	Plk4/Sak	Centriole biogenesis
SAS-6	MCPH	Sas-6	Centriole biogenesis
CEP192	MCPH	Spd-2	PCM assembly and maturation, MT organisation

One of the most prominent human pathologies that was linked to mutations in multiple centrosomal genes is autosomal recessive primary microcephaly (MCPH) (Gilmore and Walsh, 2013; Nano and Basto, 2017). MCPH is a neurodevelopmental disorder that results in non-progressive mental retardation and head circumference reduction at birth. During embryonic development, MCPH patients generate significantly fewer cerebral cortical neurons which results in a drastic reduction in brain size (Mahmood, Ahmad and Hassan,

2011). Neural progenitor cells require centrosomes for asymmetric cell division to control neurogenesis, and are therefore particularly sensitive to mutations in centrosomal proteins (Wang *et al.*, 2009). Another group of growth-related autosomal recessive pathologies that was linked to centrosome malfunction is termed microcephalic primordial dwarfism (PD), and includes Seckel syndrome, microcephalic osteodysplastic PD type I and II, and Meier-Gorlin syndrome (Chavali, Pütz and Gergely, 2014; Nano and Basto, 2017). PD patients show extreme global growth defects alongside MCPH (Klingseisen and Jackson, 2011). Many different genes have been implicated in causing these severe growth defects including genes involved in DNA replication, DNA damage response, but also in centrosome function (Rauch *et al.*, 2008; Bicknell *et al.*, 2011). Why some genes and only certain mutations cause MCPH and others PD remains unclear. Therefore, it will be important to first fully understand how each centriolar protein contributes to centrosome/cilia biogenesis and stability, and to then investigate how specific mutations can alter their functionality.

Most human cells are ciliated and mutations in genes that are involved in cilia formation and function can cause a variety of disorders termed ciliopathies. Currently, 35 ciliopathies have been defined with 187 genes involved in their aetiology (Reiter and Leroux, 2017). As cilia play a crucial sensory and signalling role in many organs such as eyes, kidneys, brain, and liver, clinical symptoms can drastically vary between individual ciliopathies (Waters and Beales, 2011). Mutations that affect immotile cilia often result in multisystemic ciliopathies like Bardet–Biedl syndrome, Meckel syndrome, and Alström syndrome. Symptoms can include polycystic kidney disease, central obesity, hearing loss, retinal dystrophy, liver fibrosis, epilepsy and many more (Reiter and Leroux, 2017).

Mutations that affect motile cilia can lead to male sterility, situs inversus (left-right patterning anomaly), and bronchitis, sinusitis and atelectasis (due to the defective clearance of lung mucus) (Reiter and Leroux, 2017).

Centrosome amplification (CA) is a hallmark of cancer, and most cancer cells display abnormalities in centrosome morphology and number (Chan, 2011; Godinho and Pellman, 2014). CA can occur through *de novo* centrosome formation, centriole overduplication, cytokinesis failure, or fragmentation of overly elongated centrioles, which can then lead to multipolar mitotic spindles and genome instability (Sabat-Pospiech *et al.*, 2019). Centrosome overduplication can contribute to cancer through causing aneuploidy (Ganem, Godinho and Pellman, 2009), increasing invasiveness (Godinho *et al.*, 2014), and compromising asymmetric stem cell division (Basto *et al.*, 2008). For a long time, it was unclear whether CA is a cause for or a consequence of cancer, but studies in flies and mice have shown that CA can be sufficient to drive tumorigenesis (Basto *et al.*, 2008; Levine *et al.*, 2017). Interestingly, the overexpression of individual centriolar proteins can cause centriole overduplication, highlighting the importance for tight expression regulation to ensure centrosome number control (Peel *et al.*, 2007; Coelho *et al.*, 2015).

1.2 Centriole duplication

Centriole biogenesis describes the process of assembling a new centriole, which can occur either through a canonical duplication pathway where the daughter centriole grows perpendicularly from its mother or *de novo* without a template (Loncarek and Khodjakov, 2009). *De novo* centriole formation occurs naturally in certain biological systems like the mouse zygote (Szollosi, Calarco and Donahue, 1972), but this mechanisms is usually suppressed in cycling somatic cells by the presence of centrioles (La Terra *et al.*, 2005).

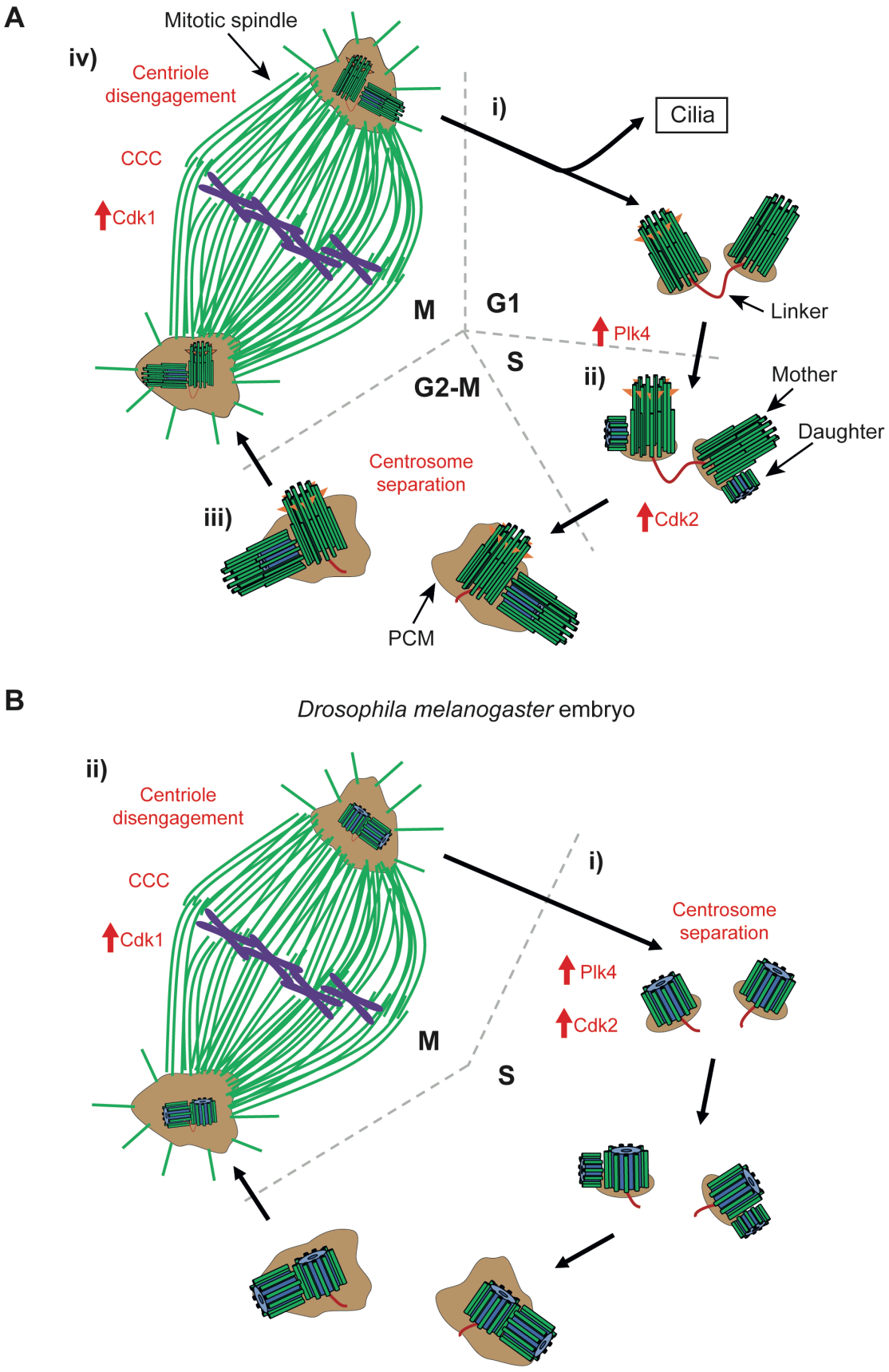


Figure 1-4: The canonical centriole duplication cycle in vertebrate cells and in the early *Drosophila* embryo
See next page.

Figure 1-4: The canonical centriole duplication cycle in vertebrate cells and in the early *Drosophila* embryo
(A) Schematic shows the centriole duplication cycle in vertebrate cells. **(i)** At the beginning of the cycle (in G1), each cell contains one disengaged but still flexibly linked centriolar pair, which can either migrate to the cell membrane to form the basal body of the primary cilium or—in cycling cells—re-enter the centriole duplication cycle. **(ii)** Upon entry into S-phase, centriole duplication is initiated, a process which requires high Plk4 and Cdk2 activity. **(iii)** By G2, daughter centriole growth is completed and the flexible linker between the two mother centrioles is broken, which allows the centrosomes to start moving to opposite sites. Mother centrioles also initiate pericentriolar material (PCM) expansion in preparation for mitosis. **(iv)** In mitosis, where Cdk1 activity is high, the expanded centrosomes form the major microtubule-organising centre of the mitotic spindle to assist with chromosome (*purple*) segregation. The tight connection between mother and daughter centriole is lost in Anaphase (centriole disengagement), and centriole-to-centrosome conversion (CCC) allows the daughter centriole to become a new mother. **(B)** Schematic shows the centriole duplication cycle in the early *Drosophila* embryo. Centriole duplication occurs very similarly to vertebrate cells, but with slightly different timings. **(i)** Due to the fast cycle speed and lack of gap phases, centrosomes separate immediately upon S-phase entry, and duplicate and migrate to opposite poles already during S-phase. **(ii)** Identical to vertebrate cells, centriole disengagement occurs in Anaphase, and CCC allows the newly formed centriole to duplicate in the following cycle.

The mechanism of *de novo* centriole formation is poorly understood, but studies in unfertilised *Drosophila* eggs have revealed that the essential components of the canonical duplication pathway are also necessary for *de novo* centriole formation (Rodrigues-Martins *et al.*, 2007). Most cells and organisms (including the early *Drosophila* embryo), however, assemble their centrioles from an existing template. The centriole duplication cycle is tightly linked to the cell cycle to control centriole number, and centrioles only duplicate once every cell cycle during interphase (Fu, Hagan and Glover, 2015) (**Figure 1-4**).

Genome-wide RNAi screens in *C. elegans* embryos identified five proteins that are essential for centriole duplication (Delattre, Canard and Gönczy, 2006; Pelletier *et al.*, 2006). This duplication pathway and its five functional homologues seem to be highly conserved (Goshima *et al.*, 2007; Dobbelaere *et al.*, 2008; Balestra *et al.*, 2013; Conduit, Wainman and Raff, 2015) (**Figure 1-5**). Within this duplication pathway, centriole assembly is initiated when the master kinase ZYG-1/Sak/PLK4 (in worms/flies/humans—hereafter referred to as Plk4 in flies) is recruited to the assembly site at the pre-existing mother (O'Connell *et al.*, 2001; Bettencourt-Dias *et al.*, 2005; Habedanck *et al.*, 2005). This

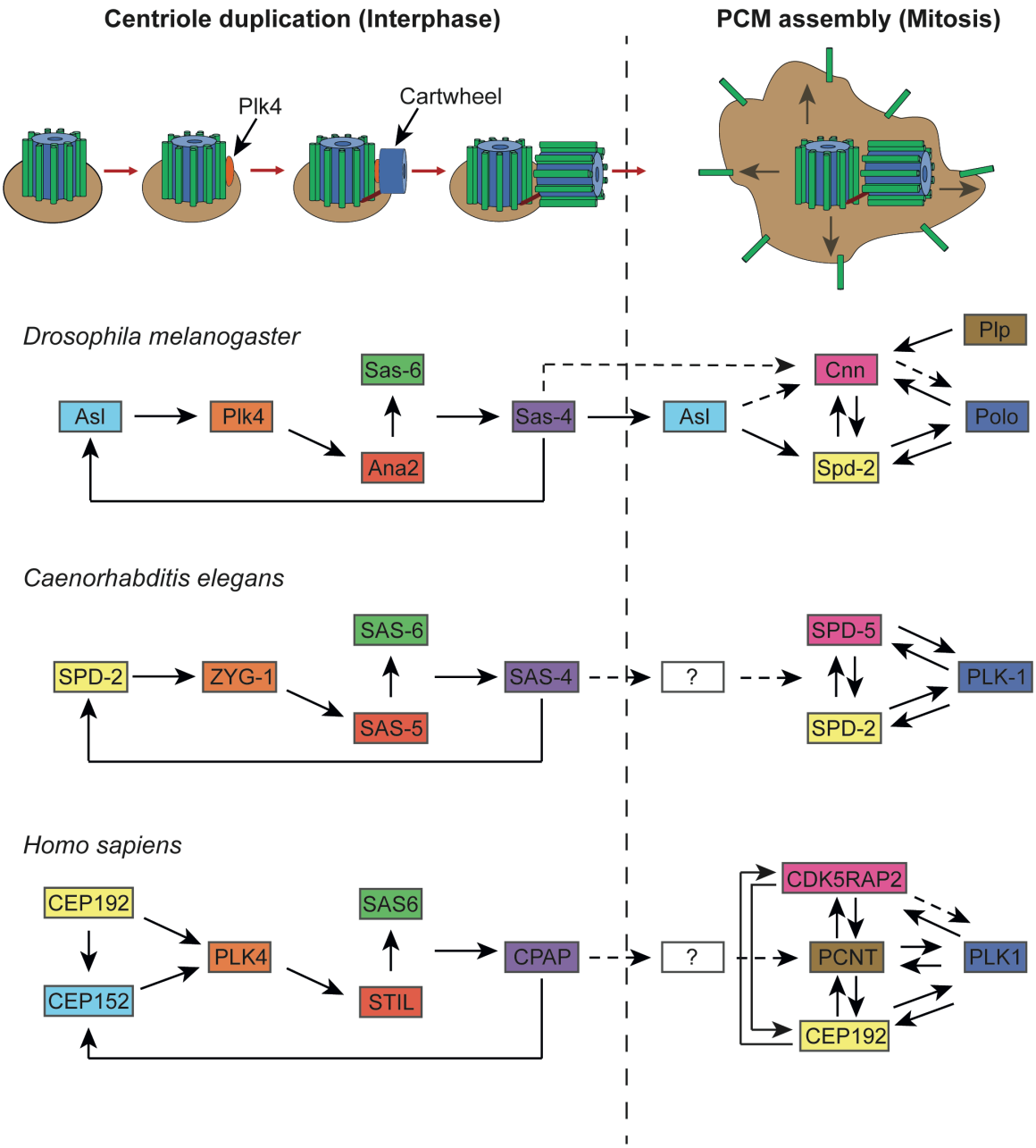


Figure 1-5: The core centriole duplication and centrosome maturation pathway are conserved in *Drosophila melanogaster, Caenorhabditis elegans,* and *Homo sapiens*
Diagrams show the centriole assembly pathway during interphase (*left of dotted line*), and the centrosome assembly pathway during mitosis (*right of dotted line*) in flies, worms, and humans. Functional homologues are highlighted in the same colour, solid arrows indicate that a protein is required for the localisation of the other, dashed arrows indicate where a localisation relationship has been inferred. See main text for details. Adapted from Conduit, Wainman and Raff (2015).

recruitment occurs through its binding to the receptor SPD-2 in worms (Delattre, Canard and Gönczy, 2006; Pelletier *et al.*, 2006), Asl in flies (Blachon *et al.*, 2008; Dzhindzhev *et al.*, 2010), and a combination of their homologues CEP152 and CEP192 in humans (Cizmecioglu *et al.*, 2010; Hatch *et al.*, 2010; Sonnen *et al.*, 2013). Upon binding, the

kinase, which forms a homodimer, phosphorylates and thereby activates itself in *trans* (Lopes *et al.*, 2015). Next, the cartwheel protein SAS-5/Ana2/STIL is recruited to the assembly site and is phosphorylated by Plk4 in its STAN domain to allow the binding and recruitment of the structural cartwheel protein SAS-6/Sas-6/HsSAS-6 (Dzhindzhev *et al.*, 2014; Ohta *et al.*, 2014; Kratz *et al.*, 2015; Fatalska *et al.*, 2020). Finally, the cartwheel proteins recruit SAS-4/Sas-4/CPAP(CENPJ) to their outer region, where it is involved in the assembly of the centriolar MTs (Pelletier *et al.*, 2006; Tang *et al.*, 2009, 2011). In the next cell cycle, after the old and new mother centriole have disengaged, Sas-4 can recruit Asl in flies to re-initiate the duplication process (Novak *et al.*, 2014). Other centriolar proteins like Bld10/CEP135 (Hiraki *et al.*, 2007; Roque *et al.*, 2012), Ana1/CEP295 (Izquierdo *et al.*, 2014; Saurya *et al.*, 2016), Ana3/RTTN (Stevens *et al.*, 2009; Chen *et al.*, 2017), and Rcd4/PPP1R35 (Panda *et al.*, 2020) have been identified as important contributors to the robustness of centriole assembly. A detailed summary of the five key centriole duplication proteins (**Figure 1-6**), with focus on *Drosophila melanogaster*, is presented in the next Section.

1.2.1 Asl

Asl is the *Drosophila* orthologue of the human protein CEP152, and is essential for centriole duplication in both systems (Varmark *et al.*, 2007; Blachon *et al.*, 2008). With a molecular weight of ~120 kDa, Asl is the largest protein of the five core duplication proteins in *Drosophila* (Varmark *et al.*, 2007), and can interact with Plk4 and Sas-4 (Dzhindzhev *et al.*, 2010).

Super-resolution microscopy revealed that Asl localises to the outer-wall of the mother centriole and is present along the entire length of the centriole in *Drosophila* (Fu and

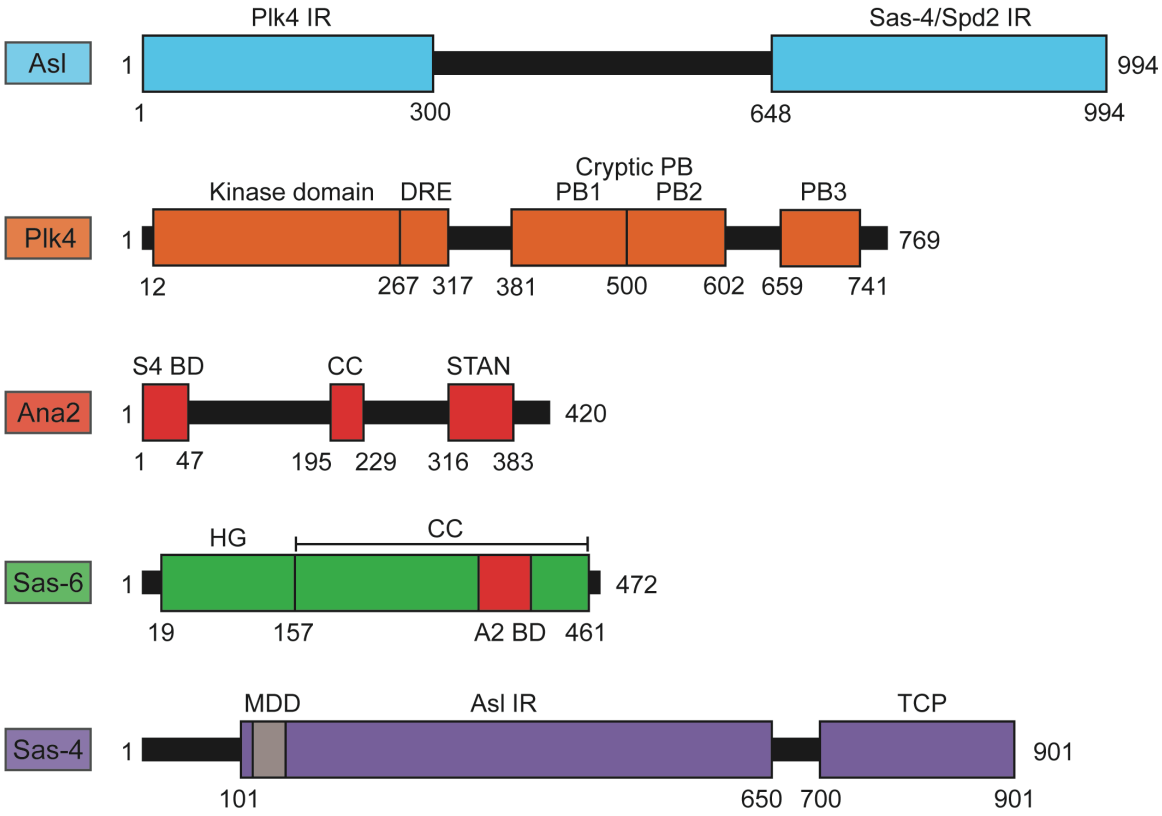


Figure 1-6: Illustration of the five core centriole duplication proteins and their known interaction sites in *Drosophila melanogaster*

Protein illustrations and annotated domains are drawn in proportion. Numbers represent the amino acid position within the protein. Further information regarding protein function can be found in the main text. **Asl:** IR—Interacting region. **Plk4:** DRE—Downstream regulatory region (degron motif); PB – Polo-box. **Ana2:** S4 BD – Sas-4 binding domain; CC—Coiled-coil domain; STAN—STil/ANa2 domain. **Sas-6:** HG—Headgroup; CC—Coiled-coil domain; A2 BD—Ana2 Binding domain. **Sas-4:** MDD—Microtubule-destabilising domain; IR—Interacting region; TCP—T complex protein 10 domain (which can bind to Ana2).

Glover, 2012; Mennella *et al.*, 2012), while CEP152 is restricted to the proximal end in human cells (Lawo *et al.*, 2012; Sonnen *et al.*, 2012). The C-terminal region of Asl/CEP152 can bind to Sas-4/CPAP (Cizmecioglu *et al.*, 2010; Dzhindzhev *et al.*, 2010), an interaction which is crucial for the recruitment of Asl to the centriole (Novak *et al.*, 2014). Ana1 was also implicated in the recruitment of Asl (Fu *et al.*, 2016), but its role seems to be rather in maintaining Asl at the centriole (Saurya *et al.*, 2016).

The N-terminus of Asl can interact with Plk4's cryptic polo box domain to recruit the master kinase to the assembly site and—upon binding—allows Plk4 to homo-dimerise and activate itself in interphase, while a C-terminal binding site stabilises Plk4 during mitosis

(Klebba *et al.*, 2015). Interestingly, Plk4 can phosphorylate Asl and alter its own stability depending on Asl's phosphorylation state (Boese *et al.*, 2018).

Asl also plays a key role in centriole-to-centrosome conversion (CCC) as its loading onto the newly built daughter centriole during mitosis is necessary for providing a primary duplication license (Novak *et al.*, 2014). In *Drosophila*, Asl also appears to play a crucial role in PCM recruitment (Conduit, Richens, *et al.*, 2014; Novak *et al.*, 2014), perhaps through its ability to interact with the centrosomal scaffold protein Spd-2/CEP192 (Sonnen *et al.*, 2013; Klebba *et al.*, 2015) (**Figure 1-6**, see next Section).

1.2.2 Plk4

Plk4/Sak (and its vertebrate homologue PLK4 and functional orthologue ZYG-1 in *C. elegans*) is the master kinase and initiator of centriole duplication (O'Connell *et al.*, 2001; Bettencourt-Dias *et al.*, 2005; Habedanck *et al.*, 2005). Plk4 is a member of the polo-like kinase family, a class of serine/threonine-kinases that plays an important role in many cell cycle events (Lee, Jang and Lee, 2014).

Polo-like kinases consist of an N-terminal kinase domain and two polo-box domains (PBDs) at the C-terminus that interact in *cis* to control phospho-selectivity, localisation, and kinase activity (Lowery, Lim and Yaffe, 2005). In contrast to other polo-like kinases, Plk4 only possesses a single complete PBD (PB3), which allows it to homo-dimerise and is needed for centriolar localisation (Leung *et al.*, 2002). In addition, Plk4 has a central conserved "cryptic polo box" (CPB) that can bind to Asl/CEP152 (Cizmecioglu *et al.*, 2010; Dzhindzhev *et al.*, 2010; Hatch *et al.*, 2010). Structural studies revealed that this CPB consists of two unique PBDs, PB1-PB2, which are not only required for binding to Asl, but are also important for robust centriole targeting and oligomerisation (Slevin *et al.*, 2012).

Plk4 is first recruited as a ring to the entire centriolar circumference, but resolves to a single dot during G1-S phase transition which marks the position of the growing daughter centriole (Sonnen *et al.*, 2012; Ohta *et al.*, 2014; Dzhindzhev *et al.*, 2017). In human cells, STIL was shown to interact with PLK4 in a bimodal manner which allows PLK4 to asymmetrically localise; binding of PLK4 to STIL's central CC region stabilises the protein while binding to another conserved C-terminal region of STIL promotes degradation (Ohta *et al.*, 2018). In accordance, mathematical modelling suggests that the symmetry breaking of PLK4 can be induced through a feedback loop between PLK4 and STIL (Leda, Holland and Goryachev, 2018).

In order to prevent unscheduled centriole biogenesis, Plk4/PLK4 activity must be strictly regulated (Habedanck *et al.*, 2005). Plk4/PLK4 dimerises and autoactivates itself through *trans*-phosphorylation, a process that requires the local Plk4/PLK4 concentration to surpass a critical threshold, which can be achieved through accumulation at the centriole (Guderian *et al.*, 2010; Lopes *et al.*, 2015). Once active, Plk4/PLK4 phosphorylates Ana2/STIL in an ordered pattern including its STAN domain to allow the assembly of the centriolar cartwheel formed by Ana2/STIL and Sas-6/SAS6 (Dzhindzhev *et al.*, 2014; Ohta *et al.*, 2014; Kratz *et al.*, 2015; McLamarrah *et al.*, 2017; Fatalska *et al.*, 2020). To avoid overduplication, activated Plk4/PLK4 acts as a suicide kinase that phosphorylates its degron motif to initiate its own destruction by the SCF-Slimb/βTrCP ubiquitin ligase complex (Guderian *et al.*, 2010; Sillibourne *et al.*, 2010; Holland *et al.*, 2012; Cunha-Ferreira *et al.*, 2013).

1.2.3 Ana2

Despite poor sequence conservation, Ana2 was identified as the functional ortholog of STIL in humans and SAS-5 in *C. elegans* (Stevens *et al.*, 2010). Ana2 localises to the central cartwheel structure (Gartenmann *et al.*, 2017), and is the first protein recruited to the assembly site by the master kinase Plk4 (Dzhindzhev *et al.*, 2017).

On the N-terminus, a conserved proline-rich motif allows the binding of Ana2/STIL with Sas-4/CPAP, an interaction that is essential for centriole assembly (Cottee *et al.*, 2013; Hatzopoulos *et al.*, 2013). The central region of Ana2 contains a coiled-coil domain (CC) which facilitates the homo-oligomerisation of Ana2. Structural studies have shown that the *Drosophila* CC domain forms a stable tetramer, and, *in vivo,* mutations that cause a disruption of this oligomerisation lead to loss of Ana2 localisation to the centrosome (Cottee *et al.*, 2015). STIL's CC domain is also able to form multimers, but the tendency to form tetramers is clearly not as strong as in flies (Cottee *et al.*, 2015). In humans, the CC domain can bind to PLK4, but whether this interaction is conserved in *Drosophila* is controversial (Cottee *et al.*, 2017; McLamarrah *et al.*, 2017). In human cell lines and *Xenopus* egg extracts CDK1 can also bind to the CC to inhibit STIL's interaction with PLK4 in order to prevent unscheduled centriole duplication during mitosis (Zitouni *et al.*, 2016). The C-terminus of Ana2/STIL contains a conserved STAN domain, which is phosphorylated by Plk4/PLK4 to allow the interaction with the structural cartwheel protein Sas-6/SAS6 to promote centriolar cartwheel assembly (Dzhindzhev *et al.*, 2014; Ohta *et al.*, 2014; Kratz *et al.*, 2015; Moyer *et al.*, 2015; Fatalska *et al.*, 2020).

Recent findings suggest an ordered pattern of Ana2 phosphorylation by Plk4: initially, Ana2 is phosphorylated on its N-terminus, which then allows the hyperphosphorylation

of the STAN domain on the C-terminus. Finally, Plk4 phosphorylates the CC region to break their interaction (McLamarrah *et al.*, 2017).

1.2.4 Sas-6

The protein structure of Sas-6 is highly conserved in *Drosophila* (Sas-6), humans (HsSAS6), and *C. elegans* (SAS-6), and is believed to be responsible for the nine-fold symmetrical shape of the centriole (Kitagawa, Vakonakis, *et al.*, 2011; Van Breugel *et al.*, 2011; Cottee *et al.*, 2015). Sas-6 contains two conserved regions; an extended C-terminal coiled-coil (CC) domain that allows its homo-dimerisation and an N-terminal headgroup through which Sas-6 dimers can interact with each other. Nine Sas-6 dimers can hereby assemble into the nine-fold symmetrical ring-like structure which sits at the core of the centriolar cartwheel (Kitagawa, Vakonakis, *et al.*, 2011; Van Breugel *et al.*, 2011; Guichard *et al.*, 2017; Yoshiba *et al.*, 2019) (**Figure 1-2B**).

Sas-6 is recruited to the assembly site through an interaction of its C-terminal CC region with the C-terminal STAN domain of Ana2 (Fatalska *et al.*, 2020). This interaction can, however, only occur after the STAN domain of Ana2/STIL has been phosphorylated by Plk4/PLK4 (Dzhindzhev *et al.*, 2014; Ohta *et al.*, 2014; Kratz *et al.*, 2015; Moyer *et al.*, 2015). FRAP (fluorescence recovery after photobleaching) experiments in the early *Drosophila* embryo showed that Sas-6 is irreversibly incorporated into the growing daughter centriole (Aydogan *et al.*, 2018). In vertebrates, the C-terminal region of SAS6, which points outwards from the central ring and forms the base of the cartwheel spoke, can also interact with CEP135 to recruit CPAP in order to bridge the inner cartwheel structure to the outer centriolar MTs (Tang *et al.*, 2009; Jerka-Dziadosz *et al.*, 2010; Lin *et al.*, 2013). The *Drosophila* homologue of Cep135/Bld10 also localises to the lumen

between the cartwheel and the centriolar MTs (Roque *et al.*, 2012). A yeast two-hybrid screen, however, did not identify a direct interaction between Sas-6 and Bld10, which suggests the presence of a different recruitment mechanism (Galletta *et al.*, 2016).

1.2.5 Sas-4

Sas-4/CPAP/SAS-4 is the last of the five core duplication proteins that is recruited to the assembly site, and localises to the interspace between the centriolar cartwheel spokes and centriolar MTs (Dammermann *et al.*, 2008; Kohlmaier *et al.*, 2009; Schmidt *et al.*, 2009; Tang *et al.*, 2009; Lawo *et al.*, 2012; Mennella *et al.*, 2012; Gartenmann *et al.*, 2017). During *Drosophila* development, embryos gradually lose their centrioles if no Sas-4 is present (Basto *et al.*, 2006).

The C-terminal conserved G-box domain of Sas-4/CPAP can interact with Ana2/STIL to allow Sas-4/CPAP's recruitment to the newly assembled cartwheel structure (Kitagawa, Kohlmaier, *et al.*, 2011; Tang *et al.*, 2011; Cottee *et al.*, 2013; Hatzopoulos *et al.*, 2013). In vertebrates, CPAP also binds to CEP135 and depletion of CEP135 impairs the centriolar localisation of CPAP (Carvalho-Santos *et al.*, 2012; Lin *et al.*, 2013). At its N-terminus, Sas-4/CPAP has a MT-binding domain which can interact with tubulin heterodimers and γ-tubulin. Sas-4/CPAP has a destabilising effect on MTs, but the mechanisms of how this influences centriolar MT assembly/structure is still unclear (Hung, Tang and Tang, 2000; Hung *et al.*, 2004; Hsu *et al.*, 2008). Sharma *et al.* (2016) showed that CPAP can bind to, and cap MT plus ends *in vitro*, which limits the MTs' growth rate *in vivo*, but also stabilises them by inhibiting catastrophes.

Another important function of Sas-4/CPAP is its interaction with and recruitment of Asl to the centriole, an important step during CCC in *Drosophila* embryos (Cizmecioglu *et al.*,

2010; Dzhindzhev *et al.*, 2010; Novak *et al.*, 2014). During mitosis, Cdk1/CyclinB phosphorylates Sas-4 in its Thr200-STP motif to recruit Polo to the centriole to subsequently promote Asl incorporation (Novak *et al.*, 2016).

1.2.6 Duplication control

Centrosome overduplication leads to the formation of multipolar spindles and genome instability (Sabat-Pospiech *et al.*, 2019). Therefore, cells need to ensure that centrosomes only duplicate once every cell cycle (**Figure 1-4**). Multiple levels of regulation have been identified that control duplication timing, centriole number, and centriole-to-centrosome conversion (CCC) (Nigg and Stearns, 2011; Nigg and Holland, 2018).

Centrioles can only duplicate during interphase and this timing is controlled by the cell-cycle dependent kinases Cdk1 and Cdk2 (Fu, Hagan and Glover, 2015). Centriole duplication requires the presence of Cdk2 and its associates cyclins, and Cdk2 activity is restricted to G1/S-phase (Hinchcliffe *et al.*, 1999; Lacey, Jackson and Stearns, 1999; Matsumoto, Hayashi and Nishida, 1999; Meraldi *et al.*, 1999). In contrast, CDK1 levels are high during mitosis, and in mammalian cells and *Xenopus* egg extract it was shown that CDK1 can prevent unscheduled centriole duplication by binding to STIL and thereby inhibiting its interaction with PLK4 (Zitouni *et al.*, 2016).

Cell fusion studies showed that it is not the cytoplasmic properties in G1/G2 phase that control centrosome number, but that recently duplicated centrosomes have an intrinsic block that inhibits further duplication within the same cycle (Wong and Stearns, 2003). Centriole disengagement, a process that requires the protease separase in *Xenopus*, is a crucial step in duplication licensing that only allows a mother centriole to assemble a new daughter after the tight connection to its previous daughter has been lost (Tsou and

Stearns, 2006; Loncarek *et al.*, 2008). Additionally, CCC prevents premature duplication and PCM assembly of the newly built daughter centriole, a Plk1-dependent process that occurs in early mitosis (Wang *et al.*, 2011). In *Drosophila* embryos, mitotic centriole conversion is initiated by the phosphorylation of Sas-4 in its Thr200-STP motif by the cell-cycle regulator Cdk1, which in turn leads to the recruitment of Polo (Novak *et al.*, 2016), followed by Cep135, Ana1, and Asl recruitment (Fu *et al.*, 2016; Saurya *et al.*, 2016). Interestingly, some Asl is irreversibly recruited to the daughter centriole only after disengagement to provide the new mother with a permanent primary duplication license (Novak *et al.*, 2014).

An additional level of control is generated through the regulation of protein abundance of key centriole duplication proteins. Plk4/PLK4, the master regulator and initiator of centriole duplication, is recruited to the assembly site in an oscillatory manner in both *Drosophila* embryos and human cell lines (Aydogan *et al.*, 2018; Yamamoto and Kitagawa, 2019). Plk4/PLK4 needs to dimerise in order to trans-autoactivate itself, and this requires the local Plk4/PLK4 concentration to surpass a critical activation threshold (Lopes *et al.*, 2015). Further, Plk4/PLK4 is a suicide kinase that—upon activation—phosphorylates itself in a degron motif to trigger its own destruction via the SCF-Slimb/βTrCP ubiquitin ligase complex (Guderian *et al.*, 2010; Sillibourne *et al.*, 2010; Holland *et al.*, 2012; Cunha-Ferreira *et al.*, 2013). In human cells not only PLK4, but also the concentration of STIL, CPAP, and SAS6 is regulated through controlled degradation in an APC/$C^{Cdc20–Cdh1}$-dependent manner during mitosis followed by increasing levels at the beginning of S-phase (Strnad *et al.*, 2007; Tang *et al.*, 2009; Arquint *et al.*, 2012). Quantitative proteomics in cultured human cells showed that the three proteins that are responsible

for the initiation of centriole duplication, PLK4, STIL and SAS6, are in general of very low abundance in the cell (Bauer *et al.*, 2016). In addition, overexpression studies in multiple systems revealed that high levels of some core centriole duplication proteins can lead to centriole overduplication, highlighting the importance of cytoplasmic concentration control (Bettencourt-Dias *et al.*, 2005; Habedanck *et al.*, 2005; Leidel *et al.*, 2005; Kleylein-Sohn *et al.*, 2007; Peel *et al.*, 2007; Stevens *et al.*, 2010; Arquint *et al.*, 2012). Interestingly, it was shown that in *Drosophila* the extent of centriole overduplication driven by the different centriolar proteins can vary between different tissues, indicating a complex interplay of multiple regulatory mechanisms that can vary between biological systems to ensure correct centriole number (Peel *et al.*, 2007).

1.3 Centrosome maturation

During interphase, a small amount of highly organised PCM is located at the centrosome in close proximity to the outer wall of the mother centriole (Fu and Glover, 2012; Lawo *et al.*, 2012; Mennella *et al.*, 2012; Sonnen *et al.*, 2012). The amount of PCM recruited increases dramatically in preparation for mitosis (Palazzo *et al.*, 1999). In *Drosophila* and *C. elegans*, an underlying scaffold of three key proteins was identified that is necessary to assemble the mitotic PCM (**Figure 1-5**). The conserved coiled-coil protein Spd-2/SPD-2 (fly/worm) interacts with the large coiled-coil domain-rich protein Cnn/SPD-5 to assemble the scaffold. This assembly is promoted by phosphorylation of Cnn/SPD-5 and Spd-2/SPD-2 by Polo/PLK-1 (Decker *et al.*, 2011; Conduit, Feng, *et al.*, 2014; Conduit, Richens, *et al.*, 2014; Woodruff *et al.*, 2015; Wueseke *et al.*, 2016; Feng *et al.*, 2017). The absence of any of the three proteins results in drastic loss of mitotic PCM assembly (Woodruff *et al.*, 2015, 2017; Feng *et al.*, 2017). Their human functional homologues CEP192 (Spd-2)

(Gomez-Ferreria *et al.*, 2007), CDK5RAP2 (Cnn) (Barr, Kilmartin and Gergely, 2010; Choi *et al.*, 2010), and PLK1 (Polo) (Lane and Nigg, 1996; Haren, Stearns and Lüders, 2009) have also been identified as important contributors to mitotic PCM assembly, suggesting the mechanism of mitotic PCM expansion is likely to be conserved (**Figure 1-5**).

In *Drosophila* embryos, both Cnn and Spd-2 are only recruited around the surface of the mother centriole and then flux outwards (Conduit *et al.*, 2010; Conduit, Richens, *et al.*, 2014), and this may be important in explaining why the centrioles are normally essential for mitotic PCM assembly (Bobinnec *et al.*, 1998; Basto *et al.*, 2006; Sir *et al.*, 2013; Bazzi and Anderson, 2014; Wong *et al.*, 2015; Cabral *et al.*, 2019). Due to the small surface area of the centriole wall, this inside-out flux in itself, however, is unlikely to explain the high rate of PCM assembly that can be observed during centrosome maturation. It was suggested that a positive feedback loop between Spd-2, Cnn, and Polo is responsible for this dramatic expansion (Alvarez-Rodrigo *et al.*, 2019). Spd-2 recruits Cnn and Polo to the centrosome, where active Polo phosphorylates Cnn to allow it to form a scaffold; the Cnn scaffold cannot recruit Spd-2, but it helps to retain Spd-2 at the centrosome (Conduit *et al.*, 2010; Conduit, Feng, *et al.*, 2014; Feng *et al.*, 2017; Alvarez-Rodrigo *et al.*, 2019). This forms a positive feedback loop where the Spd-2 fluxing away from the centriole recruits Cnn, and the Cnn then stabilises the Spd-2, allowing it to recruit more Cnn.

An alternative theory to explain mitotic centrosome expansion is that centrosomes behave as liquid droplets and the PCM accumulates through liquid-liquid phase separation (Zwicker *et al.*, 2014; Banani *et al.*, 2017). Purified SPD-5 can form micron-scale liquid-like condensates *in vitro* (Woodruff *et al.*, 2017). *In vivo*, however, a solid scaffold—

as mentioned above—seems to be better suited to explain most experimental observations in *Drosophila* embryos (Raff, 2019).

1.4 The early *Drosophila melanogaster* embryo as a model system for centriole duplication/centrosome maturation

The fruit fly *Drosophila melanogaster* is a well-established model system that provides a wide range of advantages including excellent genetic tools, fast generation times, and many evolutionary conserved pathways to more complex organisms (Tolwinski, 2017)—including centriole duplication and centrosome maturation (Conduit, Wainman and Raff, 2015). The early nuclear cycles of the *Drosophila* blastoderm display several features that make the embryo a powerful system to study centriole and centrosome assembly:

The first 13 nuclear cycles occur highly synchronously, without cytokinesis, and extremely fast (with all 13 divisions occurring within less than two hours). By cycle 8, most nuclei (and their centrosomes) start migrating to the cortex of the embryo, where they form an evenly distributed monolayer during cycle 10 (**Figure 1-7**) (Foe and Alberts, 1983). The close proximity of the nuclei and their associated centrosomes to the plasma membrane allow the observation of the centriole/centrosome assembly dynamics with conventional fluorescence live microscopy with a high signal-to-noise ratio (SNR) due to the low imaging depth (Dunst and Tomancak, 2019).

During this developmental stage, transcription is mostly suppressed, and the embryo is dependent on maternally provided transcripts, also referred to as maternal contribution (Farrell and O'Farrell, 2014). This allows nuclear cycles to occur extremely rapid and is

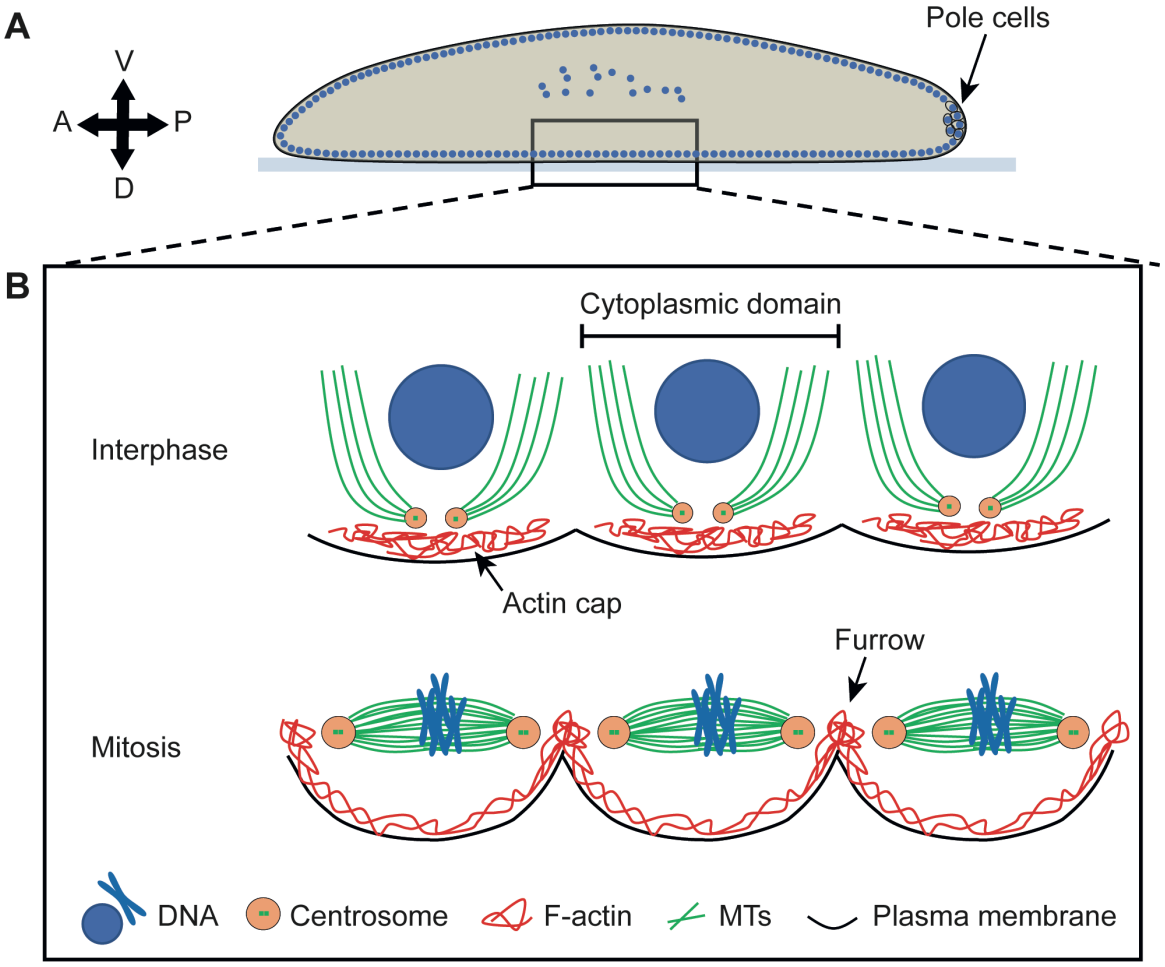


Figure 1-7: The syncytium of the early *Drosophila melanogaster* embryo is composed of individual cytoplasmic domains
(A) The early embryo is a gigantic syncytial cell where the first 13 nuclear cycles occur highly synchronously. By nuclear cycle 10, most nuclei form an evenly distributed monolayer. Only some yolk nuclei remain in the interior of the embryo, and some nuclei at the posterior end form the pole cells. **(B)** Cartoon depiction of the nuclear layer in S-phase and mitosis. See main text for further information.

further accelerated by the lack of gap phases, so that the embryo only transitions between S-phase and mitosis. As centriole/centrosome assembly only takes a few minutes rather than several hours like in human cells (Aydogan et al., 2018; Alvarez-Rodrigo et al., 2019; Takao et al., 2019), the assembly dynamics can be observed with high temporal resolution without drastic bleaching of the fluorophore (Douthwright and Sluder, 2017).

The embryo is an enormous syncytial cell with dimensions of around 0.18 mm in width, 0.51 mm in length, and 9*10-3 mm^3 in volume (Markow, Beall and Matzkin, 2009). With every cycle the number of centrioles/centrosomes doubles, with ~800 being assembled

at the cortex in cycle 11 to ~6000 in cycle 14 (Zalokar and Erk, 1976). This high number of equally distributed organelles and the synchrony their assembly allow the simultaneous observation of ~80-200 centriole duplication/centrosome maturation events (depending on the nuclear cycle) (Aydogan *et al.*, 2018, 2020; Alvarez-Rodrigo *et al.*, 2019).

A progressive increase in S-phase length between cycles 11-13 causes slowing of the cell cycle from 10 minutes in cycle 11 to 12 and 21 minutes in cycle 12 and 13, respectively (at 25 °C) (Foe and Alberts, 1983; Farrell and O'Farrell, 2014). The gradual slowing of S-phase length is thought to be caused by the increase in DNA content and the inhibition of cell cycle progression through suppression of Cdk1 activity by the Chk1-homologue *grapes* (Fogarty *et al.*, 1997). Only in cycle 14, when the embryo introduces its first G2 phase after DNA replication, the cell cycle slows drastically and takes more than 65 minutes. It is also in cycle 14 when the zygotic genome is activated and morphogenesis in form of cellularisation begins (Farrell and O'Farrell, 2014). This slowing of the cell cycle and the exponentially increasing number of organelles provide a naturally changing environment for the embryo. By comparing centriole duplication/centrosome maturation between nuclear cycles, it is possible to assess how developmental changes can influence their organelle assembly dynamics.

In addition to the above-mentioned advantages of using the early embryo as a model for centriole/centrosome assembly, also the anatomy of the syncytial blastoderm has previously been very well characterised (Karr and Alberts, 1986; Warn, 1986). Within this monolayer, all nuclei form their own cytoplasmic domain, which are held in place by the interplay of actin filaments and MTs. During interphase, each nucleus is associated with an actin cap that underlies the plasma membrane while MTs are organised by the

centrosome and reach deep throughout the cortical region of the cytoplasm. In mitosis, the actin caps spread out and together with the plasma membrane form furrows between cytoplasmic domains to separate neighbouring mitotic spindles, which originate from opposing centrosomes (**Figure 1-7B**) (Karr and Alberts, 1986; Warn, 1986).

1.5 Thesis aims

In the last decades, great technological advances in light and super-resolution microscopy pushed the boundaries of quantitative imaging to allow the investigation of dynamic cellular processes. In the centrosome field, many efforts were directed towards understanding how proteins localise to centrosomes and their recruitment dynamics, with the cytoplasmic fraction of these building blocks receiving relatively little attention. The aim of my thesis was to set up methodologies to assess the cytoplasmic pool of centriolar and centrosomal proteins in order to gain a more complete understanding of the mechanisms and principles that allow the embryo to so precisely regulate the rapid assembly of these complex organelles.

2 Materials and methods

2.1 Fly husbandry

2.1.1 Fly handling

Flies were maintained at 18 °C or 25 °C in plastic vials or bottles on *Drosophila* culture medium (0.68% agar, 2.50% yeast, 6.25% cornmeal (maize), 3.75% molasses, 0.42% propionic acid, 0.14% tegosept, and 0.70% ethanol). For microscopy/spectroscopy and western blotting experiments, embryos were collected in egg-laying cages on fruit juice plates (40% cranberry-raspberry juice, 2% sucrose, and 1.8% agar) with a drop of yeast paste. Fly handling techniques were performed as previously described (Roberts, 1986).

2.1.2 *Drosophila melanogaster* stocks

For all wild type (WT) controls *Oregon-R* flies were used (labelled *SFWT* in the Raff laboratory fly stocks). All genes that were expressed from their endogenous promoter (usually 2 kb 5' and 1 kb 3' to the main transcription start/stop-site for transgenics, and the entire endogenous locus for CRISPR/Cas9 mediated knock-ins) are labelled with the letter 'e' in front of their gene name. All CRISPR/Cas9-mediated mNeonGreen (mNG) knock-ins were generated from the *CFD2* fly line. Balancer chromosomes used to maintain fly lines and to generate the desired genotypes were previously described, but were crossed out of any stocks used for any experimental measurements (Lindsley and Zimm, 1992).

All alleles used in this thesis and their origin are listed in **Table 2** and the precise stocks used for experiments are listed in **Appendix A, Table 9**.

Table 2: Alleles used in this thesis

Alleles used in this thesis	Source or stock number and plasmid that was sent for injections
eSas-6-GFP#1/#6	(Aydogan *et al.*, 2018)
Sas-6^{c02901}	(Peel *et al.*, 2007)
p(Sas-6)-mNG#2	This thesis; P-element insertion; stock TS14; plasmid TS18
p(Plk4)-mNG#6	This thesis; P-element insertion; stock TS19; plasmid TS17
p(Sas-6)-dNG#10	This thesis; P-element insertion; stock TS16; plasmid pTS19
p(Sas-6)-mScarlet-I#1	This thesis; P-element insertion; stock TS88; plasmid pTS28
p(Sas-6)-mScarlet-I+mNG#5	This thesis; P-element insertion; stock TS97; plasmid pTS31
eAsl-mKate2	(Aydogan *et al.*, 2020) **(**LisaG13**)**
asl^{B46}	(Baumbach *et al.*, 2015)
ePlk4-mNG	(Aydogan *et al.*, 2020) **(**LisaG79**)**
Plk4^{Aa74}	(Aydogan *et al.*, 2018)
Ubq-Ana1	This thesis; P-element insertion; generated by Saroj Saurya
ana1^{mecB}	(Avidor-Reiss *et al.*, 2004)
mNG-eAna2 (#2)	This thesis; CRISPR/Cas9 knock-in; stock TS23; plasmid pTS3+11
eAna2-mNG (3.72)	This thesis; CRISPR/Cas9 knock-in; stock TS5; plasmid pTS4+12
mNG-eSas-6 (2.37)	This thesis; CRISPR/Cas9 knock-in; stock TS10; plasmid pTS1+9
eSas-6-mNG (#47)	This thesis; CRISPR/Cas9 knock-in; stock TS21; plasmid pTS2+10
mNG-eAsl (40.6)	This thesis; CRISPR/Cas9 knock-in; stock TS113; plasmid pTS5+13
eAsl-mNG (#74)	This thesis; CRISPR/Cas9 knock-in; stock TS25; plasmid pTS6+14
eSas-4-mNG (#47)	This thesis; CRISPR/Cas9 knock-in; stock TS27; plasmid pTS7+15
mNG-ePlk4 (PN36f)	This thesis; CRISPR/Cas9 knock-in; generated by Saroj Saurya
eAna2(WT)-mNG#1	This thesis; P-element insertion; stock TS70; plasmid pTS20
ana2$^{\Delta a}$	This thesis; CRISPR/Cas9 knock-out; generated by Zsofia Novak
eAna2(ΔCC)-mNG#4	This thesis; P-element insertion; stock TS75; plasmid pTS21
eAna2(ΔSTAN)-mNG#2	This thesis; P-element insertion; stock TS66; plasmid pTS22
eAna2(12A)-mNG#9	This thesis; P-element insertion; generated by Zsofia Novak

ana2$^{\Delta b}$	This thesis; CRISPR/Cas9 knock-out; generated by Zsofia Novak
eAna2(12A)#1	This thesis; P-element insertion; generated by Zsofia Novak
eAna2(S284A T301A)-mNG#3	This thesis; P-element insertion; stock TS49; plasmid pTS23
eAna2(S284E T301E)-mNG#9	This thesis; P-element insertion; stock TS54; plasmid pTS24
eAsl-GFP	(Blachon *et al.*, 2008)
ePlk4(WT)-mNG#20	(Aydogan *et al.*, 2020); P-element insertion; generated by Lisa Gartenmann (LisaG71))
ePlk4(SK1)-mNG	This thesis; P-element insertion; generated by Lisa Gartenmann (LisaG151)
ePlk4(KD)-mNG	This thesis; P-element insertion; generated by Lisa Gartenmann (LisaG145)
eAna2-mScarlet-I#12	This thesis; P-element insertion; stock TS152; plasmid pTS33
eSas-6-mScarlet-I#5	This thesis; P-element insertion; stock TS140; plasmid pTS34
sas-6$^{\Delta a}$	This thesis; CRISPR/Cas9 knock-out; generated by Zsofia Novak
Ubq-Ana2	This thesis; P-element insertion; generated by Catarina Vicente (7498-1-2M)
asl$^{\Delta b}$	This thesis; CRISPR/Cas9 knock-out; generated by Zsofia Novak
Ubq-Asl#8	This thesis; P-element insertion; generated by Saroj Saurya (S336)
sas-4$^{\Delta b}$	This thesis; CRISPR/Cas9 knock-out; generated by Zsofia Novak
Ubq-Sas-4#5	This thesis; P-element insertion; generated by Saroj Saurya
Ubq-Sas-6	This thesis; P-element insertion; generated by Catarina Vicente (7498-2-1M)
sak$^{\Delta a}$	This thesis; CRISPR/Cas9 knock-out; generated by Zsofia Novak
Ubq-Plk4#1	This thesis; P-element insertion; stock TS77; plasmid pTS25
eAna2(S318A T373A)-mNG#1	This thesis; P-element insertion; stock TS57; plasmid pTS37
eAna2(S318E T373E)-mNG#1	This thesis; P-element insertion; stock TS61; plasmid pTS38
eGrip75-GFP	(Tovey *et al.*, 2021) (CRISPR/Cas9 knock-in)
eGrip128-GFP	(Tovey *et al.*, 2021) (CRISPR/Cas9 knock-in)
ncd-γ-tubulin37c-GFP	(Hallen *et al.*, 2008)
Ubq-Aurora A-GFP	(Lucas and Raff, 2007)

Ubq-GFP-D-TACC	(Barros *et al.*, 2005)
stella^{592}	(Lee *et al.*, 2001)
Ubq-Grip71-GFP	(Conduit, Richens, *et al.*, 2014)
Ubq-MSPS-GFP	(Lee *et al.*, 2001)
cnn^{f04547}	Exelixis Stock Centre (Harvard Medical School, Boston, MA)
cnn^{HK21}	(Megraw *et al.*, 1999; Vaizel-Ohayon and Schejter, 1999)
Ubq-mNG-Cnn	This thesis; P-element insertion; generated by Lisa Gartenmann (LisaG37)
Ubq-Spd-2-GFP	(Dix and Raff, 2007)
Spd-2^{z35711}	(Giansanti *et al.*, 2008)
Spd-2^{G20143}	(Dix and Raff, 2007)
mNG-eCnn (38c**)**	This thesis; CRISPR/Cas9 knock-in; generated by Saroj Saurya
eSpd-2-mNG (S2C**)**	This thesis; CRISPR/Cas9 knock-in; generated by Saroj Saurya
ePolo-TRAP-GFP	(Buszczak *et al.*, 2007) (Gene trap)
Ubq-Spd-2-mNG	This thesis; P-element insertion; generated by Lisa Gartenmann (LisaG53)
Ubq-GFP-Cnn	(Lucas and Raff, 2007)
Ubq-GFP-Cnn(ΔLZ)#4	This thesis, P-element insertion; generated by Anna Caballe (AnnaC6)
Ubq-GFP-Cnn(ΔCM2)	This thesis, P-element insertion; generated by Zhe Feng (Violet4/82)
Ubq-Spd-2-GFP(ΔAsh1)	This thesis, P-element insertion; generated by Zhe Feng (Violet169/188)
y1 P(nos-cas9, w+) M(3xP3-RFP.attP)ZH-2A w*	(Port *et al.*, 2014) (CFD2 fly line for CRISPR/Cas9 injections)

2.1.3 CRISPR/Cas9-mediated fly line generation

For CRISPR/Cas9-mediated fly line generation, a single guide RNA (sgRNA) and donor plasmid for homology-directed repair (HDR) (see **Chapter 2, Section 2.2.2.1**) were injected into Cas9-expressing *CFD2* embryos as previously described (Port, Muschalik and Bullock, 2015). All injections were performed by 'The University of Cambridge Department of

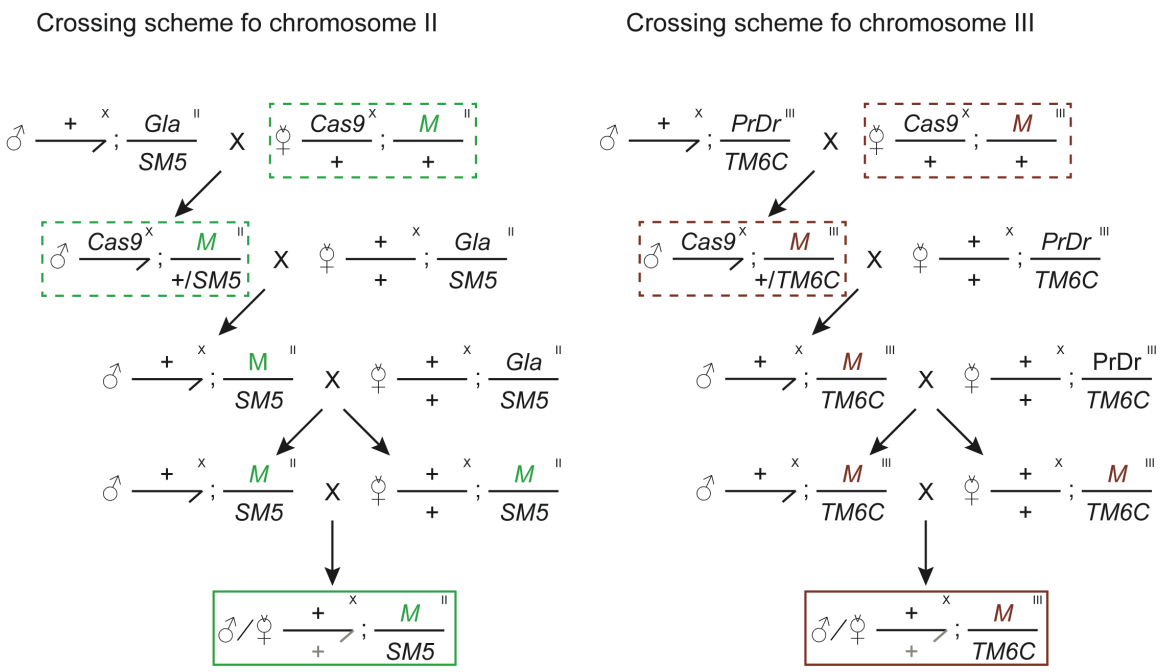


Figure 2-1: Crossing schemes for the identification and isolation of CRISPR/Cas9-mediated knock-in alleles
Crossing schemes show the screening strategy for a CRISPR/Cas9-mediated knock-in event on the second (*left*) and third (*right*) chromosome. The goal of the crossing scheme was to isolate the knock-in allele from the *Cas9* allele. All founder flies (*dashed box*) injected with the sgRNA and donor plasmid were crossed to a balancer fly line and subsequently screened by PCR for the knock-in event. If positive, 10 individual males in the next generation were crossed again to the balancer flies and screened for the knock-in allele. If the insertion was identified in this second screen (indicating germline transmission), further crosses were conducted to generate a stable line containing the knock-in allele.

Genetics Fly Facility'. After hatching, the injected founder flies were crossed to a balancer line for the second or third chromosome, *Gla/SM5* and *PrDr/TM6C* respectively. After ~10 days, single-fly lysates of the founders were generated (10 µL of microLYSIS-Plus buffer (2MLP-1000) per founder fly) and genotyped (OneTaq Quick-Load 2X Master Mix (M0486L)) for the insertion event (see screening primer combinations in **Table 3** and primer sequences and **Appendix A, Table 10**). Positive male founders were crossed 2x and positive female founders were crossed 3x to the balancer strain to isolate the mNG knock-in allele and to lose the *Cas9* allele, which was expressed from the X-chromosome (**Figure 2-1**). Afterwards, the entire gene was sequenced and compared to the same gene in the *CFD2* fly line to identify unwanted point mutations.

Table 3: Primer combinations for mNG knock-in screening

For every insertion, three potential screening primer combinations were designed: 2x with one primer binding outside of the donor plasmid sequence and one primer binding within the mNG sequence ("in+out"), and 1x with both primers binding outside the donor plasmid sequence ("Outside"). The expected size of the PCR fragment (in base pairs (bp)) for both a CRISPR/Cas9-mediated knock-in fly and WT fly is depicted.

Sas-6	**N-terminus**			**C-terminus**		
	5' in+out	3' in+out	Outside	5' in+out	3' in+out	Outside
Knock-in	1248 bp	1219 bp	2841 bp	1328 bp	1110 bp	2812 bp
WT	X	X	2100 bp	X	X	2044 bp
Primers	TS15+16	TS17+18	TS15+18	TS27+16	TS17+28	TS27+28
Ana2	**N-terminus**			**C-terminus**		
	5' in+out	3' in+out	Outside	5' in+out	3' in+out	Outside
Knock-in	1350 bp	1213 bp	2934 bp	1419 bp	1168 bp	2961 bp
WT	X	X	2193 bp	X	X	2193 bp
Primers	TS41+16	TS17+42	TS41+42	TS51+16	TS17+52	TS51+52
Asl	**N-terminus**			**C-terminus**		
	5' in+out	3' in+out	Outside	5' in+out	3' in+out	Outside
Knock-in	1275 bp	1170 bp	2819 bp	1390 bp	1186 bp	2950 bp
WT	X	X	2078bp	X	X	2182 bp
Primers	TS141+16	TS17+142	TS141+142	TS107+16	TS17+108	TS107+108
Plk4	**N-terminus**			**C-terminus**		
	5' in+out	3' in+out	Outside	5' in+out	3' in+out	Outside
Knock-in	1281 bp	1173 bp	2826 bp	1391 bp	1163 bp	2928 bp
WT	X	X	2085 bp	X	X	2160 bp
Primers	TS149+16	TS17+150	TS149+150	TS95+16	TS17+96	TS95+96
Sas-4	**C-terminus**					
	5' in+out	3' in+out	Outside			
Knock-in	1411 bp	1137 bp	2922 bp			
WT	X	X	2154 bp			
Primers	TS117+16	TS17+118	TS117+118			

The efficiency of obtaining stable mNG knock-in lines varied between genes and sgRNA target sequences. In general, I (with the help of Eline van Houtum and Saroj Saurya generated 1-4 stable, independent, CRISPR/Cas9-mediated mNG knock-in lines for each of the core centriole duplication proteins (with exception of C-terminally tagged Plk4) from ~200-500 injected *CFD2* embryos per construct.

2.1.4 Transgenic fly line generation

Transgenic fly lines were generated via random P-element insertion (injected, mapped, and balanced by 'The University of Cambridge Department of Genetics Fly Facility'). For transgene selection, the w^{+} gene marker was included in the transformation vectors and injected into the w^{1118} genetic background. Transformation vector generation for P-element insertion is described in **Chapter 2, Section 2.2.2.2**.

2.2 Molecular Biology and biochemistry

2.2.1 Purification of genomic DNA from *Drosophila melanogaster*

For initial genotype screening of CRISPR/Cas9 founder flies and recombinants, single fly lysates were generated. Individual flies were ground in 10 µL *micro*LYSIS-Plus buffer (microzone (MLP)) on ice and incubated on a thermocycler at the following temperatures to isolate the DNA:

- 65 °C for 15 minutes
- 96 °C for 2 minutes
- 65 °C for 4 minutes
- 96 °C for 1 minutes
- 65 °C for 1 minutes
- 96 °C for 0.5 minutes
- 20 °C

The microlysis mix was then directly used as DNA template for polymerase chain reaction (PCR) screening (0,2 μL/reaction).

For gene amplification and final sequencing of all CRISPR/Cas9-mediated mNG knock-in lines and P-element insertions, genomic fly DNA was used. To extract and purify the genomic DNA, 30 flies (15 male + 15 female) were ground with 400 μL Buffer A (100 mM Tris (pH 7.5), 100 mM EDTA (pH 8.0), 100 mM NaCl, 1% SDS) on ice and incubated at 65 °C for 30 minutes. Afterwards, 800 μL of Buffer B (2:7 5M Potassium acetate, 5:7 6M Lithium chloride) was added to the mix and centrifuged for 15 minutes at 12,000 RPM. 1 mL of supernatant was transferred into a new Eppendorf tube and centrifuged once more for 15 minutes at 12,000 RPM. 600 μL of isopropanol was added to the 1 mL of supernatant and spun for 15 minutes at 12,000 RPM. The supernatant was discarded, the DNA pellet washed with 1 mL of 70% ethanol (spun for 5 minutes with 12,000 RPM), dried for ~5 minutes, and resuspended in 150 μL TE buffer.

2.2.2 DNA vector design

All PCRs for cloning and sequencing were conducted using the Phusion High-Fidelity PCR Master Mix (New England Biolabs, M0531L) and for screening using the OneTaq Quick-Load 2X Master Mix (New England Biolabs, M0486L). All PCRs were conducted on a thermocycler at the temperatures and with the timings recommended by the polymerase providers. Primers were designed with a predicted annealing temperature of ~57-61 °C. All PCR products which were subsequently used for NEBuilder® HiFi DNA Assembly-based cloning were gel-purified with the QiaQuick Gel Extraction Kit (12243). For microinjections, all DNA vectors were purified using the QiaFilter Plasmid Midi Kit (12243) and the inserts were sequenced to ensure the correct nucleotide sequence. All injection

mixes were prepared according to the guidelines of the 'The University of Cambridge Department of Genetics Fly Facility' (Plan3 for P-element insertion and Plan8 for CRISPR/Cas9 genome engineering). All constructs were designed in the DNA editing software ApE (A plasmid Editor (RRID:SCR_014266)). All sequencing reactions were performed by Source BioScience (Sanger sequencing), and the sequencing data compared to its *in silico* sequence using the software MacVector.

2.2.2.1 Vector design for CRISPR/Cas-9-mediated generation of mNG knock-ins

In order to generate mNG knock-in lines for my proteins of interest, the sgRNA that directs Cas9 to the locus and the donor plasmid for HDR were injected by 'The University of Cambridge Department of Genetics Fly Facility' into the *CDF2* fly line, which expresses Cas9 in the germline from the *nos* promoter. The fly line and gRNA backbone were previously generated by and described in Port *et al.*, 2014.

sgRNA design

For each knock-in strategy, a single guide was used to induce Cas9-mediated cleavage. The sgRNA target sequences were previously chosen based on a sgRNA design algorithm (Gratz *et al.*, 2014) and tested for effectiveness by Zsofia Novak. A sgRNA target sequence close to the insertion site was chosen, preferably within the coding sequence of the gene (to allow the mutation of individual nucleotides -> see donor plasmid design). The sgRNA sequences were synthesised as primers with 5'-GTCG (for the 5' strand) and 5'-AAAC (for the 3' strand) overhangs and cloned into the linearised pCFD3 plasmid as described in Port *et al.*, 2014. The insertion of the guide sequence was confirmed by PCR screening (TS57+58) followed by sequencing of the PCR product. **Table 4** lists all the generated

sgRNA plasmids, and **Appendix A, Table 11** the primers used for the sgRNA plasmid generation.

Table 4: List of generated sgRNA plasmids

ID	Plasmid	Resistance
pTS1	sgRNA Sas-6 Nterm in pCFD3	Ampicillin
pTS2	sgRNA Sas-6 Cterm in pCFD3	Ampicillin
pTS3	sgRNA Ana2 Nterm in pCFD3	Ampicillin
pTS4	sgRNA Ana2 Cterm in pCFD3	Ampicillin
pTS5	sgRNA Asl Nterm in pCFD3	Ampicillin
pTS6	sgRNA Asl Cterm in pCFD3	Ampicillin
pTS7	sgRNA Sas-4 Cterm in pCFD3	Ampicillin
pTS8	sgRNA Plk4 Nterm in pCFD3	Ampicillin
pTS35	sgRNA Plk4 Cterm in pCFD3	Ampicillin

Donor plasmid design for HDR

Donor plasmids were generated using the NEBuilder® HiFi DNA Assembly Master Mix. 1 kb homology arms were amplified from genomic *CFD2* DNA, mNG including a linker (Nterm: TATCAAACAAGTTTGTACAAAAAAGCAGGCTTC; Cterm: GACCCAGCTTTCTTGTACAAAGTGG-TTCGATATCCAGCACAGTGGCGGCCGCTCGAG) and the plasmid backbone (pBluescript SK-) were amplified from previously generated and sequenced constructs in the lab. The donor plasmid assembly strategy is further described in **Figure 2-2**. Complementary 10 bp-overhangs on each primer (leading to a 20 bp total overhang between two fragments) allowed the simultaneous fusion of all four PCR fragments (backbone, 1 kb homology arm upstream, linker+mNG, 1 kb homology arm downstream) within one NEBuilder® reaction. To inhibit the binding of the sgRNA/Cas9 to the target sequence within the homology arm of the repair construct, point mutations—where possible and especially in the NGG

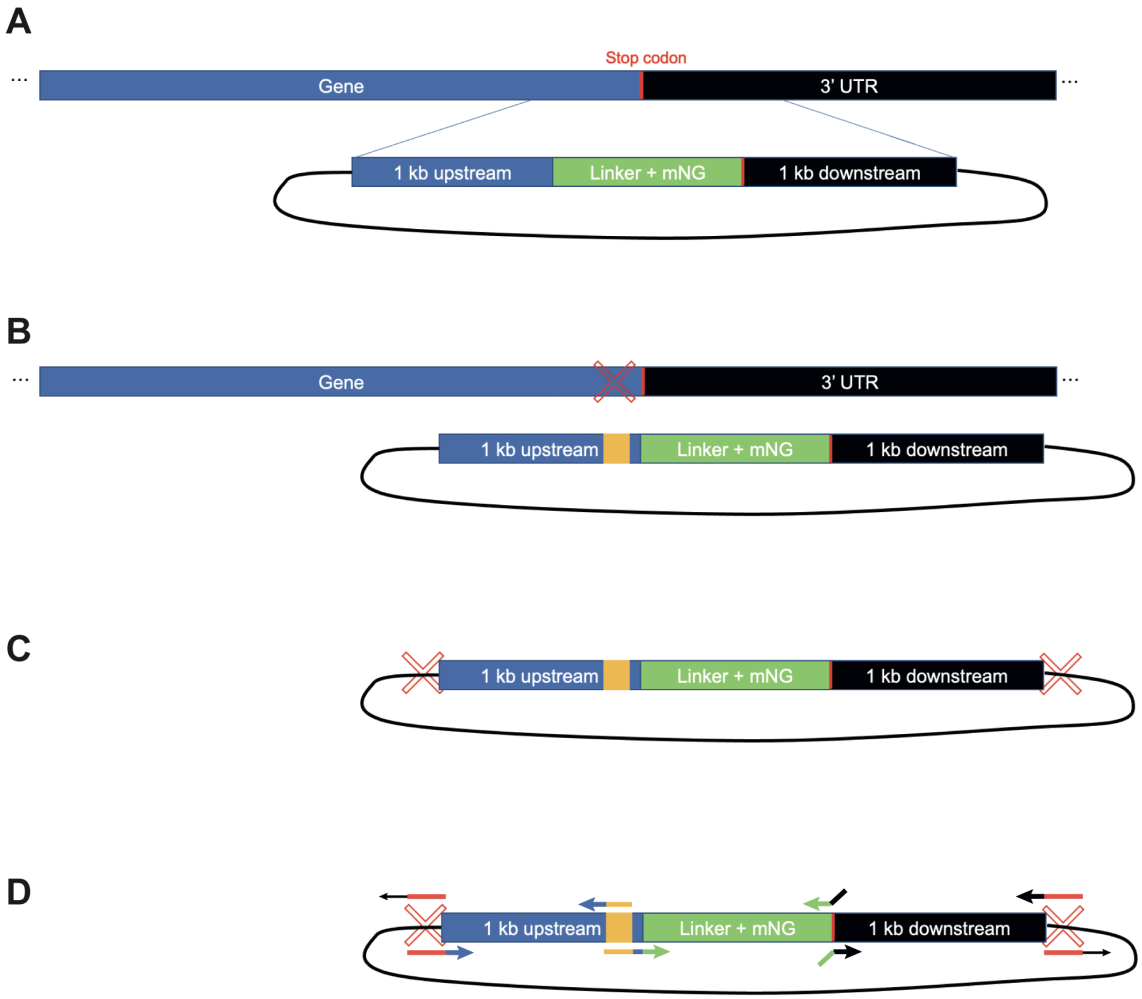


Figure 2-2: *In silico* construction of the donor plasmid for homology-directed repair (HDR)
(A) Generation of a plasmid sequence that contains the two homology arms, fluorescent protein (mNG) with linker, and backbone vector. Note that for tagging on the C-terminus (as depicted here), the fluorophore is inserted before the stop codon. **(B)** The sgRNA will target Cas9 to its complementary site (*red* cross). To avoid the cleavage of the homology arm within the donor plasmid, the binding sequence is modified (*orange* box, see main text). **(C)** In order to linearise the donor plasmid *in vivo,* the sgRNA target sequence is introduced on both flanking regions of the homology arms. **(D)** All DNA fragments are amplified via PCR with overhangs complementary to their associated fragments to allow cloning via Gibson assembly.

protospacer adjacent motif (PAM) sequence—were generated that only affected individual base pairs but not the amino acid sequence (indicated by the *orange* box in the upstream sequence in **Figure 2-2**). This strategy would prevent the Cas9 from cleaving the donor plasmid and the knock-in construct once it had been inserted into the endogenous locus. Further, I also introduced the sgRNA target sequence and PAM sequence to the outer flanks of both homology arms to induce Cas9-mediated cleavage and thereby linearisation of the repair template *in vivo*, which should increase the efficacy of HDR. The

point mutations within the homology arm and the addition of the cleavage site in the flanking regions were both introduced by extended primers (~40-50 bp) with complementary overhangs to the neighbouring fragments that were directly used for PCR amplification and subsequently for NEBuilder® HiFi DNA Assembly (**Figure 2-2D**). A list of all donor plasmids can be found in **Table 5**, and all primers designed for the donor plasmid cloning are listed in **Appendix A, Table 11.**

Table 5: List of generated HDR donor plasmids

ID	Plasmid	Resistance
pTS9	HDR template Sas-6 Nterm in pBS SK-	Ampicillin
pTS10	HDR template Sas-6 Cterm in pBS SK-	Ampicillin
pTS11	HDR template Ana2 Nterm in pBS SK-	Ampicillin
pTS12	HDR template Ana2 Cterm in pBS SK-	Ampicillin
pTS13	HDR template Asl Nterm in pBS SK-	Ampicillin
pTS14	HDR template Asl Cterm in pBS SK-	Ampicillin
pTS15	HDR template Sas-4 Cterm in pBS SK-	Ampicillin
pTS16	HDR template Plk4 Nterm in pBS SK-	Ampicillin
pTS36	HDR template Plk4 Cterm in pBS SK-	Ampicillin

2.2.2.2 Vectors for P-element-mediated insertion

In order to generate transformation vectors for P-element-mediated insertion, I used Gateway cloning (Life Technologies) where the gene of interest was cloned into a pDONR™ vector and then recombined via the Gateway LR reaction into the appropriate destination vector (DEST). pDONR and empty DEST vectors, which were used in this thesis, were previously generated by members of the Raff laboratory. All pDONRs were assembled using the NEBuilder® HiFi DNA Assembly Master Mix. For some genes, I directly generated the DEST vector via NEBuilder® HiFi DNA Assembly. Therefore, there is no

pDONR listed for those constructs in **Table 6**. All genes were expressed from their endogenous core promoter (~2 kb upstream of the start codon and ~1 kb downstream of the stop codon), except Ubq-Plk4 (pTS25), which used the Ubq promoter (Lee, Simon and Lis, 1988) (LR reaction of pDONR Plk4 cDNA (Raff lab plasmid #268) into the pUbq empty DEST vector (Raff lab plasmid #78)). For plasmids pTS21 and pTS22 the cDNA of Ana2 was initially amplified from Matthew Cottee's cDNA stocks #175 and #208, respectively. Therefore, Ana2's intron was afterwards re-introduced using the primers TS173+174 (PCR-amplification followed by NEBuilder® HiFi DNA Assembly). All fluorophores were amplified from previously generated plasmids in the lab, the Ana2 gene for pTS20 from Raff lab plasmid #131, pTS23 and pTS24 from Lisa Gartenmann's plasmids (no ID number), pTS37 from Raff lab plasmid #147, and pTS38 from Raff lab plasmid #148. For pTS33 and pTS34, an LR reaction between a DEST vector with the C-terminal mScarlet-I fluorescent tag (provided by João Monteiro) was recombined with the Raff lab plasmids #131 and #130, respectively. Afterwards, the stop codon within both genes had to be removed, which was achieved by PCR amplification of both vectors with the primers TS221+222 and TS223+224, respectively, followed by NEBuilder® HiFi DNA Assembly. A list of all pDONR and DEST plasmids can be found in **Table 6**, and all primers designed for their assembly are listed in **Appendix A, Table 12**.

Table 6: List of generated pDONR and DEST plasmids

ID	Plasmid	Resistance
pTS17	p(Plk4)-mNG pDONR	Zeocin
	p(Plk4)-mNG DEST	Kanamycin
pTS18	p(Sas-6)-mNG pDONR	Zeocin
	p(Sas-6)-mNG DEST	Kanamycin

pTS19	p(Sas-6)-dNG pDONR	Zeocin
	p(Sas-6)-dNG DEST	Kanamycin
pTS20	eAna2(WT)-mNG DEST	Kanamycin
pTS21	eAna2(ΔCC)-mNG DEST	Kanamycin
pTS22	eAna2(ΔSTAN)-mNG DEST	Kanamycin
pTS23	eAna2(S284A T301A)-mNG pDONR	Zeocin
	eAna2(S284A T301A)-mNG DEST	Kanamycin
pTS24	eAna2(S284E T301E)-mNG pDONR	Zeocin
	eAna2(S284E T301E)-mNG DEST	Kanamycin
pTS25	Ubq-Plk4 DEST	Kanamycin
pTS26	p(Sas-6)-mCardinal pDONR	Zeocin
	p(Sas-6)-mCardinal DEST	Kanamycin
pTS27	p(Sas-6)-mKate2 pDONR	Zeocin
	p(Sas-6)-mKate2 DEST	Kanamycin
pTS28	p(Sas-6)-mScarlet-I pDONR	Zeocin
	p(Sas-6)- mScarlet-I DEST	Kanamycin
pTS29	p(Sas-6)-mCardinal+mNG pDONR	Zeocin
	p(Sas-6)-mCardinal+mNG DEST	Kanamycin
pTS30	p(Sas-6)-mKate2+mNG pDONR	Zeocin
	p(Sas-6)-mKate2+mNG DEST	Kanamycin
pTS31	p(Sas-6)-mScarlet-I+mNG pDONR	Zeocin
	p(Sas-6)- mScarlet-I+mNG DEST	Kanamycin
pTS33	eAna2-mScarlet-I DEST	Kanamycin
pTS34	eSas-6-mScarlet-I DEST	Kanamycin
pTS37	eAna2(S318A S373A)-mNG DEST	Kanamycin
pTS38	eAna2(S318E S373E)-mNG DEST	Kanamycin

2.2.3 Immunoblotting

2.2.3.1 Sample collection and preparation

Embryos for SDS-PAGE followed by western blotting experiments were collected in egg-laying cages for 3 hours and then washed 3x with 1x PBS + 0.0005% Tween-20 to remove residual yeast. The embryos were then bathed in 60% bleach solution for 2 minutes to break their chorion, and subsequently washed 2x with 1x PBS + 0.0005% Tween-20. For fixation, the dechorionated embryos were transferred into a methanol-containing glass vial using heptane. The glass vial was rigorously shaken for ~30 seconds to remove the entire chorion which resulted in most embryos subsiding to the bottom of the lower methanol layer. The upper heptane layer and most of the methanol layer were carefully removed and discarded. Afterwards, the embryos were resuspended in 1 mL fresh methanol and stored at 4 °C in an Eppendorf tube (at least overnight).

To remove the methanol for the sample preparation, fixed embryos were washed and rotated 3x in 1x PBT (1x PBS + 0.1% Triton X-100) for 15 minutes each. In a watch glass containing 1x PBT and under a dissection scope, between 20 and 100 pre-cellularisation stage embryos were selected and transferred into a new Eppendorf tube (in 10-50 µL buffer (depending on the number of embryos)) and mixed with 10-50 µL of 2x SDS loading dye to a final concentration of 1x SDS loading dye and 1 embryo/µL. The mix was then boiled at ~97 °C for 10 minutes on a heat block, gently spun for a few seconds on a small lab bench centrifuge and stored at -20 °C.

2.2.3.2 SDS-PAGE and western blotting

For all SDS-PAGE followed by western blotting experiments conducted in this thesis, 10 µL of sample (which is the equivalent of 10 embryos) was loaded into each lane of a 3-8%

Tris-Acetate pre-cast SDS-PAGE gel (Invitrogen, Thermo Fisher Scientific) and run at 150V for 1.25-1.5hrs in running buffer (1x Tris-Acetate SDS Running Buffer (Life Technologies (LA0041)) in a XCell SureLock Mini-Cell. The samples were then transferred from the gel onto a nitrocellulose membrane (BIO-RAD, 0.2 μm (162-0112)) at 100V for at least 1 hour in transfer buffer (25% methanol, 1.13% Glycin, 0.58% Tris, 0.01% SDS) using a BIO-RAD Mini Trans-Blot system. Afterwards, membranes were incubated with blocking buffer (1x PBS + 4% milk powder + 0.1% Tween20) for at least 1 hour on an orbital shaker at room temperature, then for 1 hour in blocking buffer with the primary antibody (1:500 dilution). The membrane was washed 3x with TBST (1x TBS + 0.1% Tween-20)—and primary antibodies were reused several times—before the membrane was incubated for another 45 minutes in blocking buffer with the secondary antibody (1:3000 dilution, horseradish peroxidase-conjugated for chemiluminescence analysis). The membranes were washed 3x for 15 minutes with TBST buffer, before incubation for 1 minute in SuperSignal™ West Femto Maximum Sensitivity Substrate (at a concentration that was empirically determined for each different protein—see **Table 7**) and exposed to X-ray film for ~10-60 seconds. If the membranes were to be reused, they were washed 2x with 1xPBS and incubated with Restore™ Western Blot Stripping Buffer (21059) for 15 minutes. The antibodies and substrate concentrations used in this thesis can be found in **Table 7**.

Table 7: Antibodies and substrate concentrations used in this thesis

Primary antibody	Secondary antibody	Substrate dilution
α-GFP #186 (Mouse)	α-Mouse #13	1:1 (for Sas-6)
α-actin #221 (Mouse)	α-Mouse #13	1:2
α-Ana2 NT #6 (Rabbit)	α-Rabbit #39	1:2
α-Sas-6 Mid #49 (Rabbit)	α-Rabbit #39	1:2

α-mNG #254 Mouse	α-Mouse #13	1:2 (for Ana2)
α-Asl NT #11 (Rabbit)	α-Rabbit #39	1:4
α-Sas-4 NT #63 (Rabbit)	α-Rabbit #39	1:3
α-Gaga #144 (Rabbit)	α-Rabbit #39	1:5

2.3 Live microscopy and spectroscopy

2.3.1 Preparation of *D. melanogaster* embryos

Embryos were collected in egg-laying cages for 1 hour at 25 °C and then left at 25 °C to develop for another 45 minutes. Afterwards, the embryos were manually dechorionated by gently rolling them over sticky tape. The embryos were then transferred onto a line of glue (which originated from sticky tape that had previously been dissolved in heptane) on MatTek dishes (1.5H thick glass bottom, MatTek Corperation, USA) for spinning-disk confocal microscopy and on high precision 35 mm, high Glass Bottom µ-dishes (ibidi) for FCS/FCCS/PeCoS measurements. Embryos were covered in Voltalef H10S PCTFE oil (ARKEMA, France) to avoid desiccation.

2.3.2 Fluorescence correlation spectroscopy (FCS)

The FCS methodology I describe here was partially published in Aydogan *et al.*, 2020 and Alvarez-Rodrigo *et al.*, 2019.

2.3.2.1 Spectroscopy setup and measurements

Point FCS measurements were performed on a confocal Zeiss LSM 880 (Argon laser excitation at 488 nm and GaASP photon-counting detector (491-544 nm detector range)) with the Zen Black Software. A C-Apochromat 40x/1.2 W objective and a pinhole setting of 1AU were used. Measurements were conducted with a laser power of 6.31 µW (except for eAsl-GFP which was measured with a laser power of 10.00 µW), and no

photobleaching was observed for any protein. The microscope was kept between 25.0-26.0 °C using the Zeiss inbuilt heating insert P and the heating unit XL. The measurement procedure is described in detail in **Chapter 3, Section 3.2.1**, with a schematic overview in **Figure 3-3**.

The effective volume (V_{eff}) of the imaging setup was estimated to be ~0.25 fL by averaging the two most similar results (**2** and **3**) obtained from three independent methods (**Figure 3-2B**), as previously described in Ruettinger *et al.*, 2008:

1) Measuring the concentration of a soluble Alexa Fluor™ 488 NHS Ester dilution series (100 nM, 10 nM, 1 nM and 0.1 nM). The dilution series of the Alexa488 fluorophore was prepared in purified water with 0.05% Tween-20 and measured with FCS ~3 µm above the coverslip. From the height of the ACF the average number of particles can be determined and therefore the size of V_{eff} can be estimated (**Figure 2-3A**).

2) Measuring the diffusion time for Alexa Fluor™ 488 NHS Ester (same concentrations that were used for the dilution series) in water at 25 °C. The measured diffusion time was then compared to a previously reported diffusion coefficient for the Alexa Fluor™ 488 NHS Ester (Petrášek and Schwille, 2008) and V_{eff} calculated accordingly (**Figure 2-3B**).

3) Imaging subresolution beads (FluoSpheres™ Carboxylate-Modified Microspheres, 0.1 µm) and determining V_{eff} via Gaussian fitting with the *line tool* and *Z-axis profile* in ImageJ (Bethasda, USA). Multiple stacks were taken at varying correction collar position to correct for the spherical aberrations caused by the cover glass. When measured with either end of the spherical aberration correction collar, V_{eff} size increased drastically, and

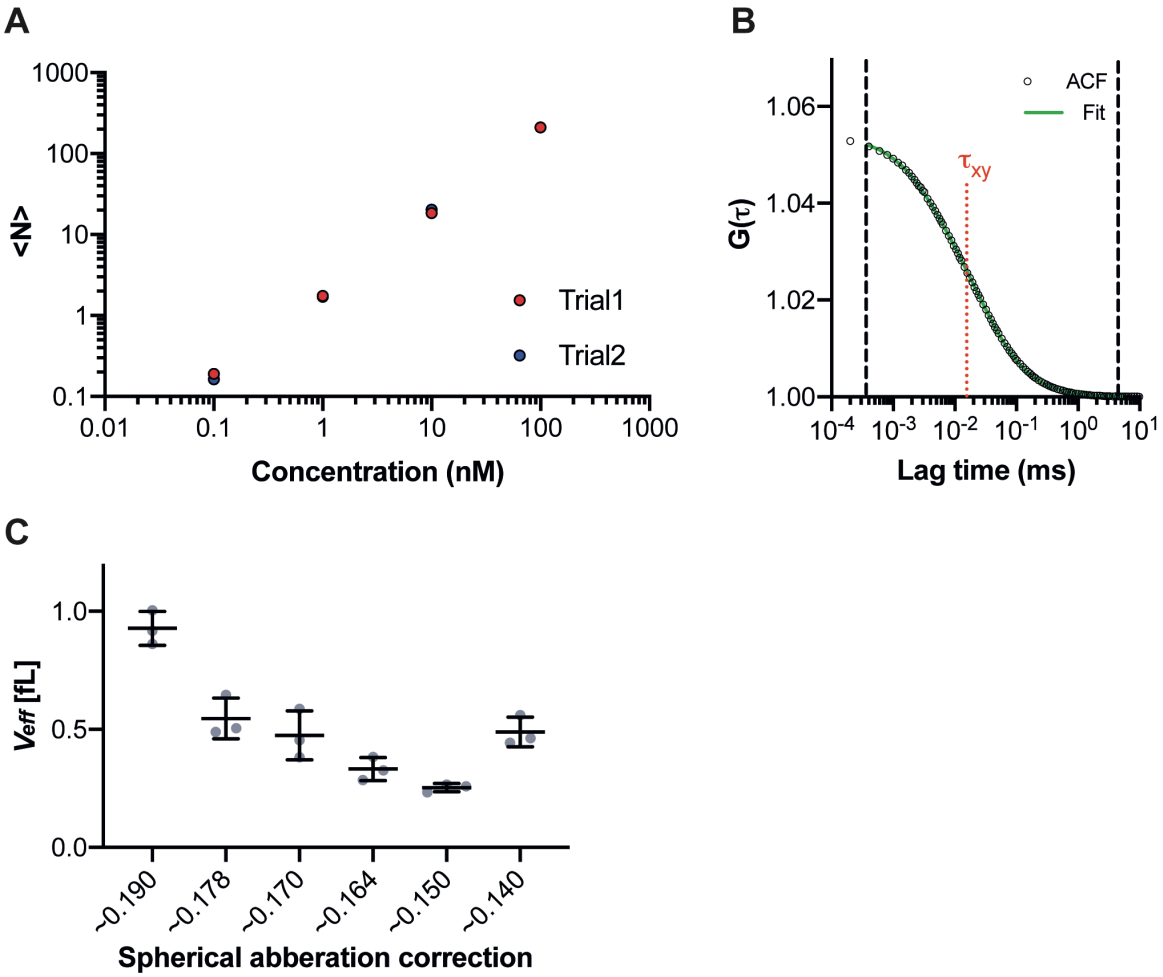


Figure 2-3: Estimation of the effective volume (V_{eff}) size
Three independent methods to estimate the size of V_{eff} were used. **(A)** Graph shows two technical repeats of an Alexa Fluor™ 488 NHS Ester dilution series of known concentration that were measured with FCS. These data highlight the reproducibility and wide range in which FCS is sensitive *in vitro*. **(B)** The mean residence time for Alexa Fluor™ 488 NHS Ester in water was measured and compared to its previously reported diffusion coefficient. **(C)** Immobilised sub-resolution beads were imaged with a wide range of spherical aberration correction collar positions. Every data point represents an independent bead measurement. Data are presented as mean±SD.

the spherical aberration position that yielded the most consistent and smallest volume was used for the calculation of V_{eff} (~0.150) (**Figure 2-3C**).

Before taking any measurements, I let the temperature of the system stabilise for 1 hour. I then adjusted the pinhole path (see microscope manual) and the correction collar of the objective to maximise the photon count-rate per molecule (CPM) in a concentrated fluorophore solution. For experimental FCS recordings, consecutive cytoplasmic measurements were made 6x for 10 seconds each at the centriolar plane of the embryo.

Individual recordings where centrioles moved through the measurement spot, which generated a highly erratic correlation curve (<1% of all recordings), were discarded. In some cases, I slightly readjusted the cytoplasmic position of the laser beam during the measurement but discarded the individual recording in which the readjustment was made.

2.3.2.2 Autocorrelation analysis and post-acquisition curve fitting

The autocorrelation function, *G(τ)*, was calculated during each measurement in the Zen Black software using **Equation 1**:

$$G(\tau) = \frac{\langle \delta I(t) \cdot \delta I(t+\tau) \rangle}{\langle I(t) \rangle^2}$$

Equation 1

where $\langle\,\rangle$ denotes a time average, $\delta I(t)$ describes the intensity fluctuation at the time point *t*, and τ states the lag time of the autocorrelation.

All 10 second-long recordings were then fitted with 8 different 3D diffusion models using **Equation 2** in the software FoCuS-Point (Waithe *et al.*, 2016):

$$G_{3D}(\tau) = \sum_{k=1}^{D_s} A_k \left(1 + \left(\frac{\tau}{\tau_{xyk}}\right)^{\alpha^k}\right)^{-1} \left(1 + \left(\frac{\tau}{AR^2\tau_{xyk}}\right)\right)^{-1/2}$$

Equation 2

where A_k defines the fraction of a diffusing species for which the sum of all diffusing species equals 1, τ_{xy} describes the average residence time of the diffusing species in V_{eff}, α accounts for anomalous subdiffusion within the cytoplasmic environment, and *AR* is a structural parameter that describes the relationship among the x-, y-, and z-axis of the excitation volume.

Dark states of the fluorophore were fitted with **Equation 3**:

$$G_T(\tau) = 1 + \sum_{j=1}^{T_s} \frac{T_j}{1 - T_j} \cdot e^{-\tau/\tau_{Tj}}$$

Equation 3

where T_j depicts the triplet population, and τ_{Tj} states the triplet correlation time during which the fluorophore remains in the dark state (Schonle *et al.*, 2014).

The data was fitted with eight different diffusion models (**Ms**): **M1)** 1 diffusing species (ds) 0 blinking states (bs) 0 triplet states (ts); **M2)** 1ds 1bs 0ts; **M3)** 1ds 0bs 1ts; **M4)** 1ds 1bs 1ts; **M5)** 2ds 0bs 0ts; **M6)** 2ds 1bs 0ts; **M7)** 2ds 0bs 1ts; **M8)** 2ds 1bs 1ts—within the boundaries of $4x10^{-4}$ ms and ~$1\text{-}3x10^{3}$ ms (depending on the protein), τ_{xy} restricted to ≥0.6 ms in models with two diffusing species (**M5-M8**), and the dark states of the fluorophore were restricted to 10-300 µs for the blinking state and 1-10 µs for the triplet state. In all models, the structural parameter *AR* was kept constant at 5, and the anomalous

subdiffusion parameter α was selected individually for each protein based on the curve's best fit (tested with 0.05 increments).

In order to avoid over-fitting the data, the most plausible diffusion model to describe a protein's cytoplasmic behaviour was selected using the Bayesian information criterion (BIC), which is based on the likelihood function (best fit), but introduces a penalty term for the complexity (number of variables) of the models (Schwarz, 1978). I collaborated with Christoffer Lagerholm (WIMM, University of Oxford), who wrote a customised Mathematica script that allows the comparison of multiple diffusion models on large datasets based on the BIC. All ACFs of an entire genotype were fitted with the diffusion model that was predicted to be the most suited one to describe the shape of the majority of correlation curves. In **Table 8**, the preferred diffusion model for each protein measured in this thesis and its most suited anomalous subdiffusion parameter are listed.

Table 8: Selected model and anomalous subdiffusion parameter α for all proteins measured with FCS
α describes the non-linearity of a protein's mean square displacement due to macromolecular crowding within the cytoplasmic environment.

Protein	Model	α
eSas-6-GFP (transgenic line) (1x, 2x, and 4x)	**M4)** 1ds 1bs 1ts	0.75
p(Plk4)-mNG (transgenic line)	**M3)** 1ds 0bs 1ts	0.70
p(Sas-6)-mNG (transgenic line)	**M3)** 1ds 0bs 1ts	0.75
p(Sas-6)-dNG (transgenic line)	**M4)** 1ds 1bs 1ts	0.85
mNG-eAna2 (CRISPR/Cas9 knock-in)	**M4)** 1ds 1bs 1ts	0.80
eAna2-mNG (CRISPR/Cas9 knock-in)	**M4)** 1ds 1bs 1ts	0.80
mNG-eSas-6 (CRISPR/Cas9 knock-in)	**M4)** 1ds 1bs 1ts	0.80
eSas-6-mNG (CRISPR/Cas9 knock-in)	**M4)** 1ds 1bs 1ts	0.80
eSas-6-mNG/+ (CRISPR/Cas9 knock-in)	**M4)** 1ds 1bs 1ts	0.80
eAsl-mNG (CRISPR/Cas9 knock-in)	**M4)** 1ds 1bs 1ts	0.75

eSas-4-mNG (CRISPR/Cas9 knock-in)	**M4)** 1ds 1bs 1ts	0.80
eAna2(WT)-mNG (transgenic line)	**M4)** 1ds 1bs 1ts	0.85
eAna2(WT)-mNG/+ (transgenic line)	**M4)** 1ds 1bs 1ts	0.80
eAna2(ΔCC)-mNG (transgenic line)	**M4)** 1ds 1bs 1ts	0.85
eAna2(ΔSTAN)-mNG (transgenic line)	**M4)** 1ds 1bs 1ts	0.85
eAna2(12A)-mNG (transgenic line)	**M4)** 1ds 1bs 1ts	0.80
eAna2(S284A T301A)-mNG (transgenic line)	**M4)** 1ds 1bs 1ts	0.80
eAna2(S284E T301E)-mNG (transgenic line)	**M4)** 1ds 1bs 1ts	0.80
eAsl-GFP (transgenic line) (laser = 10µW)	**M4)** 1ds 1bs 1ts	0.70
eAna2(S318A S373A)-mNG (transgenic line)	**M4)** 1ds 1bs 1ts	0.80
eAna2(S318E S373E)-mNG (transgenic line)	**M4)** 1ds 1bs 1ts	0.80
eGrip75-GFP (CRISPR/Cas9 knock-in)	**M4)** 1ds 1bs 1ts	0.65
eGrip128-GFP (CRISPR/Cas9 knock-in)	**M4)** 1ds 1bs 1ts	0.55
ncd-γ-tubulin-GFP (transgenic line)	**M4)** 1ds 1bs 1ts	0.65
Ubq-Aurora A-GFP (transgenic line)	**M3)** 1ds 0bs 1ts	0.75
Ubq-GFP-D-TACC (transgenic line)	**M4)** 1ds 1bs 1ts	0.45
Ubq-Grip71-GFP (transgenic line)	**M4)** 1ds 1bs 1ts	0.45
Ubq-MSPS-GFP (transgenic line)	**M4)** 1ds 1bs 1ts	0.60
mNG-eCnn (CRISPR/Cas9 knock-in) (1x and 2x)	**M4)** 1ds 1bs 1ts	0.75
Ubq-mNG-Cnn (transgenic line)	**M4)** 1ds 1bs 1ts	0.80
Ubq-GFP-Cnn (transgenic line) (1x, 2x, and 4x)	**M3)** 1ds 0bs 1ts	0.55
eSpd-2-mNG (CRISPR/Cas9 knock-in) (1x and 2x)	**M4)** 1ds 1bs 1ts	0.80
eSpd-2-mNG (CRISPR/Cas9 knock-in) (2x) +Ubq-Spd-2-mNG (transgenic line) (1x or 2x)	**M4)** 1ds 1bs 1ts	0.80
ePolo-GFP (TRAP line)	**M4)** 1ds 1bs 1ts	0.50
Ubq-GFP-Cnn(WT)/+	**M4)** 1ds 1bs 1ts	**0.60**
Ubq-GFP-Cnn(ΔLZ)/+	**M4)** 1ds 1bs 1ts	**0.55**
Ubq-GFP-Cnn(ΔCM2)/+	**M3)** 1ds 0bs 1ts	**0.55**

Ubq-Spd-2(WT)-GFP/+	**M3)** 1ds 0bs 1ts	**0.65**
Ubq-Spd-2(ΔAsh1)-GFP/+	**M3)** 1ds 0bs 1ts	**0.65**

The cytoplasmic concentration was calculated from the FoCuS-point fit data of the preferred model (**Equation 4**):

$$\langle N \rangle = \frac{1}{G_0} \quad ; \quad conc. = \frac{\langle N \rangle}{V_{eff}}$$

Equation 4

where *N* states the average number of particles within the effective volume V_{eff}, and G_0 represents the height of the autocorrelation function at *t=0*.

In order to estimate the contribution of the background noise, WT embryos were measured with the same laser intensity (6,31 µW and 10 µW) and in roughly the same position and developmental stage as the embryos of interest. Despite no observable correlated background, the uncorrelated background contributed up to ~40% of the total detected signal (also referred to as the total photon-count rate), presumably due to the low concentration of some centriolar proteins and the high autofluorescence of the embryo itself. Background corrections were performed after the autocorrelation analysis by calculating the correction factor χ^2 using **Equation 5** (Koppel, 1974):

$$\frac{1}{\chi^2} = \frac{1}{\left(1 + \frac{\langle b \rangle}{\langle f \rangle}\right)^2} \quad ; \quad \langle N_{cor} \rangle = \frac{1}{\chi^2 G_0}$$

Equation 5

where $\langle b \rangle$ denotes the average total photon-count rate of the background and $\langle f \rangle$ states the average total photon-count rate of the sample.

In order to calculate the diffusion coefficient *D* (**Equation 6**), the mean residence time τ_{xy} (that describes how long the particle—on average—resides in V_{eff}) was extracted from the inflection point of the ACF. Further, it is necessary to know the lateral laser beam radius ω_{xy} which was previously determined during the estimation of V_{eff}.

$$D = \frac{\omega_{xy}^2}{4\,\tau_{xy}}$$

Equation 6

FCS also allows the determination of a protein's average cytoplasmic stoichiometry by quantifying the average number of photons detected per fluorescent particle passing through the excitation spot (see **Chapter 3** for further explanation). For stoichiometry measurements, the total photon-count rate (after subtraction of the background fluorescence) was divided by the average number of particles present in V_{eff} to obtain the average photon-count rate per molecule (CPM), also referred to as molecular brightness (**Equation 7**):

$$\langle CPM \rangle = \frac{\langle Total\ photon\text{-}count\ rate^{SAMPLE} \rangle - \langle Total\ photon\text{-}count\ rate^{CONTROL} \rangle}{\langle N_{cor} \rangle}$$

Equation 7

In some FCS measurements a sudden drop in CPM was observed, possibly due to movements within the embryo or the embryo drifting away from the measurement plane. When this happened, a strong, often unreasonable increase in concentration and decrease in CPM was observed (Ruettinger *et al.*, 2008). These outliers were therefore discarded based on a ROUT outlier test (with the aggression factor Q=1%) (Motulsky and Brown, 2006), which was performed on all 10-second-long measurements. FCS measurements with at least 4x10 second recordings (after discarding outliers and erratically shaped ACFs) were included in the final analysis. For measurements throughout an entire nuclear cycle, only embryos where all measurements consisted of at least 4x10 second recordings were kept for the final analysis.

2.3.3 Fluorescence cross-correlation spectroscopy (FCCS)

The same spectroscopy setup as for FCS measurements was used but now using two laser lines (488 nm excitation with a 508-543 nm detector range and 561 nm excitation with a 579-695 nm detector range). The pinhole size was set to 1AU and the light path was adjusted using both laser lines and a concentrated green and red fluorophore solution as previously described in Bacia and Schwille, 2007. This resulted in a similar pinhole position in both channels indicating a good overlap in xy for the two laser lines. FCCS measurements were conducted for 20 or 30 seconds, and the laser powers chosen for the initial experiments were ~3-6 µW for 488 nm and ~25-30 µW for 561 nm. These settings were chosen based on attempts to maximise the amplitude of the cross-correlation

function measured in positive control embryos. As I will discuss in **Chapter 3, Section 3.2.2.2**, I overall only managed to obtain a very low cross-correlation amplitude, and I therefore believe that further optimisation of the spectroscopy conditions (or change to a different red fluorophore) will be necessary to obtain higher cross-correlations. Before every FCCS measurement, the measurement spot was pre-bleached for 3 seconds with the same laser intensities that were used for the recordings to avoid cross-correlation of the bleaching of the background fluorescence.

The cross-correlation function, $G_X(\tau)$, was calculated during each measurement in the Zen Black software using the following equation:

$$G_X(\tau) = \frac{\langle \delta I_G(t) \cdot \delta I_R(t+\tau) \rangle}{\langle I_G(t) \rangle \cdot \langle I_R(t) \rangle}$$

Equation 8

The calculation of the cross-correlation function (**Equation 8**) is very similar to the calculation of the autocorrelation function (**Equation 1**) but compares the intensity fluctuations of one channel over time with the fluctuations in a second channel rather than with itself (in **Equation 8**, G=Green channel, R=Red channel). FCCS measurements also allow the simultaneous generation of the individual ACFs of both channels, and the amplitude of the cross-correlation function at t=0 ($G_X(0)$) relative to the amplitude of the ACFs ($G_G(0)$ and $(G_R(0)$) infers the fraction of mutually diffusing particles (**Equation 9-11**). n_{GR} depicts the number of green-red labelled particles, n_G the number of green labelled particles, and n_R the number of red labelled particles.

$$G_G(0) = \frac{1}{n_G + n_{GR}} \quad ; \quad G_R(0) = \frac{1}{n_R + n_{GR}} \quad ; \quad G_X(0) = \frac{n_{GR}}{(n_G + n_{GR}) \cdot (n_R + n_{GR})}$$

Equation 9

$$\frac{G_X(0)}{G_R(0)} = \frac{n_{GR}}{n_G + n_{GR}} = Fraction\ of\ green\ in\ complex\ with\ red$$

Equation 10

$$\frac{G_X(0)}{G_G(0)} = \frac{n_{GR}}{n_R + n_{GR}} = Fraction\ of\ red\ in\ complex\ with\ green$$

Equation 11

For the curve fitting of the FCCS control experiments, only the green ACFs (as described in the FCS methodology) and the cross-correlation functions were analysed in the software FoCuS-point as the time scale of the mean residence time and of the dark states of the red fluorophore seemed to be in a similar range and therefore indistinguishable for the model fitting. The cross-correlation function was fitted with a diffusion model of a single diffusing species without any dark states of the fluorophore (as previously described (Bacia and Schwille, 2007)), and with an anomalous subdiffusion parameter of *α=1* (as *α* only influences the inflection point of the curve, but not the amplitude which is extracted for FCCS measurements).

2.3.4 Peak counting spectroscopy (PeCoS)

The PeCoS methodology I describe here was partially published in Aydogan *et al.*, 2020.

PeCoS uses the same setup as the point FCS protocol described above (except for a laser power of 10 µW), but it differs in terms of its data acquisition and analysis. In PeCoS, the intensity peaks, which are generated by a fluorophore moving through V_{eff}, are counted as a proxy for relative cytoplasmic concentration. Due to the low abundance of the fluorescently tagged protein of interest, spherical aberrations could not be corrected within the same embryo where the measurements were taken. Therefore, embryos that expressed a bright fluorescent centriolar marker were positioned next to the experimental embryos on the same imaging dish and these were used for correction collar adjustment. Experimental recordings were then captured for 180 seconds (instead of 6x10 seconds), as the number of particles that pass through the laser beam was usually very low. Before every measurement, the observation region was pre-bleached with the same laser intensity (10 µW) for 3 seconds to bleach away the background intensity.

Instead of autocorrelation analysis, the resulting intensity traces were quantified for their number of peaks, which originate from a fluorophore moving through the excitation volume and causing a detectable burst of photons. In order to determine the cut-off threshold, which was used to subtract the background noise, control embryos were measured during each experiment and on the same imaging dishes. These control embryos were from mothers expressing Asl-mKate2 to allow measurements at the centriolar plane and at the right nuclear cycle stage (beginning of S-phase in nuclear cycles 11-14). “Mean + n*SD” (where n = 1,2,3,…) of all control recordings was subtracted from each control recording, and the threshold that resulted in an average of less than 5 peaks

(per 180 second control measurement) was subtracted from all intensity traces. This threshold was found to be a good compromise for minimising the background noise without discarding too much information. I collaborated with Siu-Shing Wong, who wrote a Python script to automate this procedure, which is available via <https://github.com/RaffLab/PeCoS>. In the peak detection algorithm, a peak was defined as any consecutive value (photon count) that surpasses the subtracted threshold. A graphical explanation of the PeCoS methodology can be found in **Figure 3-6A**.

2.3.5 Spinning-disk confocal microscopy

Embryos were imaged at room temperature using an Andor Dragonfly 505 spinning-disk system (with 40 µm pinholes) which was mounted on a Leica DMi8 stand. A 488 nm solid state diode laser and a HC PL APO 63x/1.40 oil immersion objective were used. For the image acquisition, stacks consisting of 17 slices with a spacing of 0.5 µm in z were taken every 30 seconds using an Andor iXon Ultra 888 EMCCD camera.

Post-acquisition, the resulting images were first processed using Fiji (National Institutes of Health), and then further analysed either using GraphPad Prism (for Sas-6-mNG incorporation, methodology published in Aydogan *et al.*, 2018) or in a customised Python script written by Siu-Shing Wong (for Ana2-mNG incorporation).

In Fiji, the stacks were first reduced to maximum-intensity projections, which were then bleach-corrected using the exponential fit algorithm. Afterwards, the background was subtracted using a rolling ball radius of 10 pixels, and the centriolar pairs (which are displayed as a single dot as they cannot be resolved with conventional light microscopy) tracked using the Fiji plug-in TrackMate (Tinevez *et al.*, 2017). The following settings were chosen within TrackMate: spot diameter: 1.1 µm, no gaps between frames, only centriolar

pairs that could be tracked from the beginning of nuclear cycle 12 until nuclear envelope breakdown (NEB) (for Sas-6)/beginning of nuclear cycle 13 (for Ana2) were kept for the final analysis.

For the Sas-6 incorporation dynamics, the regression of all centriolar pairs of each individual embryo was calculated in Prism and fitted with both a 'linear growth+plateau' and a 'linear growth only' model (Aydogan *et al.*, 2018). Depending on the best fit, the incorporation parameters were extracted and normalised from either of the two models. For the Ana2 incorporation dynamics, the mean intensity curve was not modelled but directly displayed from the normalised raw data, and the incorporation parameters extracted from the initial timepoint and the datapoint with the maximum intensity. For both methodologies, all embryos were aligned to NEB to generate the mean regression curves for each genotype (for Sas-6 from the modelled regressions, for Ana2 from the mean intensity profiles).

2.4 Data visualisation and statistical analysis

All data graphs were generated, and all statistical analysis were performed in GraphPad Prism 7 or 8. The statistical tests applied to individual datasets are described in the corresponding figure legends. In general, a D'Agostino-Pearson omnibus normality test was applied to each data set to assess whether its data values resembled a Gaussian distribution. Statistical significance was defined as $P<0.05$.

3 Developing spectroscopy methods to probe the cytoplasmic properties of centriolar and centrosomal proteins

3.1 Introduction

Over the last decades many efforts were directed towards optimising fluorescence microscopy for the *Drosophila* embryo to characterise cellular structures and investigate dynamic biological processes (Dunst and Tomancak, 2019). The methodology to describe the cytoplasmic component of proteins of interest have, however, received relatively little attention. While some methods are available for the *in vivo* characterisation of fluorescently tagged proteins in the cytoplasm (Bacia and Schwille, 2007; Kim, Heinze and Schwille, 2007), these protocols were designed to study cells in culture rather than cells in larger, more complex tissues like the *Drosophila* embryo.

In order to characterise the cytoplasmic pool of centriolar and centrosomal proteins in the early *Drosophila* blastoderm embryo, I set out to establish robust spectroscopy protocols to measure cytoplasmic concentrations, diffusion dynamics, potential protein interactions, and average cytoplasmic protein stoichiometry. I validated these methods using *in vitro* and *in vivo* controls.

3.2 Results

3.2.1 Fluorescence correlation spectroscopy (FCS)

FCS was first experimentally tested by Magde et al. in 1972, but its applicability for *in vivo* measurements only became feasible in 1993 when FCS was combined with confocal microscopy, which lead to a dramatic increase in signal-to-noise ratio (SNR) (Rigler *et al.*, 1993). In FCS, a laser beam is positioned in a single location in an aqueous medium (e.g., cytoplasm) and the fluorescence fluctuations, which are caused by fluorophores moving

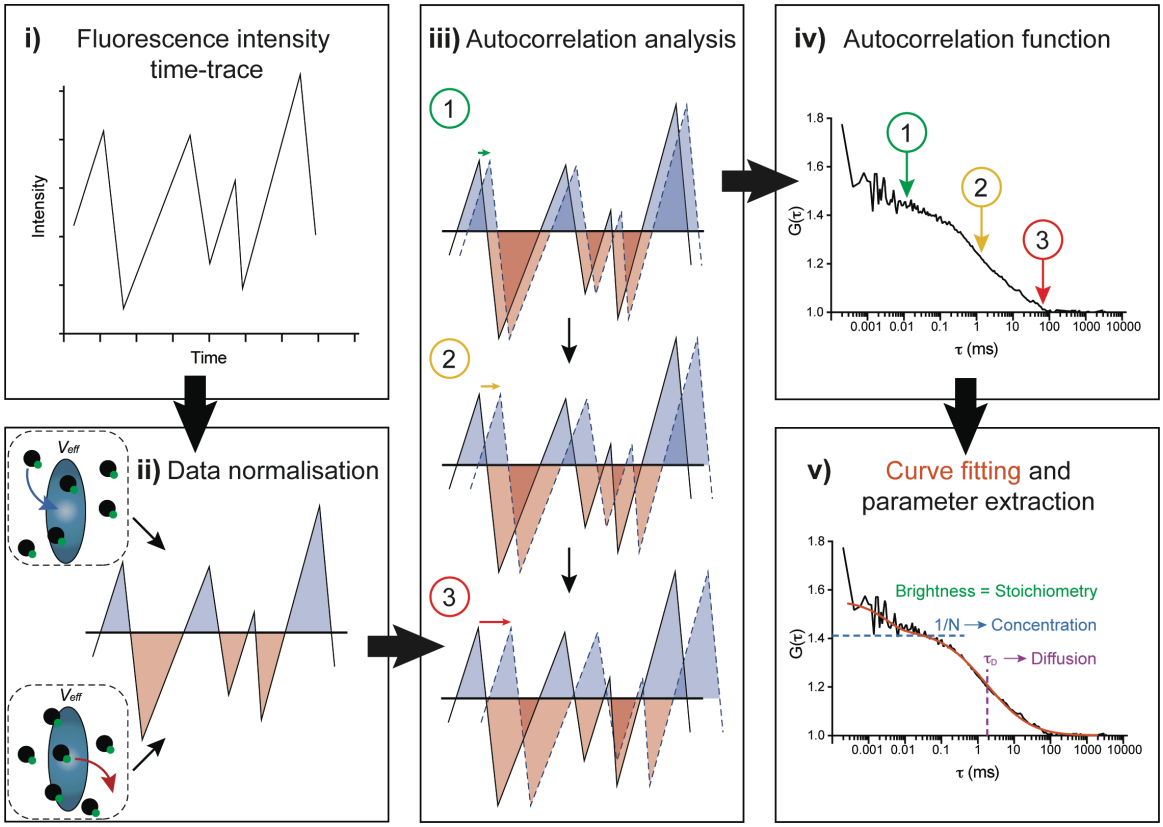


Figure 3-1: Description of Fluorescence correlation spectroscopy (FCS)
Mathematical equations and further details can be found in *Materials & methods*. **(i)** Using a confocal microscopy setup, a parked laser beam measures fluorescence intensity fluctuations over time in a liquid medium. **(ii)** The mean intensity value is subtracted from the intensity trace, so that every positive spike corresponds to fluorophores moving into and every negative spike with fluorophores moving out of the effective volume V_{eff}. **(iii)** The normalised intensity trace is then autocorrelated, where the entire trace is shifted with itself in every measurement point (called lag time τ) and the similarity between the original and the shifted trace is calculated in every lag time (here depicted as overlap between the two intensity traces). With increasing lag time *(green, yellow* and *red* arrow*)* the similarity between the intensity traces decreases. **(iv)** An autocorrelation function *G* (ACF) is generated, which is a function of the lag time τ. The decay of the slope describes the loss of similarity between the two time-traces. **(v)** The generated ACF can then be fitted with a suitable diffusion model which allows the extraction of various parameters. The height of the ACF is inversely proportional to the average number of particles in V_{eff} and the inflection point to their mean residence time τ_D. When the size of V_{eff} is known, the concentration and diffusion coefficient can be calculated. Further, the molecular brightness of the fluorophore (measured as photon-count rate per molecule per second (CPM)) provides information about the fluorescent particle's average stoichiometry.

through the excitation spot, are recorded over time using a photon-counting detector. The time-trace of fluorescence intensity is then autocorrelated and an autocorrelation function (ACF) is generated from which a fluorescent particle's concentration, average diffusion speed, and average stoichiometry can be calculated (**Figure 3-1**) (see **Chapter 2, Section 2.3.2**).

3.2.1.1 Characterisation of the Zeiss 880 FCS system

All FCS measurements conducted in this thesis were recorded on a Zeiss 880 LSM using an inbuilt GaAsP photon counting detector. For precise stoichiometry measurements, it is important to avoid the saturation of the system. To determine the detector's limit, I conducted control measurements of a concentrated fluorophore solution across a wide range of laser intensities. With increasing laser power, the photon-count rate per molecule (**CPM**)—the average number of photons detected per second for an individual fluorophore moving through the excitation spot—is expected to scale in a linear fashion until the detector/detector electronics become saturated. This saturation leads to a non-linear CPM increase until it reaches a plateau. For the Zeiss 880 system, the saturation threshold (i.e., where the linear response became non-linear) was observed around the total photon count rate of ~260 kHz (**Figure 3-2Ai**). All FCS recordings in living embryos that I used to assess the average cytoplasmic stoichiometry based on their CPM were below this threshold (**Figure 3-2Aii**), suggesting that my *in vivo* measurements with these proteins were within the linear range.

FCS allows the determination of the average number of particles and their mean residence time in the excitation volume, but in order to translate these parameters into concentrations and diffusion coefficients it is necessary to determine the size of the excitation spot, termed effective volume (V_{eff}). V_{eff} is defined as the detection volume in which the probability to detect a fluorescent molecule is higher than $1/e^2$. To assess the size of V_{eff}, three previously published, independent methods were used (Ruettinger *et al.*, 2008): (1) The measurement of an Alexa488 dilution series of known concentration; (2) A comparison of the obtained diffusion coefficient with a previously reported

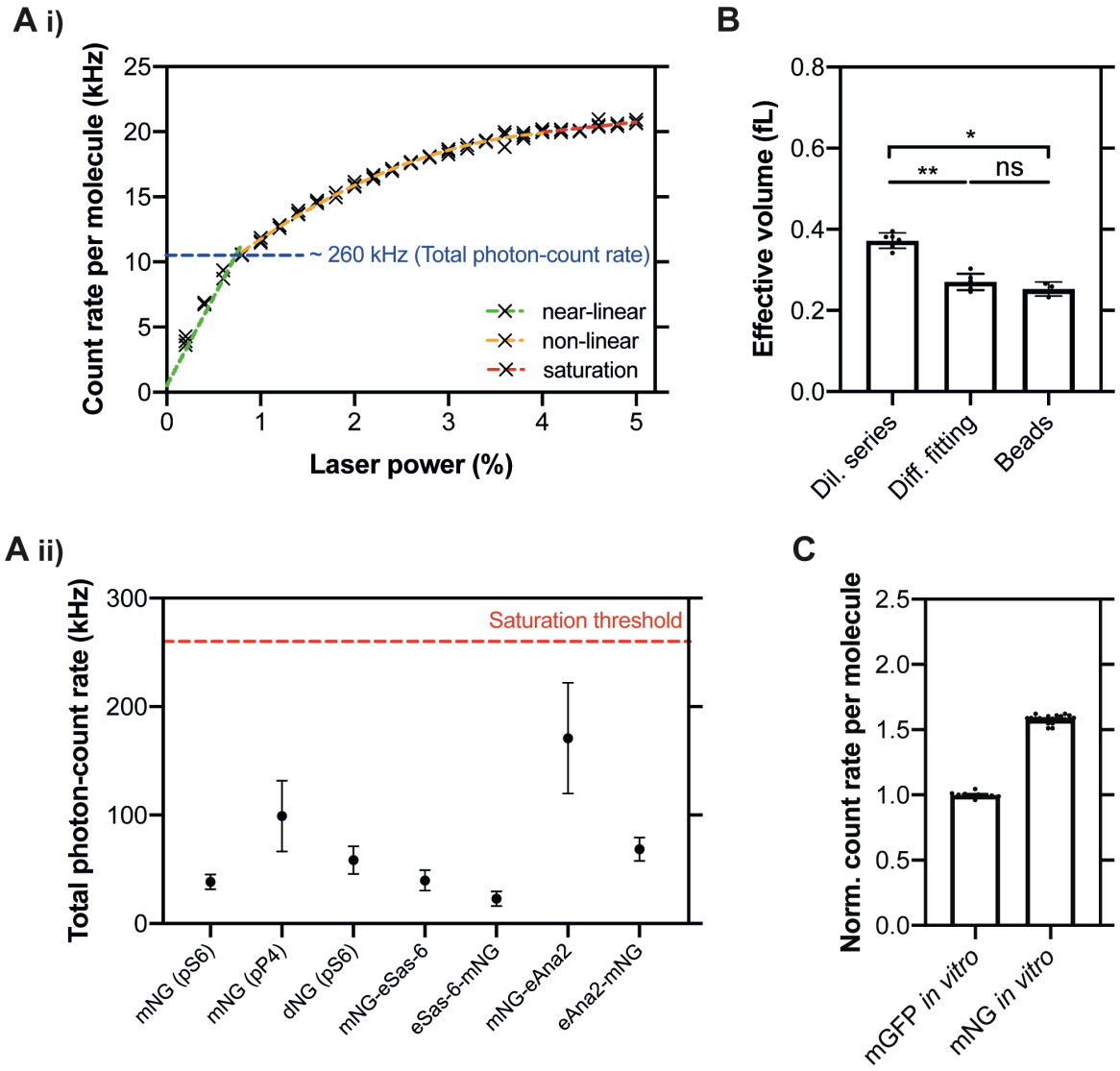


Figure 3-2: Characterisation of the spectroscopy setup

(A) (i) In order to determine the saturation threshold of the GaAsP photon-counting detector, a concentrated fluorophore solution was measured with increasing laser intensities. A non-linear response was first observed ~260 kHz. **(ii)** Graph shows the total photon-count rate (mean±SD) obtained by FCS for all proteins that were used for stoichiometry measurements grouped by genotype. None of the FCS recordings surpassed the saturation threshold. **(B)** Graph quantifies the size measurements of the effective volume V_{eff} (mean±SD) with three independent methods (see main text). Statistical significance was assessed using a Mann-Whitney test (**, P<0.01; *, P<0.05; ns, not significant). **(C)** Graph shows the increased molecular brightness (mean±SEM) of mNeonGreen (mNG) compared and normalised to mGFP measured with FCS *in vitro*. Each data point represents the average of 4-6x 10-second-long recordings.

coefficient (Petrášek and Schwille, 2008); (3) Imaging of sub-resolution beads immobilised on a coverslip. The comparison with a previously reported diffusion coefficient and imaging of immobilised sub-resolution beads, resulted in a very similar V_{eff} size estimation, so the average volume of the two methods (~0.25 fL) was used for all further calculations

(**Figure 3-2B**). The larger volume size calculated from the dilution series is probably an overestimation due to imprecise pipetting of small volumes.

As a good SNR is crucial for robust FCS measurements, I aimed to tag all proteins of interest with a bright and photostable fluorescent protein. A recently identified fluorophore, mNeonGreen (mNG) (derived from *Branchiostoma lanceolatum*), was reported to have an enhanced molecular brightness compared to GFP (Shaner *et al.*, 2013). In order to compare the two, both fluorescent proteins were expressed and purified from *E. Coli* (with help from Andreas Hänsele and members of the van der Merwe laboratory) and I measured their brightness *in vitro* at the same 488 nm laser power. The CPM of mNG, which can be used as a measure for molecular brightness, showed a ~1.6-fold increase compared to GFP (**Figure 3-2C**), similar to what was previously reported (Steiert, 2016). Therefore, mNG was chosen as the fluorophore of choice for the new transgenic fly lines I subsequently generated.

3.2.1.2 In vivo validation of FCS

In order to establish robust and reproducible FCS measurements, I developed an experimental procedure and analysis protocol where I recorded six consecutive 10-second-long fluorescence intensity measurements at the centrosomal plane in the embryo (**Figure 3-3**). I fitted each recording with eight different diffusion models and selected the most likely model based on the Bayesian information criterion (BIC); I then applied a background correction and removed data points that failed a statistical outlier test (see **Chapter 2, Section 2.3.2)**.

To determine whether my FCS methodology was sensitive enough to measure cytoplasmic concentration changes of centriolar and centrosomal proteins in the early

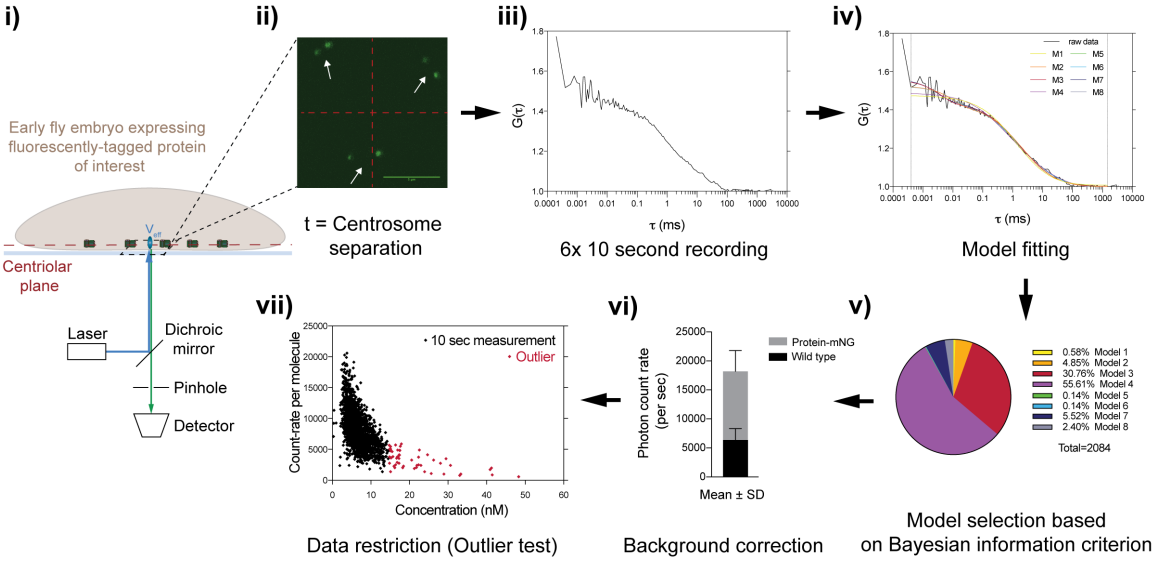


Figure 3-3: Fluorescence correlation spectroscopy workflow for *in vivo* measurements
Schematic workflow describes the acquisition and analysis of point Fluorescence correlation spectroscopy (FCS) measurements (see *Materials & methods* for further details). **(i)** The 488 nm laser beam is positioned at the centrosomal plane in embryos expressing a fluorescently tagged protein of interest. **(ii)** At the beginning of every cycle, when the old and new mother centrioles have just separated (*white* arrows), 6x 10-second-long FCS measurements are taken at a point in the cytoplasm maximally distant from the centrosomes (centre of *red* crosshair). **(iii)** This generates six autocorrelation functions (ACFs) (a typical example is shown here). **(iv)** In the FoCuS-point software, eight different models are fitted to each ACF. **(v)** The model that best fits the majority of the data is chosen based on the Bayesian information criterion (BIC), and all ACFs are then fitted to this model. **(vi)** The fitted ACFs are corrected for background noise which was determined by measurements in WT embryos. **(vii)** The ACFs used for further analysis are then restricted by excluding individual outlier measurements based on a ROUT-outlier test (Q=1%) (these outlier measurements usually have a poor signal-to-noise ratio and give concentration/diffusion/CPM values that are often biologically unrealistic and are presumably generated when a non-specific fluorescent structure passes through the excitation spot).

Drosophila embryo, I examined blastoderm embryos laid by females expressing either one (1x), two (2x), or four (4x) copies of the fluorescently tagged centriole cartwheel protein eSas-6-GFP in a homozygous *Sas-6*$^{-/-}$ mutant background (**Figure 3-4Ai**). This fusion-protein was expressed transgenically from its endogenous promoter (Aydogan *et al.*, 2018). As two different eSas-6-GFP transgenic lines were used to generate the 4x embryos, I also compared the two 2x lines to each other. All measurements were taken at the beginning of S-phase of nuclear cycles 11-14, when centriole duplication is initiated. Reassuringly, the two 2x lines both expressed eSas-6-GFP at a similar concentration (~14-15 nM), which was approximately halved in the 1x line (~7 nM) and was significantly

increased, but not precisely doubled, in the 4x line (~20 nM) (**Figure 3-4Aii**). It is unclear why the concentration did not double in the 4x embryos, but this is unlikely to be due to technical limitations, as Sas-6 fusion proteins are expressed at relatively low levels that should be within the linear range of the detector (see **Figure 3-2** and results presented later in this thesis). It could be for biological reasons; for example, the cytoplasmic levels of Sas-6 may be regulated so that it is hard to overexpress the protein. Moreover, I noticed that many of the 4x embryos exhibited developmental defects, perhaps making these measurements less reliable. Importantly, I used western blotting to confirm that the 1x, 2x, and 4x embryos were expressing approximately the expected relative levels of eSas-6-GFP (**Figure 3-4Aiii**).

To test the sensitivity of FCS in regard to diffusion and stoichiometry measurements, I generated fly lines expressing untagged monomeric NeonGreen (mNG) and untagged dimeric NeonGreen (dNG), where the two fluorophores are connected by a five amino acid (aa)-long linker. As dNG has twice the molecular weight compared to mNG, I expected to detect a strong decrease in its diffusion speed compared to mNG, which was indeed the case (**Figure 3-4Bi**). The stoichiometry analysis of FCS measurements is based on the comparison of the average photon-count rate per molecule per second (CPM). If the same laser intensity and fluorescent tag are used for all measurements, the CPM should be constant across samples. If the fluorescently tagged protein of interest oligomerises in the cytoplasm, an increase in CPM would be detected—as multiple fluorophores are moving through the excitation spot as one diffusing molecule. To test this concept, I compared the CPM of mNG and dNG, and observed a significant difference between the two proteins (**Figure 3-4Bii**). In an ideal system, where a fluorophore's fluorescence

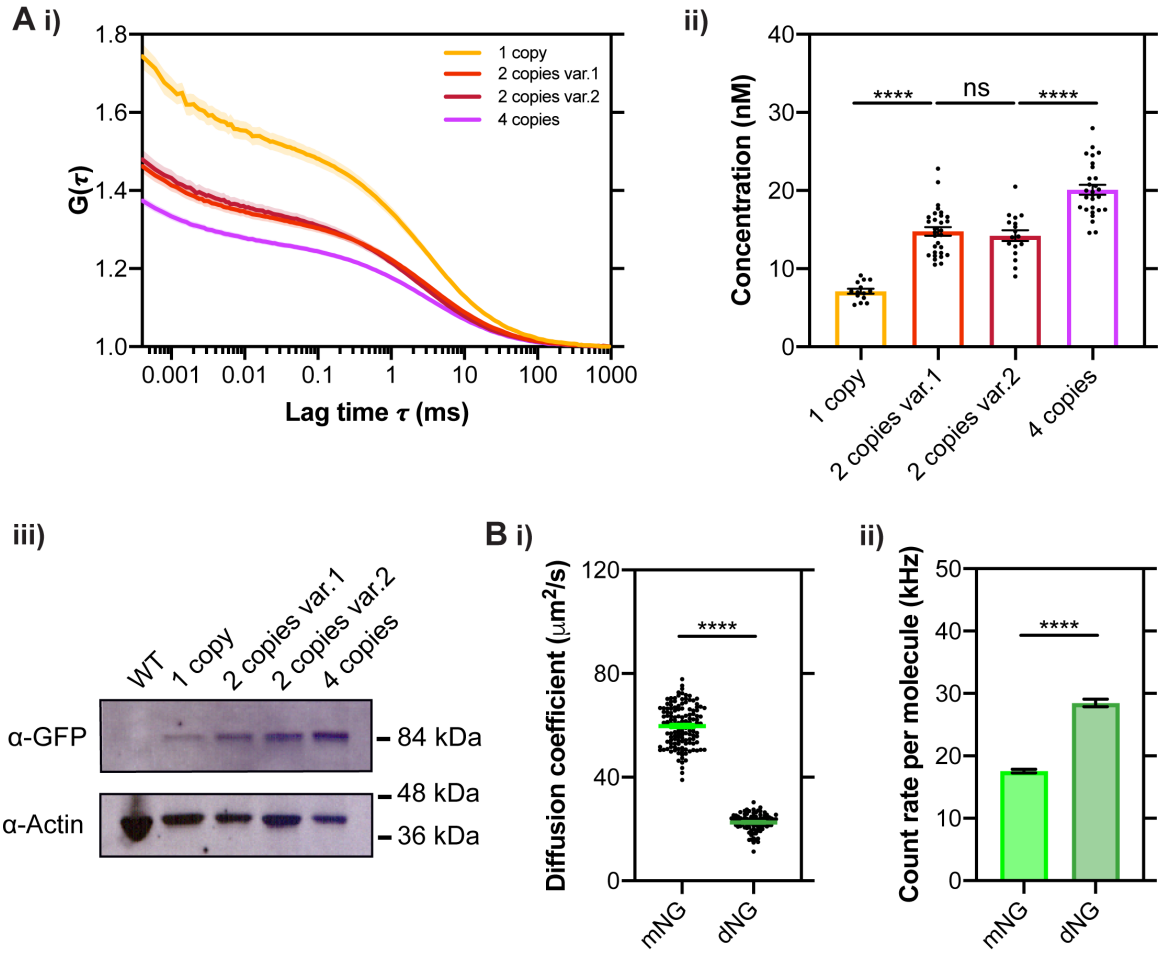


Figure 3-4: FCS is a suitable method to measure cytoplasmic concentrations, diffusion dynamics, and protein stoichiometry within the *Drosophila* syncytial embryo

(A) (i) Graph shows the average ACFs (mean±SEM) for four genotypes expressing 1, 2 or 4 alleles of eSas-6-GFP. **(ii)** These ACFs were used to calculate the cytoplasmic concentration (mean±SEM), as the height of the ACF is inversely proportional to the average number of particles present in V_{eff}. **(iii)** Western blot depicts the overall protein levels of eSas-6-GFP in the embryo lines used in (i) and (ii). Actin is shown as a loading control. **(B)** Cytoplasmic FCS measurements of untagged mNG and dNG were used to test the sensitivity of FCS for diffusion and CPM analysis. **(i)** Graph shows a strong difference in cytoplasmic diffusion speed (mean±SEM) between mNG (~27 kDa) and dNG (~54 kDa). **(ii)** Graph quantifies the average molecular brightness (mean±SEM) of m/dNG.

Each data point represents the average of 4-6x 10-second-long recordings. Statistical significance was assessed using an ordinary unpaired t-test (for Gaussian-distributed data) or a Mann-Whitney test (****, P<0.0001; ns, not significant).

probability is 100%, the molecular brightness of dNG would be twice as high as mNG. In reality, however, dark states and limited maturation of the fluorophore affect the fluorescence probability and reduce its average molecular brightness (Dunsing *et al.*, 2018). Comparing the CPM of dNG to mNG, therefore, allows the determination of the fluorescence probability of mNG. As dNG showed a 1.62-fold increase in CPM, the fluorescence probability for mNG at 25 °C in the syncytium of the *Drosophila* embryo was

estimated to be ~81%, which is similar to previously described fluorescence probabilities for GFP in cell culture (Dunsing *et al.*, 2018) and in *Xenopus laevis* oocytes (Ulbrich and Isacoff, 2007).

In summary, the FCS setup described in this chapter appears to be suited to conduct *in vivo* measurements of cytoplasmic concentrations, diffusion coefficients and average protein stoichiometry for centriole and centrosome proteins within the *Drosophila* embryo. It needs to be stressed that all concentration and diffusion measurements are not absolute values but only estimates—from which relative comparisons can be usefully made. This is because, despite the thorough characterisation of the FCS setup, there are some uncertainties that cannot be accounted for. Perhaps most importantly, the size of V_{eff} was estimated *in vitro*, and it is not possible to determine whether its size would be slightly different when positioned inside the embryo's cytoplasm.

3.2.2 Fluorescence cross-correlation spectroscopy (FCCS)

FCCS uses a similar experimental setup and is based on the same photophysical principle as FCS, but with the major difference that two spectrally shifted fluorophores are simultaneously observed with two separate laser beams in an overlapping excitation spot (Eigen and Rigler, 1994; Schwille, Meyer-Almes and Rigler, 1997). By cross-correlating the signal detected in the two channels, the similarity between the two time-traces of fluorescence intensity can be assessed. If the two fluorophores interact with each other, and therefore co-diffuse in the cytoplasm, they will display similarities in their intensity traces and show a positive cross-correlation (**Figure 3-5A**) (see **Chapter 2, Section 2.3.3**).

3.2.2.1 Generating control lines for in vivo FCCS measurements

As previously mentioned, a good SNR is crucial for robust FCS measurements. For FCCS, in addition, the photostability and maturation speed of the fluorophore become increasingly important—as both fluorophores have to simultaneously be in their fluorescent state to be detected as interacting molecules. I therefore set out to find a suitable red fluorescent protein that fulfils these requirements, and which is spectrally sufficiently shifted to not interfere with the emission spectrum of the green/yellow fluorophore mNG.

I tested three relatively bright and photostable red fluorescent proteins for an initial FCCS screen: mKate2 (Shcherbo *et al.*, 2009), mCardinal (Chu *et al.*, 2014), and mScarlet-I (Bindels *et al.*, 2016). To characterise the proteins' behaviour within the cytoplasmic context, I generated fly lines where either both the red and green fluorescent protein were separately expressed as a monomer or jointly as a heterodimer with a 5-aa-long linker between the fluorophores. All fluorescent proteins were expressed from the *Sas-6* core promoter to optimise the FCCS setup for the concentration range which is similar to the concentration of the core centriole duplication proteins. The fly lines expressing both monomeric fluorophores, on the one hand, serve as a negative control as I expect that none of the fluorophores should be interacting with each other in the cytoplasm. Any positive cross-correlation value in the negative control is therefore presumably caused by the cross-excitation/cross-detection between the two channels. The fly lines expressing the fused heterodimeric fluorophore, on the other hand, act as positive control.

To assess the feasibility of using the three red fluorescent proteins for FCCS, I initially conducted FCS measurements using only the 561 nm laser excitation in embryos in

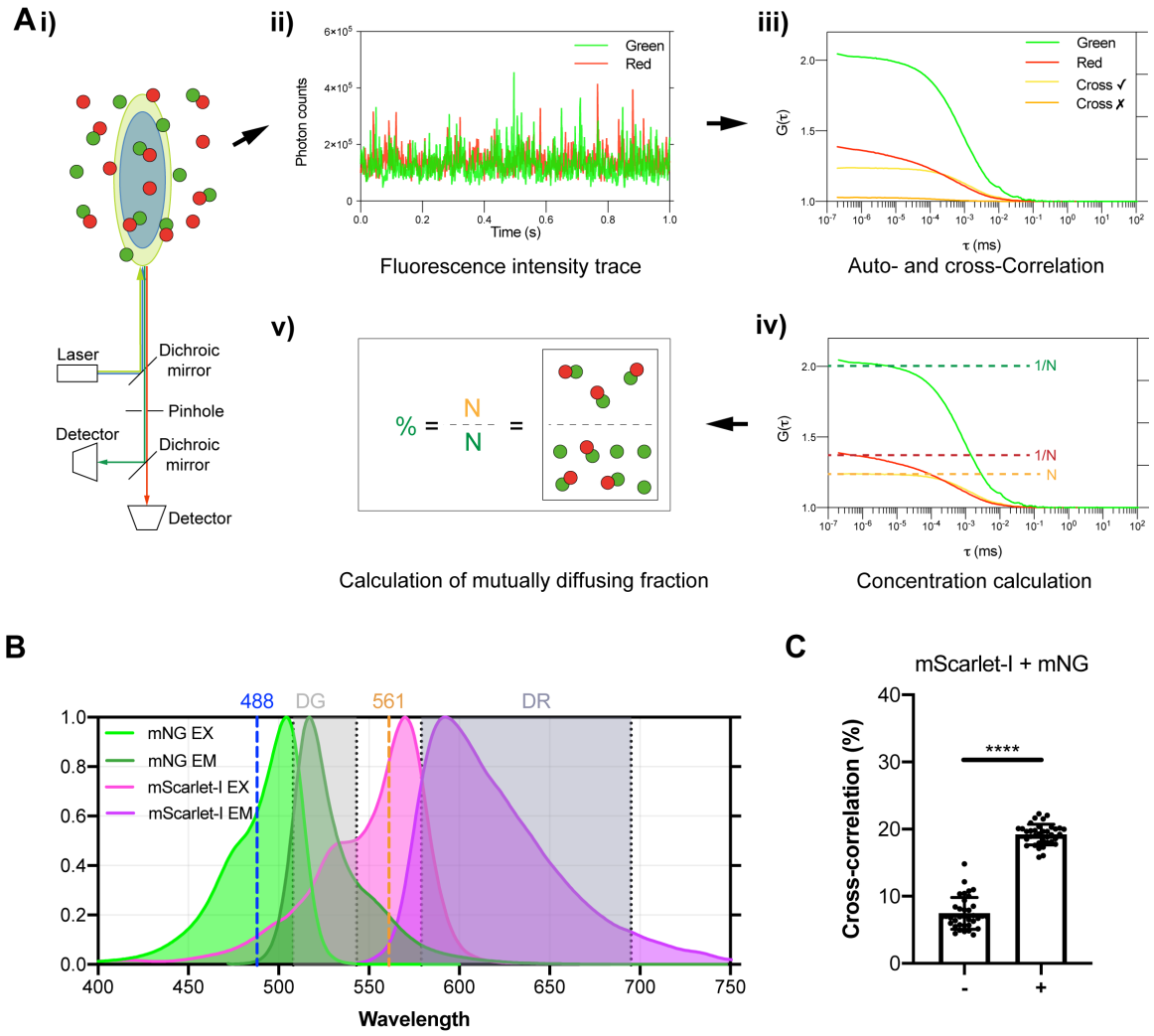


Figure 3-5: Basis of the FCCS setup, and *in vivo* validation for FCCS measurements of mScarlet-I and mNG
(A) Schematic workflow describes the basis of point Fluorescence cross-correlation spectroscopy (FCCS). **(i)** Two spectrally shifted fluorophores (*red* and *green*) are simultaneously measured in an overlapping excitation spot. **(ii)** For each fluorophore, an individual time-trace of fluorescence intensity is generated, which can be autocorrelated to generate ACFs (like FCS), but also cross-correlated to identify the similarity of the two traces. **(iii)** Any similarity between the traces caused by the interaction of the fluorophores leads to an elevated amplitude of the cross-correlation function (*yellow* curve). If the fluorophores do not interact, no elevated amplitude will be observed (*orange* curve). **(iv)** The amplitude of the ACFs at t=0 is inversely proportional to the number of particles present in the excitation spot and the amplitude of the cross-correlation function is directly proportional to the number of co-diffusing particles—allowing the calculation of the fraction of mutually diffusing particles **(v)**. **(B)** Diagram shows the excitation (EX)/emission (EM) spectra for mNG (*light green/dark green*) and mScarlet-I (*pink/purple*). The laser lines used for excitation and the boundaries selected for the detection of the green (DG) and red (DR) fluorescent protein are indicated. The spectral data was taken from FPbase (Lambert, 2019). **(C)** Bar graph quantifies the fraction of cross-correlated protein (mean±SD) measured in the negative (-) and positive (+) control line where the fluorescent proteins were either expressed in their monomeric form or linked to each other as a heterodimer. Each data point represents individual 20-second-long recordings. Statistical significance was assessed using a Mann-Whitney test (****, P<0.0001).

nuclear cycles ~9-11 to optimise the laser power for the individual fluorophores. Unfortunately, for mKate2 and mCardinal I did not obtain robust ACFs with a consistent

CPM, indicating that neither fluorescent protein is suited for FC(C)S measurements in the early *Drosophila* embryo. In contrast, I obtained clear ACFs with high molecular brightness values from my FCS measurements in embryos expressing the red fluorescent protein mScarlet-I. Therefore, I decided to test how mScarlet-I performs together with mNG in FCCS measurements.

3.2.2.2 mScarlet-I and mNG can be used for FCCS measurements within the Drosophila cytoplasm, but they only exhibit a very low cross-correlation amplitude

As two fluorophores are being simultaneously excited and detected during an FCCS measurement, it is important to choose suited detection boundaries for both channels. If the filter boundaries are very broad (to collect more signal) and therefore too close to each other, there will be increased crosstalk between the channels; if the filter boundaries are too narrow, a lot of the emitted light is excluded which will result in a low CPM and noisy measurements. On a trial-and-error basis, I tested a wide range of filter boundaries to find a good compromise between minimising the crosstalk and increasing the CPM, and the best combination was used for all FCCS measurements conducted in this thesis (**Figure 3-5B**).

I then used my optimised FCCS setup to assess how efficiently it can detect cytoplasmic protein interactions by conducting FCCS measurements in my control lines in nuclear cycles ~9-11. During the course of these initial tests I identified several technical limitations, including incomplete detection volume overlap due to chromatic aberrations and the non-fluorescent states of the fluorophores (which are influenced by the maturation and folding efficiency, dark states, and photobleaching) which led to a surprisingly low overall cross-correlation amplitude for my heterodimeric positive control

(~19%, **Figure 3-5C**), while my monomeric negative controls exhibited a relatively high cross-correlation amplitude (~7%, **Figure 3-5C**). Therefore, the heterodimeric controls, where every red fluorophore is associated with a green fluorophore (=100% cytoplasmic interaction), represents the maximum level of cross-correlation that can be detected with this FCCS system, and this can be used as a scaling factor to calculate the fraction of interacting molecules in biological measurements of proteins of interest.

Nevertheless, the system was still able to detect a significant difference between the hetero-dimeric (mScarlet-I+mNG) positive control (~19%) and the monomeric (mScarlet-I and mNG) negative control (~7%), indicating that I can use FCCS to detect cytoplasmic protein interactions in the *Drosophila* embryo (although with very low sensitivity). I expect that, if centriole and centrosome proteins were to interact with each other in the cytoplasm, only a fraction of their cytoplasmic pool would form complexes. Therefore, further optimisation to increase the sensitivity of the cross-correlation detection will be necessary to identify such potential cytoplasmic protein interactions. Alternatively, the selection of a different red fluorescent protein that was not characterised in this chapter might be necessary to increase the cross-correlation detection.

3.2.3 Peak counting spectroscopy (PeCoS)

FCS is a sensitive technique that allows accurate concentration measurements in the low nanomolar concentration range (Ruettinger *et al.*, 2008). *In vivo,* high background noise and short recording durations due to non-equilibrium conditions do not, however, allow for the same precision as *in vitro* samples. Almost all the centriole and centrosome proteins I characterised in this thesis were present in the low-medium nanomolar concentration range (~5-200 nM) within the *Drosophila* syncytium. Unfortunately, I found

that Plk4, the master regulator of centriole duplication, was present at too low a concentration to be measured accurately by FCS. This was frustrating, as measuring the cytoplasmic concentration of Plk4 was a major priority for my project in trying to understand how an oscillation in centriolar Plk4 levels was generated at each nuclear cycle within the embryo (Aydogan, Steinacker *et al.*, 2020). To address this question, I therefore developed an alternative approach I termed Peak Counting Spectroscopy (PeCoS) (**Figure 3-6A**), which allowed me to measure the relative concentration of Plk4 at different nuclear cycles (see **Chapter 5, Section 5.2.3**).

3.2.3.1 PeCoS methodology

In FCS, the number of particles in the excitation spot can be calculated from the variance of the measured fluorescence fluctuation, which decreases with increasing particle number. If the number of particles is too low to show fluctuations from a mean fluorescence intensity, the autocorrelation analysis does not provide reliable information and leads to the calculation of inconsistent ACFs. Due to its low cytoplasmic abundance, ePlk4-mNG measurements only showed infrequent intensity spikes from a low background baseline in the time-trace of intensity fluctuations (**Figure 3-6Aiii**). This made it impossible to investigate the cytoplasmic pool of ePlk4-mNG using the Zeiss 880 LSM FCS setup.

As I was not able to find any suited method in the literature to dynamically measure such low concentrated proteins, I set out to develop a novel spectroscopy technique, which can measure relative cytoplasmic concentrations of very low abundance particles where FCS becomes inconsistent. As intensity spikes were observed to rise from a low background baseline (**Figure 3-6Aiii**), I reasoned that each individual peak might

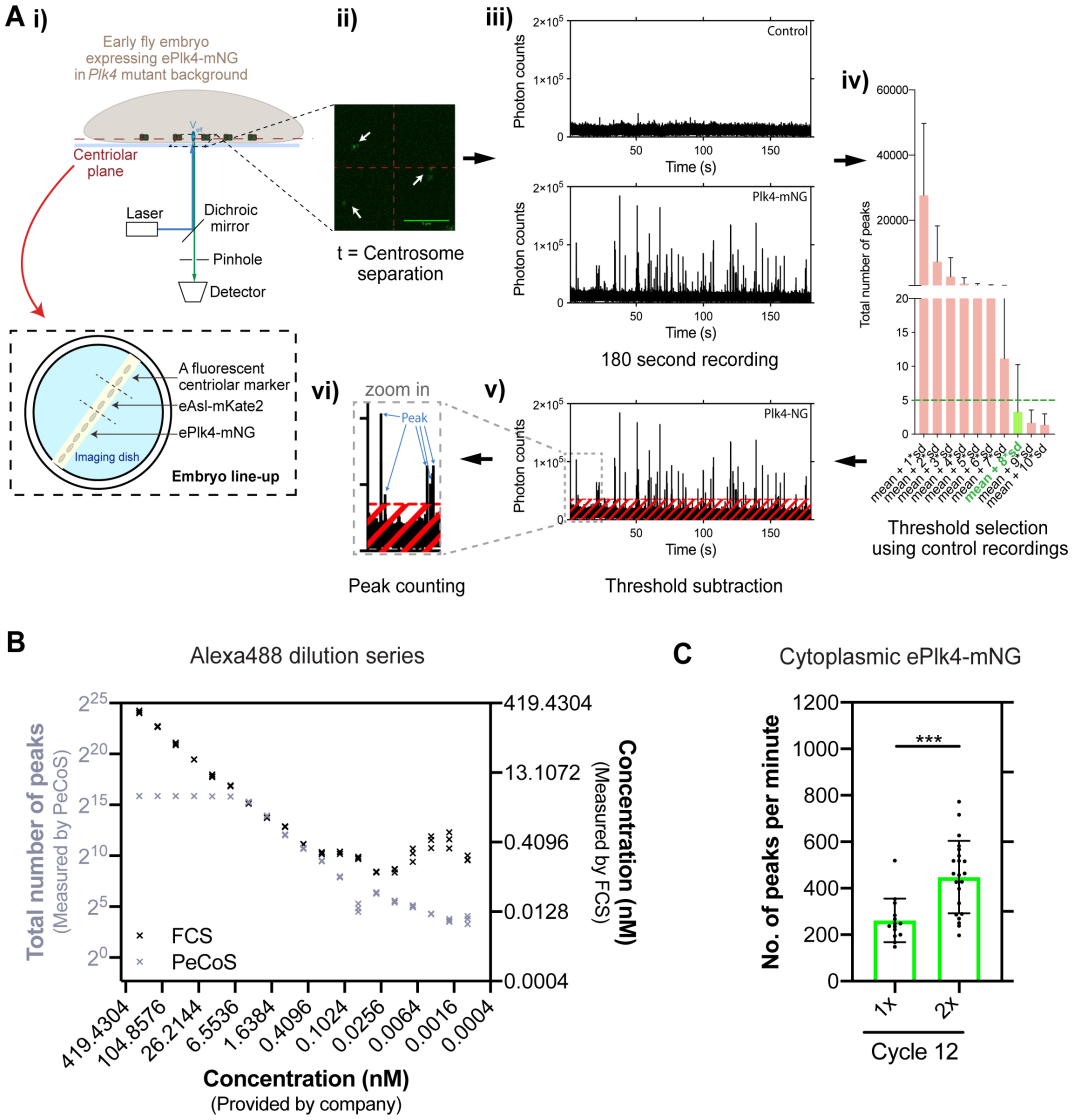


Figure 3-6: PeCoS allows relative concentration measurements of very low abundant proteins
(A) Schematic workflow describes the acquisition and analysis of PeCoS measurements. **(i)** Embryos expressing the fluorescent protein of interest (here ePlk4-mNG) are aligned with embryos of two other genotypes: one expressing a green-fluorescent centriole marker to allow correction of the spherical aberration caused by coverslip thickness variation, the other expressing eAsl-mKate2 to determine the autofluorescence background levels in the centriole plane. **(ii)** As for FCS, a 488 nm laser beam is positioned near the cortex of embryos, and a measurement is taken at a single point in the cytoplasm (*red* crosshair) at the beginning of S-phase, but for 1x 180 seconds. **(iii)** The measurements from control and experimental embryos are compared, allowing an appropriate threshold to be calculated from the control embryos, so that the background contributes less than 5 peaks on average during each recording **(iv)**. Following background subtraction, (**v** and **vi**) the number of peaks is quantified. **(B)** Graph compares the effective linear concentration range of FCS and PeCoS when measuring an Alexa488 dilution series *in vitro*. **(C)** Bar chart shows the number of peaks per minute (mean±SD) observed by PeCoS in embryos expressing either 1x or 2x copies of ePlk4-mNG (in a *Plk4*$^{-/-}$ mutant background), measured at the beginning of S-phase in nuclear cycle 12. Each data point represents a 180-second-long recording. Statistical significance was assessed using Mann-Whitney test (***, P<0.001).

correspond to an individual event of a fluorophore moving through the observation spot. The rationale behind PeCoS was to quantify the number of intensity peaks as a proxy for relative cytoplasmic concentration. A robust experimental PeCoS workflow was established to ensure reproducibility of the measurements (**Figure 3-6A**). With an identical measurement setup as FCS, extended measurements of 1x 180 seconds were recorded to allow for a longer sampling duration due to the low number of occurring events. In addition, background measurements were conducted for every experiment in wild type (WT) embryos to identify the background threshold that was subtracted from all measurements to identify and quantify the number of peaks. In collaboration with Siu-Shing Wong, a python script was written to automate this analysis (see **Chapter 2, Section 2.3.4**).

3.2.3.2 In vitro and in vivo validation of PeCoS

To assess the validity and effective concentration range of the PeCoS methodology *in vitro*, I measured an Alexa488 NHS Ester dilution series using both FCS and PeCoS (**Figure 3-6B**). As expected, FCS (*black* crosses, **Figure 3-6B**) exhibited a near linear response in the ~0.5-400 nM concentration range, but this broke down at concentrations below ~0.5nM. In contrast, PeCoS (*grey* crosses, **Figure 3-6B**) did not perform well at concentrations >~5 nM (presumably because too many particles move simultaneously through the excitation volume) but exhibited a near-linear response in the ~0.1-5 nM range and was still sensitive to protein concentrations in the ~0.002-0.1 nM range.

To test the sensitivity of PeCoS *in vivo*, I measured the cytoplasmic concentration of ePlk4-mNG at the beginning of nuclear cycle 12 in embryos expressing either one (1x) or two (2x) copies of ePlk4-mNG expressed from its endogenous promoter in the *Plk4*$^{-/-}$

mutant background. PeCoS analysis indicated a ~90% increase in the number of peaks per minute in 2x embryos compared to 1x embryos, demonstrating the utility of PeCoS at measuring the relative cytoplasmic concentration of very low abundant proteins (**Figure 3-6C**). I conclude that PeCoS is a suitable method for determining the relative cytoplasmic amounts of very low abundance proteins in the early *Drosophila* embryo.

Another centriolar protein that exhibited a very low cytoplasmic abundance in the *Drosophila* embryo was Ana1. This protein is involved in recruiting PCM to the mother centriole (Saurya *et al.*, 2016; Alvarez-Rodrigo *et al.*, 2021), and we realised that it was important to measure its cytoplasmic concentration during nuclear cycles 11-14 to understand its function (Wong et al., *manuscript in preparation*). I found that while eAna1-GFP showed a more frequent spike pattern and relatively consistent ACFs compared to ePlk4-mNG, the background noise contributed ~66% to the total fluorescence signal, which did not allow for sensitive concentration measurements and presumably resulted in an overestimation of its cytoplasmic concentration when measured with FCS (Ruettinger *et al.*, 2008). Therefore, I used PeCoS to quantify the relative cytoplasmic levels of eAna1-GFP during nuclear cycles 11-14 (**Appendix B**). Reassuringly, I observed a ~50% decrease in the number of peaks when I measured the relative cytoplasmic abundance of embryos from mothers expressing one compared to two copies of the eAna1-GFP transgene, highlighting the sensitivity and broad applicability of PeCoS to analyse the relative concentration of low abundance proteins **(Appendix B)**.

3.2.4 Characterisation of the biophysical properties of the *Drosophila* embryo during nuclear cycles 11-14

3.2.4.1 Determination of the background fluorescence

In the early *Drosophila* embryo, the rapid divisions of nuclear cycles 11-14 (the blastoderm divisions) occur close to the cortex in a common cytoplasm (the syncytium) (Foe and Alberts, 1983). This allows for the simultaneous high-resolution observation of hundreds of near-synchronous centriole duplication and centrosome maturation events (Aydogan *et al.*, 2018; Alvarez-Rodrigo *et al.*, 2019).

As I hoped to measure the concentration and biophysical properties of various centriole and centrosome proteins in the cytoplasm of embryos progressing through the blastoderm cycles, it was important to first establish how the biophysical properties of the cytoplasm might change during these cycles. Wessel *et al.* (2015) combined micron-sized fluorescent bead injections with passive microrheology analysis to assess the properties of the nuclear layer of the *Drosophila* syncytium. They reported that its viscoelasticity on short time scales is rather homogenous, mainly driven by thermal fluctuations, and does not change throughout nuclear cycle progression. To be able to compare FCS/PeCoS measurements between the four nuclear cycles 11-14, I wanted to determine how the background autofluorescence of the syncytium changes during these stages. To allow the identification of the correct nuclear cycle and cell cycle stage, I used embryos for background measurements that expressed the centriolar protein Asl, which was tagged with a red fluorophore (eAsl-mKate2, generated by Lisa Gartenmann) (**Figure 3-7A**). Due to the red-shifted excitation spectrum (compared to the 488nm laser), mKate2 does not interfere with FCS/PeCoS measurements.

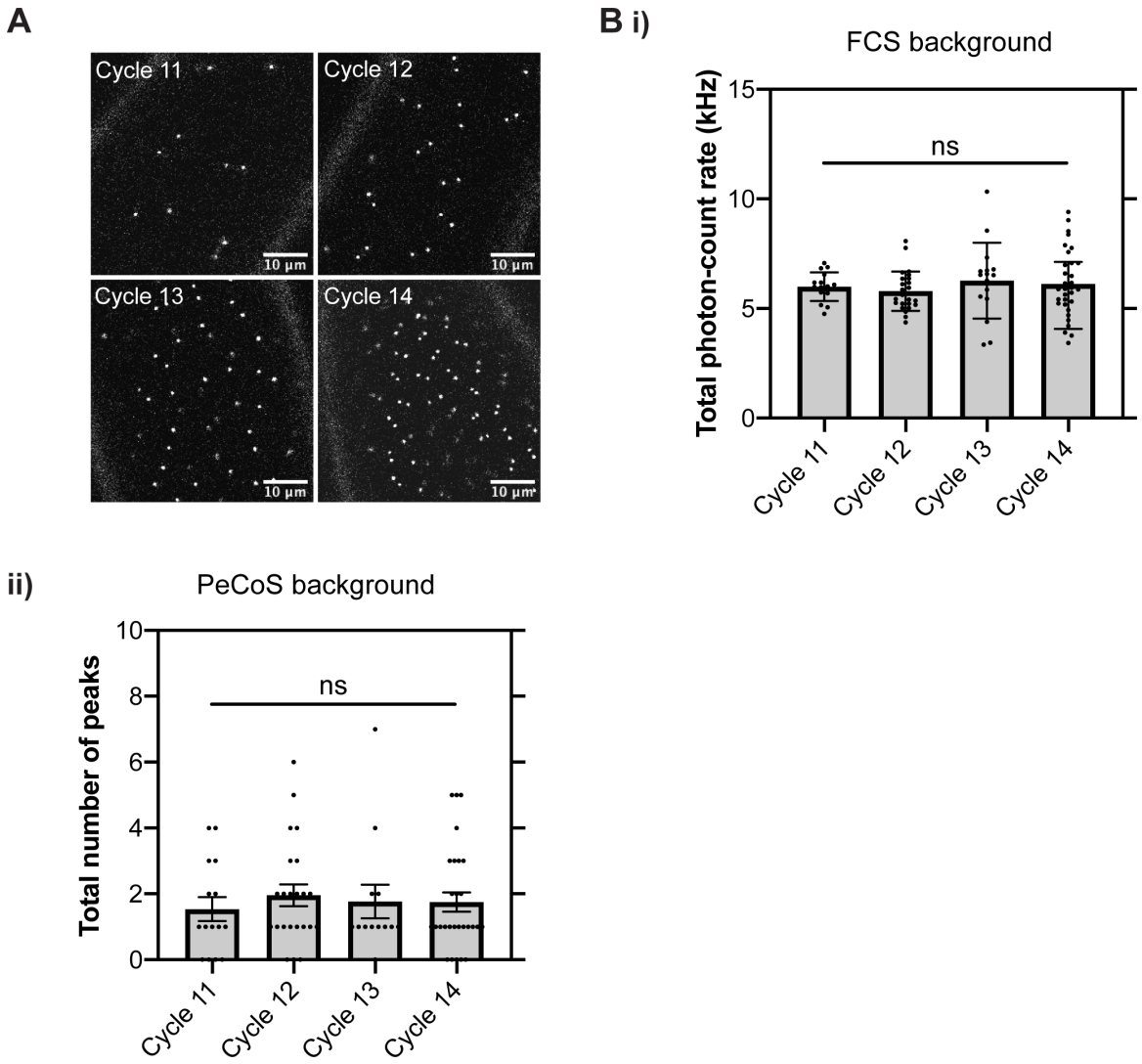


Figure 3-7: Characterisation of the fluorescence background of the embryonic syncytium between the nuclear cycles 11-14

(A) Micrographs show images of individual embryos expressing a centriolar marker at the start of each nuclear cycle (as indicated). Centrosomes are positioned close to the embryo cortex, and their number doubles at every cycle. **(B) (i)** Graph quantifies the total photon-count rate per second (mean±SD) obtained from FCS measurements in control embryos that expressed eAsl-mKate2—to identify the correct cell cycle stage and the centrosomal plane—but no green fluorophore. **(ii)** Graph shows the number of peaks above the background threshold (mean±SD) measured by PeCoS in the same control embryos. Each data point represents a 180-second-long recording.

Statistical significance was assessed using an ordinary one-way ANOVA test (for Gaussian-distributed data) or a Kruskal-Wallis test (ns, not significant).

To assess the overall background, which—if not corrected for—can cause concentration overestimation of FCS measurements, the average total photon-count rate per second was compared between the beginning of S-phase of nuclear cycles 11-14. Reassuringly, no correlated background was observed, and no significant difference in cytoplasmic background fluorescence between the four nuclear cycles was detected (**Figure 3-7Bi**). As

PeCoS measurements are analysed differently, I also extracted the number of peaks above the defined background threshold for all control recordings and grouped them by their nuclear cycle. Once again, the background measurements showed no statistical difference between the nuclear cycles 11-14 (**Figure 3-7Bii**). Thus, background noise is constant and does not affect FCS/PeCoS concentration comparisons between these nuclear cycles.

3.2.4.2 Determining how the biophysical properties of an inert protein change between nuclear cycles 11-14

I next wanted to test how any changes in the biophysical properties of the developing blastoderm embryo might influence the concentration and biophysical properties of an inert protein. I therefore used FCS to characterise the behaviour of untagged mNeonGreen (mNG) expressed from either the *Sas-6* or *Plk4* promoter or untagged dimeric-NeonGreen (dNG) expressed from the *Sas-6* promoter (so hopefully in a similar concentration range to the centriolar proteins of interest for my studies). As untagged m/dNG does not localise to centrosomes or any other cell organelle in the embryo, eAsl-mKate2 was also expressed as a centriolar marker to identify the nuclear cycle stage and the centrosomal plane. These proteins were all expressed at cytoplasmic concentrations which were suitable for FCS (~15-30 nM), but were too high to be measured with PeCoS. Surprisingly, the expression of mNG from the *Plk4* promoter resulted in a higher concentration (~30 nM) than the expression from the *Sas-6* promoter (~15 nM) (even though Sas-6 is normally expressed at much higher levels than Plk4) (**Figure 3-8Bi+ii**). This suggests that the low levels of Plk4 in the cytoplasm are not due to low levels of expression of the *Plk4* gene in the embryo.

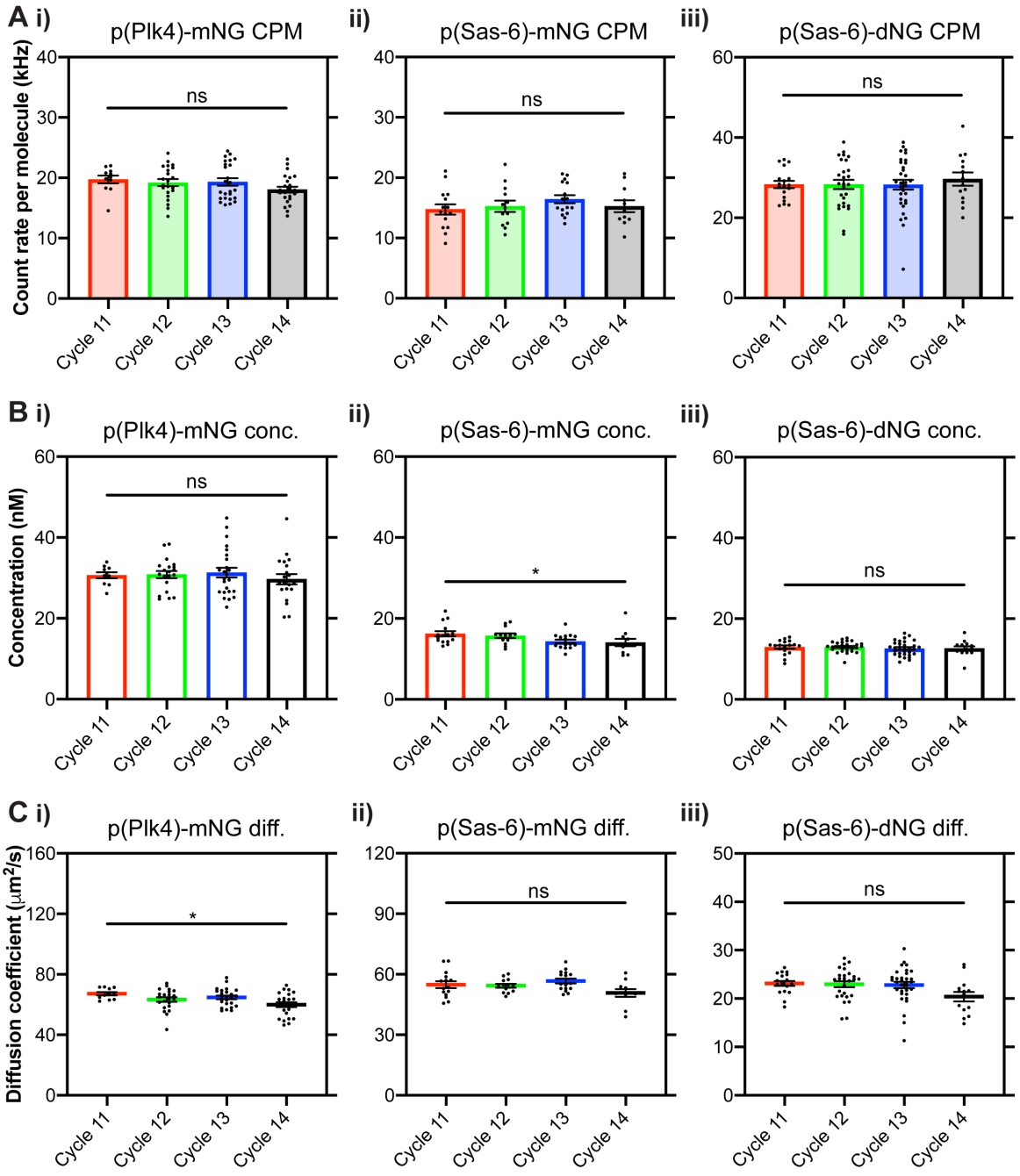


Figure 3-8: Characterising the behaviour of inert fluorescent proteins during nuclear cycles 11-14
Graphs show molecular brightness (CPM) **(A)**, cytoplasmic concentration **(B)**, and diffusion coefficient **(C)** measurements of untagged m/dNG at the beginning of nuclear cycle 11-14 (mean±SEM). mNG was expressed from the *Plk4* (i) or *Sas-6* (ii) promoter and dNG was expressed from the *Sas-6* (iii) promoter. Each data point represents the average of 4-6x 10-second-long recordings. Statistical significance was assessed using an ordinary one-way ANOVA test (for Gaussian-distributed data) or a Kruskal-Wallis test (*, P<0.05; ns, not significant).

To confirm that the quality of the FCS recordings is consistent between the four nuclear cycles, I measured the molecular brightness of mNG and dNG at the beginning of each cycle. The CPM did not change between cycles 11-14 in any of these lines, demonstrating that FCS can be used to compare the cytoplasmic concentration and diffusion coefficients for proteins between the four cycles (**Figure 3-8A**). Reassuringly, also the cytoplasmic concentrations and diffusion coefficients of the inert fluorescent proteins stayed relatively constant between the nuclear cycles 11-14 (**Figure 3-8B+C**).

3.2.4.3 Determining how the biophysical properties of an inert protein change during nuclear cycle 12

In addition to the comparison between the individual nuclear cycles, I also wanted to examine the cytoplasmic dynamics of proteins of interest throughout an entire nuclear cycle—especially during S-phase when the incorporation of centriolar and centrosomal proteins occurs. Nuclear cycle 12 was chosen as a representative cycle. Importantly, only those embryos with a similar cycle length were used for this analysis, allowing me to calculate a more accurate "average" value at each time-point.

For the dynamic measurements, 6x 10-second-long measurements were taken every two minutes from the beginning of cycle 12 until the beginning of cycle 13 (both events were judged by centrosome separation, which occurs at the start of S-phase in these embryos) (**Figure 3-9A**). Between measurements, the laser position was readjusted to avoid centrosomes moving through the excitation spot and to account for any movement of the centrosomal plane in the z-direction. Nuclear envelope breakdown (NEB) was identified by the loss of a robust centrosomal plane caused by the slightly irregular movement of the centrioles in the z-axis as they entered mitosis; the average time of NEB is indicated

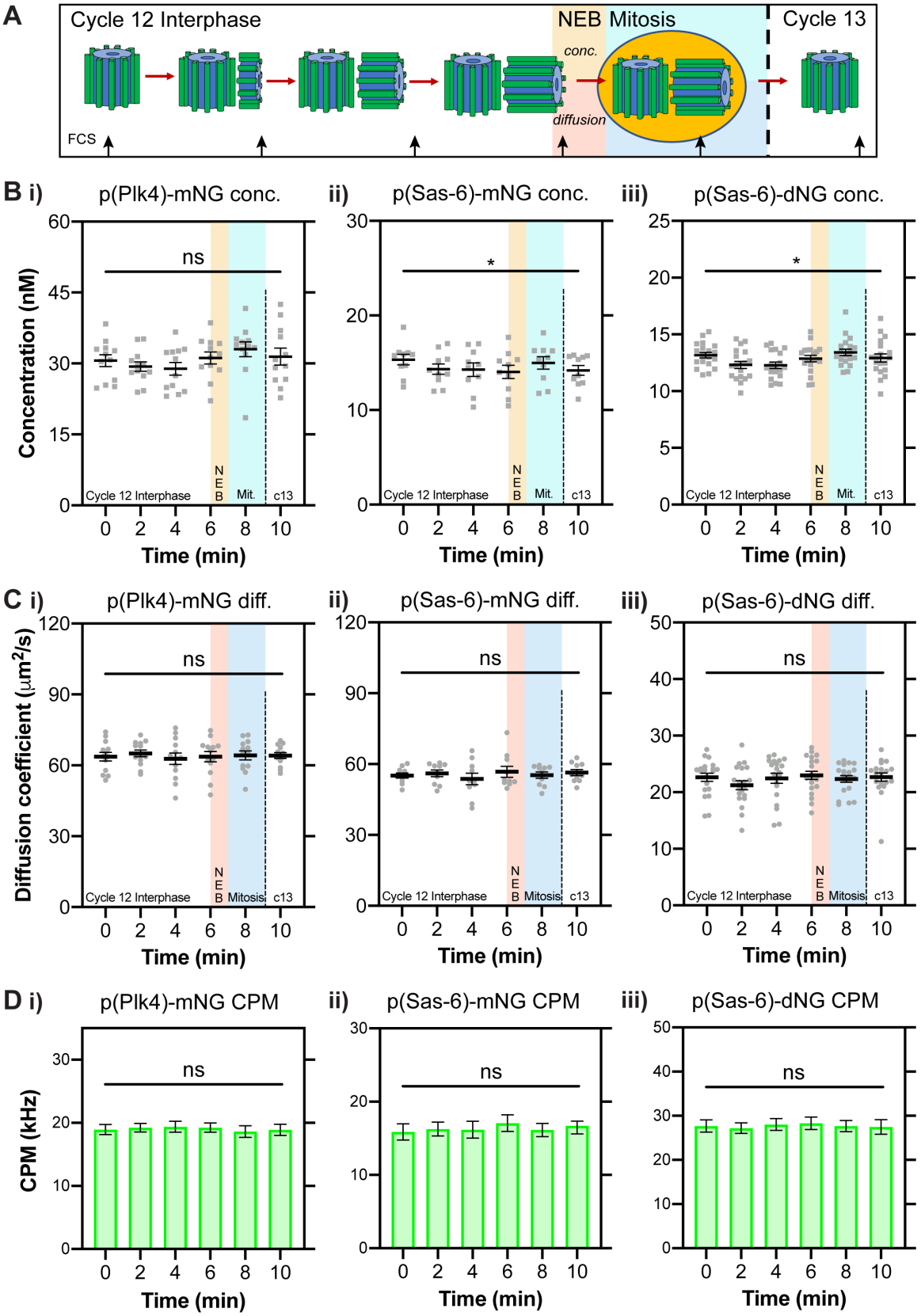


Figure 3-9: Characterising the behaviour of inert fluorescent proteins during nuclear cycle 12
See next page.

Figure 3-9: Characterising the behaviour of inert fluorescent proteins during nuclear cycle 12
(A) The cartoon depicts a schematic of centrosome behaviour during the time that FCS measurements were taken (6x 10 seconds every two minutes, *black* arrows) from the beginning of nuclear cycle 12 to the beginning of nuclear cycle 13. **(B-D)** Graphs quantify cytoplasmic concentration (B), diffusion coefficient (C), and CPM (D) measurements of untagged m/dNG (mean±SEM) from the start of nuclear cycle 12-13, expressed from either the *Plk4* (i) or *Sas-6* (ii and iii) promoter. Each data point represents the average of 4-6x 10-second-long recordings. Statistical significance was assessed using an RM one-way ANOVA test with Geiser-Greenhouse correction (for Gaussian-distributed data) or a Friedman test (*, P<0.05; ns, not significant).

in the graphs. The cytoplasmic concentration of all three untagged m/dNG proteins fluctuated slightly during the cycle (**Figure 3-9B**). These fluctuations were relatively minor (no more than 10-15%) but consistently the concentration tended to decrease slightly during early S-phase, and then increase slightly during mitosis. This may suggest that the physical properties of the cytoplasm (e.g., its density) fluctuates slightly during the nuclear cycle. As I will show later, however, these changes were very minor when compared to some of the changes I observed when assessing the behaviour of certain centriole and centrosome proteins. In addition, the diffusion speed (**Figure 3-9C**) and CPM (**Figure 3-9D**) in all three control lines did not change significantly during the nuclear cycle.

3.3 Conclusions

The *Drosophila* blastoderm embryo seems to be an excellent system for robust FCS/PeCoS measurements. The total background fluorescence and the number of background intensity peaks in the control recordings, showed the consistency of the background noise between the nuclear cycles 11-14. Control measurements of untagged m/dNG further confirmed this observation, and validated FCS for measurements throughout the entire nuclear cycle. Unfortunately, I could not generate a suitable inert mNG control line expressed at sufficiently low levels for PeCoS validation within and between nuclear cycles.

4 Investigation of the cytoplasmic pool of centriolar proteins

4.1 Introduction

How cells control the size and number of their organelles is still poorly understood (Marshall, 2016). Most organelles display a complex three-dimensional structure and are composed of a high number of associated proteins, making it difficult to dynamically characterise organelles throughout the cell cycle or to identify the critical component that best describes an organelle's size (Marsh *et al.*, 2001; Chan and Marshall, 2010).

Centriole biogenesis is strictly regulated in space and time (Fu, Hagan and Glover, 2015), making this duplication process an excellent model system to identify novel regulatory mechanisms that allow a cell to sense and/or control the size and number of its organelles. Centrioles only duplicate once every cycle, and the daughter centriole grows perpendicularly from its mother and to the same size. Centriole size varies greatly between organisms and even between tissues in the same organism but is very consistent within a cell type (Loncarek and Bettencourt-Dias, 2018). Pioneering studies in multiple model systems have identified a core set of only five centriole duplication proteins that are essential to form a new daughter centriole – Asl (CEP152), Plk4 (PLK4), Ana2 (STIL), Sas-6 (SAS6), and Sas-4 (CPAP/CENPJ) using *Drosophila* nomenclature (human homologues in brackets) (see **Chapter 1, Section 1.2** for detailed description) (Conduit, Wainman and Raff, 2015). This surprisingly low number allows for a relatively systematic analysis of not only the role of each protein in the assembly process, but also how perturbing the function of one protein influences the behaviour and function of the others.

In the Raff laboratory we use the early nuclear cycles 11-14 of the *Drosophila* embryo as a model system to study centriole duplication, which occurs highly synchronously and very rapidly in the shared cytoplasm of the syncytial embryo (Foe and Alberts, 1983). During these "blastoderm" cycles, the majority of the nuclei are positioned in a monolayer close to the cortex (Foe and Alberts, 1983). In these embryos, the behaviour of fluorescently tagged proteins of interest at hundreds of simultaneously duplicating centrioles can be followed (**Figure 4-1Ai**)—allowing one to discern patterns of behaviour that would not be possible from the relatively noisy data generated from observing individual centrioles in individual cells (Aydogan *et al.*, 2018; Alvarez-Rodrigo *et al.*, 2019).

Previous studies in our lab investigated centriole growth dynamics by measuring the irreversible incorporation of the fluorescently tagged cartwheel protein Sas-6-GFP as a proxy for centriole size (Aydogan *et al.*, 2018). These observations revealed that centrioles grow in an approximately linear fashion and then rapidly plateau once they reach their final size (**Figure 4-1Aii**). Moreover, this growth appears to be driven by a local oscillation in the levels of Plk4 at the base of the growing daughter centriole—some of this work is described in **Chapter 5** of this thesis (Aydogan, Steinacker *et al.*, 2020). Mathematical modelling and further experiments suggested that the Plk4 oscillation could be generated by a classical negative feedback loop in which Asl recruits and activates Plk4 at the base of the growing daughter centriole: the activated Plk4 phosphorylates Ana2 to promote Sas-6 incorporation into the centriole, but also phosphorylates Asl at multiple sites to turn-off the ability of Asl to recruit Plk4 (Aydogan, Steinacker *et al.*, 2020).

This mathematical model could successfully recapitulate the Plk4 oscillation (Aydogan, Steinacker *et al.*, 2020). Interestingly, however, although initial attempts to extend the

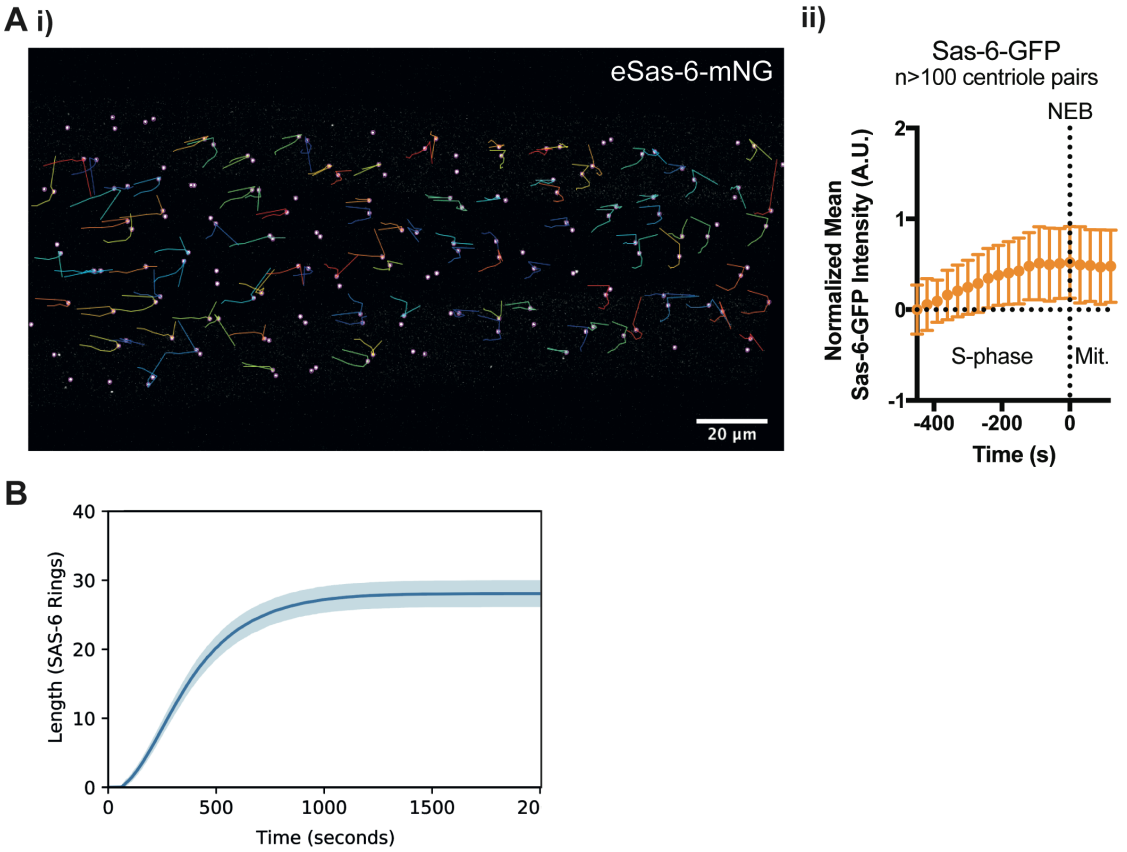


Figure 4-1: Centrioles grow in a linear fashion and plateau when they reach their final size
(A) (i) Image shows an embryo expressing eSas-6-mNG in which many of the centrioles have been tracked using the Trackmate plug-in in Fiji. Sas-6-mNG is irreversibly incorporated into the growing daughter centriole and its intensity increase can be used as a proxy for centriole growth. Due to their small size (~120-150 nm), the mother and daughter centrioles cannot be resolved so each intensity spot consists of a centriolar pair. **(ii)** Graph shows how the normalised centriolar Sas-6-GFP intensity (mean±SD) varies in a single embryo from the beginning of S-phase in nuclear cycle 12 (judged by centrosome separation) until soon after the entry into mitosis (as judged by nuclear envelope breakdown—NEB). Graph was modified from Aydogan *et al.*, 2018. **(B)** A mathematical network was generated to recapitulate the centriole growth dynamics (Michael Boemo, *unpublished*); this can generate reasonable growth curves, but it fails to capture the abrupt cessation of growth (seen in (Aii)) when centrioles reach their final size.

model to describe Sas-6 incorporation dynamics successfully recapitulated several features of cartwheel growth (such as the growth alterations caused by varying the concentration of individual centriolar proteins) they consistently failed to capture well the rather abrupt cessation of centriole growth when the centrioles reach their final size, generating instead a more gradual slowing of growth over a prolonged period (**Figure 4-1B**) (Michael Boemo, *unpublished*). I hypothesised that as the embryos proceed through S-phase, the amounts or properties of one or more of the core centriole duplication proteins might be altered in the cytoplasm to help ensure that centrioles abruptly stop

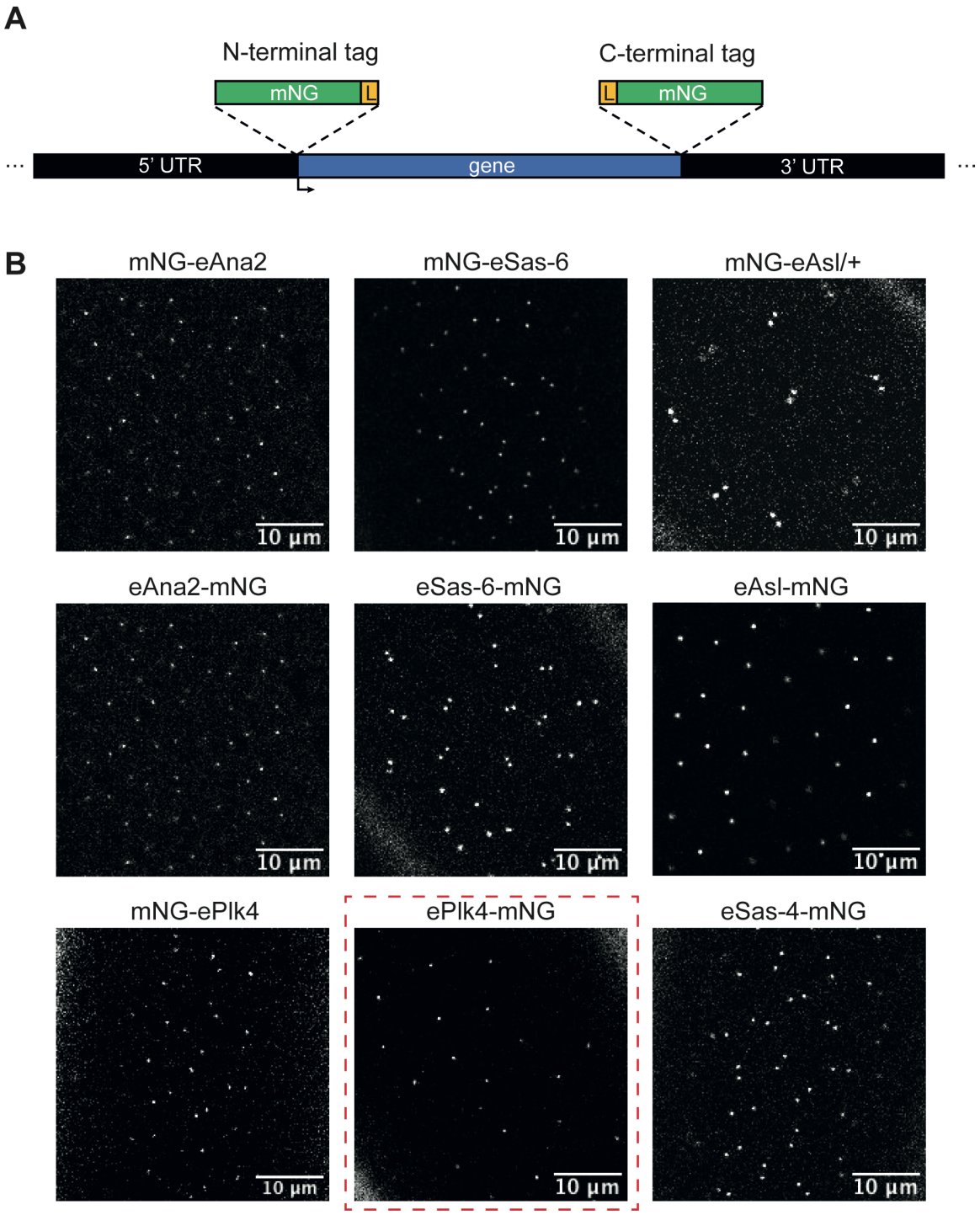


Figure 4-2: Endogenously mNG-tagged centriolar proteins localise to the centriole
(A) Schematic illustration of the strategy to "knock-in" mNG on either the N- or C-terminus of an endogenous locus. A linker sequence (L) was introduced between the fluorescent tag and the gene of interest to minimise any disruption to protein function. **(B)** Images show the centriolar localisation of the mNG-tagged CRISPR/Cas9-mediated knock-in alleles in the embryo. All proteins were—where possible—tagged on their N- and C-termini. N-terminally tagged Asl did not rescue the *asl*$^{-/-}$ mutant lethal phenotype and had to be expressed in a heterozygous background. N-terminally tagged Plk4 caused centriole overduplication (see Figure 4.3). As I failed to generate a C-terminally tagged Plk4 CRISPR/Cas9 knock-in line, a P-element insertion of Plk4-mNG expressed from its endogenous promoter in the *Plk4*$^{-/-}$ mutant background was used for all experiments (*red dashed* box).

growing as they approach the end of S-phase. I therefore set out to use FCS to analyse the behaviour of the cytoplasmic pool of all five core centriole duplication proteins.

4.2 Results

4.2.1 Generating CRISPR/Cas-9 mNG knock-ins at the endogenous loci of the core centriole duplication genes

I attempted to fluorescently tag all five core duplication proteins (Asl, Plk4, Sas-6, Ana2 and Sas-4) at their endogenous locus using CRISPR/Cas9, which I hoped would allow me to analyse these protein's behaviour in conditions that are most similar to their native expression profiles (**Figure 4-2A**). I designed the cloning strategy for each gene, and this work was performed largely by myself with help from Eline van Houtum, a visiting Master's student whom I supervised for nine months, and also Saroj Saurya, the Raff Lab Manager, who occasionally helped me with PCR screening to identify positive fly lines. All the final lines were sequenced to confirm the appropriate insertion of the fluorescent marker (a more detailed description of the strategy for each construct and how the fly lines were generated and validated is presented in **Chapter 2, Sections 2.1.3** and **2.2.2**).

We successfully generated between 1-4 "knock-in" lines expressing N- or C-terminally mNG-tagged versions of Asl, Ana2 and Sas-6, and C-terminally mNG-tagged Sas-4 (as previous work in the lab had shown that an N-terminally-tagged GFP-Sas-4 fusion was non-functional—Jordan Raff, personal communication); all of these fusion proteins appeared to localise correctly to centrioles (**Figure 4-2B**). These lines were viable as homozygotes, except for mNG-eAsl, which could only be maintained as a heterozygous stock (presumably indicating that this fusion protein was not fully functional). I used western blotting to confirm that all proteins were fluorescently tagged and expressed at similar levels as the endogenous protein (**Figure 4-3A**).

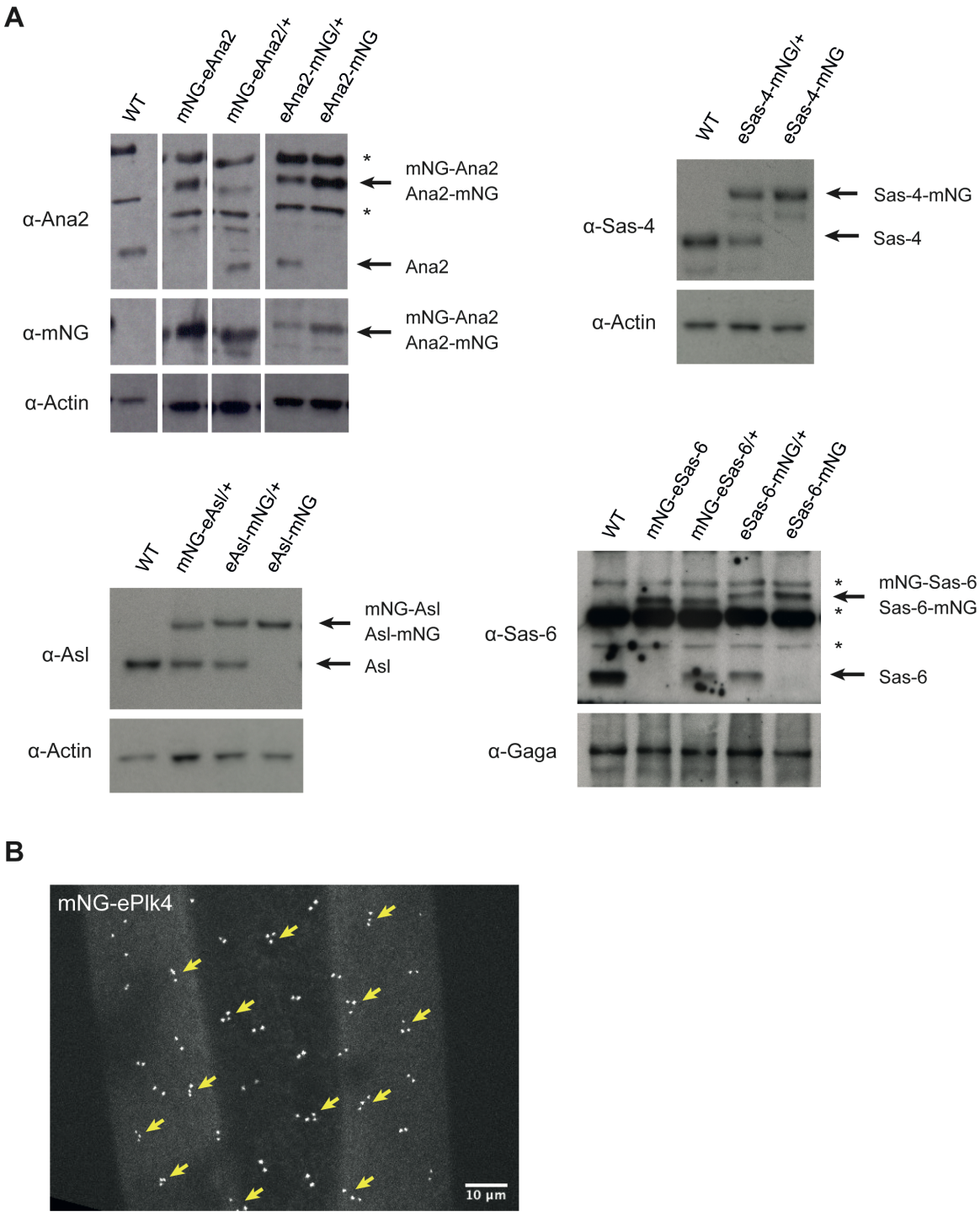


Figure 4-3: Western blots confirm the successful mNG knock-in at the endogenous loci
(A) Western blot analysis of embryos from heterozygous embryos expressing one copy of endogenously mNG-tagged and one copy of untagged protein. Prominent unspecific bands are indicated (*). For Ana2, the N-terminally tagged protein only showed a very dim signal when the α-Ana2 primary antibody was used (which contradicted my FCS concentration measurements in Appendix D). I therefore also used an α-mNG primary antibody, which revealed a higher protein abundance for the N-terminally tagged protein. This suggests that the fluorescent tag, when located at the N-terminus, interferes with efficient binding of the α-Ana2 primary antibody. Actin and Gaga factor were used as loading controls. **(B)** Image of an embryo from a mother homozygous for N-terminally tagged mNG-ePlk4 (CRISPR/Cas9 knock-in line). *Yellow* arrows indicate centriole overduplication.

Despite multiple attempts, we were unable to recover an endogenous ePlk4-mNG knock-in line. The PCR analysis of the founder flies suggested that mNG was successfully being inserted into the *Plk4* locus, but that this was not successfully transmitted through the germline. I subsequently learnt that the Bettencourt-Dias laboratory had also attempted, but failed, to generate an endogenous ePlk4-mNG knock-in line (Jordan Raff, personal communication). We were, however, able to generate an endogenously tagged mNG-ePlk4 fusion. This was homozygously viable, and I noticed that early embryos exhibited significant centriole overduplication, suggesting that the fusion protein was overexpressed (**Figure 4-3B**). Unfortunately, I could not compare levels of mNG-ePlk4 to the endogenous protein as their levels are so low in the embryo (see **Chapter 3, Section 3.3**) that they cannot be detected by western blotting. Interestingly, an endogenous mNG-ePlk4 knock-in line was also recently generated by the Bettencourt-Dias laboratory and this also led to centriole overduplication (although this was not characterised in detail) (Nabais *et al.*, 2021). Because these endogenous mNG-ePlk4 knock-in lines lead to centriole overduplication, I decided to analyse Plk4 behaviour in subsequent experiments using previously generated lines in the lab in which ePlk4-mNG is expressed from a transgene under the control of its endogenous promotor (~2 kb of sequence upstream from the transcription start site), as the centrioles do not overduplicate in these lines (Aydogan, Steinacker *et al.*, 2020).

4.2.2 The cytoplasmic concentration of the core centriole duplication proteins does not change dramatically during the nuclear cycle

For all the core duplication proteins, I conducted cytoplasmic FCS measurements throughout an entire nuclear cycle to investigate how their cytoplasmic concentrations changed. 6x 10-second-long FCS measurements were obtained every two minutes within

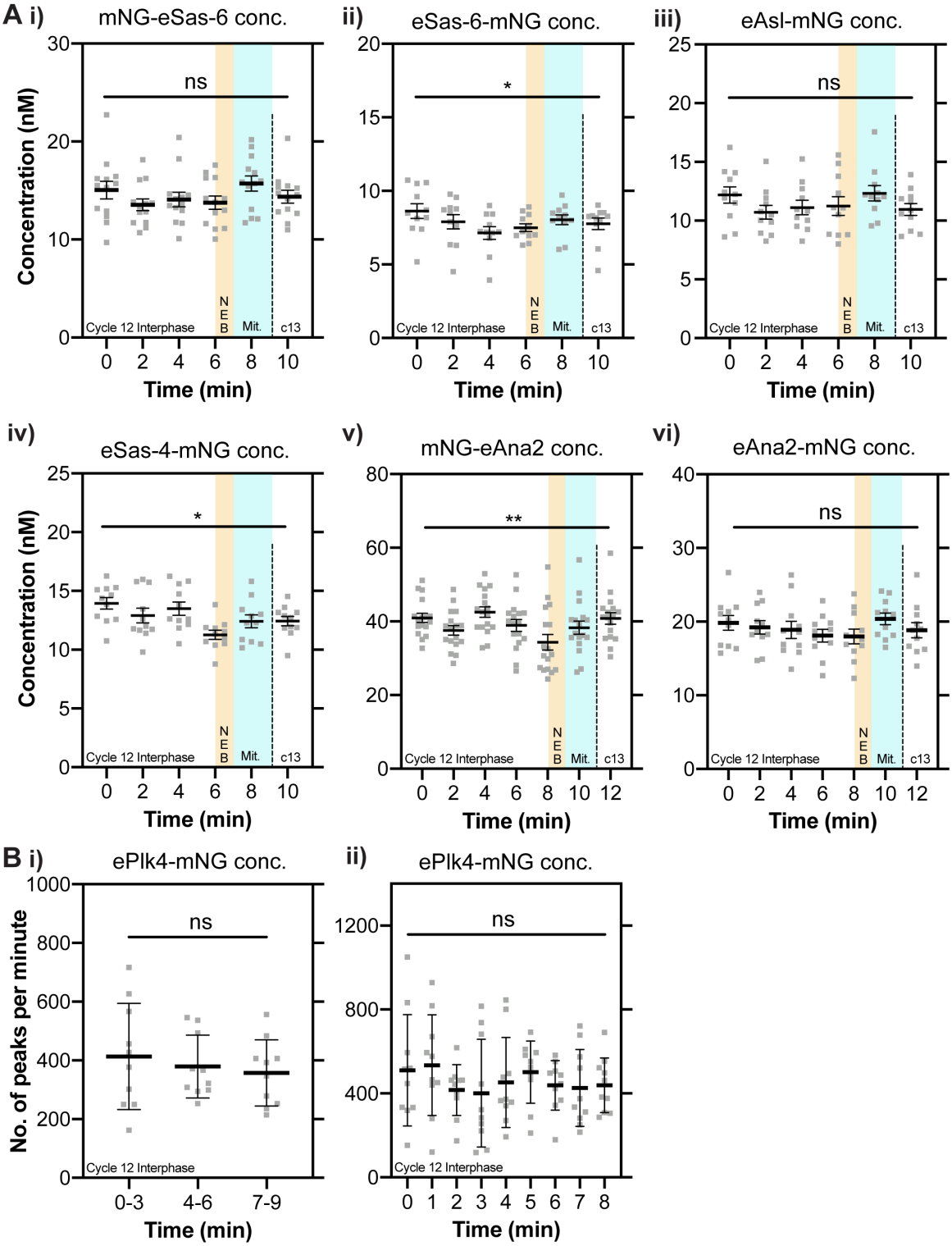


Figure 4-4: The cytoplasmic concentration of all five core centriole duplication proteins does not change dramatically during nuclear cycle 12

(A) Graphs show cytoplasmic FCS concentration measurements (mean±SEM) of the core centriole duplication protein knock-in lines that were taken every two minutes from the start of nuclear cycle 12-13. The estimated NEB timing is depicted in *yellow*, mitosis in *green*. Each data point represents the average of 4-6x 10-second-long recordings. **(B)** Graphs show PeCoS measurements (mean±SD) of ePlk4-mNG throughout nuclear cycle 12 both with the normal 180-second measurement interval **(i)** and also when this measurement is divided into 60-second intervals **(ii)**. Each data point represents an individual 180/60-second-long PeCoS measurement. Statistical significance was assessed using a paired one-way ANOVA test (for Gaussian-distributed data) or a Friedman test (**, P<0.01; *, P<0.05; ns, not significant).

the centrosomal layer from the beginning of nuclear cycle 12 until the beginning of nuclear cycle 13 (judged by centrosome separation (CS) (**Figure 4-4A**). Unfortunately, ePlk4-mNG levels in the cytoplasm were too low to be reliably measured by FCS, but my newly established spectroscopy technique (PeCoS—see **Chapter 3, Section 3.2.3**) allowed me to retrieve information about its relative cytoplasmic concentration at different timepoints throughout the cycle (**Figure 4-4Bi**).

Perhaps surprisingly, although all five proteins appeared to be present at relatively low concentrations (~5-40 nM, with ePlk4-mNG being too low to be measured), they did not show a dramatic change in cytoplasmic concentration during the nuclear cycle, even when the centrioles were being assembled in S-phase (**Figure 4-4**). Although I detected a small downward trend in concentration of all the centriole proteins measured by FCS during the first two minutes of S-phase, I detected a similar downward trend with all three untagged mNG/dNG controls (**Figure 3-9B**), suggesting that this is likely to be a feature of the technique. The trend after the first two minutes was variable between the different centriole proteins (and indeed the mNG/dNG controls), and all of the changes in concentration I measured were relatively small, suggesting they are likely due to random variation (either technical or biological). As the PeCoS measurements of ePlk4-mNG were conducted in consecutive 180-second-long intervals, I reasoned that they might be insensitive to any rapid changes in its cytoplasmic concentration (**Figure 4-4Bi**). I therefore split all measurements into 60-second-long intervals but still did not observe any significant concentration fluctuations (**Figure 4-4Bii**). From these measurements I conclude that the centriole growth dynamics in the early *Drosophila* embryo are not influenced by the cytoplasmic depletion of any of the core centriole duplication proteins.

4.2.3 The cytoplasmic diffusion rate of Ana2 changes significantly as embryos prepare to enter mitosis

These observations suggest that the depletion of one or more of the core centriole duplication proteins does not contribute to the rapid slowing of centriole growth towards the end of S-phase (**Figure 4-4**). I wondered, however, whether any of these proteins might be modified during the nuclear cycle in a way that effectively switched off their ability to contribute to centriole growth, and, if so, whether this modification might cause a detectable change in the diffusion rate of the protein. Such a behaviour was previously reported for Plk1, which exhibited diffusion speed changes throughout the cell cycle that were dependent on its kinase activity (Mahen *et al.*, 2011). I therefore used my FCS data to examine how the diffusion rate of the core duplication proteins changed over the course of nuclear cycle 12 (although, unfortunately, I cannot extract this information from my PeCoS measurements of ePlk4-mNG) (**Figure 4-5**).

In general, the diffusion coefficient of most of the core duplication proteins tended to increase slightly (meaning that the proteins diffused more quickly) as S-phase progressed, and then decrease slightly as the embryos went through mitosis and entered the next nuclear cycle 13 (**Figure 4-5A**). Although in the case of mNG-eSas-6, eSas-6-mNG, eAsl-mNG and eSas-4-mNG this tendency was not, or was only just, statistically significant, it was consistent, and no similar trend was observed with my mNG and dNG controls (**Figure 3-9C**)—although these control proteins diffuse much faster than the core centriole proteins. I conclude that all these proteins have a slight tendency to migrate more slowly in the cytoplasm during early S-phase, when the centrioles are assembling—perhaps indicating that a fraction of the cytoplasmic pool of these proteins is either

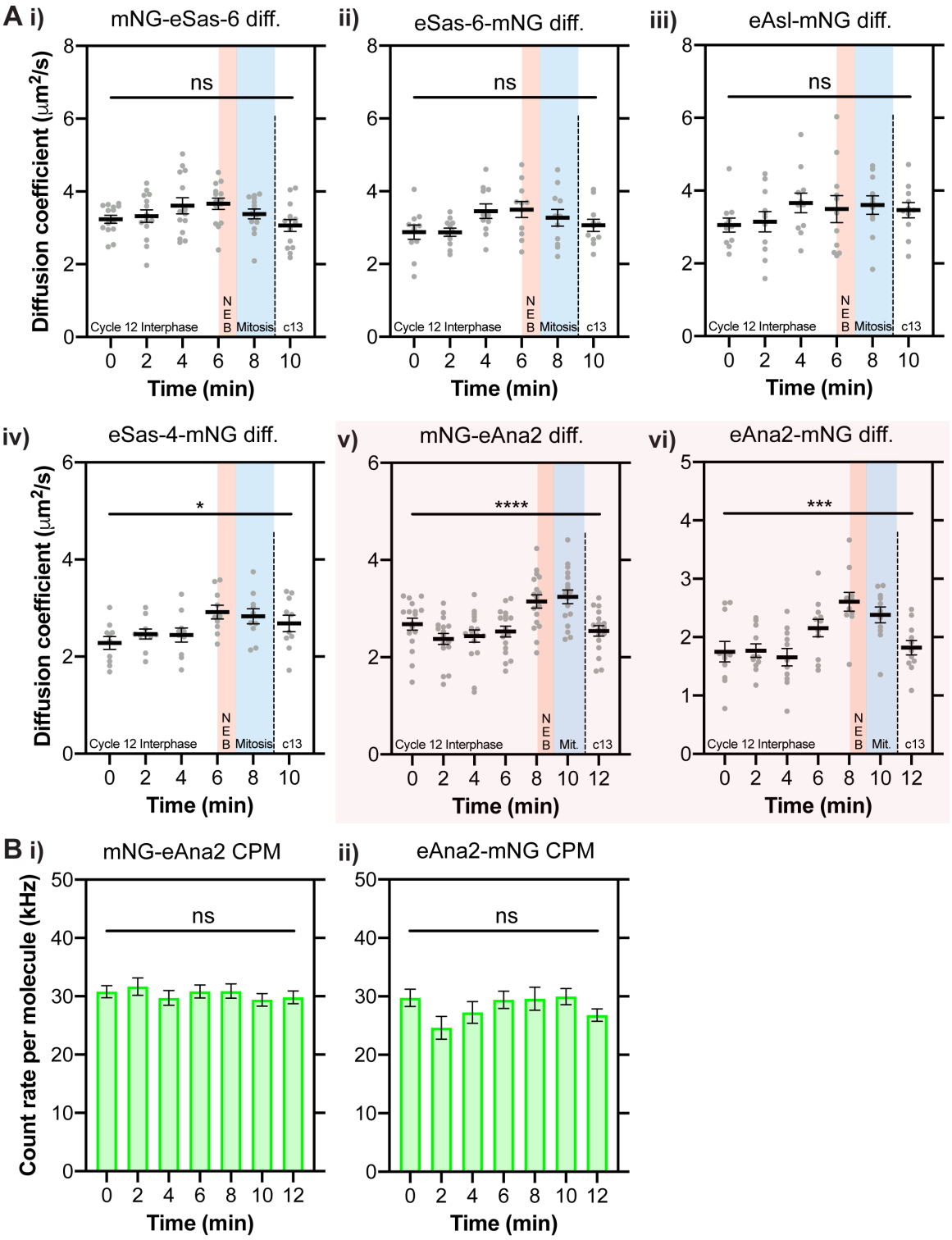


Figure 4-5: The cytoplasmic diffusion rate of Ana2 changes significantly as embryos prepare to enter mitosis

(A) Graphs show cytoplasmic FCS diffusion measurements (mean±SEM) of the core centriole duplication protein knock-in lines that were taken every two minutes from the start of nuclear cycle 12-13. The estimated NEB timing is depicted in *orange*, mitosis in *blue*. Each data point represents the average of 4-6x 10-second-long recordings. **(B)** Graphs show cytoplasmic FCS CPM measurements (mean±SEM) of mNG-eAna2 **(i)** and eAna2-mNG **(ii)** that were taken every two minutes from the start of nuclear cycle 12-13.

Statistical significance was assessed using a paired one-way ANOVA test (for Gaussian-distributed data) or a Friedman test (****, P<0.0001; ***, P<0.001; *, P<0.05; ns, not significant).

modified or can form complexes with other proteins specifically during the assembly period.

Most strikingly, however, the diffusion rates of both mNG-eAna2 and eAna2-mNG exhibited the same tendency to change over the cycle, but these changes were much more obvious—particularly the large increase in their diffusion coefficients in late S-phase—and were highly statistically significant (**Figure 4-5v+vi**). As Ana2 plays a crucial role in promoting the incorporation of Sas-6 into the growing daughter centriole cartwheel, this observation suggests that Ana2's behaviour in the cytoplasm might change in late S-phase in such a way that inhibits its ability to promote centriole growth.

4.2.4 The change in Ana2's diffusion speed is largely independent of its ability to homo-oligomerise and to interact with Sas-6

I reasoned that there are at least three reasons why the diffusion speed of Ana2 might change during the nuclear cycle: (1) Ana2's homo-oligomerisation state might change—as Ana2/STIL proteins have been shown to homo-oligomerise, and this ability is crucial to their function (Cottee *et al.*, 2015; David *et al.*, 2016); (2) Ana2's ability to interact with another protein in the cytoplasm might change—for example, Ana2/STIL proteins are known to interact with Sas-6/SAS6 and Sas-4/CPAP, and these interactions are crucial for centriole assembly (Cottee *et al.*, 2013; Hatzopoulos *et al.*, 2013; Dzhindzhev *et al.*, 2014; Ohta *et al.*, 2014; Kratz *et al.*, 2015; Moyer *et al.*, 2015; Fatalska *et al.*, 2020). (3) Ana2 might be post-translationally modified in the cytoplasm in a cell cycle-dependent manner, leading to a conformational change that affects its shape and therefore its diffusion—for example, Ana2/STIL proteins are phosphorylated in their conserved STAN domain to promote their interaction with Sas-6 (Dzhindzhev *et al.*, 2014; Ohta *et al.*, 2014; Kratz *et al.*, 2015; Moyer *et al.*, 2015; Fatalska *et al.*, 2020). These three possibilities are not

mutually exclusive; for example, Ana2 may be post-translationally modified in the cytoplasm and this could influence its cytoplasmic interaction with itself or with a binding partner.

To check if Ana2's cytoplasmic stoichiometry (i.e., its oligomerisation state) changed during nuclear cycle 12, I first examined whether Ana2's molecular brightness (CPM) varied during the cycle. CPM analysis is based on the concept that on average the same number of photons per second will be detected for each fluorophore diffusing through the laser beam if the same fluorophore and laser power are used for every measurement. The molecular brightness can therefore only change if the fluorescently labelled protein of interest oligomerises and multiple fluorophores move through the laser beam together as a single species. I previously showed in **Chapter 3** that my FCS setup is sensitive to cytoplasmic stoichiometry changes, and I detected a significant difference in the molecular brightness of mNG and dNG (**Figure 3-4Bii**). The CPM for both mNG-eAna2 and eAna2-mNG, however, remained constant between all measurements within nuclear cycle 12, indicating that Ana2's cytoplasmic stoichiometry does not change during the cycle (**Figure 4-5B**).

I next examined whether specific domains of Ana2 that have been shown to be required for its oligomerisation or interaction with Sas-6 were required for the change in Ana2's diffusion speed. The central coiled-coil (CC) region of Ana2/STIL proteins is essential for their homo-oligomerisation (Cottee *et al.*, 2015; David *et al.*, 2016), as well as for an interaction with CDK1 kinase in human cells (Zitouni *et al.*, 2016), while the conserved STAN domain is required for their interaction with Sas-6 proteins (Dzhindzhev *et al.*, 2014; Ohta *et al.*, 2014; Kratz *et al.*, 2015; Moyer *et al.*, 2015; Fatalska *et al.*, 2020). I generated

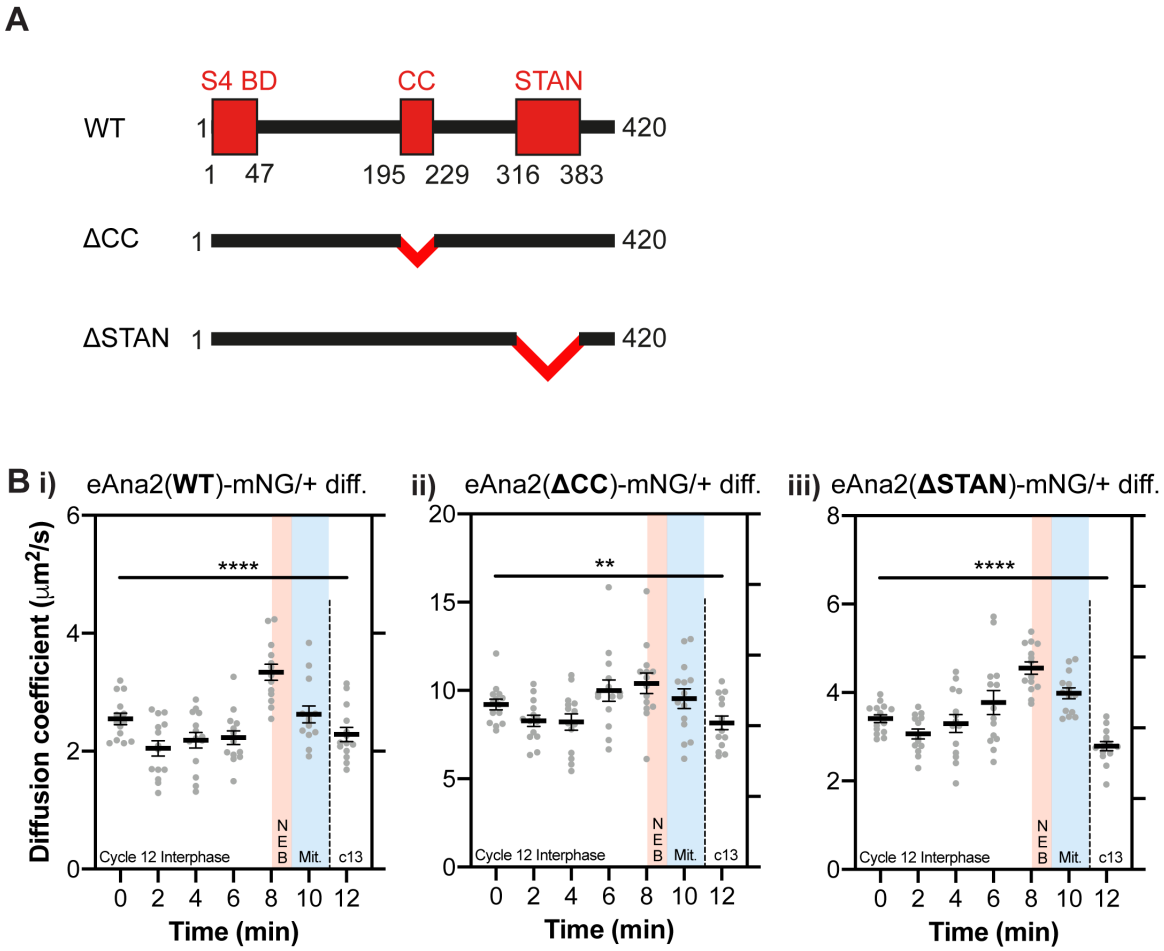


Figure 4-6: Ana2's change in diffusion rate is insensitive to the deletion of either the CC or STAN domain
(A) Schematic illustration of the Ana2 protein and its known interaction domains: S4 BD (Sas-4 Binding Domain, CC (Coiled-Coil domain), STAN (STil/ANa2 domain). For further information see Chapter 1, Section 1.2.3. Two mutant forms of Ana2 are depicted, for which the diffusion behaviour throughout nuclear cycle 12 was assessed: deletion of the entire CC domain (Δaa195-230) and deletion of the entire STAN domain (Δaa316-383). **(B)** Graphs show cytoplasmic FCS diffusion measurements (mean±SEM) of WT eAna2-mNG/+ **(i)**, eAna2(ΔCC)-mNG/+ **(ii)**, and eAna2(ΔSTAN)-mNG **(iii)** that were taken every two minutes from the start of nuclear cycle 12-13. The estimated NEB timing is depicted in *orange*, mitosis in *blue*. Each data point represents the average of 4-6x 10-second-long recordings. Statistical significance was assessed using a paired one-way ANOVA test (for Gaussian-distributed data) or a Friedman test (****, P<0.0001; **, P<0.01).

fly lines transgenically expressing mutant forms of eAna2-mNG in which either the CC or STAN domain was deleted (eAna2(ΔCC)-mNG and eAna2(ΔSTAN)-mNG, respectively) (**Figure 4-6A**).

Ana2 is essential for centriole duplication, so embryos laid by *ana2*$^{-/-}$ mutant females do not develop. As both the CC and STAN domains are essential for Ana2's centriole growth promoting function, the mutated transgenes (unlike WT Ana2 transgenes) did not rescue

this phenotype, so I generated fly lines expressing one copy of untagged WT Ana2 and one copy of the mNG-tagged WT or mutant Ana2 proteins. All these embryos developed normally, which allowed me to conduct FCS measurements throughout nuclear cycle 12. Interestingly, although the overall diffusion coefficient of both truncated proteins was elevated compared to WT Ana2-mNG—from ~2 $\mu m^2/s$ (WT) to ~9 $\mu m^2/s$ (ΔCC) and ~3 $\mu m^2/s$ (ΔSTAN)—the significant increase in diffusion speed around NEB remained (**Figure 4-6B**). This suggests that the change in Ana2's diffusion in the cytoplasm does not depend on its ability to homo-oligomerise or to interact with Sas-6. The significantly increased diffusion speed of eAna2(ΔCC)-mNG indicates that it (as expected) can no longer homo-oligomerise in the cytoplasm, and the slightly increased diffusion speed of eAna2(ΔSTAN)-mNG can either be explained by the reduction of its protein size (due to the deletion of an entire interaction domain) or by the inhibition of its cytoplasmic interaction with Sas-6 (see **Appendix C**).

4.2.5 The change in Ana2's diffusion speed appears to largely be dependent on phosphorylation by Cdk1

As the diffusion speed increase of Ana2 seems to be restricted to late S-phase/mitosis, I reasoned that this might be caused by a cell-cycle stage specific phosphorylation by a protein kinase. Cdk1 is a promising candidate for such a kinase as in the early *Drosophila* embryo its activity increases throughout S-phase, remains high during early mitosis, and abruptly decreases in late mitosis (Deneke *et al.*, 2016). Further, CDK1-CyclinB was shown to interact with STIL's CC domain in human cells and *Xenopus* egg extracts to block its binding to PLK4 and to inhibit unscheduled centriole duplication during mitosis (Zitouni *et al.*, 2016). Moreover, studies in CHO, DT40, and *Drosophila* wing disc cells observed centriole overduplication when CDK1/Cdk1 was inhibited (Vidwans, Wong and O'Farrell,

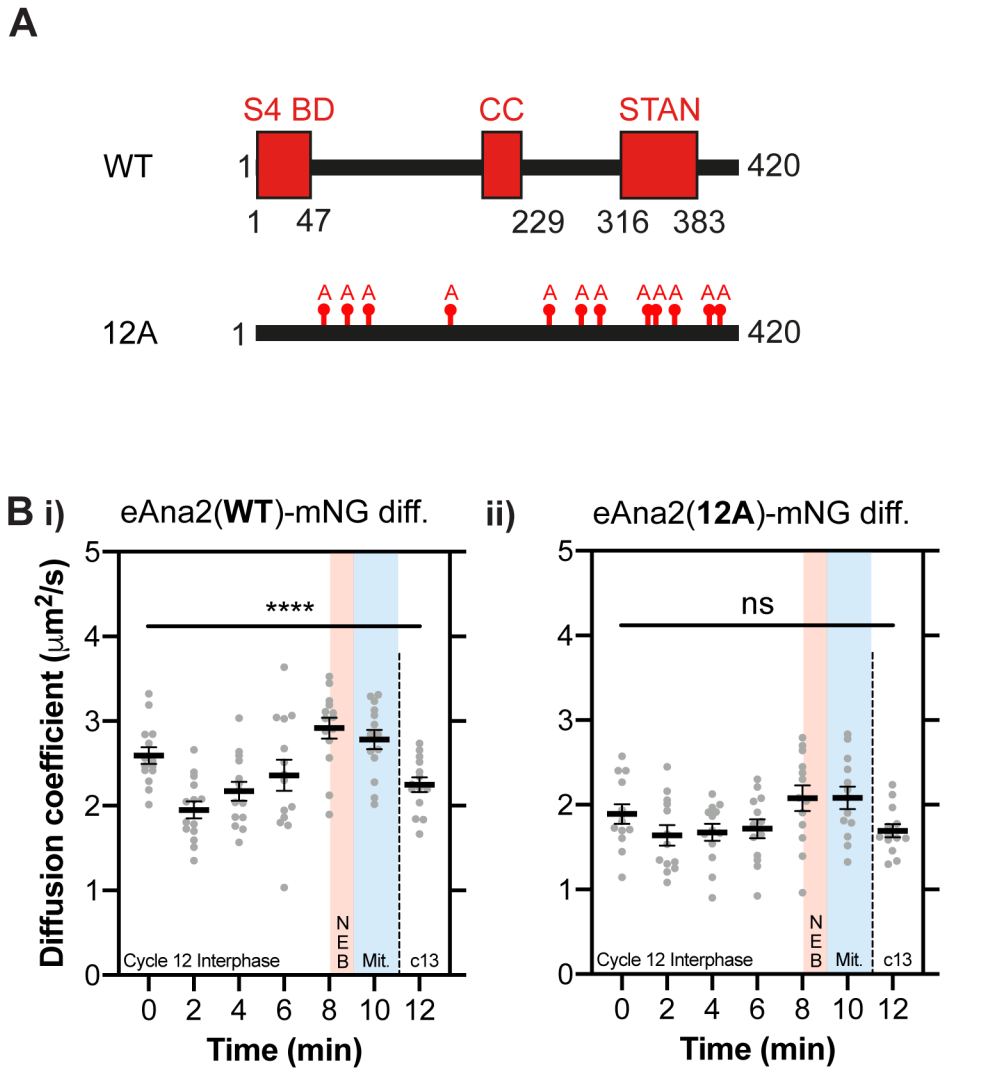


Figure 4-7: Ana2's change in diffusion rate is significantly reduced when it cannot be phosphorylated by Cdk1

(A) Schematic illustration of the WT Ana2 protein (top) with a mutant form of Ana2 (bottom) indicating where the 12 potential Cdk phosphorylation sites (S/T-P) were mutated to alanine (A-P) (=phosphonull). **(B)** Graphs show cytoplasmic FCS diffusion measurements (mean±SEM) of WT eAna2-mNG **(i)** and eAna2(12A)-mNG **(ii)** that were taken every two minutes from the start of nuclear cycle 12-13. The estimated NEB timing is depicted in *orange*, mitosis in *blue*. Each data point represents the average of 4-6x 10-second-long recordings. Statistical significance was assessed using a paired one-way ANOVA test (for Gaussian-distributed data) or a Friedman test (****, P<0.0001; ns, not significant).

2003; Steere *et al.*, 2011). CDK1 cannot only bind STIL's CC domain but is also capable of phosphorylating its N-terminus. Both mechanisms are independent of each other as STIL(ΔCC) can still be phosphorylated by CDK1-CyclinB *in vitro* (Zitouni *et al.*, 2016).

As eAna2(ΔCC)-mNG still displayed the diffusion change during NEB/mitosis in the embryo, I reasoned that if Cdk1 were to be responsible for Ana2's diffusion change, it

would more likely be achieved through a phosphorylation-dependent mechanism rather than direct binding to the CC region. Zsofia Novak, a postdoc in the lab, generated fly lines expressing either an untagged or mNG-tagged mutant form of Ana2 expressed from its endogenous core promoter in which all 12 potential Cdk phosphorylation sites (S/T-P motif) in Ana2 were mutated to alanine (A-P)—eAna2(12A) and eAna2(12A)-mNG, respectively (**Figure 4-7A**). Perhaps surprisingly, both mutant proteins rescued the *ana2*$^{-/-}$ mutant phenotype so the transgenic lines could be kept as a homozygous stock in the homozygous *ana2*$^{-/-}$ mutant background. Embryos laid by these females developed relatively normally, which allowed me to measure eAna2(12A)-mNG's cytoplasmic diffusion behaviour throughout nuclear cycle 12. Strikingly, the diffusion change of eAna2(12A)-mNG was much less prominent compared to WT eAna2-mNG and was no longer statistically significant (**Figure 4-7B**). This suggests that phosphorylation by Cdk1 might be largely responsible for Ana2's cell cycle stage-specific diffusion change, although I cannot rule out that one or more of the 12 S/T-A substitutions alters the mutant protein's diffusion rate for some other reason. Unfortunately, it was not possible to investigate Ana2's diffusion behaviour throughout the cycle after Cdk1 inhibition, because Cdk1 inhibition also blocks mitotic entry (Oliveira *et al.*, 2010).

4.2.6 eAna2(12A)-mNG is recruited to the centriole until the onset of mitosis

To further investigate my hypothesis that Ana2 is phosphorylated by Cdk1 to alter its cytoplasmic state (observed as a change in diffusion) and block its ability to promote centriole growth, I used spinning-disk confocal microscopy to characterise eAna2-mNG's recruitment dynamics at the assembly site and to evaluate how the 12A Cdk phosphonull mutations affect Ana2's recruitment pattern. Like my FCS experiment, I measured the

recruitment dynamics of eAna2-mNG from the beginning of nuclear cycle 12 until the beginning of nuclear cycle 13, but here in 30 second intervals.

Similarly to the other core cartwheel protein Sas-6 (Aydogan *et al.*, 2018), WT eAna2-mNG is initially incorporated into the growing daughter centriole in a nearly linear fashion, but it exhibits a different behaviour in the later stages of the cycle (*black* line, **Figure 4-8Ai**). While Sas-6 incorporation largely plateaus as centrioles reach their final size at approximately mid-S-phase (Aydogan *et al.*, 2018), Ana2 continues to be incorporated until ~1.5 minutes before NEB when its levels peak and then start to rapidly decline (*black* line, **Figure 4-8Ai**). Fluorescence recovery after photobleaching (FRAP) experiments have shown that, unlike Sas-6, Ana2 turns over at the growing daughter centriole (Aydogan *et al.*, 2018). I speculate, therefore, that centriolar eAna2-mNG levels start to decline in late S-phase because, like Sas-6, the Ana2 incorporation rate slows/stops (perhaps when centrioles have stopped growing), but, unlike Sas-6, Ana2 molecules can continue to leave the centriole. It will be important to test this hypothesis using FRAP.

Unexpectedly, eAna2(12A)-mNG was present at significantly higher levels on centrioles than the WT protein (*red* line and bars, **Figure 4-8A**). This could either be explained by increased recruitment/decreased release of Ana2 at the centriole or by higher expression levels of the eAna2(12A)-mNG transgene compared to the WT eAna2-mNG CRISPR/Cas9 knock-in line. To distinguish between the two possibilities, I used FCS to measure the cytoplasmic concentration of WT eAna2-mNG and eAna2(12A)-mNG at the beginning of nuclear cycle 12. Perhaps surprisingly, the cytoplasmic levels of eAna2(12A)-mNG were significantly reduced compared to WT eAna2-mNG (**Figure 4-8B**). I suspect that this is

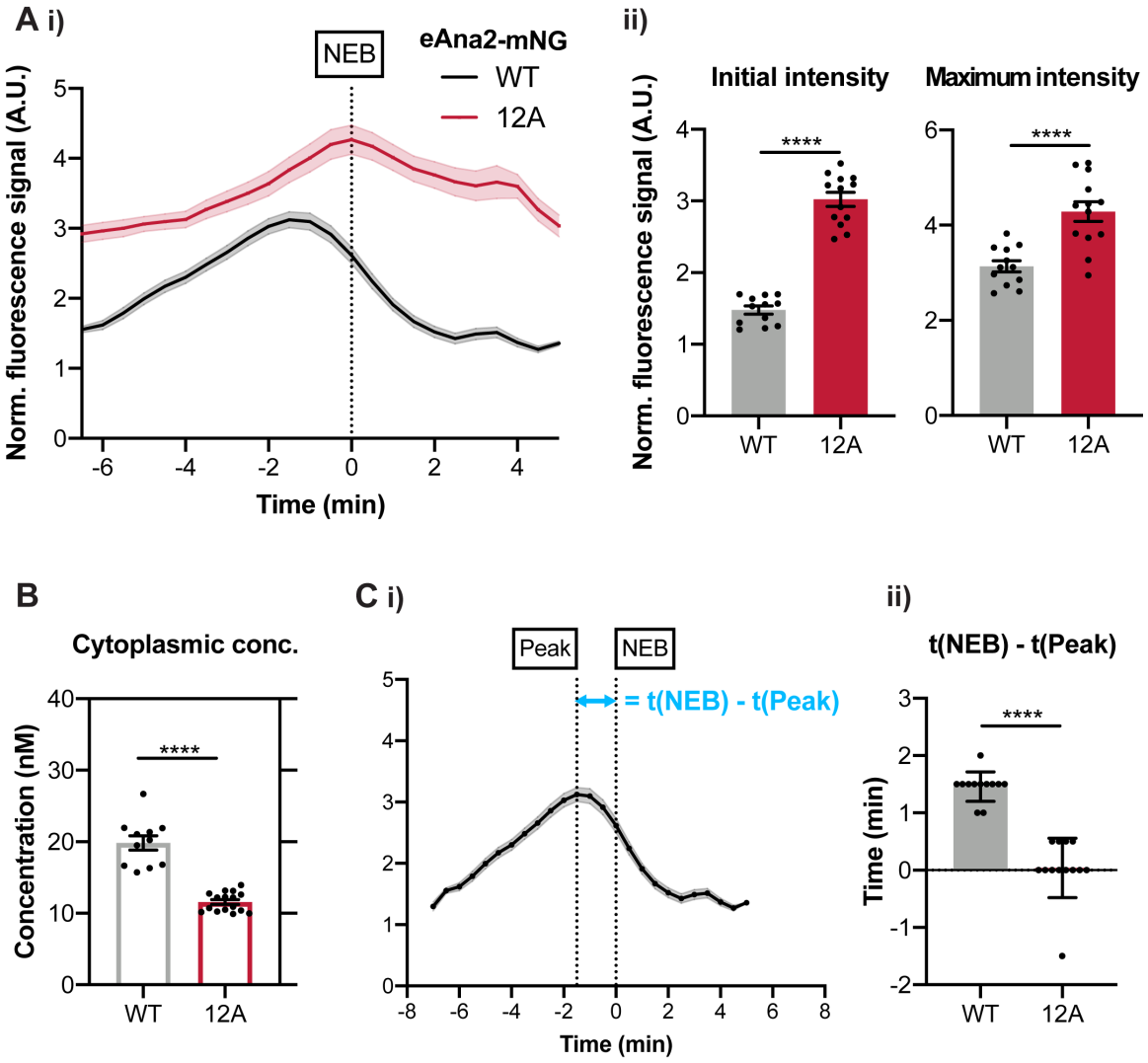


Figure 4-8: eAna2(12A)-mNG exhibits an abnormal pattern of centriolar recruitment
(A) (i) Graph shows the normalised mean±SEM centriolar recruitment dynamics for WT eAna2-mNG (*black*) and eAna2(12A)-mNG (*red*) during nuclear cycle 12 aligned by nuclear envelope breakdown (NEB). N≥12 embryos, n~100-150 centrioles per embryo. **(ii)** Bar charts quantify the normalised initial intensity and maximum intensity (mean±SEM). Each data point represents the average value of all centrioles from an embryo. **(B)** Bar chart quantifies the cytoplasmic concentration (mean±SEM) of WT eAna2-mNG and eAna2(12A)-mNG at the beginning of nuclear cycle 12. Each data point represents the average of 4-6x 10-second-long recordings. **(C) (i)** Graphic explanation and **(ii)** quantification of the timing (mean±SD) when Ana2 levels start decreasing at the centriole in comparison to NEB/mitosis.
Statistical significance was assessed using an unpaired t-test with Welch's correction (for Gaussian-distributed data) or a Mann-Whitney test (****, P<0.0001).

because eAna2(12A)-mNG has a greater ability to accumulate at centrioles than the WT protein, leading to its relative depletion from the cytoplasm.

Most importantly, there was a great discrepancy in the timing of the recruitment pattern between the two forms of Ana2. Whereas WT eAna2-mNG levels peaked and started declining before NEB, eAna2(12A)-mNG levels kept increasing until the onset of mitosis

(**Figure 4-8C**). This elongated phase of incorporation, together with the increased accumulation at centrioles, supports my hypothesis that Cdk1 normally phosphorylates Ana2 during the later stages of S-phase to inhibit its ability to be recruited to centrioles. This would explain why eAna2(12A)-mNG can be recruited to centrioles for a longer period, and why it accumulates at centrioles to higher levels, than the WT protein. Interestingly, centriolar eAna2(12A)-mNG levels still declined during mitosis (**Figure 4-8Ai**), indicating that additional mechanisms must be in place that allow even the Cdk phosphonull mutant form of Ana2 stop accumulating and ultimately leave the centrioles. This may explain why embryos from mothers expressing only eAna2(12A)-mNG can duplicate their centrioles and still develop relatively normally.

4.2.7 Centriole growth dynamics are significantly altered in the presence of Ana2(12A)

To assess how the 12 alanine substitutions in Ana2 affect the assembly of the centriole cartwheel I monitored eSas-6-mNG incorporation in the presence of either untagged WT Ana2 or untagged Ana2(12A). Embryos from flies homozygous for the knock-in eSas-6-mNG gene that were also homozygous for eAna2(12A) in the homozygous *ana2*$^{-/-}$ mutant background were very sick, and data from our lab indicates that fluorescently tagging Sas-6 leads to slower centriole cartwheel growth (Laura Hankins, personal communication). I therefore decided to measure embryos from mothers heterozygous for eSas-6-mNG but homozygous for the eAna2(12A) transgene and *ana2*$^{-/-}$ mutant background as these developed normally.

For eSas-6-mNG in the presence of WT Ana2 I observed a very similar incorporation profile as previously described for eSas-6-GFP (Aydogan *et al.*, 2018) with a near-linear increase when centrioles grow followed by a plateau when they reached their final size (*black* line,

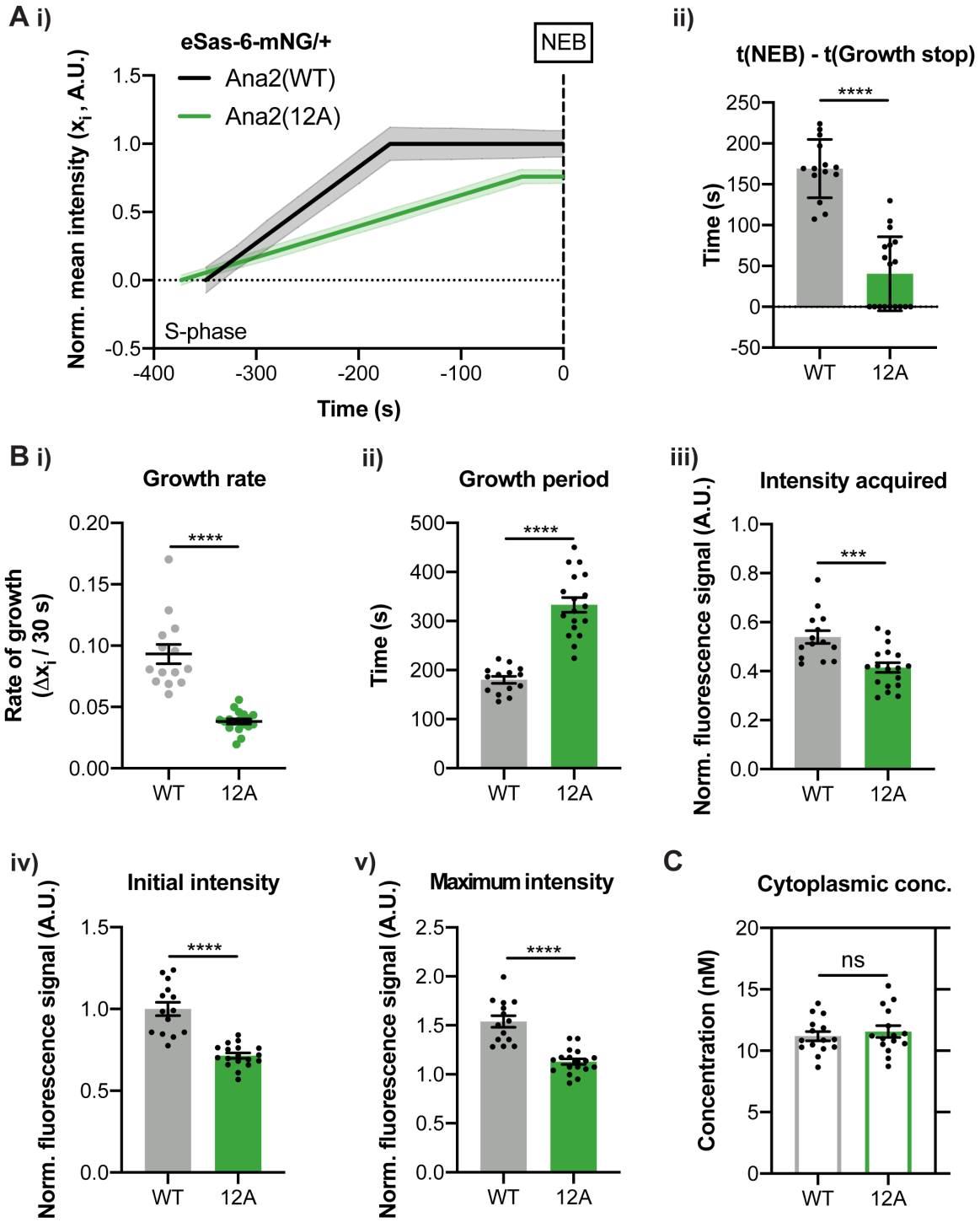


Figure 4-9: Centrioles grow slower and for longer in the presence of Ana2(12A)

(A) (i) Graph shows the normalised mean±SEM centriole growth dynamics during nuclear cycle 12 (monitored by eSas-6-mNG incorporation) in the presence of WT Ana2 (*black*) and Ana2(12A) (*green*) aligned to nuclear envelope breakdown (NEB). N≥14 embryos, n~100-150 centrioles per embryo. **(ii)** Bar chart depicts the timing (mean±SD) of when centrioles stop growing in comparison to NEB/mitosis. **(B)** Bar charts quantify and compare several centriole growth parameters (mean±SEM) extracted from the data shown in (A). The values were derived from the fitted regression curve of the mean eSas-6-mNG intensity of each individual embryo. Each datapoint represents the average value of all centrioles from an embryo. **(C)** Bar chart quantifies the cytoplasmic concentration (mean±SEM) of eSas-6-mNG in the presence of WT Ana2 and Ana2(12A) at the beginning of nuclear cycle 12. Each data point represents the average of 4-6x 10-second-long recordings. Statistical significance was assessed using an unpaired t-test with Welch's correction (****, P<0.0001; ***, P<0.001; ns, not significant).

Figure 4-9A). Strikingly, centriole growth was greatly altered in the presence of Ana2(12A). Centrioles grew for much longer, and in 50% of embryos (9/18) Sas-6-mNG was incorporated right up until NEB (*green* line*,* **Figure 4-9A**). This is consistent with my hypothesis that if Ana2 cannot be phosphorylated by Cdk1, its centriole growth promoting function cannot be switched off and so Sas-6-mNG will be incorporated for a longer period.

Surprisingly, however, I also noticed that the centrioles in these embryos incorporated Sas-6-mNG much more slowly than in controls so that, despite the extended growth period, the growing centrioles ultimately incorporated less total Sas-6-mNG (**Figure 4-9Bi-iii**). By convention, we usually normalise these Sas-6 incorporation data by subtracting the initial fluorescence intensity of the centrioles at the start of S-phase (Aydogan *et al.*, 2018). This allows us to focus on the fluorescence that is acquired by the daughter centriole, and it means that at the start of S-phase the average fluorescence intensity of the centrioles in every embryo is set to zero (**Figure 4-9Ai**). When I looked at the raw data, however, it was clear that in the embryos from mothers expressing eAna2(12A) much less Sas-6-mNG was recruited to centrioles at the start of S-phase (**Figure 4-9Biv**) and at the end of S-phase when the centrioles had reached their maximal intensity (**Figure 4-9Av**). Thus, although Ana2(12A) is recruited to centrioles at significantly higher levels than normal, Sas-6 is recruited at significantly lower levels than normal. I suspect that this is why the Sas-6 growth rate is slowed in embryos expressing Ana2(12A). Importantly, FCS measurements showed that the discrepancy in Sas-6-mNG recruitment in embryos expressing WT Ana2 or Ana2(12A) was not due to any difference in the cytoplasmic concentration of eSas-6-mNG (**Figure 4-9C**).

These observations support my hypothesis that the centriolar recruitment of Ana2 is normally inhibited in late S-phase by Cdk1-dependent phosphorylation, and this helps to "switch off" centriole growth. It is currently unclear, however, why the excess recruitment of Ana2(12A) to centrioles leads to a decrease in the centriolar recruitment of Sas-6, which in turn seems to slow the rate of centriole growth.

4.2.8 Mutating two conserved potential Cdk1 phosphorylation sites in Ana2 seems to destabilise the protein

In an attempt to narrow down the putative phosphorylation sites in Ana2 that might be responsible for inhibiting its activity in late S-phase/mitosis, I generated fly lines expressing a mutant form of Ana2 in which only two of the 12 potential Cdk phosphorylation sites (S284 and T301) were mutated. Both sites are highly conserved in *Drosophila* species and there is some evidence that these sites influence the interaction between Ana2 and Sas-6. When Sas-6 and Ana2 are overexpressed together in early embryos, they assemble into large **S**as-6/**A**na2 **P**article**s** (SAPs) that can recruit many other centriole and centrosome proteins (Stevens, Roque and Raff, 2010; Gartenmann *et al.*, 2020). Lisa Gartenmann, a former PhD student in the laboratory, found that mutating S284 and T301 to alanine (Ana2(2A)-GFP) increased SAP assembly, while mutating these amino acids to potentially phospho-mimicking glutamic acid (Ana2(2E)-GFP) decreased SAP assembly (Lisa Gartenmann thesis (2018)). This suggests that the phosphorylation of these sites can inhibit the interaction between Ana2 and Sas-6. Lisa Gartenmann also used synthetic peptides to show that both sites could be phosphorylated by Cdk1/Cyclin B *in vitro*.

I found that eAna2(2A)-mNG and eAna2(2E)-mNG both exhibited the typical increase in diffusion speed in late-S-phase/mitosis, although this was perhaps somewhat dampened

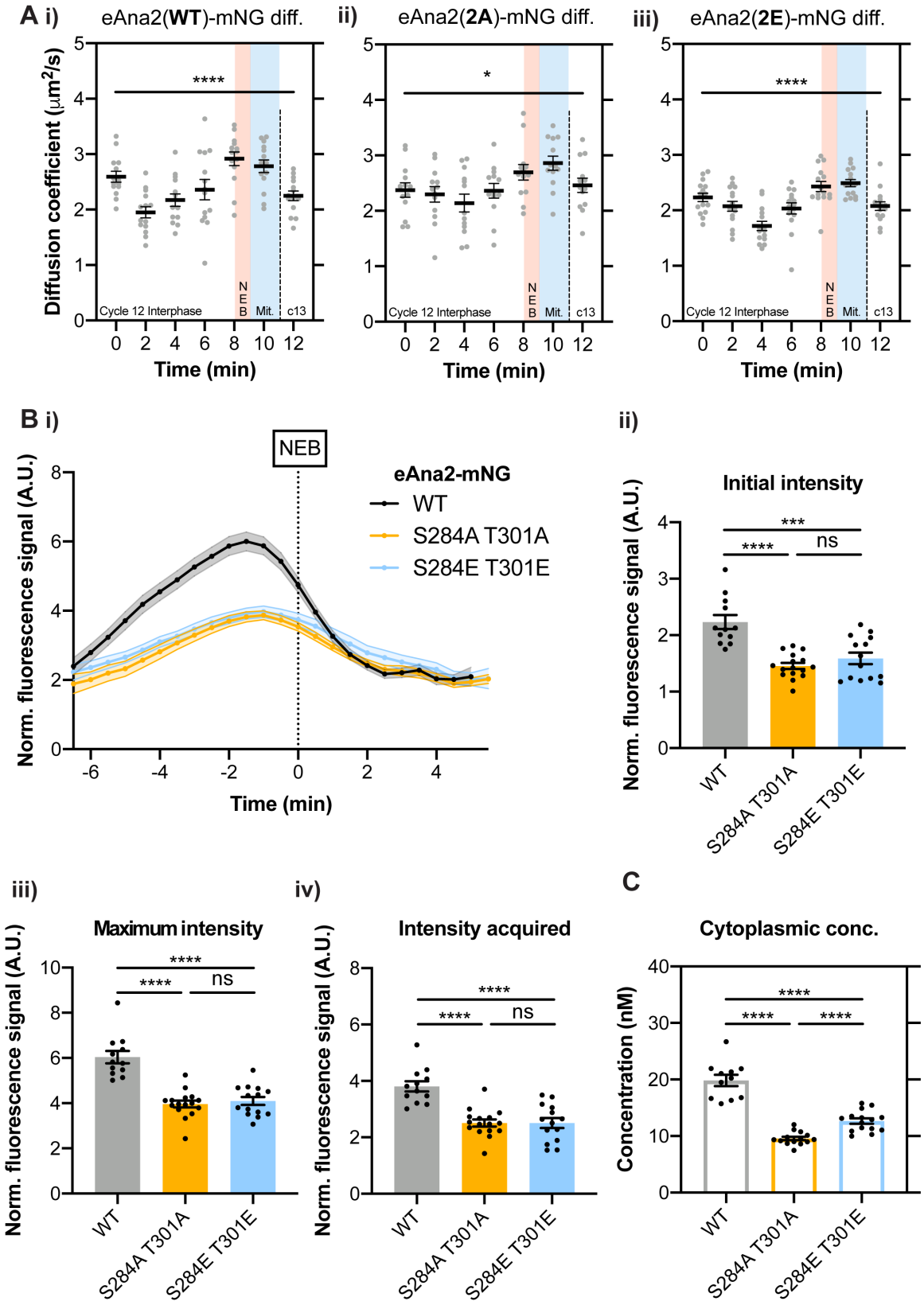


Figure 4-10: The two conserved potential Cdk phosphorylation sites S284 and T301 are not responsible for eAna2(12A)-mNG's abnormal recruitment pattern

See next page.

Figure 4-10: The two conserved potential Cdk phosphorylation sites S284 and T301 are not responsible for eAna2(12A)-mNG's abnormal recruitment pattern
(A) Graphs show cytoplasmic FCS diffusion measurements (mean±SEM) of WT eAna2-mNG **(i)**, eAna2(S284A T301A)-mNG (2A) **(ii)**, and eAna2(S284E T301E)-mNG (2E) **(iii)** that were taken every two minutes from the start of nuclear cycle 12-13. The estimated NEB timing is depicted in *orange*, mitosis in *blue*. Each data point represents the average of 4-6x 10-second-long recordings. Statistical significance was assessed using a paired one-way ANOVA test (for Gaussian-distributed data) or a Friedman test (****, P<0.0001; *, P<0.05). **(B) (i)** Graph shows the normalised mean±SEM centriolar recruitment dynamics for WT eAna2-mNG (*black*), eAna2(S284A T301A)-mNG (*orange*), and eAna2(S284E T301E)-mNG (*blue*) during nuclear cycle 12 aligned by nuclear envelope breakdown (NEB). N≥12 embryos, n~100-150 centrioles per embryo. **(ii-iv)** Bar charts quantify and compare several incorporation parameters (mean±SEM) extracted from the data shown in (i). Each data point represents the average value of all centrioles from an embryo. **(C)** Bar chart quantifies their cytoplasmic concentration (mean±SEM) at the beginning of nuclear cycle 12. Each data point represents the average of 4-6x 10-second-long recordings. For (B) and (C), statistical significance was assessed using an unpaired t-test with Welch's correction (for Gaussian-distributed data) or a Mann-Whitney test (****, P<0.0001; ***, P<0.001; ns, not significant).

for the eAna2(2A)-mNG mutant (**Figure 4-10A**). Surprisingly, both mutants exhibited a nearly identical centriole incorporation behaviour, and this differed from both WT eAna2-mNG and eAna2(12A)-mNG. Although the timing of Ana2's peak intensity was not significantly altered compared to WT, much less total Ana2 was recruited during interphase (**Figure 4-10B**). Importantly, FCS measurements showed that the cytoplasmic concentration of both mutant proteins was significantly reduced, suggesting that these proteins may be destabilised (**Figure 4-10C**). I suspect this may explain why these proteins are recruited to the centrioles at much lower levels than normal.

These observations are difficult to interpret, but it is interesting to note that these same mutations do not seem to destabilise Ana2 in the context of the full Ana2(12A) mutant protein. Clearly further work will be required to dissect how the potential phosphorylation of Ana2 by Cdk1 might inhibit its localisation to centrioles.

4.3 Discussion

In this chapter I used FCS to conduct an initial characterisation of some of the biophysical properties of the cytoplasmic pool of the five core centriole duplication proteins during a complete nuclear cycle of the *Drosophila* blastoderm. To recapitulate their most native

expression profile, I attempted to fluorescently tag all five proteins with mNG at their endogenous locus using CRISPR/Cas9. This strategy was largely successful, although I failed to generate an ePlk4-mNG line, and my mNG-ePlk4 line showed centriole overduplication, suggesting that the fusion protein is overexpressed. The Bettencourt-Dias laboratory obtained similar results when they attempted to generate these lines (Jordan Raff, personal communication). Interestingly, for Sas-6 and Ana2 I observed a discrepancy in their cytoplasmic protein abundance depending on the position of the mNG tag. In my FCS measurements, both proteins were present at nearly double the cytoplasmic concentration when tagged on their N-termini compared to their C-terminally tagged versions (**Appendix D**). I observed a similar overexpression of the N-terminally tagged Ana2 protein in my western blotting experiment (**Figure 4-3A**). For Sas-6, which is expressed at much lower levels and difficult to detect in western blots, the signal was too noisy to draw any conclusions (**Figure 4-3A**). These findings suggest that, although the tagging of endogenous genes using CRISPR/Cas9 technology is widely considered the gold-standard of experimental genetic manipulation, one cannot simply assume that any tagged protein will be expressed at endogenous levels.

To my knowledge, this work represents the first systematic characterisation of the cytoplasmic properties of centriolar proteins throughout an entire cell cycle. Perhaps most importantly, I showed that the cytoplasmic concentration of all five core duplication proteins remains relatively constant throughout the nuclear cycle. This suggests that centriole assembly in the *Drosophila* embryo is not regulated by a limiting cytoplasmic pool of organelle building blocks (Goehring and Hyman, 2012). *A priori*, this is perhaps surprising, as the cytoplasmic concentration of all these proteins seems low—in the

~5-40 nM range for Ana2, Asl, Sas-4 and Sas-6, and probably well below 5 nM for Plk4. Given that these embryos produce so many centrioles in such a short space of time I would have intuitively expected these proteins to be present at a relatively high concentration, and also that I would be able to detect at least their transient depletion from the cytoplasm during the period in S-phase when the centrioles are being assembled (I show in **Chapter 6** that such a transient depletion can be detected for at least one centrosomal protein).

These findings highlight two points. First, it may be very dangerous for these embryos to express one or more of these core centriole duplication proteins at too-high a level, presumably because they have a strong tendency to self-assemble (Kitagawa, Vakonakis, *et al.*, 2011; Van Breugel *et al.*, 2011; Cottee *et al.*, 2015; David *et al.*, 2016; Gartenmann *et al.*, 2020). Second, the cytoplasmic concentration of these proteins is likely to be tightly regulated to ensure that they are maintained at precisely the correct level. It will be fascinating to study the mechanisms that allow the embryo to maintain the correct concentration of these proteins given that they have to make an exponentially increasing number of centrioles every ~10 minutes. This is a subject I will touch on in later Chapters.

As described in **Chapter 3**, FCS can be used to extract various parameters of protein behaviour and I observed a significant increase in the diffusion speed of Ana2 around the time of NEB and during mitosis. I identified Cdk1 as the potential source of Ana2's diffusion change, and the altered recruitment dynamics of eAna2(12A)-mNG and the elongated centriole growth period in the presence of Ana2(12A) suggest that Cdk1 can phosphorylate Ana2 to suppress its centriole growth promoting capability in late S-phase. This finding is potentially important because, as described in **Chapter 4, Section 4.1**, our

initial mathematical modelling of how an oscillation in Plk4 activity might lead to the observed dynamics of centriole cartwheel growth cannot explain why centrioles stop growing relatively abruptly towards the end of S-phase (**Figure 4-1B**). Under a wide range of conditions, the model always predicts that centrioles gradually stop growing over a timescale of several minutes, which is not what we observe *in vivo*. My findings suggest that the Cdk1-dependent phosphorylation of Ana2 in late S-phase provides at least one additional mechanism (and there may well be others) that works together with the Plk4 oscillation to ensure that centrioles stop growing at the appropriate time.

Clearly more work is required to identify the potentially relevant phosphorylation sites in Ana2, to confirm that they are genuine Cdk1 targets, and to investigate how these phosphorylation events might influence Ana2 behaviour and the centriole assembly process. A multiple sequence alignment of Ana2 from several *Drosophila* species reveals multiple conserved S/T-P sites (in addition to the S284 and T301 sites that I have already tested) that are potential candidates and that will be investigated by making suitable phosphonull and phosphomimetic versions (**Figure 4-11**). I would predict that phosphomimetic mutations, where all potential phosphorylation sites are replaced by a negatively charged amino acid to mimic the phosphorylated state, would lead to permanent inhibition of Ana2's growth promoting function. To assess this possibility, I have generated fly lines expressing phosphomimetic variants of Ana2, where all 12 potential phosphorylation sites were substituted by either an aspartic acid/glutamic acid or two aspartic acids (to more accurately mimic the electric charge of phosphorylated residues). While I was not yet able to assess how these mutations affect the recruitment dynamics of Ana2 and centriole growth, none of the alleles that I generated (both mNG-

tagged and untagged) rescued the *ana2*$^{-/-}$ mutant phenotype. This suggests that the phosphomimetic mutation of the 12 potential Cdk phosphitylation sites may affect Ana2's role in centriole assembly.

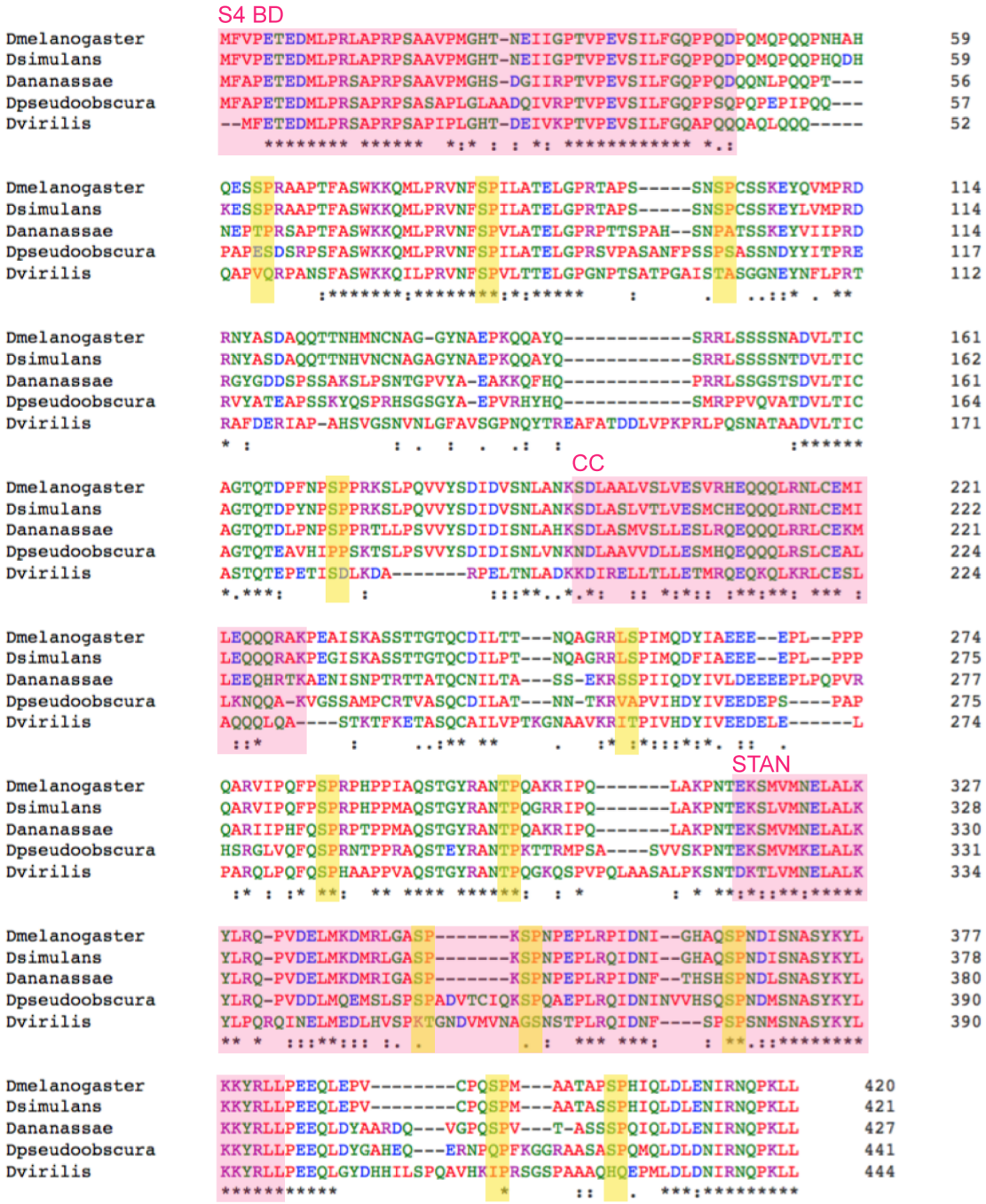


Figure 4-11: A multiple sequence alignment between *Drosophila* species highlights the high conservation of multiple potential Cdk1 sites within Ana2

The sequence alignment was performed in Clustal Omega (1.2.4) (Sievers *et al.*, 2011) by Zsofia Novak. The 12 potential Cdk sites (S63, S84, S101, S172, S257, S284, T301, S345, S348, S365, S395, S403) are highlighted in *yellow*, the three known interaction domains (S4 BD (Sas-4 binding domain, CC (doiled-doil domain), STAN (STil/ANa2 domain)) in *red*. High conservation between all species is annotated with '*****', intermediate conservation with '**:**', and low conservation with '**.**' .

5 FCS and PeCoS analyses reveal important insights into the regulation of centriole assembly

5.1 Introduction

Having established FCS and PeCoS techniques (**Chapter 3**) and shown their utility in analysing the behaviour of the cytoplasmic pool of the core centriole duplication proteins in embryos (**Chapter 4**), I sought to apply these techniques to address several questions, which I describe in this chapter. First, I worked on a collaborative project to investigate how centrioles might generate an adaptive Plk4 oscillation to promote centriole cartwheel assembly. Second, I examined how the behaviour of the core centriole duplication proteins changes between nuclear cycles 11-14, where the embryo has to make an exponentially increasing number of centrioles during each cycle. Third, I used FCS to measure the molecular brightness of the two central cartwheel proteins Ana2 and Sas-6 to characterise their average cytoplasmic stoichiometry.

During the early nuclear cycles 11-14, the embryo experiences a gradual slowing of its nuclear cycles: from ~11 minutes in cycle 11 to ~12 minutes, ~21 minutes and >40 minutes in cycles 12, 13 and 14, respectively (Foe and Alberts, 1983; Farrell and O'Farrell, 2014). It was recently shown that during these cycles the embryos homeostatically adapt their centriole growth rate and growth period to ensure that the centrioles grow to a similar size (Aydogan *et al.*, 2018) (**Figure 5-1**). In cycle 11, the centrioles grow relatively quickly, but for a relatively short time while in cycles 12 and 13 the centriole growth rate gets progressively slower, while the centriole growth period gets progressively longer. As a result, the centrioles grow to approximately the same size in each cycle (indicated by the fluorescent *intensity acquired*, **Figure 5-1B**). Interestingly, halving the genetic dose of Plk4, the master regulator of centriole biogenesis, led to a decrease in the centriole growth

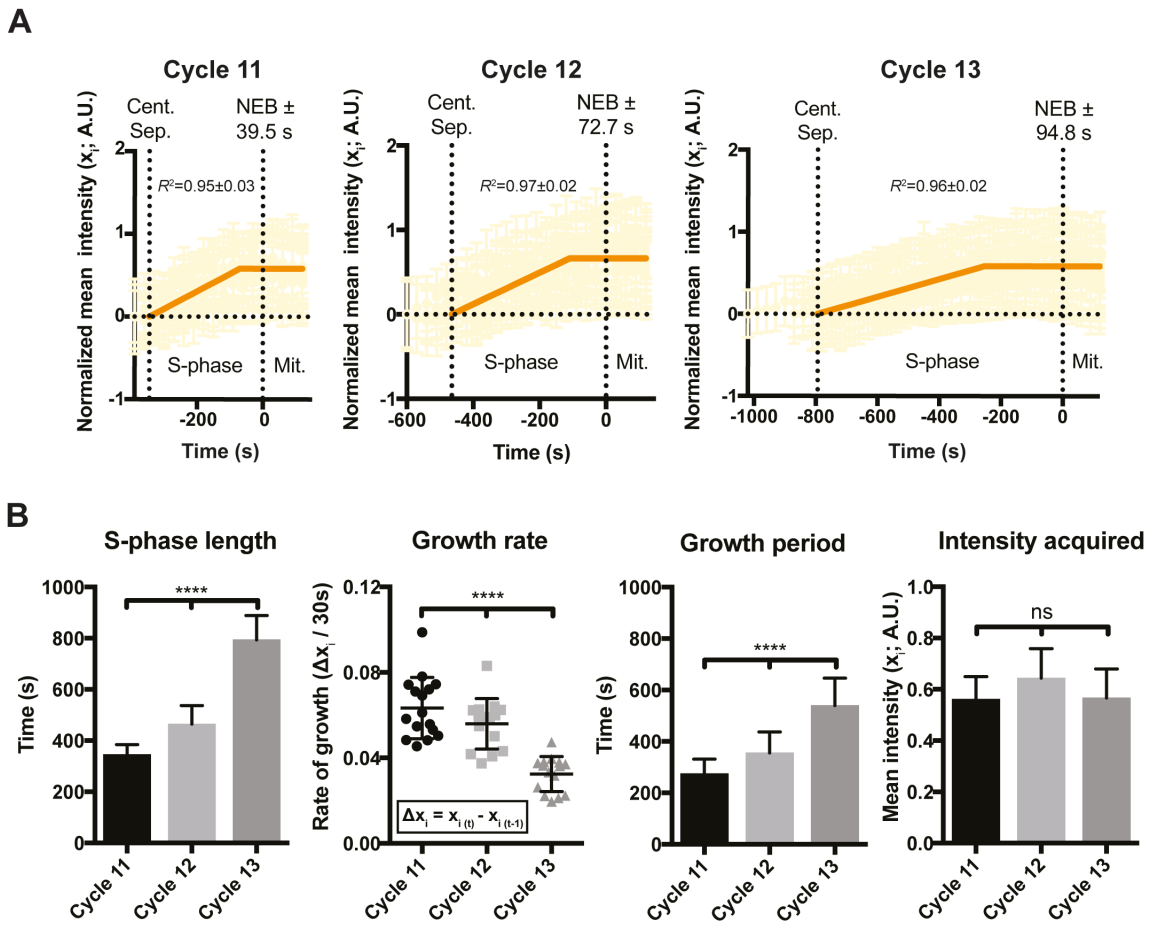


Figure 5-1: Centriole size is regulated by an inverse relationship between growth rate and period in the early *Drosophila* embryo

(A) Graphs show the normalised mean centriolar Sas-6-GFP intensity (±SD for each individual embryo) during nuclear cycles 11, 12, and 13. Sas-6 is irreversibly incorporated into the growing daughter centriole and can be used as a proxy for centriole growth and size. **(B)** Bar graphs quantify growth parameters (mean±SD) extracted from the individual Sas-6-GFP incorporation profiles. Statistical significance was assessed using an ordinary one-way ANOVA test (for Gaussian-distributed data) or a Kruskal-Wallis test (****, P<0.0001; ns, not significant). Data and graphs were generated by Mustafa Aydogan, and the figure modified from Aydogan *et al.*, 2018.

rate, as one might have predicted; surprisingly, however, it also led to an increase in the centriole growth period, so that the daughter centrioles ultimately grew to nearly their normal size (Aydogan *et al.*, 2018). How Plk4 influenced both the centriole growth rate and growth period was unclear.

In collaboration with Mustafa Aydogan (investigating the recruitment dynamics at the centrosome) and Michael Boemo and Zachary Willmott (mathematically modelling the recruitment pattern) we aimed to investigate how Plk4's behaviour might be modified

during successive nuclear cycles to help ensure this centriole size homeostasis. Some of the work described in this collaborative project was recently published (Aydogan, Steinacker *et al.*, 2020).

5.2 Results

5.2.1 A centriolar Plk4 oscillation helps to time and execute centriole biogenesis

Mustafa Aydogan performed a spinning-disk confocal microscopy analysis of embryos from mothers expressing ePlk4-mNG from its endogenous promoter in its mutant *Plk4*$^{-/-}$ background. This revealed that centriolar Plk4 levels oscillated during each nuclear cycle (**Figure 5-2A**). The Plk4 oscillations showed an adaptive behaviour, with an increasing period and a decreasing amplitude between cycles 11-13. Simultaneous observation of ePlk4-mNG recruitment and centriole growth dynamics (judged by Sas-6-mCherry incorporation) suggested that the Plk4 oscillation helps to time and execute centriole biogenesis (**Figure 5-2B**). These findings indicate that there is a nuclear cycle-specific threshold level of centriolar Plk4 activity that is required to initiate centriole growth, and that centriole growth stops once centriolar Plk4 levels fall below this threshold.

5.2.2 A simple mathematical model can potentially explain Plk4's oscillatory behaviour

To try to understand how these adaptive Plk4 oscillations might be generated, the lab initiated a collaboration to mathematically model this process. In *Drosophila*, Plk4 is recruited to the assembly site by its receptor Asl. Upon binding, Plk4 is activated, which allows Plk4 to phosphorylate Ana2 to initiate the assembly of the centriole cartwheel (Dzhindzhev *et al.*, 2014; Ohta *et al.*, 2014; Kratz *et al.*, 2015; Moyer *et al.*, 2015), but also to phosphorylate Plk4 itself and its Asl receptor—both at multiple sites (Dzhindzhev *et al.*,

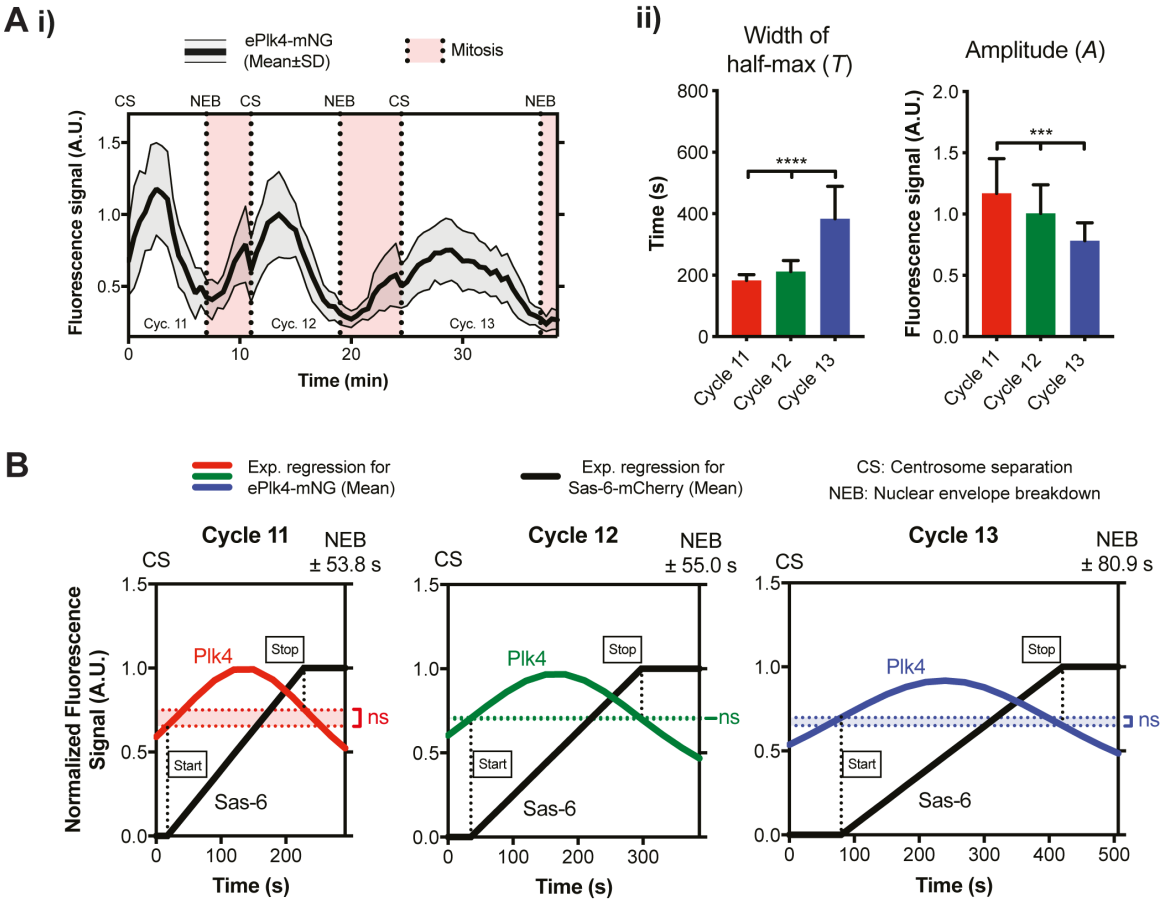
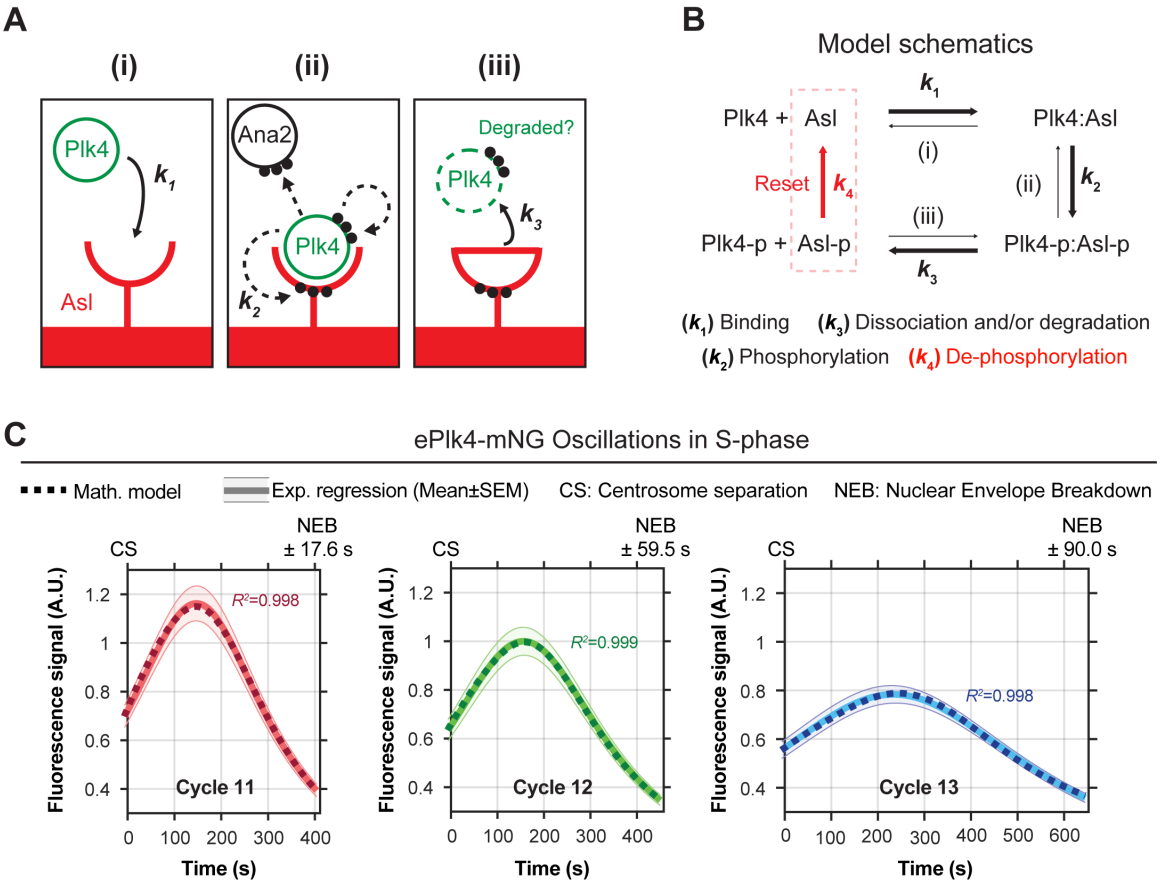


Figure 5-2: Plk4 levels oscillate at the base of the mother centriole and initiate and time centriole assembly

(A) (i) Graph shows the mean±SD centriolar ePlk4-mNG intensity of a single embryo during nuclear cycles 11-13. Centriolar ePlk4-mNG levels oscillate during each cycle, but the oscillation dampens over successive cycles. **(ii)** Bar graphs quantify the ePlk4-mNG oscillation parameters (mean±SD) derived from N≥15 embryos. Statistical significance was assessed using an ordinary one-way ANOVA test (for Gaussian-distributed data) or a Kruskal-Wallis test (****, P<0.0001; ***, P<0.001). **(B)** Graphs show the normalised mean regression of the ePlk4-mNG oscillation and the simultaneously measured centriole growth dynamics (Sas-6-mCherry incorporation) during nuclear cycles 11-13. *Dotted* lines indicate the ePlk4-mNG levels at which centrioles started and stopped growing. N=17 embryos for cycles 11 and 12, N=8 embryos for cycle 13. Statistical significance was assessed using an unpaired t-test with Welch's correction (for Gaussian-distributed data) or a Mann-Whitney test (ns, not significant). Data and graphs were generated by Mustafa Aydogan, and the figure modified from Aydogan, Steinacker *et al.*, 2020.

2010; Klebba *et al.*, 2015; Boese *et al.*, 2018). It is not clear what function the phosphorylation of Asl serves, but we realised that if these phosphorylations ultimately inhibited the interaction between Asl and Plk4, the system could form a time-delayed negative feedback network capable of generating an oscillatory Plk4 recruitment behaviour (**Figure 5-3A+B**). Based on these interactions, Michael Boemo and Zachary Wilmott developed a simple ODE-based model that could recapitulate the experimentally



D

Parameters	Cycle 11	Cycle 12	Cycle 13
k_1	0.004762	0.003644	0.001272
k_2	0.03756	0.03443	0.02164
k_3	0.06906	0.06906	0.06906
A_{tot}	1713	1577	1587

Figure 5-3: A simple mathematical model can recapitulate Plk4's oscillatory recruitment to centrioles
(A, B) Schematic illustrations of the mathematical model. **(i)** In mitosis, Plk4 (*green*) starts binding to its receptor Asl (*red*) on the surface of the mother centriole with high affinity. The parameter k_1 is dependent on the cytoplasmic concentration of Plk4. **(ii)** Upon binding, Plk4 auto-activates itself, which allows it to phosphorylate itself, Ana2 (*black*), and Asl (k_2) (depicted by *dotted* arrows and *black* dots). **(iii)** Once Asl is phosphorylated by Plk4 a sufficient number of times, we speculate that it is converted into a state with low affinity for Plk4 (shown as a change in the receptor shape). This causes Plk4 to be released from its receptor Asl (k_3), and probably degraded. We speculate that Asl can no longer bind Plk4 until it is dephosphorylated during mitosis (*red* arrow, k_4) to allow another round of centriole duplication in the following cycle. **(C)** Graphs depict the mean±SEM regression of the experimentally observed ePlk4-mNG oscillations (*solid* line) overlayed with the best fit curve generated by the mathematical model (*dotted* line). R^2 values show the goodness-of-fit. **(D)** The table displays the "best-fit" parameter values used in the mathematical model to generate Plk4 oscillations in cycles 11-13. Highlighted in *orange* are the two parameters, k_1 and A_{tot}, which describe the rate of Plk4 recruitment (which is determined by the cytoplasmic abundance of Plk4) and the total amount of Asl in the system, respectively. Note that Plk4 abundance (k_1) is predicted to decrease over successive cycles while Asl (A_{tot}) is predicted to remain relatively constant. Data and graphs were generated by Mustafa Aydogan and Michael Boemo, and the figure modified from Aydogan, Steinacker *et al.*, 2020.

derived oscillatory recruitment dynamics of Plk4 at each nuclear cycle well (R^2>0.99; **Figure 5-3C**). Fitting the mathematical model to the experimentally observed oscillations, which dampen over successive cycles, allowed the extraction of "best-fit" parameters for each cycle (**Figure 5-3D**). Interestingly, the model suggested that the decrease in amplitude of the Plk4 oscillation over successive nuclear cycles was primarily driven by a cytoplasmic reduction of Plk4 levels (which determines k_1 in the mathematical model). In contrast, the abundance of the receptor Asl (A_{tot}) was predicted to remain relatively constant between nuclear cycles. In this way, the Asl at the centriole acts as an "integrator" that can sense changes in the "input" (the amount of cytoplasmic Plk4) to adapt the oscillation to maintain a constant "output" (centriole size).

5.2.3 Using FCS and PeCoS to test predictions of the mathematical model

The mathematical modelling highlighted the importance of understanding how the concentration of Asl and Plk4—and indeed all the other core centriole duplication proteins—change during the course of these blastoderm divisions. This is a very demanding period for the developing embryo, as it has to accurately duplicate an exponentially increasing number of centrioles—from ~800 at cycle 11 to ~6000 at cycle 14—in a very short period of time. I set out to measure how Asl and Plk4 levels change at the start of nuclear cycles 11-14, to test if the model's predictions (that Asl levels would remain constant at each cycle while Plk4 levels would fall) were correct.

I first measured the cytoplasmic concentration of eAsl-GFP expressed from its endogenous promoter in its *asl*$^{-/-}$ mutant background between nuclear cycles 11-14. All measurements were conducted at the beginning of S-phase when centriole duplication is initiated. As predicted by the model, the abundance of Asl did not change between the

nuclear cycles (**Figure 5-4Ai**), and Mustafa Aydogan showed that the centriolar levels of Asl also remained constant (**Figure 5-4B**). Interestingly, however, I subsequently repeated this experiment after I had generated the endogenously tagged eAsl-mNG knock-in line using CRISPR/Cas9. Unexpectedly, the knock-in eAsl-mNG protein behaved differently to the initial transgenic eAsl-GFP and I observed a slight, but significant, downward trend in concentration over successive cycles (**Figure 5-4Ci**).

I repeated my analysis with both the original eAsl-GFP transgenic line (**Figure 5-4Aii**) and the eAsl-mNG knock-in line (**Figure 5-4Cii**) and confirmed that this difference in behaviour is reproducible. I do not understand the basis for this difference, but I note that the depletion I observed with the eAsl-mNG knock-in line was quite modest (falling from a concentration of ~14 nM at cycle 11 to ~11 nM at cycle 14), and also that the mathematical model actually predicts a decrease of similar magnitude between cycles 11 and 12 (although not between cycles 12 and 13; cycle 13-14 was not modelled as Mustafa Aydogan had not measured this cycle) (**Figure 5-3D**). Taken together, these data suggest that Asl levels in the embryo remain relatively constant and, at most, are only slightly lower at the start of each nuclear cycle. These findings are broadly consistent with our model.

As ePlk4-mNG (expressed transgenically from its endogenous promoter in its *Plk4*$^{-/-}$ mutant background) was present at too low abundance in the *Drosophila* syncytium to be reliably measured with FCS, I determined its relative cytoplasmic abundance between cycles 11-14 using my newly developed PeCoS technique. These measurements revealed a drastic drop in cytoplasmic ePlk4-mNG abundance between nuclear cycles 11-14 (**Figure 5-4Di**). As I was not able to find a suited inert control to test the reproducibility of PeCoS

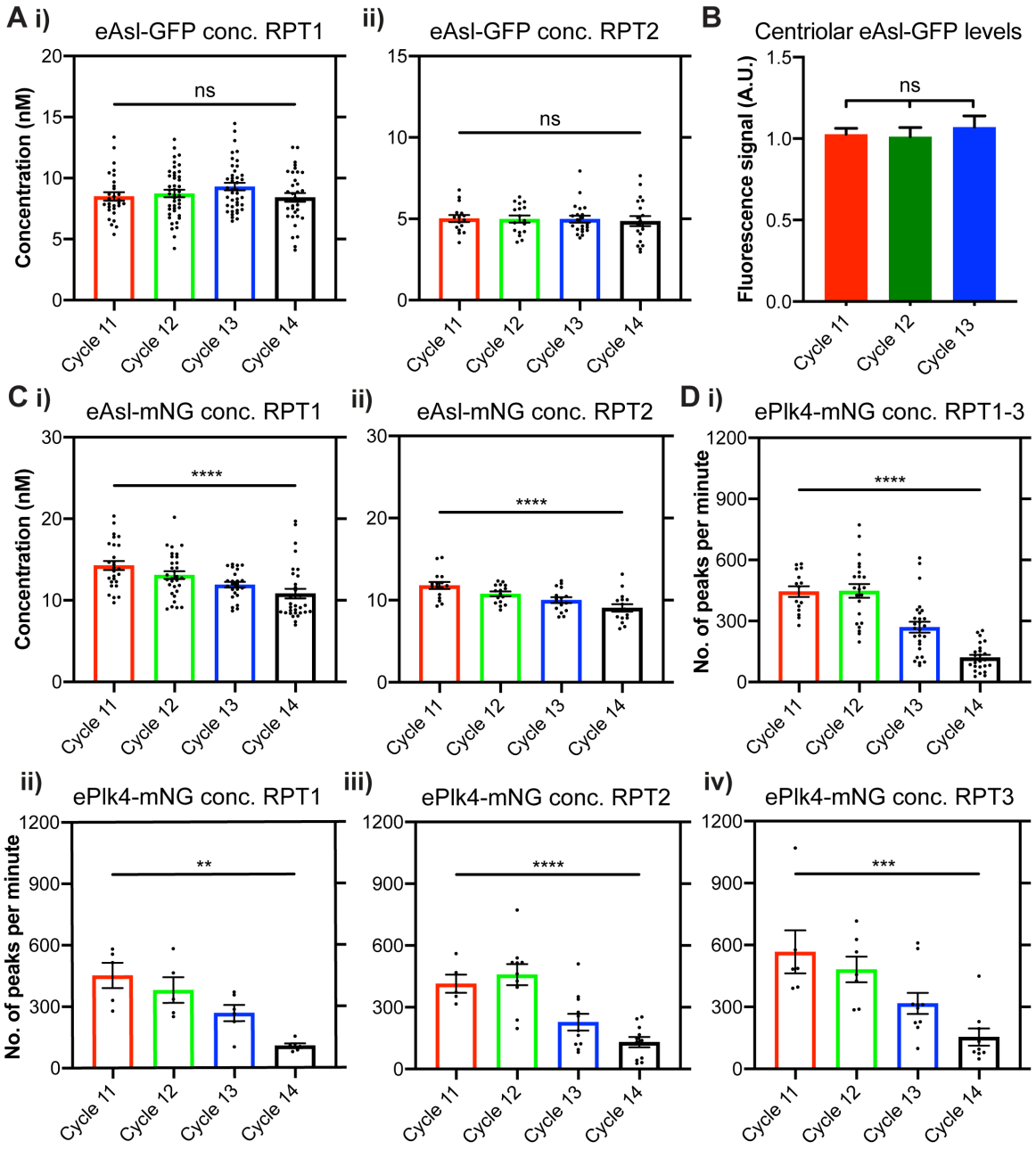


Figure 5-4: The cytoplasmic concentration of Asl remains relatively constant between nuclear cycles 11-14 while Plk4 exhibits a gradual depletion

(A) Bar graphs quantify the cytoplasmic concentration (mean±SEM) of eAsl-GFP in two biological repeats (**i** and **ii**) measured with FCS at the beginning of S-phase. Note that these repeats were performed several months apart, potentially explaining why the eAsl-GFP concentration is consistent within each repeat, but varies slightly (from ~8 nM to ~5 nM) between repeats. **(B)** Bar graph displays the mean±SEM intensity of eAsl-GFP at the centriole measured at the beginning of S-phase of cycles 11-13. N≥14 embryos per cycle and ~50-130 centrioles/embryo. **(C)** Bar graphs quantify the cytoplasmic concentration (mean±SEM) of endogenously tagged eAsl-mNG in two biological repeats (**i** and **ii**) measured with FCS at the beginning of S-phase. **(D) (i)** Bar graph quantifies the cytoplasmic concentration (mean±SD) of ePlk4-mNG measured with PeCoS at the beginning of S-phase. Data was acquired in three independent biological repeats (**ii-iv**).

For FCS measurements, each data point represents the average of 4-6x 10-second-long recordings. For PeCoS measurements, each data point represents an individual 180-second-long recording. Statistical significance was assessed using an ordinary one-way ANOVA test (for Gaussian-distributed data) or a Kruskal-Wallis test (****, P<0.0001; ***, P<0.001; **, P<0.01; ns, not significant). Data and graph for panel B were generated by Mustafa Aydogan, and the figure partially published in Aydogan, Steinacker *et al.*, 2020.

measurements between these four blastoderm cycles, I performed this experiment as three independent biological repeats that all showed a similar trend (**Figure 5-4Dii-iv**), which were then combined to generate the final quantification (**Figure 5-4Di**). Interestingly, there was very little, if any, drop in Plk4 levels between cycles 11 and 12 (although I note the cycle 12 data was particularly noisy), and a much more drastic drop between cycles 12 and 13 and between cycles 13 and 14. This is in agreement with the model, which also predicts a much greater drop in Plk4 concentration between cycles 12-13 than 11-12 (cycle 13-14 has not been modelled as no data was acquired for this cycle). Taken together, these data suggest that Plk4 levels in the cytoplasm show a downward trend during these nuclear cycles, consistent with our model.

5.2.4 The kinase activity of Plk4 helps to destabilise the protein in *Drosophila* embryos

It is not clear why Plk4's levels decrease over successive cycles, but I envisage at least two potential explanations that are not mutually exclusive: (1) As Plk4 is present at low concentrations in the cytoplasm, the drop in cytoplasmic levels could be explained by an increasing sequestration of Plk4 at the exponentially increasing number of centrioles; (2) As the binding of Plk4 to Asl activates Plk4 (Dzhindzhev *et al.*, 2010; Klebba *et al.*, 2015; Boese *et al.*, 2018), this would allow the centriole-bound fraction of Plk4 to phosphorylate itself and so target itself for degradation (Guderian *et al.*, 2010; Sillibourne *et al.*, 2010; Holland *et al.*, 2012; Cunha-Ferreira *et al.*, 2013). Thus, as centriole numbers increase at each successive cycle, more Plk4 would be targeted for destruction at each cycle.

To test the plausibility of this latter explanation, I used PeCoS to compare the cytoplasmic concentration at the start of nuclear cycle 12 of two mutant forms of ePlk4-mNG that exhibit either a reduced kinase activity (ePlk4(SK1)-mNG—which contains a "Shokat"

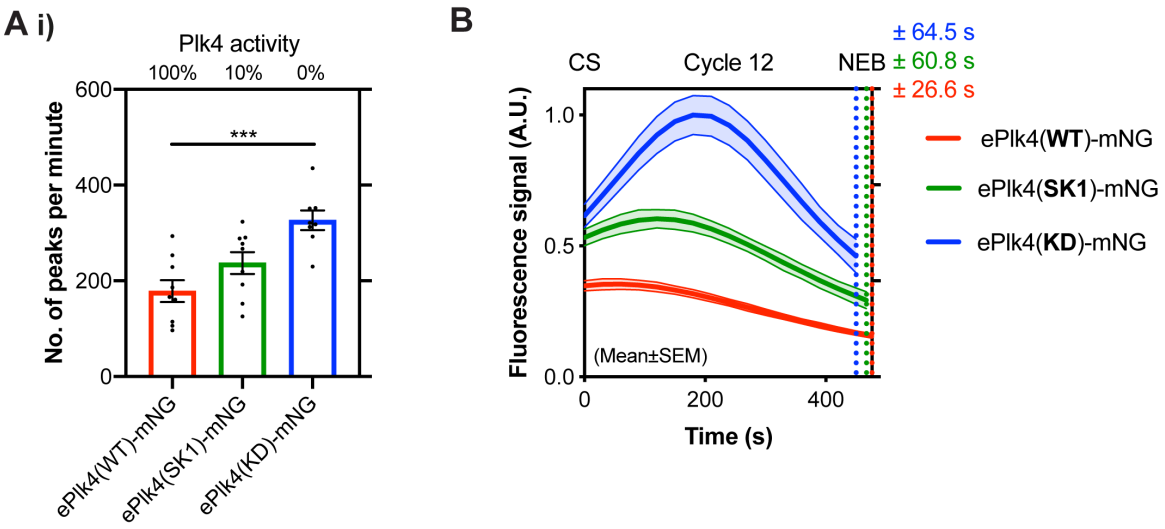


Figure 5-5: A reduction in Plk4 kinase activity leads to increased Plk4 levels in the cytoplasm and at the centriole

(A) Bar graph displays the quantification of cytoplasmic PeCoS measurements (mean±SD) at the beginning of nuclear cycle 12 from mothers expressing one copy of mNG-tagged Plk4 with varying kinase activity in its wild type background. WT – Wild type (100% kinase activity) ; SK1 – Shokat1 (~10% kinase activity) ; KD – Kinase-dead (0% kinase activity). Each data point represents an individual 180-second recording. **(B)** Graph shows the recruitment dynamics (mean±SEM) of the same ePlk4-mNG genotypes as listed in (A) during S-phase of nuclear cycle 12 imaged with spinning-disk confocal microscopy. N≥14 embryos per cycle. Statistical significance was assessed using a Kruskal-Wallis test (***, P<0.001). Data and graph for panel (B) was generated by Mustafa Aydogan.

mutation in the kinase domain (Bishop *et al.*, 2000) that appears to reduce the kinase activity of Plk4 to ~10% of WT (Holland *et al.*, 2010)) or a Kinase-Dead (ePlk4(KD)-mNG) (all constructs were made by Saroj Saurya). Plk4 is believed to function as an obligate dimer (Guderian *et al.*, 2010; Lopes *et al.*, 2015), and I was able to generate viable and fertile lines expressing either mutant protein in the presence of endogenous WT Plk4, but not in its absence. If Plk4 is already present as a dimer in the cytoplasm, then in my PeCoS experiments I would be analysing the average behaviour of a bulk population that contains both WT:mutant-mNG heterodimers and mutant-mNG:mutant-mNG homodimers (any WT:WT homodimers will be invisible in the PeCoS analysis).

Although the number of embryos I analysed was relatively small, there was a clear trend for the reduction in Plk4 kinase activity to correlate with an increased cytoplasmic Plk4 concentration (**Figure 5-5A**). This indicates that, perhaps not surprisingly, forms of Plk4

with reduced or no kinase activity tend to accumulate in the embryo. In agreement, Mustafa Aydogan detected increased levels of Plk4 at the centriole when its kinase activity was reduced/abolished (**Figure 5-5B**). This is consistent with the idea that the activation of Plk4 at centrioles might contribute to its ultimate degradation. Interestingly, in either of the scenarios discussed above, the number of centrioles in the embryo can influence how much Plk4 is present in the cytoplasm at the start of each nuclear cycle. This would potentially allow the embryo to effectively "count" the number of centrioles it contains, and to adjust its daughter centriole growth parameters accordingly.

5.2.5 The cytoplasmic concentration of Sas-6 and Ana2 remains relatively constant at the start of nuclear cycles 11-14, but the concentration of Sas-4 falls slightly

My FCS measurements indicate that the cytoplasmic concentration of eAsl-GFP/eAsl-mNG in the embryo remains relatively constant throughout nuclear cycles 11-14 (**Figure 5-4A+C**). *A priori*, I found this surprising, as its cytoplasmic concentration appears to be relatively low (~5-10 nM), and the embryo must assemble an exponentially increasing number of blastoderm centrioles at each cycle—~6000 during S-phase of cycle 14 (Zalokar and Erk, 1976). I therefore wondered whether the cytoplasmic concentration of the other core centriole duplication proteins changed during nuclear cycles 11-14. To my surprise, FCS revealed that the cytoplasmic concentrations of mNG-eSas-6, eSas-6-mNG, mNG-eAna2 and eAna2-mNG all remained relatively constant during this period (**Figure 5-6i-iv**). In contrast, eSas-4-mNG exhibited a small, but significant, gradual decrease in its cytoplasmic concentration during these cycles—dropping from ~15 nM at the start of cycle 11 to ~12 nM at the start of cycle 14 (**Figure 5-6v**). In biochemical terms, I suspect that this drop in concentration is unlikely to have major biological consequences; it seems

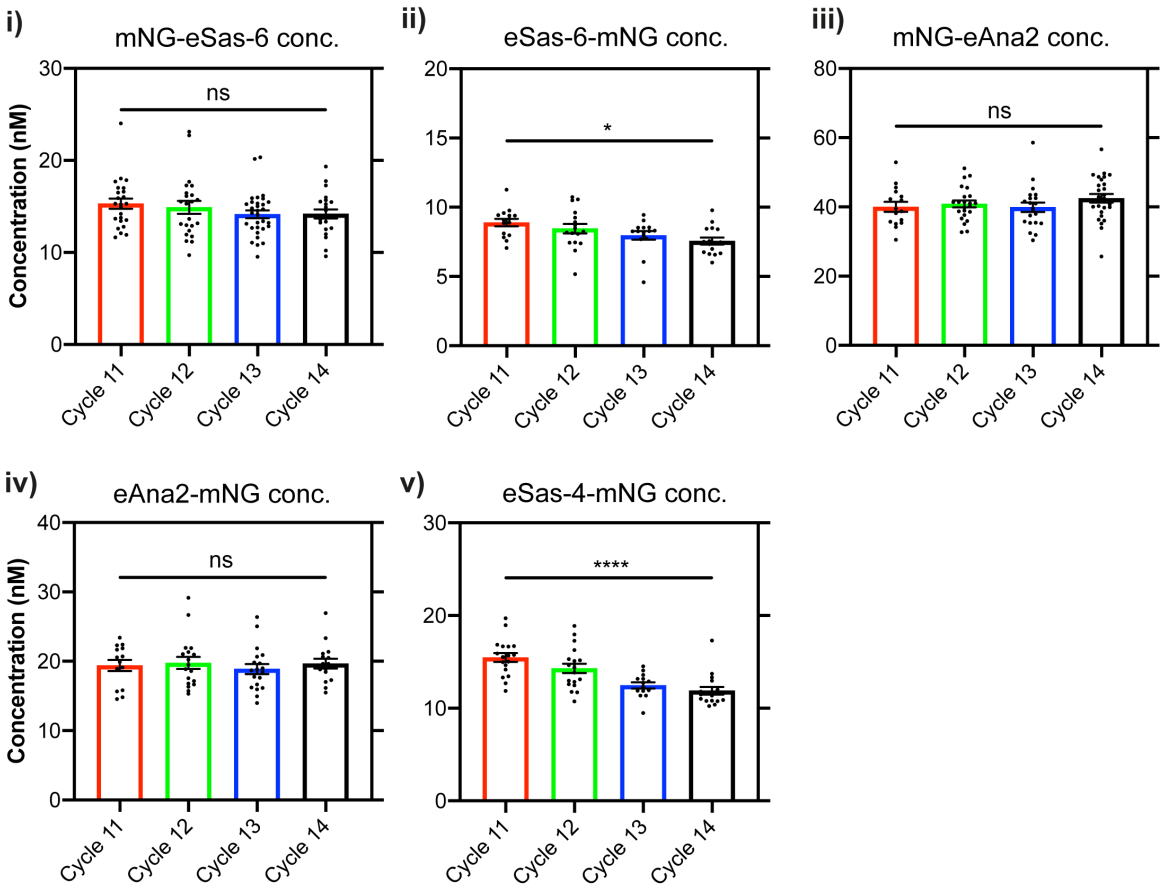


Figure 5-6: The cytoplasmic concentration of Sas-6 and Ana2 remains relatively constant between nuclear cycles 11-14, but the concentration of Sas-4 falls slightly over successive cycles
Bar graphs quantify the cytoplasmic concentration (mean±SEM) of mNG-eSas-6 **(i)**, eSas-6-mNG **(ii)**, mNG-eAna2 **(iii)**, eAna2-mNG **(iv)**, and eSas-4-mNG **(v)** at the beginning of S-phase during nuclear cycles 11-14. Each data point represents the average of 4-6x 10-second-long recordings. Statistical significance was assessed using an ordinary one-way ANOVA test (for Gaussian-distributed data) or a Kruskal-Wallis test (****, P<0.0001; *, P<0.05; ns, not significant).

implausible, for example, that it could explain the approximately halving of the centriole cartwheel growth rate observed between cycles 11 and 13 (**Figure 5-1**).

Taken together, my observations suggest that all of the core centriole duplication proteins maintain a relatively constant concentration in the cytoplasm during nuclear cycles 11-14 except for Plk4, whose concentration drops significantly. I conclude that either the cytoplasmic levels of Asl, Sas-6, Ana2, and Sas-4 is precisely regulated over very short time scales to ensure that they remain at constant levels throughout these rapid cycles, or that the total amount of these proteins that is ultimately sequestered at centrioles is

insignificant compared to the amount that remains in the cytoplasmic pool (see **Chapter 5, Section 5.3.2**).

5.2.6 Sas-6 and Ana2 appear to be largely monomeric and dimeric in the cytoplasm, respectively

The relatively low cytoplasmic concentration that I measured for the core centriole duplication proteins raised another issue that I was keen to explore further. It is widely accepted that the two core centriolar cartwheel proteins Sas-6 and Ana2 form homo-oligomers, and that this is essential for their function. For Sas-6, structural studies in multiple model organisms have shown that it dimerises through its C-terminal coiled-coil domain, and that nine Sas-6 dimers, which can also interact with each other's N-terminal headgroup, come together to form the nine-fold symmetrical cartwheel structure (Kitagawa, Vakonakis, *et al.*, 2011; Van Breugel *et al.*, 2011; Hilbert *et al.*, 2013; van Breugel *et al.*, 2014; Cottee *et al.*, 2015) (see **Chapter 1, Section 1.2.4** (**Figure 1-2**)). Ana2/STIL/SAS-5's structure within the centriolar cartwheel has yet to be determined, but homo-oligomerisation appears to be essential for its function (Cottee *et al.*, 2015; Rogala *et al.*, 2015; David *et al.*, 2016), and structural/biophysical studies of fragments of these proteins expressed and purified from *E. coli* indicate that the central coiled-coil (CC) region—that is present in all of these proteins—can assemble into either trimers (*C. elegans* SAS-5) or tetramers (*D. melanogaster* Ana2, and human STIL) (Cottee *et al.*, 2015; Rogala *et al.*, 2015; David *et al.*, 2016).

These studies were all performed with highly concentrated purified protein fragments in the μM concentration range, but all of the endogenously tagged centriolar proteins I characterised in this thesis showed expression levels in the low-nM range. Given the functional requirement for homo-oligomerisation, it is widely assumed that Ana2 and

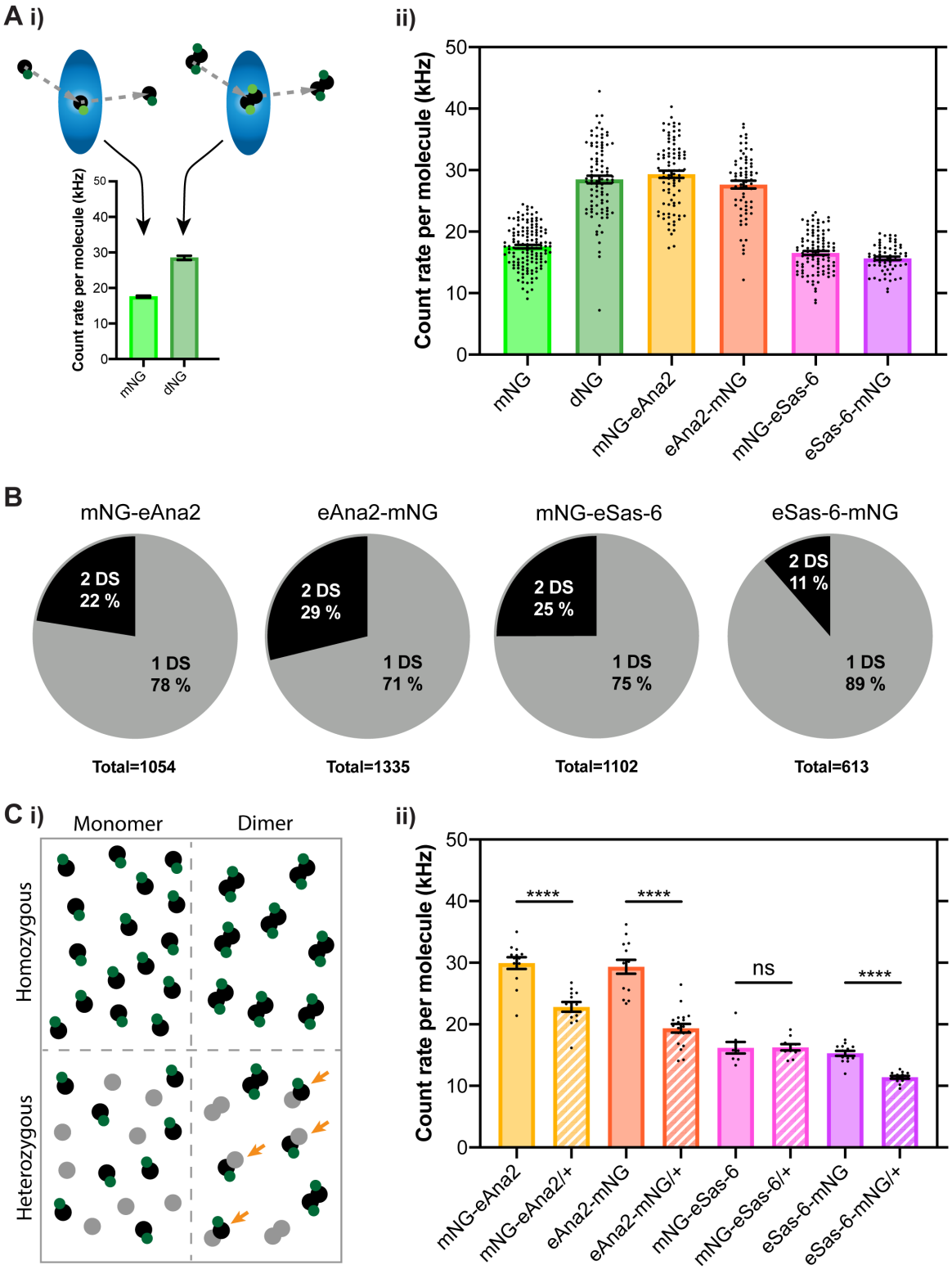


Figure 5-7: FCS-derived CPM analysis indicates that Ana2 is mostly dimeric and Sas-6 mostly monomeric in the early *Drosophila* syncytium

See next page.

Figure 5.7: FCS-derived CPM analysis indicates that Ana2 is mostly dimeric and Sas-6 mostly monomeric in the early *Drosophila* syncytium

(A) (i) Cartoon depicts the basis of FCS-derived stoichiometry measurements. **(ii)** Bar graph quantifies cytoplasmic CPM measurements (mean±SEM) of N- and C-terminally mNG-tagged Ana2 and Sas-6 in comparison to untagged monomeric and dimeric NeonGreen (mNG/dNG) controls. **(B)** Pie charts display the preferred diffusion model for the FCS measurements of mNG-tagged Ana2 and Sas-6 based on the Bayesian information criterion (BIC). The BIC comparison uses eight different diffusion models (four models with one diffusing species and four models with two diffusing species). For simplicity I only show here whether a model with one diffusing species (1 DS) or with two diffusing species (2 DS) was best suited to describe the shape of the ACFs. **(C) (i)** Cartoon illustrates the rationale of the CPM comparison between embryos from mothers homozygous or heterozygous for the fluorescently labelled protein of interest. If a protein is monomeric, the addition of untagged protein (*grey* circles) will not affect the average molecular brightness as FCS only detects fluorescently labelled molecules. If the protein of interest is dimeric, the addition of untagged protein will lead to the formation of heterodimers (*orange* arrows), which will lead to a reduction of its average molecular brightness when compared to embryos from homozygous mothers where every dimeric molecule comprises two fluorophores. **(ii)** Bar graph quantifies the average cytoplasmic molecular brightness (mean±SEM) of N- and C-terminally tagged Ana2 and Sas-6 in embryos from mothers heterozygous or homozygous for the fluorescently tagged protein of interest.

Each data point represents the average of 4-6x 10-second-long recordings. Statistical significance was assessed using an ordinary unpaired t-test with Welch's correction (for Gaussian-distributed data) or a Mann-Whitney test (****, P<0.0001; ns, not significant).

Sas-6 are already present in the cytoplasm in their oligomeric states (trimer/tetramer and dimer, respectively). In support of this possibility, FCS measurements in human cells concluded that Sas-6 was largely dimeric in the cytoplasm (Keller *et al.*, 2014). Given the lack of information regarding Ana2's and Sas-6's cytoplasmic oligomerisation state, I aimed to characterise their stoichiometry in the *Drosophila* embryo.

I first measured the molecular brightness of mNG-tagged Ana2 and Sas-6 and compared their average molecular brightness to my monomeric and dimeric NeonGreen control lines. Unexpectedly, Ana2 had a similar molecular brightness as dimeric NeonGreen (dNG), while Sas-6 exhibited a similar molecular brightness to monomeric NeonGreen (mNG) (**Figure 5-7A**). In both cases, the N-terminally and C-terminally tagged version of each cartwheel protein displayed the same average molecular brightness, highlighting the reproducibility of this methodology and indicating that the position of the fluorescent tag does not interfere with either of the protein's cytoplasmic oligomerisation state (**Figure 5-7A**).

FCS is a single-molecule sensitive technique, but parameters are extracted from the average behaviour of thousands of individual molecules diffusing through the observation spot during each measurement. Thus, even though Ana2 is on average present as a dimer in the cytoplasm, its average molecular brightness (count rate per molecule, CPM) could be generated by a mixture of various oligomeric states (e.g., an equal mix of monomers and tetramers would have the same average CPM as a homogeneous population of dimers). In theory, FCS can distinguish if different populations of molecules are passing through the observation spot if their diffusion speeds differ, which can be identified by the shape of the ACF. For both Sas-6 and Ana2 the diffusion model that best explained the shape of their ACFs had a single diffusing species (1 DS, *grey* part of pie chart, **Figure 5-7B**) (see **Chapter 2, Section 2.3.2**). This strongly suggests that Ana2's average CPM is predominantly generated by a single dimeric mNG-Ana2 or Ana2-mNG species rather than by a mix of monomers and higher-order oligomers.

To further assess the cytoplasmic stoichiometry of Sas-6 and Ana2, I measured their molecular brightness in embryos from mothers either homozygously expressing the fluorescently labelled protein of interest (so 100% of the protein in the embryo was fluorescently tagged) or heterozygously expressing one copy of tagged and one copy of untagged protein (so only ~50% of the protein in the embryo was fluorescently tagged). If a protein is only present as a monomer, the expression of the WT allele will not affect the average molecular brightness—as FCS cannot detect untagged particles. If a protein is present in a higher oligomeric state, the addition of the untagged protein will lead to the formation of heterooligomers, which will result in a decrease of the average molecular brightness (CPM) due to the reduction in fluorophore number per diffusing molecule

(*orange* arrows, **Figure 5-7Ci**). For both mNG-eAna2 and eAna2-mNG, I observed a significant reduction in the CPM in embryos from heterozygous mothers (mNG-eAna2/+ or eAna2-mNG/+) compared to embryos from homozygous mothers (**Figure 5-7Cii**). This strongly suggests that Ana2 is present in a higher oligomeric state in the cytoplasm.

For Sas-6, the result was unfortunately less clear. For N-terminally tagged mNG-eSas-6, I did not observe a significant change in CPM between embryos from mothers heterozygous or homozygous for the fluorescently tagged allele, supporting my previous result that Sas-6 is mostly monomeric in the cytoplasm. Surprisingly, however, I did detect a significant decrease in CPM in the embryos from heterozygous mothers expressing the C-terminally tagged eSas-6-mNG (**Figure 5-7Cii**). This would suggest that this C-terminally tagged eSas-6-mNG can form complexes with untagged Sas-6, even though the CPM did not indicate this when the protein was expressed without the WT protein, and the N-terminally tagged mNG-eSas-6 appears unable to do so. Importantly, both proteins appear to be fully functional as both of these knock-in lines can be maintained as healthy, fertile homozygous stocks.

This result was very puzzling, but I realised there was a very plausible explanation. In FCS the average number of fluorophores present in the excitation spot (and therefore their concentration) is calculated from the normalised variance of the fluorescence signal over time. Background noise, which "mimics" the presence of additional fluorophores, can therefore lead to an overestimation of the measured concentration (Kim, Heinze and Schwille, 2007) and so needs to be corrected for (Koppel, 1974; Ruettinger *et al.*, 2008). In my experiments, background corrections were applied based on measurements in WT control embryos which do not express a fluorophore. Thus, they are only estimates of the

actual background present during the FCS measurement, and they introduce an error that increases as the total signal decreases. To calculate the molecular brightness of my proteins of interest, the total signal is divided by the average number of particles present in the excitation spot, and so *any overestimation of protein concentration would lead to a reduced CPM*. As I argue below, I believe that I am overestimating the concentration of eSas-6-mNG in the heterozygous line, and this leads to the reduced CPM I observe (**Figure 5-7Cii**).

The eSas-6-mNG knock-in line expresses Sas-6-mNG at a very low concentration (~8 nM, **Figure 5-6Cii)**; this is the lowest concentration of any of the other centriole proteins that could be measured by FCS, and about half of what I observed for mNG-eSas-6 (~15 nM). By halving the Sas-6-mNG levels in embryos from mothers heterozygously expressing eSas-6-mNG/+, not only the concentration but also the SNR is reduced, and so the measurements become more sensitive to the errors introduced by the background correction (as described above). Interestingly, the measured concentration of eSas-6-mNG in embryos from heterozygous mothers was ~5 nM (data not shown), which is ~25% more than half of the concentration detected in embryos from homozygous mothers (~8 nM). If the measured concentration of ~5 nM is an overestimate (and the real cytoplasmic concentration is ~4 nM), this 25% concentration overestimation could explain the CPM reduction of ~25% that I observed between embryos from homozygous and heterozygous mothers (**Figure 5-7Cii**).

5.2.7 An attempt to establish Fluorescence cross-correlation spectroscopy (FCCS) in the early *Drosophila* embryo to investigate Sas-6's and Ana2's cytoplasmic stoichiometry

Although the data with Sas-6 is currently inconclusive, these observations raise the interesting possibility that Sas-6 exists in the cytoplasm as a monomer (rather than as a functional dimer), while Ana2 exists in the cytoplasm as a dimer (rather than as an assumed functional tetramer). This is potentially important as, if correct, it would mean that even though the embryo has to build hundreds of centrioles in a very short period, it stores its pool of the essential building blocks Sas-6 and Ana2 in forms that are not competent for immediate assembly.

I therefore wanted to use a different method to investigate Sas-6's and Ana2's cytoplasmic stoichiometry. As described in **Chapter 2, Section 2.3.3**, FCCS is a modification of FCS where two spectrally shifted fluorophores are simultaneously observed with two different lasers in an overlapping excitation spot to determine potential cytoplasmic protein interactions. My initial control experiments suggested this technique was not very sensitive in living *Drosophila* embryos, as even a covalently coupled mScarlet-I+mNG fusion protein exhibited a cross-correlation of only ~20%, while co-expressed monomeric forms gave a "background" cross-correlation of ~7% (**Figure 3-5C**). Nevertheless, I decided to test whether I could use this technique to probe the stoichiometry of Sas-6 and Ana2.

I generated fly lines expressing one copy of mNG-tagged and one copy of mScarlet-I-tagged Sas-6 or Ana2 in their mutant background and obtained 30-second-long FCCS measurements around nuclear cycles 10-12. If a protein homo-oligomerises in the cytoplasm, I would expect to detect co-diffusion of the red and green fluorophore and therefore a positive cross-correlation curve. Unfortunately, I had to use even lower laser

powers in these experiments compared to the control measurements, as the red fluorophore mScarlet-I seemed to be very sensitive to photobleaching by both the 488 nm and 561 nm lasers. It is unclear why I observed such a discrepancy in the molecular brightness and bleach behaviour of mScarlet-I in the Sas-6/Ana2 lines compared to the control lines. I hypothesise that the lower CPM might be caused by the bleaching of the red fluorophore before it can pass through the centre of the laser beam—where the laser intensity is at its maximum—due to the reduced diffusion speed of the centriolar protein compared to the inert control. This might also explain why I, in general, only observe such a low cross-correlation in the control line (**Figure 3-5C**). Despite these technical limitations, I measured the cross-correlation amplitude of Sas-6 and Ana2 (*orange* lines, **Figure 5-8**), and noticed that in all six embryos that I analysed for each genotype, my Ana2 measurements exhibited a more prominent cross-correlation curve (judged by the height of the less noisy part of the cross-correlation) compared to Sas-6 (*black* arrows, **Figure 5-8**). Clearly this method will need to be further optimised before I can use it to answer this important question.

5.3 Discussion

5.3.1 The cytoplasmic concentration of Plk4 decreases between nuclear cycles 11-14 to slow the centriole growth dynamics

In a collaborative effort, we have identified that an adaptive Plk4 oscillation times and executes centriole duplication, and that Plk4's incorporation rate at the centriole declines over successive cycles (Aydogan, Steinacker *et al.*, 2020). Mathematical modelling predicted that the dampening of the Plk4 oscillation over successive cycles was mainly driven by a decline in its cytoplasmic protein abundance while the levels of its receptor,

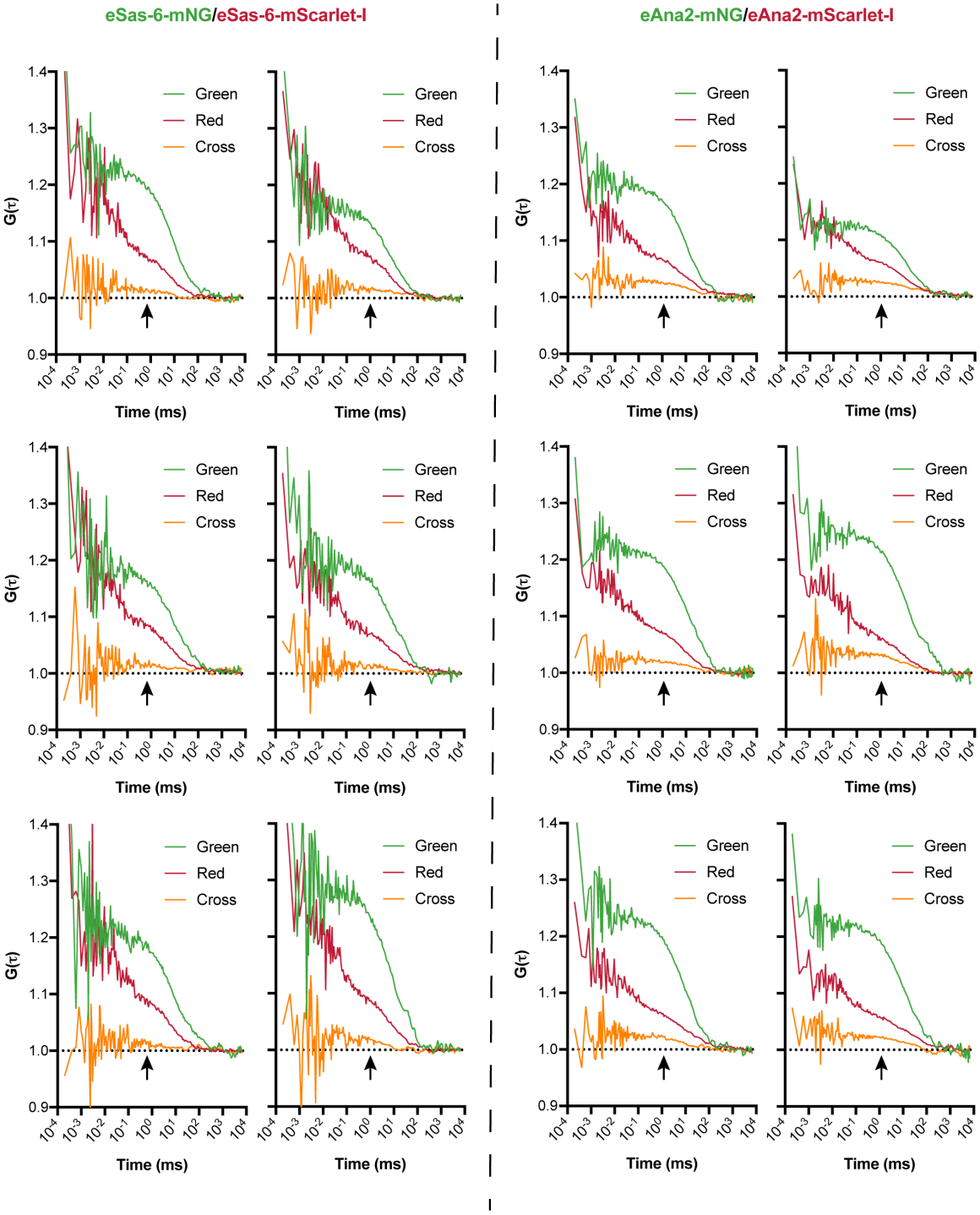


Figure 5-8: FCCS measurements potentially indicate that Sas-6 is monomeric and Ana2 oligomeric in the cytoplasm

Graphs depict exemplary ACFs and cross-correlation functions between mNG-tagged and mScarlet-I-tagged Sas-6 (*left*) and Ana2 (*right*) from 30-second-long cytoplasmic FCCS measurements. The amplitude of the cross-correlation function divided by the amplitude of the ACF depicts the fraction of co-diffusing and therefore oligomerised protein in the cytoplasm. A positive cross-correlation is judged by the height of the cross-correlation curve (*orange*) away from the *dotted* baseline. Despite many experimental limitations, the amplitude of the cross-correlation curves (highlighted with *black arrows*) appears to reproducibly be higher for Ana2 than for Sas-6.

Asl, were predicted to remain constant. By using FCS and PeCoS, I was able to confirm both predictions.

Plk4 is a suicide kinase that triggers its own destruction upon activation (Guderian *et al.*, 2010; Sillibourne *et al.*, 2010; Holland *et al.*, 2012; Cunha-Ferreira *et al.*, 2013), so it seems plausible that with every successive cycle the exponentially increasing number of centrioles will trigger increasing levels of self-destruction of Plk4 (which is activated by binding to its centriole receptor Asl) and so to an increasing reduction of its cytoplasmic pool. Alternatively, the increased sequestration of Plk4 to the growing number of centrioles could also lead to the observed drop in cytoplasmic abundance. Interestingly, either of these mechanisms would allow the embryo to effectively "count" its number of centrioles and to adapt the centriole's growth dynamics accordingly.

Such a mechanism is potentially very interesting. A rather puzzling phenomenon of the early *Drosophila* embryo's development is the progressive slowing of S-phase from ~9 minutes in nuclear cycle 10 to ~15 minutes in nuclear cycle 13, before an abrupt transition and an extended cycle length of >45 minutes in nuclear cycle 14 (Farrell and O'Farrell, 2014). The progressive lengthening of the cell cycle in nuclear cycles 10-13 is caused by an increase in S-phase length, which is thought to be due to a delay in the initiation of DNA replication at repetitive satellite sequences (Shermoen, McCleland and O'Farrell, 2010). This delay activates the DNA checkpoint kinase Chk1-homologue *grapes*, leading to the inhibition of Cdk1 and a delay in the entry into mitosis (Fogarty *et al.*, 1997). Our observation that Plk4 recruitment—which controls the rate of centriole growth (Aydogan *et al.*, 2018)—slows over successive cycles creates a conundrum: if the cycle length extends due to the delayed replication initiation of the satellite sequences, how do

the centrioles grow more slowly from the very beginning of the cycle? This would suggest that the centrioles already "know" the cycle duration and adapt their assembly dynamics from the very start of S-phase. One plausible explanation is that the centriole "counting" mechanisms described above act to slow the rate of daughter centriole assembly in embryos independently of the mechanisms that slow DNA replication and activate Chk1.

5.3.2 The cytoplasmic concentration of all other core centriole duplication proteins remains relatively constant between nuclear cycles 11-14

Unlike Plk4, the cytoplasmic concentration of all other core centriole duplication proteins (Asl, Sas-6, Ana2 and Sas-4) remained relatively constant, or showed only a very minor depletion, between nuclear cycles 11-14. This was unexpected, especially as all core centriole duplication proteins appear to be present in the low-nM concentration range and the embryo is faced with the challenge of doubling centriole numbers four times in less than an hour (from ~800 in cycle 11 to ~6000 in cycle 14 (Zalokar and Erk, 1976)). There are at least two possible explanations for this observation: 1) The synthesis of new protein replenishes the used up centriolar material, and this synthesis rate is regulated to provide more new protein at each successive cycle; 2) The amount of protein incorporated into the newly assembled centrioles is too small to significantly affect the amount of protein present in the much larger cytoplasmic pool.

To examine the plausibility of this second possibility, I have tried here to roughly estimate the cytoplasmic pool of centriolar proteins that might be available to each assembling centriole. My FCS measurements only allow me to extract relative cytoplasmic concentrations but, due to the thorough characterisation of my setup (**Chapter 3**), I believe that the cytoplasmic concentrations I measure by FCS are likely to be reasonably accurate. I estimated the size of the domain associated with each nucleus (see **Figure 1-7**)

in cycles 11-13 by measuring the distance between individual nuclei in embryos from mothers expressing a fluorescent nuclear marker (images provided by Siu-Shing Wong). Unfortunately, the depth of the cytoplasmic layer that surrounds the nucleus (and in which I conducted my FCS/PeCoS measurements) is not known, so I estimated the nuclear layer to be as deep as the fluorescent signal that I can observe in z, which was ~15 μm. This is most likely an underestimation, and the deeper the nuclear layer reaches into the centre of the embryo, the more cytoplasmic building blocks will be available to the embryo for the assembly of its organelles.

According to this very rough calculation, a protein that is present at a cytoplasmic concentration of 10 nM is present at a total of ~9,000 molecules/centriole in cycle 11, ~6,000 molecules/centriole in cycle 12, and ~2,800 molecules/centriole in cycle 13. Bauer *et al.*, 2016 used targeted proteomics combined with fluorescence imaging in human cells to quantify the total amount of centriolar proteins present at the centriole and predicted that all core centriole duplication proteins are present in a relatively low copy number of ~50-150 per centriole. If the *Drosophila* centriole consists of roughly the same amount of protein copy numbers as the human cell (which seems plausible as the centriole cartwheel size is quite similar (Debec *et al.*, 1999; Klena *et al.*, 2020), the increased sequestration over the cycles might indeed be negligible for the centriole core proteins Asl, Sas-6, Ana2, and Sas-4. As the diffusion speed of all four core centriole duplication proteins is relatively fast (~1-3 μm^2/second) compared to the timescale of centriole assembly (which occurs over several minutes), I assume that diffusion is unlikely to be limiting for centriole assembly. Interestingly, when I calculated the same scenario for a very low abundant protein (like Plk4) that might be expressed at a cytoplasmic concentration of 1 nM, my

calculations suggested that there would only be ~280 molecules/centriole available in cycle 13. Therefore, it seems plausible that the sequestration to the exponentially increasing number of centrioles might contribute to Plk4's stepwise cytoplasmic depletion between nuclear cycles 11-14. However, the synthesis of new Plk4 molecules and the self-destruction of activated Plk4 will most likely also influence its cytoplasmic abundance.

5.3.3 Ana2 and Sas-6 appear to be kept in a lower oligomeric state in the cytoplasm than at the centriole

Multiple studies have shown that both core centriole cartwheel proteins, Ana2 and Sas-6, can homo-oligomerise and that point mutations within the oligomerisation domains perturb centriole assembly (Kitagawa, Vakonakis, *et al.*, 2011; Van Breugel *et al.*, 2011; Hilbert *et al.*, 2013; van Breugel *et al.*, 2014; Cottee *et al.*, 2015; Rogala *et al.*, 2015; David *et al.*, 2016). It is commonly believed that Ana2 and Sas-6 are already present in their functional oligomerisation state in the cytoplasm. My FCS-based stoichiometry measurements dispute this assumption and indicate that both proteins might be present in a lower oligomeric state in the early *Drosophila* syncytium: Ana2—on average—as a dimer, and Sas-6 as a monomer.

My observations suggest that, similarly to Plk4's concentration threshold that needs to be surpassed to initiate centriole assembly (Lopes *et al.*, 2015), both Ana2 dimers and Sas-6 monomers require a specific local environment (like the centriole assembly site) to promote their oligomerisation and to potentially restrict cartwheel assembly to a specific site on the side of the existing mother centriole. The local environment which allows the formation of Ana2 tetramers and Sas-6 dimers could either be generated by an increased local protein concentration to promote oligomerisation or a specific protein interaction/ modification which only occurs at the centriole through the presence of additional

centriolar proteins. For Sas-6's homologue SAS-6 (*C. elegans*), the disassociation constant (K_D) was previously reported *in vitro* to be 0.9 ± 0.1 μM (Kitagawa, Vakonakis, *et al.*, 2011), which is much higher than the observed cytoplasmic concentration of ~10 nM in my endogenously tagged eSas-6-mNG embryos. Although the central coiled-coil domain of Ana2 was only observed as a tetramer *in vitro* (Cottee *et al.*, 2015), the lowest fragment concentration assessed was 36 μM which cannot be compared to the cytoplasmic environment where Ana2 is present in the lower nanomolar concentration range.

My measurements also contradict a previous FCS study in human cells, which concluded that SAS6 is mostly dimeric in the cytoplasm (Keller *et al.*, 2014). Their measurements of transiently transfected Sas6-GFP, however, showed expression levels that were nearly 10-fold higher compared to my endogenously tagged eSas-6-mNG line. A potential explanation for this discrepancy is that the transient transfection of SAS6-GFP might have caused an overexpression of the transgene, and that the elevated concentration levels surpass the K_D of Sas-6. This could allow the spontaneous formation of cytoplasmic Sas-6 dimers which might otherwise be restricted to the centriole where the local concentration of Sas-6 is higher. Surprisingly, their SAS6-GFP concentration of <0.1 μM (at which they observed dimer formation) was significantly lower than the K_D for SAS-6 measured in *vitro* (~0.9 μM) (Kitagawa et al., 2011). This suggests that the cytoplasmic environment might promote the oligomerisation of Sas-6.

Another possible explanation for the difference in cytoplasmic Sas-6 stoichiometry between human cells and the *Drosophila* embryo is that this mechanism of keeping proteins in their lower oligomeric state in the cytoplasm might be embryo-specific. The embryonic system has to cope with an enormous cell cycle speed where centrioles need

to duplicate every ~10-12 minutes (Foe and Alberts, 1983). My FCS measurements revealed that the cytoplasmic concentration of most core centriole duplication proteins remains constant throughout and between nuclear cycles 11-14 (see **Chapter 4, Section 4.2.2,** and **Chapter 5, Sections 5.2.3** and **5.2.5**). In human cells, in contrast, centriole duplication takes ~10 hours (Takao *et al.*, 2019), and most core centriole duplication proteins are degraded during mitosis to prevent unscheduled centriole duplication (Strnad et al., 2007; Tang et al., 2009; Guderian et al., 2010; Sillibourne et al., 2010; Arquint et al., 2012). This suggests that the embryo keeps its cytoplasmic concentrations constantly at elevated levels to allow the fast pace of centriole duplication throughout the blastoderm cycles. Therefore, additional control mechanisms like the cytoplasmic stoichiometry restriction of both core cartwheel proteins might exist in the embryo to ensure that centrioles only duplicate once every cycle.

6 Investigation of the cytoplasmic pool of centrosomal proteins

6.1 Introduction

Centrosomes are membrane-less, electron-dense cell organelles that form through the nucleation of the pericentriolar material (PCM) around mother centrioles (**Figure 6-1A**). Centrosomes have an important role in cell organisation (Moritz *et al.*, 1995; Conduit, Wainman and Raff, 2015), recruiting microtubule-growth promoting factors like the γ-TuRC to form the major MTOC of the mitotic spindle (Meraldi, 2016), and also acting as signalling hubs which concentrate many signalling molecules and cell cycle regulators (Arquint, Gabryjonczyk and Nigg, 2014).

During interphase, a relatively small, but highly structured, PCM is present in close proximity to the mother centriolar wall (Fu and Glover, 2012; Lawo *et al.*, 2012; Mennella *et al.*, 2012; Sonnen *et al.*, 2012). In preparation for mitosis the PCM expands dramatically in size (Palazzo *et al.*, 1999). During symmetric cell divisions, centrosomes within the same cell have to grow to the same size to ensure faithful chromosome segregation, but it is largely unknown how this size regulation is achieved (Meraldi, 2016). Centrioles are essential for PCM nucleation (Bobinnec *et al.*, 1998; Basto *et al.*, 2006; Conduit *et al.*, 2010; Sir *et al.*, 2013; Bazzi and Anderson, 2014; Wong *et al.*, 2015), and in *C. elegans* it was recently shown that the presence of the centriole is needed throughout the entire centrosome growth period (Cabral *et al.*, 2019).

In *Drosophila* embryos, the interplay of three proteins—Polo, Spd-2 and Cnn—is believed to be responsible for the formation of an underlying "PCM scaffold" that recruits the many "PCM client" proteins to the centrosome (Conduit, Richens, *et al.*, 2014; Alvarez-Rodrigo *et al.*, 2019) (**Figure 6-1**). Spd-2 is thought to be phosphorylated as cells prepare to enter

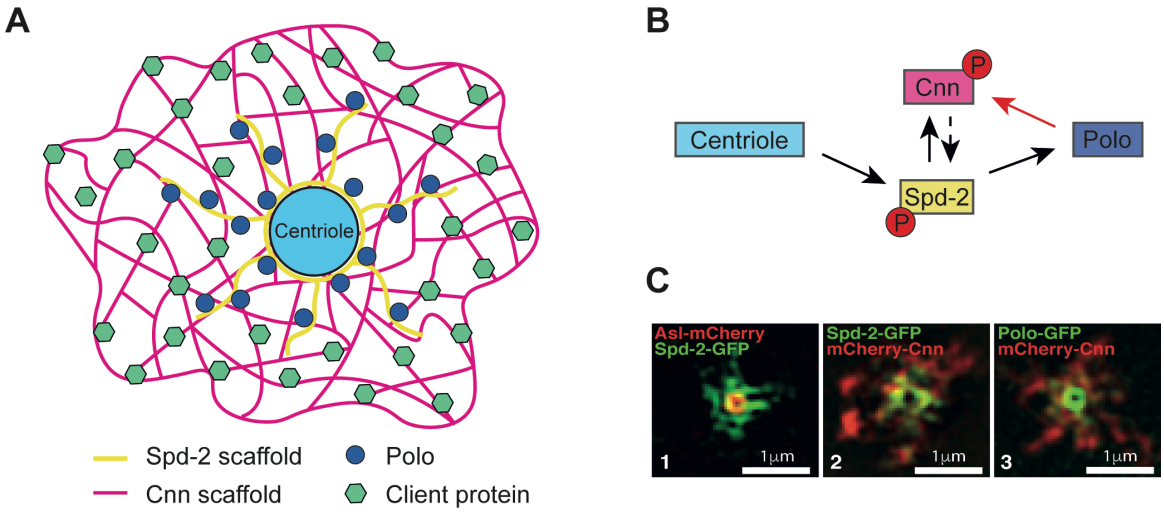


Figure 6-1: A positive feedback loop between the scaffold proteins Spd-2, Polo, and Cnn drives centrosome maturation

(A) Cartoon depicts the structure of the underlying scaffold of the mitotic PCM. Spd-2 (*yellow*) forms a scaffold in close proximity to the centriole wall and recruits Polo (*dark blue* circles). Polo's phosphorylation of Cnn leads to Cnn scaffold formation (*pink*), which spreads out further than the Spd-2 scaffold and allows the concentration of PCM client proteins (*green* hexagons). **(B)** Diagram shows the potential molecular mechanism of the positive feedback loop between the three scaffold proteins Spd-2, Polo, and Cnn. During interphase, Spd-2 is recruited to the outer centriole wall. PCM expansion is initiated when Spd-2 is phosphorylated, which allows the recruitment of both Polo and Cnn (*black solid* arrows) to the centrosome. Polo can then phosphorylate Cnn (*red solid* arrow) to initiate Cnn scaffold formation. The Cnn scaffold can recruit PCM proteins but also helps to retain Spd-2 at the centrosome (*black dotted* arrow), which allows the formation of a positive feedback loop (Alvarez-Rodrigo et al., 2019). **(C)** Images show the centrosomal localisation of the three scaffold proteins viewed by 3D-SIM super-resolution microscopy. Asl-mCherry was used to identify the position of the centriole within the PCM. Images were modified from Conduit, Wainman and Raff, 2015.

mitosis, allowing it to recruit Polo and Cnn to the outer wall of the mother centriole. Binding to Spd-2 actives Polo, which phosphorylates Cnn to allow Cnn to assemble into a scaffold. The Cnn scaffold cannot recruit Spd-2, but it helps to maintain Spd-2 at the centrosome (indicated by *dashed* arrow, **Figure 6-1B**). In this way, these proteins are thought to form a positive feedback loop that can drive the expansion of the PCM scaffold around the mother centriole (Conduit, Richens, *et al.*, 2014; Alvarez-Rodrigo *et al.*, 2019) (**Figure 6-1B**).

In this chapter, I collaborated with another PhD student in the lab, Siu-Shing Wong, to systematically and quantitatively characterise PCM assembly dynamics to gain insight into the mechanisms and regulation of the assembly process.

6.2 Results

6.2.1 Centrosome size is homeostatically regulated in the early *Drosophila* embryo

As described in the previous chapter, the number of centrioles and centrosomes in the early *Drosophila* embryo doubles at each nuclear cycle, and the length of S-phase (the period when centrioles and mitotic centrosomes are growing in the embryos) increases at each cycle. This prompted us to ask how the mitotic centrosome growth dynamics change between nuclear cycles. Studies in *C. elegans* embryos indicated that the total volume of PCM combined from all the centrosomes in the embryo remained constant throughout the early cell divisions, so that the centrosomes halved in size after each division (Decker *et al.*, 2011). The total amount of SPD-2 in the worm embryo appears to remain constant between cell stages, and it is thought that SPD-2 acts as a limiting component for centrosome growth. The idea that organelle assembly might be regulated by a limiting cytoplasmic pool of a key component has been influential (Goehring and Hyman, 2012), so we wanted to test if a similar mechanism operates in the early *Drosophila* embryo.

Siu-Shing Wong measured the incorporation dynamics of seven PCM-client proteins throughout nuclear cycles 11-13 (GFP-D-TACC, MSPS-GFP, γ-tubulin-GFP, Grip71-GFP, Grip75-GFP, Grip128-GFP, and Aurora A-GFP). All seven proteins were recruited to the centrosome in an oscillatory manner with levels increasing through most of S-phase and then rapidly decreasing just before mitosis (judged by NEB, *grey* area indicates mitosis, **Figure 6-2A**; only TACC and γ-tubulin are shown here as examples). Unexpectedly, and in contrast to *C. elegans* embryos, centrosomes grew to an approximately similar size (here we define "size" as the total fluorescence intensity) in each cycle (**Figure 6-2B**). Moreover,

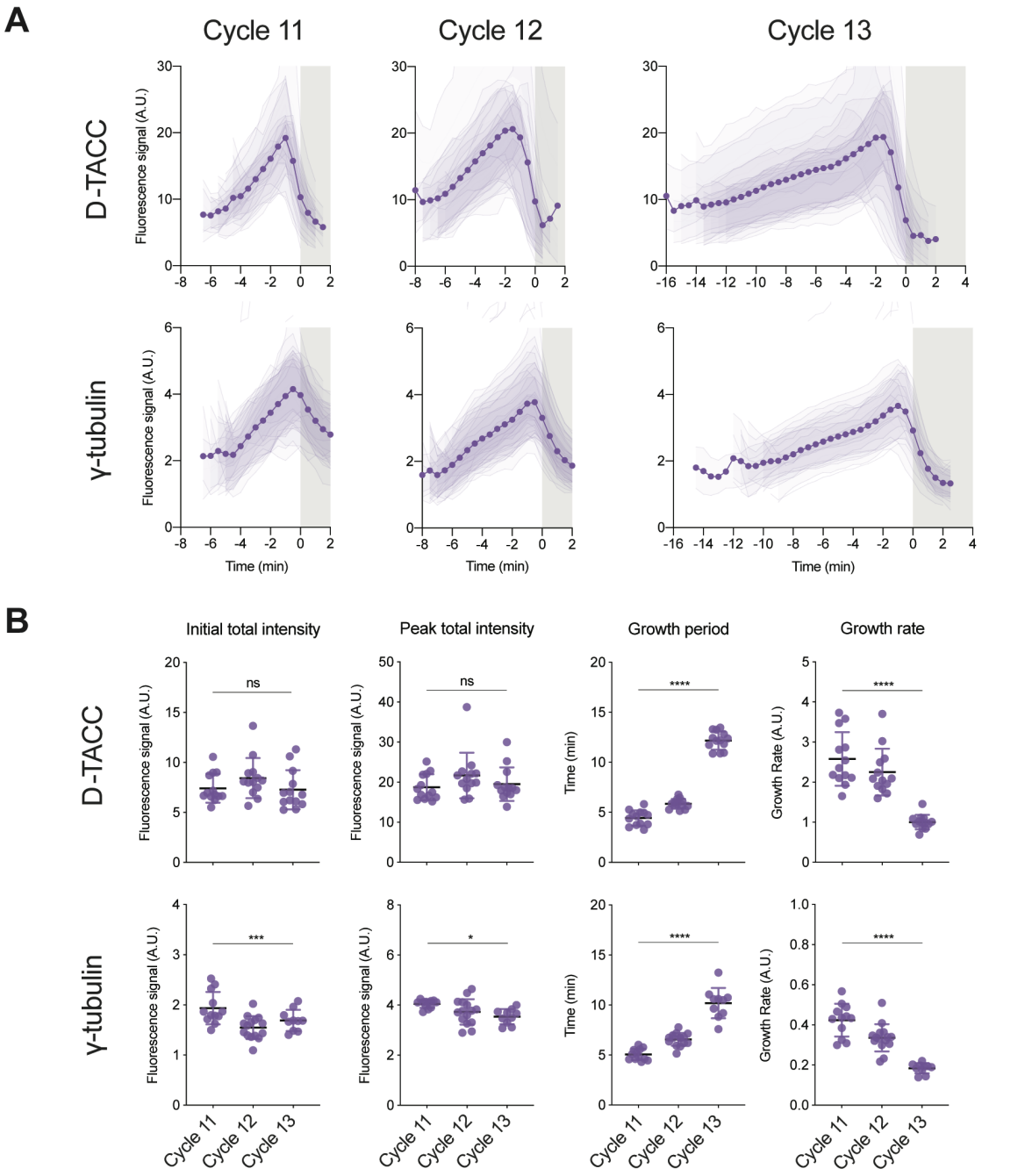


Figure 6-2: PCM client proteins are recruited to the centrosome in an oscillatory manner and grow to a similar size over successive cycles 11-13

(A) Graphs show the mean centrosomal recruitment dynamics (±SD for each individual embryo) of Ubq-GFP-D-TACC and ncd-γ-tubulin-GFP during nuclear cycles 11-13. Incorporation profiles were aligned to NEB to account for variability in nuclear cycle length. *White* background indicates S-phase, *grey* background mitosis. **(B)** Bar charts quantify and compare several centrosome growth parameters (mean±SD) from (A). Each data point represents the average value of all centrosomes from an individual embryo. Statistical significance was assessed using an ordinary one-way ANOVA test (for Gaussian-distributed data) or a Kruskal-Wallis test (****, P<0.0001; ***, P<0.001; *, P<0.05; ns, not significant). Data and graphs were generated by Siu-Shing Wong.

similarly to centriolar cartwheel assembly in *Drosophila* embryos (Aydogan *et al.*, 2018), centrosome size seemed to be homeostatically regulated: the centrosome growth rate decreased at successive cycles but the growth period increased, so that centrosomes grew to a similar size in all three cycles (**Figure 6-2B**). These findings would seem to rule out the idea of a size-limiting component for centrosome growth in these embryos.

6.2.2 The growth rate reduction of the PCM client proteins between nuclear cycles 11-13 is not caused by the depletion of their cytoplasmic pool

We reasoned that the homeostatic relationship between the centrosome growth rate and period could be a passive consequence of embryo development. Over nuclear cycles 11-14, the embryo experiences a natural elongation of interphase that slows many processes (Farrell and O'Farrell, 2014), and this could lead to a passive elongation of the centrosome's growth period. Similarly, due to the doubling in centrosome number with every successive cycle, the reduction in growth rate could be a passive consequence of the gradual cytoplasmic depletion of the centrosomal client proteins as more protein becomes sequestered in the PCM at each cycle.

To test this latter possibility, I used FCS to measure the cytoplasmic concentration of all seven centrosomal client proteins at the beginning of nuclear cycles 11-14. The cytoplasmic concentration of the individual PCM components varied considerably, with Ubq-Grip71-GFP being present at ~30 nM (a similar concentration to some of the centriole proteins I measured in the previous Chapters) and Ubq-MSPS-GFP being present at >400 nM. Nevertheless, the cytoplasmic concentration of all the individual client proteins remained relatively constant between the four nuclear cycles (**Figure 6-3**). I conclude that the general decrease in the growth rate of the client proteins over successive cycles is not simply the consequence of their cytoplasmic depletion. Instead, it appears that the

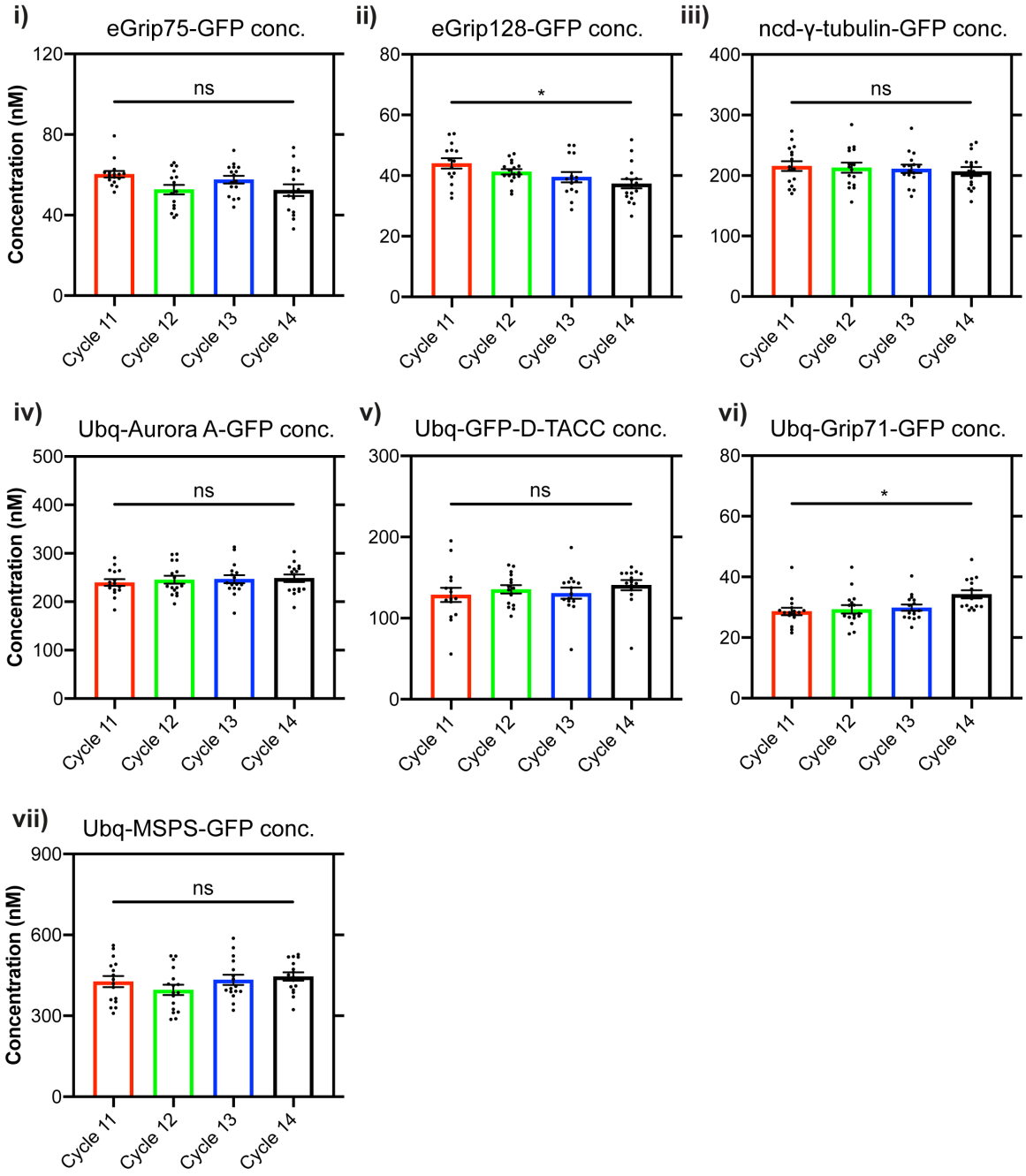


Figure 6-3: The cytoplasmic concentration of all seven PCM client proteins remains relatively constant between nuclear cycles 11-14

Bar graphs quantify the cytoplasmic concentration (mean±SEM) of several PCM client proteins at the beginning of S-phase between nuclear cycles 11-14. Each data point represents the average of 4-6x 10-second-long recordings. Statistical significance was assessed using an ordinary one-way ANOVA test (for Gaussian-distributed data) or a Kruskal-Wallis test (*, P<0.05; ns, not significant).

cytoplasmic concentration of the centrosomal client proteins may be actively maintained at a constant (presumably optimal) concentration, which varies from protein to protein, throughout these blastoderm divisions.

6.2.3 The PCM scaffold-forming proteins exhibit distinct recruitment dynamics to the client proteins

We wondered whether the decreasing growth rate of the client proteins was due to a decreasing growth rate of the underlying PCM scaffold. Siu-Shing Wong measured the centrosomal recruitment dynamics of all three scaffold proteins (Cnn, Spd-2 and Polo) during nuclear cycles 11-13 (**Figure 6-4A**). Ubq-mNG-Cnn's recruitment to the centrosome was quite distinct from the recruitment dynamics of the PCM client proteins, indicating that the amount of PCM clients recruited to the centrosome does not merely reflect the centrosomal levels of the underlying Cnn scaffold. In contrast, Ubq-Spd-2-GFP and ePolo-GFP/+ exhibited an oscillatory recruitment pattern that was similar to the PCM client proteins (**Figure 6-4B**). These data reveal an unexpected complexity in the dynamics of mitotic centrosome maturation.

6.2.4 Cnn and Spd-2 show a stepwise drop in cytoplasmic levels between nuclear cycles 11-14

We noticed that, like the PCM client proteins, the PCM scaffold proteins tended to grow to the same size at each nuclear cycle (although significantly more Cnn was recruited during cycle 11, than in cycle 12 and 13) (**Figure 6-4B**). This size homeostasis also seemed to be enforced by a reciprocal relationship between the scaffold protein's growth rate and growth period (**Figure 6-4B**). Again, we wondered if the reduction in the growth rate of the PCM scaffolding proteins at successive cycles was due to their depletion from the cytoplasm as they become sequestered at the centrosomes, and I used FCS to test this

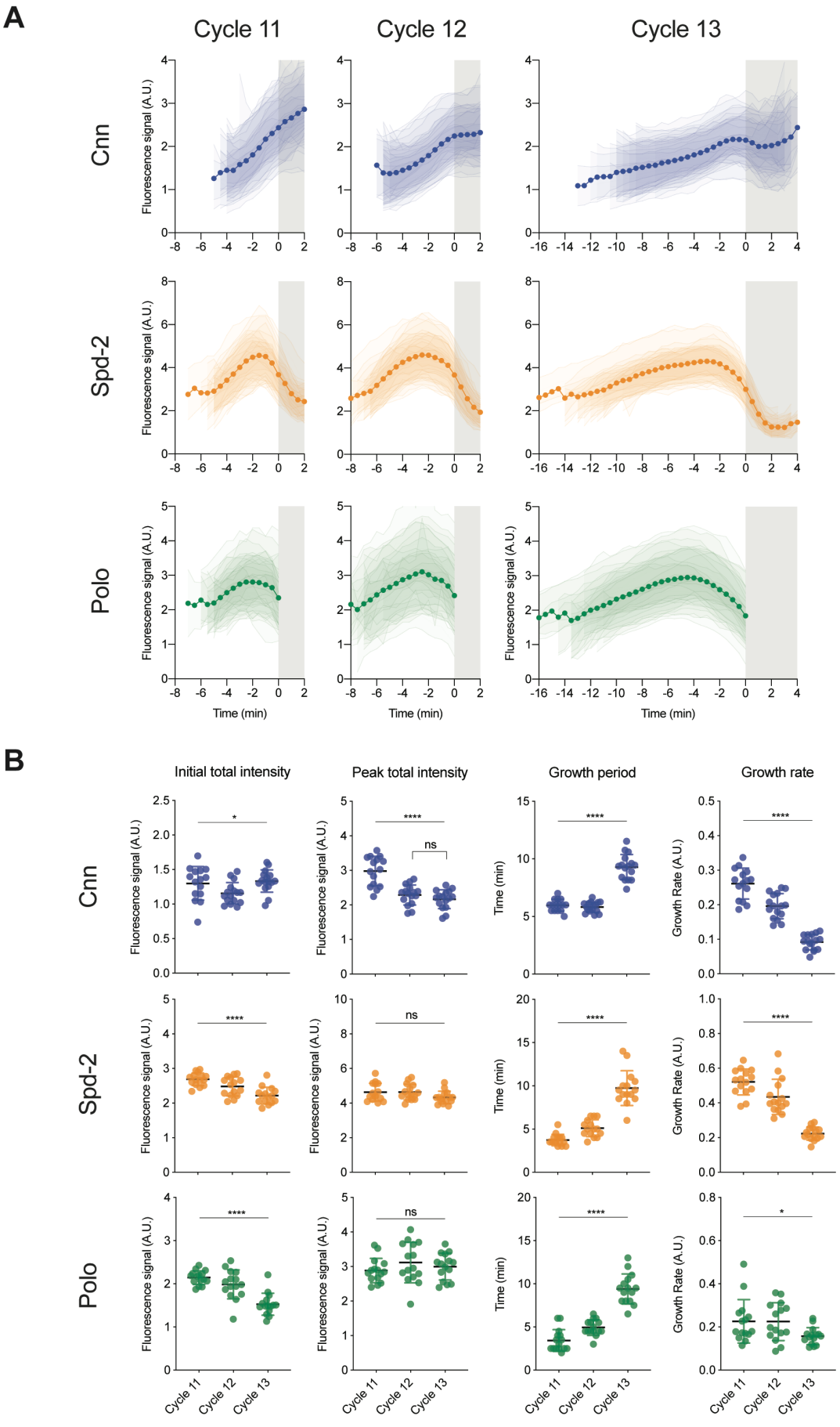

A
Cycle 11
Cycle 12
Cycle 13
Cnn
Spd-2
Polo
Fluorescence signal (A.U.)
Time (min)
B
Initial total intensity
Peak total intensity
Growth period
Growth rate
Time (min)
Growth Rate (A.U.)
ns
Cycle 11
Cycle 12
Cycle 13

Figure 6-4: The recruitment dynamics of the three centrosomal scaffold proteins Cnn, Spd-2, and Polo differ from the recruitment dynamics of the client proteins
(A) Graphs show the mean centrosomal recruitment dynamics (±SD for each individual embryo) of Ubq-mNG-Cnn, Ubq-Spd-2-GFP, and ePolo-GFP/+ during nuclear cycles 11-13. Incorporation profiles were aligned to NEB to account for variability in nuclear cycle length. *White* background indicates S-phase, *grey* background mitosis. **(B)** Bar charts quantify and compare several centrosome growth parameters (mean±SD) from panel A. Each data point represents the average value of all centrosomes from an individual embryo. Statistical significance was assessed using an ordinary one-way ANOVA test (for Gaussian-distributed data) or a Kruskal-Wallis test (****, P<0.0001; *, P<0.05; ns, not significant) for the comparison between all three cycles, and an unpaired t-test with Welch's correction (ns, not significant) for comparison between two cycles. Data and graphs were generated by Siu-Shing Wong.

possibility. For Cnn and Spd-2, I examined embryos from mothers expressing an endogenously CRISPR/Cas9 mNG-tagged fusion (generated by Saroj Saurja), while for Polo-GFP I used a previously generated protein trap line (Buszczak *et al.*, 2007). This line was not viable as a homozygote, so I measured ePolo-GFP in a heterozygous background with one untagged allele (ePolo-GFP/+).

The cytoplasmic concentration (hereafter referred to as [Protein]) remained relatively constant at successive cycles for ePolo-GFP, but for both mNG-eCnn and eSpd-2-mNG it dropped significantly (**Figure 6-5**). Thus, in contrast to the PCM client proteins, a decrease in [Cnn] and/or [Spd-2] could contribute to their decreasing growth rate between nuclear cycles 11-13. This is potentially an exciting observation as it raises the possibility, also discussed in **Chapter 5** in relation to centrioles and Plk4, that embryos may be able to use the sequestration of key building blocks (in this case Cnn and/or Spd-2) as a way to effectively "count" the number of centrosomes in the embryo and to adjust their centrosome growth parameters accordingly.

6.2.5 The drop in [Cnn] at successive cycles is proportional to the amount of Cnn in the cytoplasm

Western blotting experiments revealed that in embryos laid by heterozygous females, the endogenously CRISPR/Cas9 tagged mNG-eCnn knock-in allele was expressed at slightly lower levels than endogenous untagged Cnn (**Figure 6-7A**), while a single copy of an

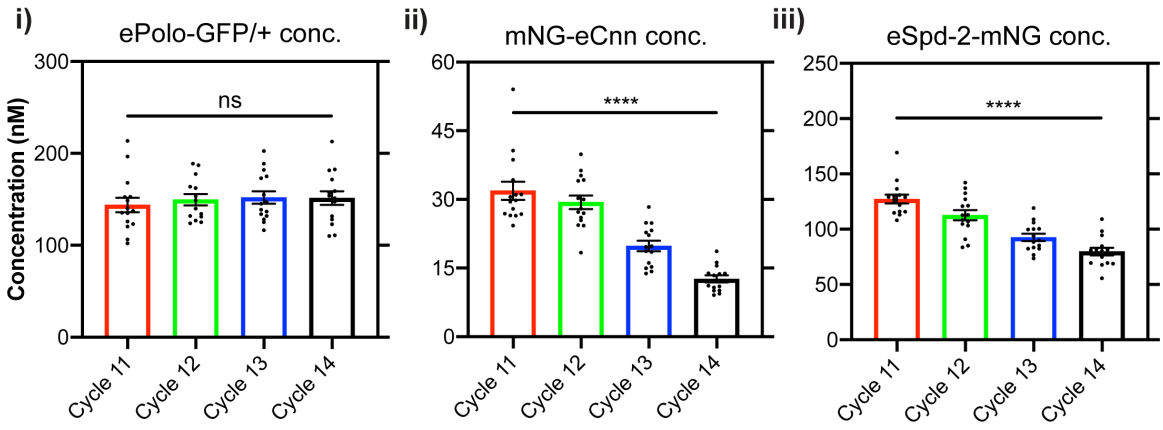


Figure 6-5: [Cnn] and [Spd-2] exhibit a stepwise drop between nuclear cycles 11-14 while [Polo] remains constant

Bar graphs quantify the cytoplasmic concentration (mean±SEM) of ePolo-GFP/+ **(i)**, mNG-eCnn **(ii)**, and eSpd-2-mNG **(iii)** at the beginning of S-phase between nuclear cycles 11-14. Each data point represents the average of 4-6x 10-second-long recordings. Statistical significance was assessed using an ordinary one-way ANOVA test (for Gaussian-distributed data) or a Kruskal-Wallis test (****, P<0.0001; ns, not significant).

mNG-eCnn transgene expressed from the Ubq-promoter (generated by Lisa Gartenmann) was expressed at similar levels to the endogenous protein in WT embryos (data from Siu-Shing Wong; not shown).

I therefore repeated my cytoplasmic FCS measurements between nuclear cycles 11-14 for mNG-Cnn, but this time comparing the levels of expression in embryos laid by females expressing either 1x or 2x copies of the mNG-eCnn CRISPR/Cas9 knock-in or 1x copy of the Ubq-mNG-Cnn transgene (always, where relevant, in a *cnn*$^{-/-}$ mutant background so that the mNG-fusion was the only source of Cnn in the embryo). In broad agreement with the western blotting experiments, the single copy of the Ubq-mNG-Cnn transgene was expressed at a ~2.5-fold higher level than the 2x CRISPR/Cas9 mNG-eCnn knock-in line, which was expressed at a ~1.8-fold higher level than the 1x line.

Despite the ~4.5-fold range of expression levels in these embryos, I noticed that the percentage drop in [Cnn] at each cycle was similar in each genotype (**Figure 6-6A**). This meant that the *absolute* drop in concentration at each cycle in each genotype varied

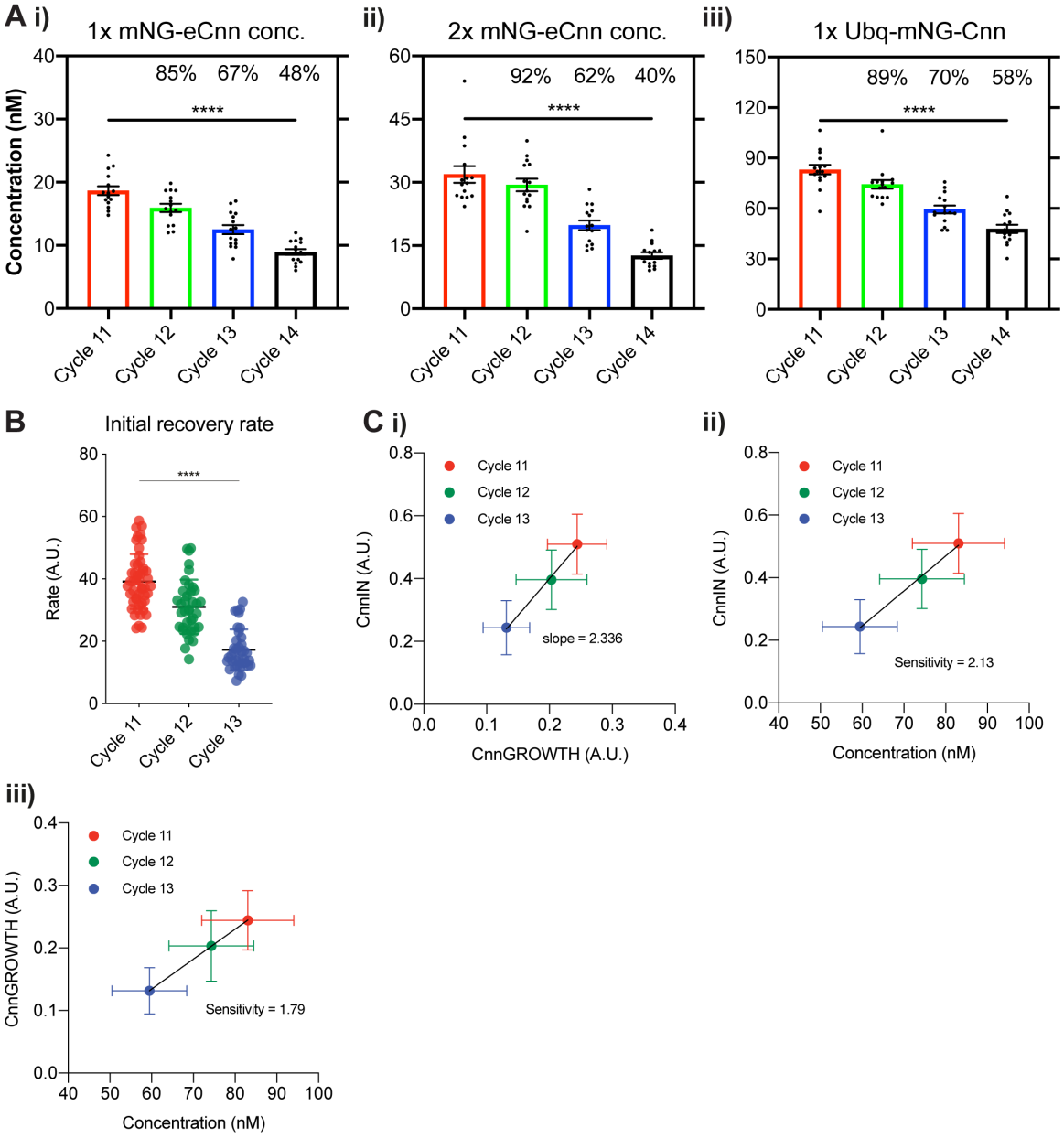


Figure 6-6: The stepwise drop in [Cnn] is insensitive to changes in its expression levels and might be responsible for Cnn's decreased centrosomal growth rate over cycles

(A) Bar graphs quantify the cytoplasmic concentration (mean±SEM) of 1x mNG-eCnn **(i)**, 2x mNG-eCnn **(ii)**, and 1x Ubq-mNG-Cnn **(iii)** at the beginning of S-phase between nuclear cycles 11-14. Each data point represents the average of 4-6x 10-second-long recordings. Statistical significance was assessed using an ordinary one-way ANOVA test (for Gaussian-distributed data) or a Kruskal-Wallis test (****, P<0.0001). **(B)** Graph depicts the initial recovery rate (mean±SD) of 1x Ubq-mNG-Cnn (within 30 seconds) from FRAP measurements of individual centrosomes. Statistical significance was assessed using an ordinary one-way ANOVA test (****, P<0.0001). **(C)** Graphs show the correlation between Cnn's incorporation rate *(CnnIN)* and Cnn's total growth rate *(CnnGROWTH)* **(i)**, *CnnIN* and [Cnn] **(ii)**, and *CnnGROWTH* and [Cnn] **(iii)** at the beginning of nuclear cycles 11-13. The sensitivity for Cii+iii was calculated using the mid-point method and the slope was extracted from a linear regression model in Prism (by Siu-Shing Wong). Data are presented as mean±SD. Centrosomal incorporation and growth dynamics were measured, and correlation graphs generated by Siu-Shing Wong.

considerably. Whereas [Cnn] dropped by ~10 nM between nuclear cycles 11-14 in the 1x CRISPR/Cas9 mNG-eCnn embryos, it dropped by ~35 nM in the 1x Ubq-mNG-Cnn embryos, indicating that a much larger number of Cnn molecules are removed from the cytoplasm at each cycle in these latter embryos. Although I was at first puzzled by this result, I realised that it was potentially consistent with the centrosomal sequestration hypothesis if the amount of mNG-Cnn sequestered at each individual centrosome increased as its cytoplasmic concentration increased. In **Chapter 6, Section 6.2.7** I show that this is indeed the case.

6.2.6 The drop in [Cnn] is correlated with a drop in the centrosomal Cnn incorporation and growth rate

Previous studies in *Drosophila* embryos have shown that Cnn and Spd-2 molecules are largely recruited into the middle of the PCM close to the centriolar wall, and then flux outwards—mostly leaving the PCM from the periphery (Conduit *et al.*, 2010; Conduit, Feng, *et al.*, 2014; Conduit, Richens, *et al.*, 2014; João Monteiro, personal communication)). This means that the size of the Cnn centrosome scaffold can be considered to be regulated by two factors: (1) The rate of Cnn incorporation in the central region (*CnnIN*); (2) The rate of Cnn loss from the periphery (*CnnOUT*) (Conduit *et al.*, 2010; Conduit, Feng, *et al.*, 2014; Conduit, Richens, *et al.*, 2014). If *CnnIN* is larger than *CnnOUT*, the Cnn scaffold will grow, and this growth rate (*CnnGROWTH*) is equal to *CnnIN* minus *CnnOUT*. This is also true for Spd-2, and I will use a similar nomenclature when considering the behaviour of this protein in later Sections.

Siu-Shing Wong had already measured *CnnGROWTH* at cycles 11-13 and found that this decreased significantly at each successive cycle (**Figure 6-4**). He then used fluorescence recovery after photobleaching (FRAP) to estimate *CnnIN* at the start of each nuclear cycle

and found that this also decreased dramatically (**Figure 6-6B**). Interestingly, the initial fluorescence recovery rate obtained from FRAP measurements (*CnnIN*) was consistently ~2.3x higher than the total centrosomal growth rate at the start of each nuclear cycle (*CnnGROWTH*) (**Figure 6-6Ci**). This is presumably because *CnnIN* only measures the incorporation of new Cnn molecules into the central region of the PCM (as these newly incorporated molecules have not had time to migrate to the periphery where they can leave the PCM), whereas *CnnGROWTH* measures the difference between *CnnIN* and *CnnOUT*.

These findings suggest that the reduction in the total centrosome growth rate over successive cycles is at least partially due to a reduction in *CnnIN*. We wondered whether this reduction in *CnnIN* could be explained by the reduction in [Cnn] that I had observed by FCS (**Figure 6-6A**). When we plotted [Cnn] from the 1x Ubq-mNG-Cnn line (that is most similar in concentration to the endogenous protein) against *CnnGROWTH* or *CnnIN*, we observed a near-linear correlation over cycles 11-13 (**Figure 6-6Cii+iii**). The slope of this line (~2 in both cases) gives an indication of how sensitive *CnnIN* and *CnnGROWTH* might be to changes in [Cnn]. Thus, if the observed correlation was causative (i.e., the change in *CnnIN* and *CnnGROWTH* was completely explained by the change in [Cnn]), then a 1% decrease in [Cnn] would cause a ~2% decrease in *CnnIN* and *CnnGROWTH*.

6.2.7 Manipulating [Cnn] alters the centrosomal Cnn growth rate

Although the strong correlation between the drop in [Cnn] and the slowing of *CnnGROWTH* at successive cycles is suggestive of causation, this is not necessarily the case. To directly test this, Siu-Shing Wong generated fly lines expressing fluorescently tagged Cnn at different concentrations and we measured how this influenced Cnn's

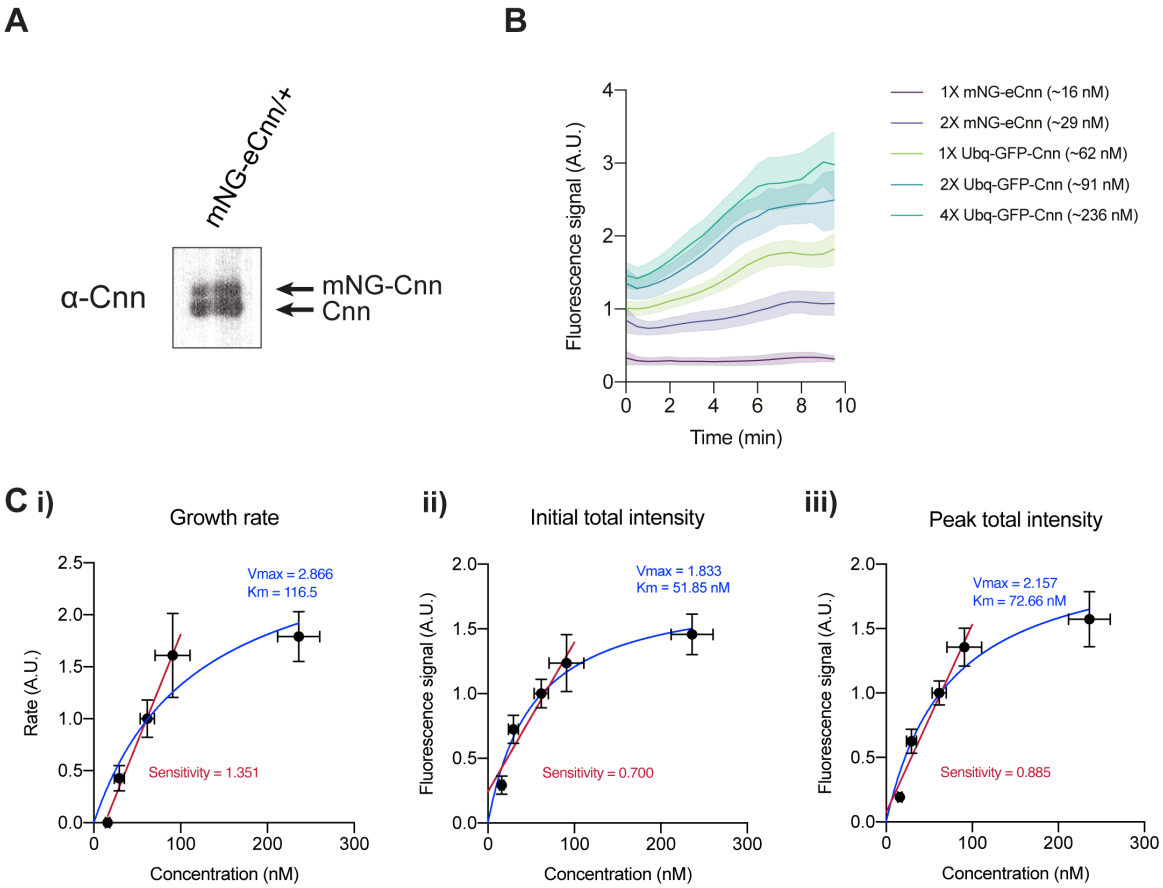


Figure 6-7: The centrosomal Cnn growth dynamics are sensitive to cytoplasmic concentration changes, but saturate at high expression levels

(A) Western blot analysis of embryos from heterozygous mothers expressing one copy of endogenously mNG-tagged and one copy of endogenous untagged Cnn. **(B)** Graph shows the mean±SD centrosomal growth dynamics of mNG-Cnn/GFP-Cnn at different expression levels (as measured by FCS at the beginning of S-phase) during nuclear cycle 12. N>14 embryos for each genotype. **(C)** Graphs depict how Cnn's growth rate **(i)**, initial total intensity **(ii)**, and peak total intensity **(iii)** change with increasing expression levels. At low concentrations all parameters scale in a near-linear fashion (*red* lines) but seem to saturate at very high concentrations, which suggests that Cnn scaffold formation follows Michaelis-Menton kinetics (*blue* lines). Regression curves were modelled in Prism. Data are presented as mean±SD. Centrosomal growth dynamics were measured, and western blot and graphs generated by Siu-Shing Wong.

growth dynamics in nuclear cycle 12. In these experiments Siu-Shing Wong and I used embryos from the same cages of flies: he would measure centrosomal Cnn dynamics, while I would measure the protein concentration.

We performed this experiment with five different lines (**Figure 6-7B**), all of which expressed a Cnn-fusion protein at different concentrations in a *cnn*$^{-/-}$ mutant background (where relevant) so that the only Cnn protein present in the embryo in these experiments was the fusion-protein. The concentration I measured in each line is shown in brackets:

1x mNG-eCnn (CRISPR/Cas9 knock-in) (~16 nM), **2x mNG-eCnn** (~29 nM), **1x Ubq-GFP-Cnn** (P-element transgene) (~62 nM), **2x Ubq-GFP-Cnn** (~91 nM), **4x Ubq-GFP-Cnn** (~236 nM). To account for varying fluorophore brightness between mNG and GFP, we applied a scaling factor derived from the comparison of the centrosomal brightness of 1x Ubq-mNG-Cnn and 1x Ubq-GFP-Cnn.

When we plotted [Cnn] against *CnnGROWTH* at nuclear cycle 12 there was a near-linear correlation in the lower concentration range of 16 nM-91 nM (*red* line, **Figure 6-7Ci**). This was also true when we plotted how [Cnn] influenced the initial and peak amount of Cnn recruited to the centrosomes during cycle 12 (*red* lines, **Figure 6-7Cii+iii**). This data shows that centrosomes do indeed sequester increasing amounts of Cnn as [Cnn] increases and, in this concentration range, there is a near linear response between [Cnn] and the rate and amount of Cnn recruitment to the centrosome.

Importantly, the concentration of the endogenous Cnn protein is most similar to the 1x Ubq-mNG-Cnn line characterised in **Figure 6-6Aiii**, and this drops from ~83 nM at cycle 11 to ~48 nM at cycle 14 (**Figure 6-6Aiii**). This is within the linear response range we measured here (16-91 nM, **Figure 6-7**), indicating that the drop in [Cnn] at each cycle is almost certain to contribute to the concomitant drop in *CnnGROWTH*. Interestingly, however, the slope of the line in **Figure 6-7Ci** (measuring how sensitive *CnnGROWTH* is to changes in [Cnn] during cycle 12) was ~1.35 whereas the slope in **Figure 6-6Ciii** (measuring how sensitive *CnnGROWTH* was to changes in [Cnn] at the start of nuclear cycles 11-13) was ~1.79. This suggests that the drop in [Cnn] at the start of each successive nuclear cycle may only partially explain the drop in *CnnGROWTH* at successive cycles.

From our analysis it was also clear that Cnn scaffold assembly saturates at very high Cnn concentrations and increasing [Cnn] from ~91 nM to ~236 nM only slightly increased *CnnGROWTH* and the amount of Cnn recruited to the centrosomes (**Figure 6-7**). Thus, Cnn scaffold assembly appears to follow typical Michaelis-Menton kinetics where the reaction kinetics are strongly influenced by the concentration of the reactants at relatively low concentrations, but the system becomes saturated and therefore insensitive to concentration changes at high concentrations. It is interesting to note that *CnnGROWTH* appears to be zero at a [Cnn] of ~16 nM. This does not mean that Cnn molecules are no longer incorporating into the PCM at this concentration, but rather that any incorporation in the central regions (*CnnIN*) is precisely balanced by loss at the periphery (*CnnOUT*).

6.2.8 [Spd-2] influences its incorporation dynamics at the centrosome

As Spd-2 also exhibited a stepwise decrease in its cytoplasmic concentration between nuclear cycles 11-14 (**Figure 6-5iii**), Siu-Shing Wong and I again collaborated to test if, like Cnn, this played a part in reducing Spd-2's growth rate during these cycles. We performed a similar set of experiments to those described for Cnn and came to a similar conclusion: (1) The drop in [Spd-2] at successive cycles is proportional to the amount of Spd-2 in the cytoplasm (**Figure 6-8A**); (2) The drop in [Spd-2] at successive cycles is correlated with a decrease in *Spd-2IN* and *Spd-2GROWTH* (**Figure 6-8B+C**); (3) During nuclear cycle 12, changes in [Spd-2] within the range of ~60-200 nM are correlated with a near-linear response in *Spd-2GROWTH* and in the amount of Spd-2 recruited to centrosomes (**Figure 6-9**). Importantly, this concentration range is within that which we observed during nuclear cycles 11-14 (~127 nM at the start of cycle 11 and ~80 nM at the start of cycle 14) in embryos expressing two copies of endogenously tagged eSpd-2-mNG that is expressed

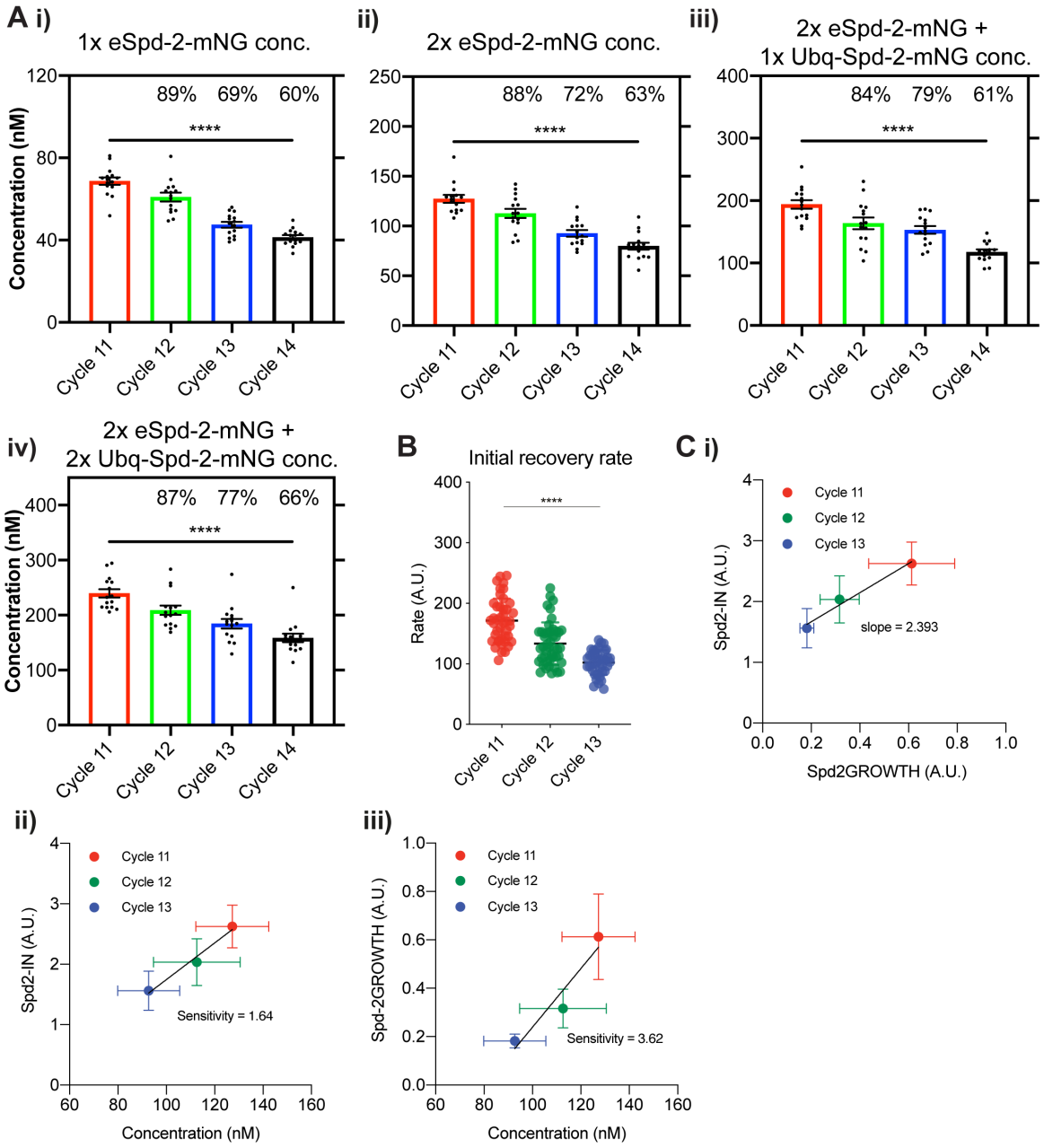


Figure 6-8: The stepwise drop in [Spd-2] is insensitive to changes in its expression levels and might be responsible for Spd-2's decreased growth rate over cycles

(A) Bar graphs quantify the cytoplasmic concentration (mean±SEM) of 1x eSpd-2-mNG **(i)**, 2x eSpd-2-mNG **(ii)**, 3x (2x eSpd-2-mNG + 1x Ubq-Spd-2-mNG) **(iii)**, and 4x (2x eSpd-2-mNG + 2x Ubq-Spd-2-mNG) **(iv)** at the beginning of S-phase between nuclear cycles 11-14. Each data point represents the average of 4-6x 10-second-long recordings. Statistical significance was assessed using an ordinary one-way ANOVA test (for Gaussian-distributed data) or a Kruskal-Wallis test (****, P<0.0001). **(B)** Graph depicts the initial recovery rate (mean±SD) of 2x eSpd-2-mNG (within 30 seconds) from FRAP measurements of individual centrosomes. Statistical significance was assessed using an ordinary one-way ANOVA test (****, P<0.0001). **(C)** Graphs show the correlation between Spd-2's incorporation rate *(Spd-2IN)* and Spd-2's total growth rate *(Spd-2GROWTH)* **(i)**, *Spd-2IN* and [Spd-2] (**ii**), and *Spd-2GROWTH* and [Spd-2] (**iii**) at the beginning of nuclear cycles 11-13. The sensitivity for Cii+iii was calculated using the mid-point method and the slope was extracted from a linear regression model in Prism (by Siu-Shing Wong). Data are presented as mean±SD. Centrosomal incorporation and growth dynamics were measured, and correlation graphs generated by Siu-Shing Wong.

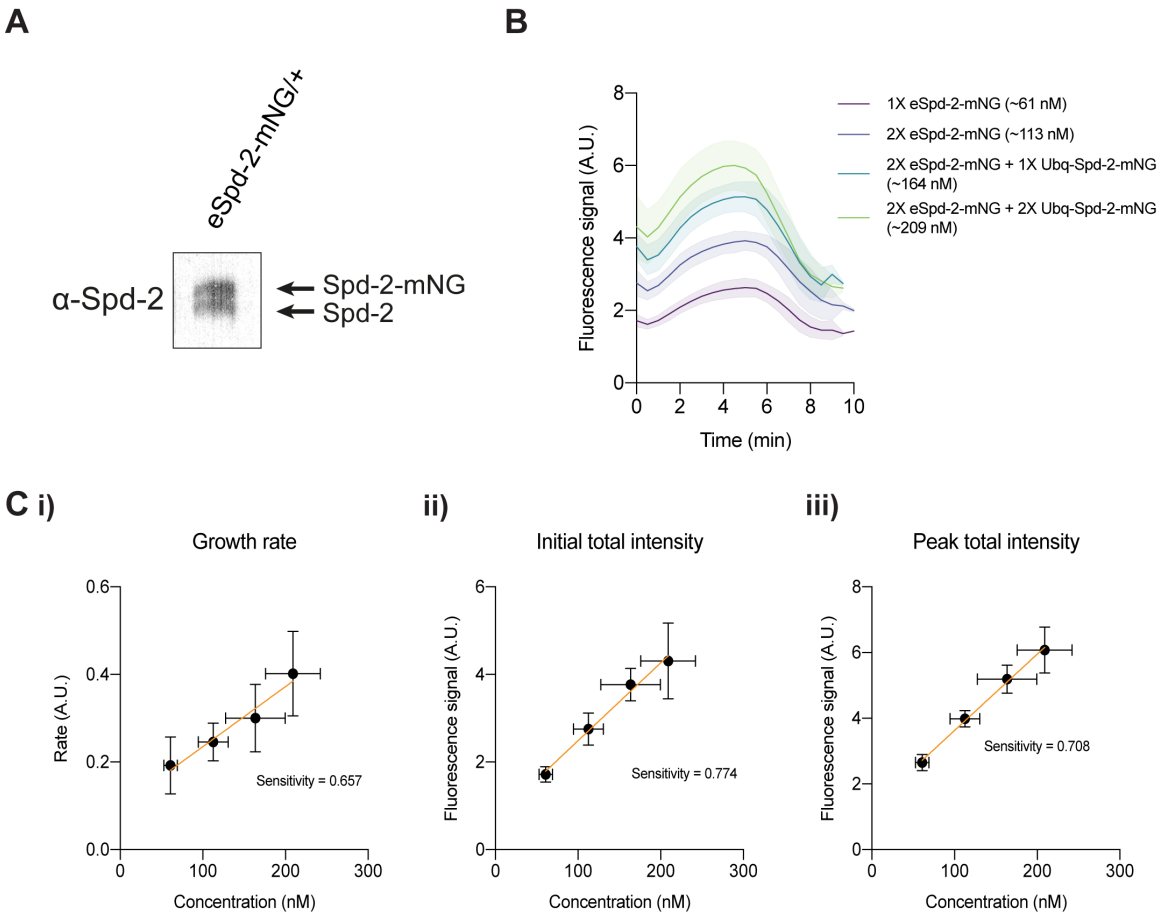


Figure 6-9: The centrosomal Spd-2 growth dynamics are sensitive to cytoplasmic concentration changes
(A) Western blot analysis of embryos from heterozygous mothers expressing one copy of endogenously mNG-tagged and one copy of endogenous untagged Spd-2. **(B)** Graph shows the mean±SD growth dynamics of Spd-2-mNG at different expression levels (as measured by FCS at the beginning of S-phase) during nuclear cycle 12. N>10 embryos for each genotype. **(C)** Graphs depict how Spd-2's growth rate **(i)**, initial total intensity **(ii)**, and peak total intensity **(iii)** change with increasing expression levels. In all measured concentrations the incorporation parameters scale in a near-linear fashion. The sensitivity was calculated using the mid-point method and the linear regression model was fitted in Prism (by Siu-Shing Wong). Data are presented as mean±SD. Centrosomal growth dynamics were measured, and western blot and graphs generated by Siu-Shing Wong.

at similar levels to the endogenous protein (**Figure 6-9A**). We also considered the sensitivity of the Spd-2 growth rate to [Spd-2], which during nuclear cycle 12 was ~0.66 (**Figure 6-9Ci**), meaning that halving [Spd-2] was correlated with a ~0.66-fold decrease in *Spd-2GROWTH*. In contrast, during nuclear cycles 11-13 the drop in [Spd-2] from ~127 nM to ~93 nM (a ~27% decrease) was correlated with a ~3-4-fold decrease in *Spd-2GROWTH*. This suggests that although the drop in Spd-2 concentration between cycles 11-14 is likely to contribute to the concomitant decrease in *Spd-2GROWTH*, it is unlikely to entirely

explain it—and this sensitivity analysis would suggest that it may only make a minor contribution to it.

While Cnn's growth parameters plateaued at very high cytoplasmic expression levels (**Figure 6-7C**), Spd-2 did not show such a saturation (**Figure 6-9C**). However, we only tested conditions where we halved or doubled Spd-2's near-endogenous concentration (between ~61-209 nM). In comparison, Cnn was examined in a broader concentration range (between ~16-236 nM), in which Cnn was overexpressed by ~3.8-fold. We suspect that Spd-2's incorporation dynamics would also reach a saturation point if Spd-2 was expressed at even higher levels.

6.2.9 The centrosomal sequestration of Cnn and Spd-2 is not responsible for the decrease in their cytoplasmic concentration at successive nuclear cycles

These findings suggest that the decrease in [Cnn] and [Spd-2] at the start of nuclear cycles 11-13 (**Figure 6-5**) is likely to, at least partially, contribute to the concomitant slowing of their centrosomal growth rates (**Figure 6-4B**), but they do not explain *why* the cytoplasmic concentrations of both proteins falls. *A priori*, I had assumed that this decreasing concentration was likely to be caused by the increasing sequestration of these proteins at centrosomes due to the doubling of centrosome numbers after each nuclear division, but I had no evidence that this was the case. In **Chapter 3** and **Chapter 4** I showed that I could use FCS to follow how the concentration of a protein changed during nuclear cycle 12 and that the concentration of inert mNG and dNG controls (**Figure 3-9B**) and of most of the core centriole assembly proteins (**Figure 4-4**) did not change significantly as the centrioles were being assembled in S-phase. I applied this methodology to examine the behaviour of the PCM scaffold proteins, as I was interested to see if I could detect their cytoplasmic pools being depleted during S-phase as the centrosome scaffold assembles (**Figure 6-10**).

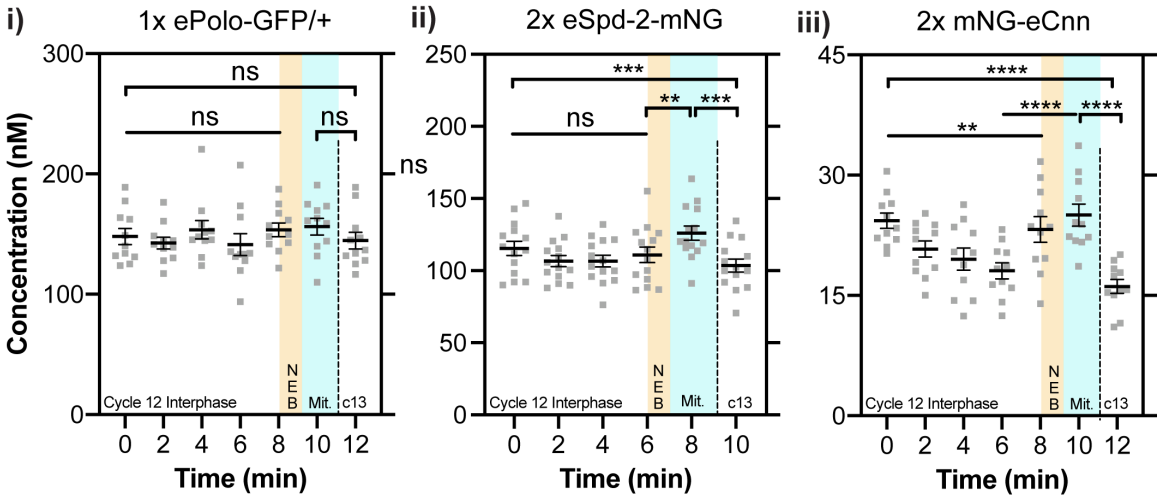


Figure 6-10: [Spd-2] and [Cnn] increase at the beginning of mitosis, but exhibit a significant drop at the end of mitosis

Graphs show cytoplasmic FCS concentration measurements (mean±SEM) of ePolo-GFP/+ **(i)**, eSpd-2-mNG **(ii)**, and mNG-eCnn **(iii)** every two minutes from the start of nuclear cycle 12-13. The estimated NEB timing is depicted in *yellow*, mitosis in *green*. Each data point represents the average of 4-6x 10-second-long recordings. Statistical significance for was assessed using a paired one-way ANOVA test (for Gaussian-distributed data) or a Friedman test (**, P<0.01; ns, not significant) for the comparison of multiple timepoints, and a paired t-test (****, P<0.0001; ***, P<0.001; ns, not significant) for the comparison of two timepoints.

ePolo-GFP levels are relatively high in the embryo and the protein showed no significant cytoplasmic depletion during nuclear cycle 12, so its cytoplasmic concentration at the start of cycle 12 was the same at the start of cycle 13 (**Figure 6-10i**) (as I had observed previously—**Figure 6-5i**). I also detected no significant cytoplasmic depletion of eSpd-2-mNG during S-phase (**Figure 6-10ii**), suggesting either that the incorporation of Spd-2 into centrosomes does not significantly deplete the cytoplasmic pool, or that any depletion is compensated for by the synthesis of new protein in the cytoplasm. I also noticed that [Spd-2] appeared to significantly increase during mitosis, and then to fall at the end of mitosis, so that at the start of cycle 13 its concentration was significantly lower than at the start of cycle 12 (as I had observed previously—**Figure 6-5iii**). In contrast, I observed a significant decrease in mNG-eCnn levels during S-phase (**Figure 6-10iii**), consistent with the idea that its cytoplasmic pool is being depleted as it is gradually sequestered by the assembling centrosomes. Surprisingly, however, cytoplasmic levels

started to significantly rise again as the embryos entered mitosis, before falling again at the end of mitosis so that at the start of cycle 13 its concentration was significantly lower than at the start of cycle 12 (as I had observed previously—**Figure 6-5ii**).

From these results I conclude that I can detect the depletion of mNG-eCnn from the cytoplasm during S-phase, and that this is presumably because it is being sequestered at the assembling centrosomes in S-phase. Most unexpectedly, however, this sequestration does not appear to be responsible for the drop in [Cnn] that I observe at the start of successive nuclear cycles. Although [Cnn] falls initially as the centrosomes assemble, it starts to rise again in late S-phase and mitosis, even though Cnn levels at the centrosome have largely plateaued at this stage (so there is no net flow of Cnn molecules back into the cytoplasm from molecules being released from the centrosome). This suggests that Cnn is being continuously synthesised in the cytoplasm to replace the sequestered protein. Thus, although the sequestration of Cnn at the assembling centrosomes does appear to transiently deplete the cytoplasmic pool, this phenomenon cannot explain the drop in its cytoplasmic concentration that I observe at successive cycles. Rather, this decrease appears to be explained by the rapid drop in Cnn levels that occurs at the end of mitosis.

I suspect that eSpd-2-mNG is actually behaving in a very similar manner to Cnn, but that this is harder to appreciate because Spd-2 is expressed at higher levels in this analysis (~100-120 nM) than Cnn (~15-25nM), so subtle changes in [Spd-2] might be harder to detect. Even if this is not the case, however, it is clear from my data that any sequestration of Spd-2 at centrosomes cannot be responsible for the drop in its cytoplasmic

concentration at successive nuclear cycles. Rather, its cytoplasmic concentration drops rapidly at the end of mitosis, as I observed for Cnn.

6.2.10 The centrosomal recruitment of Cnn and Spd-2 may target them for destruction in the cytoplasm at the end of mitosis

To explain these observations, we hypothesised that the fractions of Cnn and Spd-2 that flux through the centrosome during each nuclear cycle might be targeted for destruction in the cytoplasm at the end of mitosis. In such a scenario, the Cnn and Spd-2 molecules recruited to the PCM would be modified in some way that persists even after the proteins have left the PCM. This modification would then target the proteins for subsequent degradation in the cytoplasm at the end of mitosis. Importantly, such a mechanism would still link the amount of protein removed from the cytoplasm at each cycle to the number of centrosomes present and to the concentration of each protein in the cytoplasm—as more protein would cycle through the centrosomes if the cytoplasmic concentration is higher, as I observe (**Figure 6-6A** and **Figure 6-8A**). If this hypothesis is correct, we would predict that mutant forms of Cnn or Spd-2 that are not efficiently recruited to centrosomes, would not be degraded efficiently at the end of mitosis, and so their cytoplasmic concentration would no longer be reduced at successive nuclear cycles.

To test this possibility, I measured the cytoplasmic concentration at the start of nuclear cycles 11-14 of truncated versions of Cnn and Spd-2 that do not localise efficiently to the centrosome. For Cnn, the deletion of the conserved C-terminal 68aa (CM2) domain drastically reduces the recruitment of Cnn to centrosomes, while the deletion of a 54a central leucine-zipper region (LZ) has a weaker effect on Cnn recruitment as it does not prevent the centrosomal recruitment of Cnn, but severely perturbs its ability to assemble into a scaffold (Conduit, Feng, *et al.*, 2014; Feng *et al.*, 2017). I used already available

transgenic lines expressing GFP-fusions of either the WT or individual mutant proteins expressed from the Ubq promoter (**Figure 6-11A**). Encouragingly, while the WT Ubq-GFP-Cnn protein recapitulated the significant drop in protein concentration between nuclear cycles 11-14 that I had observed previously (**Figure 6-11Ai**), Ubq-GFP-Cnn(ΔLZ) was present at slightly higher concentrations than the WT protein at cycle 11 (~160 nM vs ~120 nM, respectively), and its concentration actually increased at successive cycles, reaching ~210 nM by the start of cycle 14 (**Figure 6-11Aii**—note the different scales between the graphs in this Figure). Ubq-GFP-Cnn(ΔCM2) was present at an even higher concentration at the start of cycle 11 (~300 nM), although its concentration appeared to remain constant at successive cycles (**Figure 6-11Aiii**). These findings are broadly consistent with my hypothesis that recruiting Cnn to centrosomes helps to target it for destruction in the cytoplasm.

Mutations that effect the recruitment of Spd-2 to centrosomes are less well characterised, but unpublished data from Alan Wainman in the lab has shown that deleting an internal 108aa **A**spM-**S**pd-2-**H**ydin (ASH1) domain severely perturbs centrosomal recruitment. Again, I showed that the WT Ubq-Spd-2-GFP protein recapitulated the significant drop in protein concentration between nuclear cycles 11-14 that I had observed previously (**Figure 6-11Bi**). In contrast, the Ubq-Spd-2(ΔASH1)-GFP mutant protein was present at slightly lower levels than the WT protein at cycle 11 (~22 nM vs ~33 nM, respectively), but its levels remained constant between the four nuclear cycles (**Figure 6-11Bii**). This result is harder to interpret, but one possibility is that Spd-2(ΔASH1) is intrinsically less stable than the WT protein (so it is degraded at a higher "background" rate, explaining why it is initially present at a lower concentration), but it is also not specifically targeted for

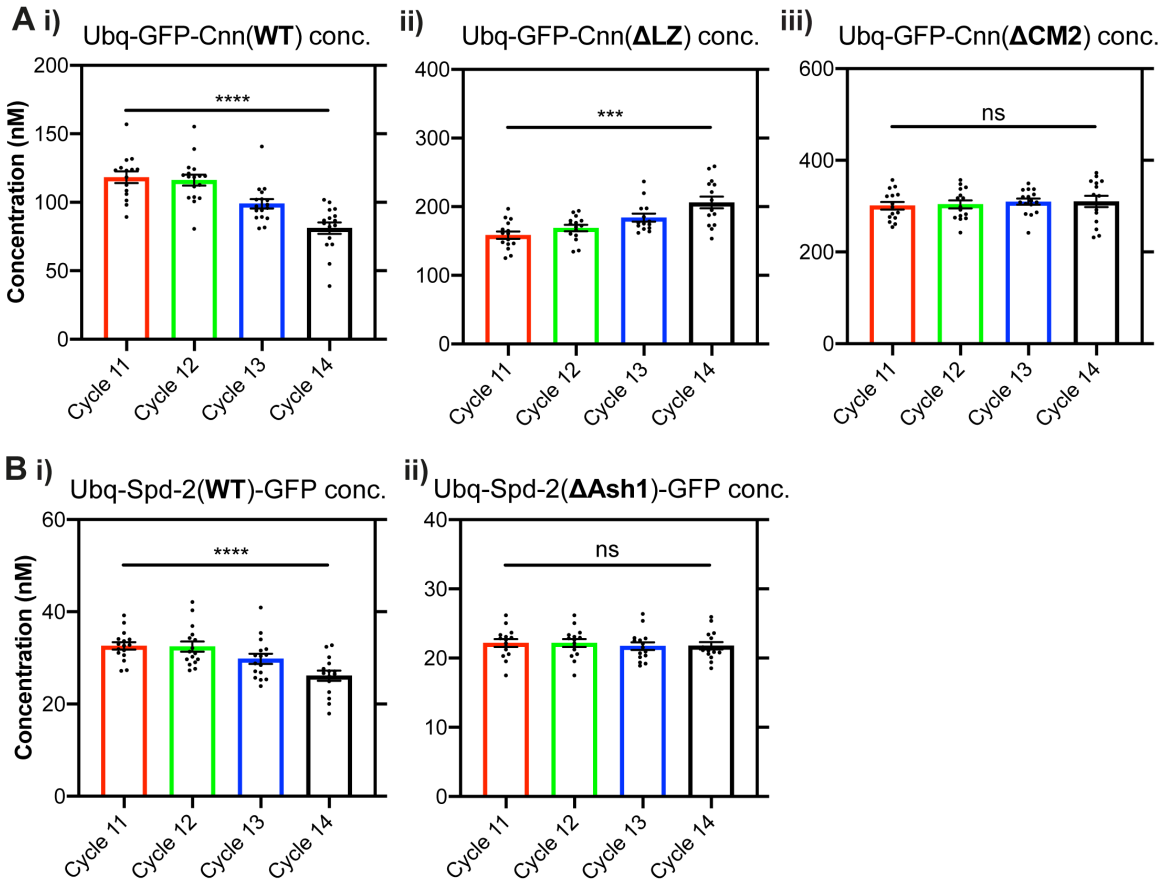


Figure 6-11: Truncated forms of Cnn and Spd-2 that show very little centrosomal localisation do not exhibit a stepwise drop in cytoplasmic concentrations between nuclear cycles 11-14
Bar graphs quantify the cytoplasmic concentration (mean±SEM) of Ubq-GFP-Cnn(WT) **(Ai)**, Ubq-GFP-Cnn(ΔLZ) **(Aii)**, Ubq-GFP-Cnn(ΔCM2) **(Aiii)**, Ubq-Spd-2(WT)-GFP **(Bi)**, and Ubq-Spd-2(ΔAsh1)-GFP **(Bii)** at the beginning of S-phase in nuclear cycles 11-14. Each data point represents the average of 4-6x 10-second-long recordings. Statistical significance was assessed using an ordinary one-way ANOVA test (for Gaussian-distributed data) or a Kruskal-Wallis test (****, P<0.0001; ***, P<0.001; ns, not significant).

destruction by the "centrosomal" pathway. Thus, its concentration in the embryo remains relatively constant no matter how many centrosomes are present in the embryo.

6.3 Discussion

6.3.1 Centrosome size is homeostatically regulated in the early *Drosophila* embryo

In this chapter, I collaborated with Siu-Shing Wong to work towards understanding how centrosome size is regulated in the early *Drosophila* embryo. First, we examined the recruitment dynamics of several PCM client proteins and identified that centrosomes grew to a similar size over the successive nuclear cycles 11-13 (despite a doubling in

centrosome number with every cycle). This contrasts with the centrosome size regulation in the *C. elegans* embryo, where centrosomes halve in size after every cell division (Decker *et al.*, 2011). I note that the cytoplasmic concentration of SPD-2 was not measured in the *C. elegans* experiments, so it will be important to confirm that SPD-2 is really being depleted from the cytoplasm due to its sequestration at the centrosome. My experiments in fly embryos suggest that although such depletion seems intuitive, it may not occur to the extent that one might expect. It is unclear why centrosome size seems to be regulated in fundamentally different ways in these two systems, particularly as PCM expansion in both *Drosophila* and *C. elegans* embryos uses a similar set of conserved core proteins. I suspect that these similar systems are simply regulated slightly differently to ensure that centrosomes halve in size at each division in the worm embryo, but remain at a relatively constant size after each nuclear cycle in the fly embryo.

We observed that centrosome size is regulated in a homeostatic manner in the *Drosophila* embryo. When centrosomes grew faster (in the earlier cycles) they grew for a shorter period, when they grew slower (in the later cycles) they grew for a longer period, so that they ultimately reached a similar size. Importantly, the cytoplasmic concentration of all measured client proteins remained relatively constant between these early nuclear cycles. This demonstrates that the observed reduction in PCM client growth rate at successive cycles is not a consequence of their cytoplasmic depletion.

6.3.2 [Cnn] and [Spd-2] decrease between nuclear cycles 11-14 and influence their incorporation rate at the centrosome

We also identified that the underlying scaffold-forming proteins, Polo, Spd-2 and Cnn, behave differently to the client proteins, both at the centrosome and in the cytoplasm. While Polo and Spd-2 were recruited to the assembly site in a similar oscillatory manner

to the PCM client proteins, Cnn was incorporated in a near-linear fashion and then plateaued (even after Polo and Spd-2 levels started declining). These recruitment dynamics show a certain similarity to centriole biogenesis as in both processes a local centriolar oscillation in a regulating kinase (Polo/Plk4) leads to the linear increase of an organelle size-defining component (Cnn/Sas-6) (Aydogan *et al.*, 2018, 2020). This suggests the exciting possibility that the mechanism of a localised organelle-specific oscillation that times and executes the organelle's biogenesis might also be present at other cellular structures to control their size.

Cnn and Spd-2 show a stepwise drop in cytoplasmic concentration between nuclear cycles 11-14 while the levels of all measured PCM client proteins and Polo remained relatively constant. Interestingly, [Cnn] and [Spd-2] exhibited a strong near-linear correlation with their incorporation rates at the centrosome (**Figure 6-6C** and **Figure 6-8C**), suggesting that their cytoplasmic abundance can influence their growth rate. It is unclear why in centriole duplication the cytoplasmic levels of the master regulator Plk4 decrease over cycles and the centriolar cartwheel proteins remain constant (Sas-6 and Ana2) while in centrosome maturation Polo levels (which acts as the driver of PCM expansion) remain constant and the structural scaffold proteins decrease (Cnn and Spd-2). As Plk4 is extremely low abundant in the cytoplasm and only localises to the centriole, it seems energetically favourable for the embryo to only adjust its Plk4 levels to influence the centriole growth dynamics. Polo, in contrast, is highly abundant in the embryo and is involved in many cellular processes. Therefore, it seems reasonable that the embryo instead adapts the abundance of the two scaffold-forming proteins that are restricted to the centrosome, to control the centrosome growth dynamics over successive nuclear cycles.

6.3.3 Centrosomal Spd-2 might be limiting for Cnn recruitment

To directly test the potential causality between the linear relationship of [Cnn] and [Spd-2] and the growth rate of their centrosomal scaffolds, Siu-Shing Wong and I measured the growth dynamics and cytoplasmic concentrations of both proteins in nuclear cycle 12 over a wide range of expression levels (~16-236 nM for Cnn, ~61-209 nM for Spd-2). For both proteins, we observed a near-linear relationship between their cytoplasmic abundance and centrosomal growth rate in low and moderate overexpression levels (**Figure 6-7C** and **Figure 6-9C**). For Cnn, however, we observed a saturation of its growth rate when we significantly overexpressed its cytoplasmic concentration (~3.8-fold) (**Figure 6-7C**). This indicates that some component at the centrosome must be limiting for Cnn's incorporation/growth rate. In our proposed molecular model, which leads to the positive feedback loop that drives the drastic expansion of the mitotic PCM (Conduit, Richens, *et al.*, 2014; Alvarez-Rodrigo *et al.*, 2019), Cnn is recruited to the centrosome by Spd-2, and the presence of the Cnn scaffold in turn leads to the stabilisation of Spd-2 at the centrosome which recruits even more Cnn (**Figure 6-1B**). Ultimately, as Spd-2 is recruited to the centrosome by the centriole (Dix and Raff, 2007; Klebba *et al.*, 2015), there might simply not be any more Spd-2 present at the assembly site to allow any extra Cnn to accumulate. It will be interesting to test how different dosages of Cnn and Spd-2 can not only affect the growth rate of their own centrosomal scaffold, but also how they can influence each other's incorporation rates.

6.3.4 Cnn and Spd-2 might be targeted for degradation at the end of mitosis

My investigation of [Cnn] and [Spd-2] throughout an entire nuclear cycle revealed that the stepwise reduction in cytoplasmic levels at successive cycles was not caused by the gradual sequestration of the proteins at the assembling centrosomes, but rather through

a sudden drop in their concentration that occurred between the end of mitosis and the beginning of the following S-phase (**Figure 6-10**). This suggested that the concertation drop could be generated through targeted degradation of the fractions of the Cnn and Spd-2 proteins that have cycled through the centrosome.

In support of this possibility, I showed that truncated versions of Cnn and Spd-2 that showed very little localisation at the centrosome, did not exhibit the cytoplasmic depletion between nuclear cycles 11-14 (**Figure 6-11**). Interestingly, however, the two truncated versions of Cnn that I measured between nuclear cycles 11-14 behaved differently: [Cnn(ΔCM2)] remained relatively constant between cycles, but [Cnn(ΔLZ)] kept increasing over successive cycles (**Figure 6-11Aii+iii**). The increase in [Cnn] that I observed during mitosis of nuclear cycles 12 indicates that Cnn is being actively translated during the early blastoderm cycles (**Figure 6-10iii**). Therefore, it seems likely that Cnn that cannot be targeted for degradation by its prior association with the centrosome will keep accumulating in the cytoplasm. This raises the question of why [Cnn(ΔCM2)] remained constant at successive cycles. I note that Ubq-GFP-Cnn(ΔCM2) was expressed at higher levels (~300 nM) than Ubq-GFP-Cnn(ΔLZ) (~160-210 nM) and WT Ubq-GFP-Cnn (~81-118). Thus, I suspect that by nuclear cycle 11, Cnn(ΔCM2) may have reached a steady-state concentration where a "background" level of degradation in the cytoplasm is balanced by new protein synthesis.

Finally, as was the case with Plk4 and the centriole, the putative centrosomal targeting of Cnn and/or Spd-2 for degradation at the end of mitosis could provide the embryo with a mechanism to effectively "count" its centrosomes and to adapt its PCM assembly dynamics accordingly. As discussed in **Chapter 5**, many aspects of embryo development

gradually slow during nuclear cycles 11-13, and it is not clear how all of these events are coordinated. The gradual depletion of Plk4 and Spd-2/Cnn in response to the increasing number of centrosomes would provide an attractive mechanism that would allow embryos to slow their centriole and centrosome growth kinetics.

7 Discussion

How cells control the number and size of their cell organelles is still largely unclear (Marshall, 2016). In order to dynamically characterise organelle biogenesis, it is common practise to measure the intensity changes of the fluorescently labelled building blocks at the organelle over time. In this thesis, I have shown that it is not sufficient to just focus on the incorporation dynamics at the organelle (in my case centrioles and centrosomes), but that it is also necessary to characterise the cytoplasmic pool of the individual building blocks to further understand how their recruitment to the forming organelle is controlled. I developed/optimised spectroscopy techniques (**Chapter 3**) to provide an initial systematic characterisation of the cytoplasmic pool of the core centriole and centrosome proteins during the early blastoderm cycles of the *Drosophila* embryo (**Chapters 4-6**). Surprisingly, I have identified quite a variability in how certain proteins behave during centriole and centrosome assembly.

7.1 The cytoplasmic concentration of Plk4, Cnn, and Spd-2 decreases between nuclear cycles 11-14

The nuclear cycles 11-14 in the early *Drosophila* embryo display a unique framework to study the question of how centriole and centrosome assembly is regulated as the number of organelles increases exponentially with every division, and the embryo experiences a natural slowing of its cell cycle (Foe and Alberts, 1983). Mustafa Aydogan (**Figure 5-1**), Aydogan *et al.*, 2018) and Siu-Shing Wong (**Figure 6-4**) showed that the growth rate of both organelles slows over successive cycles, but that their growth dynamics are homeostatically regulated, so that centrioles and centrosomes grow to a similar size in every cycle. Strikingly, I have identified that the slowing in growth rate of both organelles

is—at least partially—caused by the cytoplasmic reduction of certain key proteins while others (rather surprisingly) remain relatively constant (**Figure 5-4Figure 5-6, Figure** 6-3**Figure 6-5**). For centriole assembly the master regulator Plk4 and for PCM scaffold formation the structural proteins Cnn and Spd-2 exhibit a stepwise drop in cytoplasmic concentration between nuclear cycles 11-14, which in turn leads to their reduced incorporation at the assembly sites.

While FCS and PeCoS allowed me to determine the cytoplasmic concentration of the core centriole and centrosome proteins, I do not know how their cytoplasmic abundance is generated or maintained. It will be very interesting to identify the underlying regulatory mechanisms that allow the cytoplasmic concentration of some proteins to remain relatively constant (despite twice the amount of material being sequestered to the assembly sites with every cycle) while others show a stepwise decrease over cycles. Protein synthesis to replenish the depleted cytoplasmic pool and targeted degradation to restrict the total amount of protein in the embryo could influence the cytoplasmic levels.

While transcription in the early *Drosophila* embryo is mostly inhibited until nuclear cycle 14, maternally supplied mRNA can be translated during the blastoderm cycles (Farrell and O'Farrell, 2014). The increase in the cytoplasmic concentration that I observed for some centriole and centrosome proteins at the beginning of mitosis suggests that new building blocks are indeed being constantly synthesised. In support of this assumption, a ribosome profiling study showed that many centriole and centrosome proteins are actively translated in the early *Drosophila* embryo (Kronja *et al.*, 2014). Data mining allowed me to extract the mRNA levels, ribosome footprint densities, and translation efficiencies (a value that takes both mRNA abundance and footprint density into account

to reveal translational regulation) of all centriole and centrosome proteins that I characterised in this thesis with exception of Spd-2, which was not present in these data sources (**Figure 7-1**). Counter-intuitively, Plk4 and Cnn, which both exhibit a significant drop in cytoplasmic levels between nuclear cycles 11-14, showed a stronger translation efficiency than most other centriole and centrosome proteins (**Figure 7-1iii**). Most core centriole proteins, and in particular Plk4, are present at very low levels in the cytoplasm, but they need to be recruited to the centriole assembly site during only a very short period of time (~3-4 minutes) to form a new centriole. I wondered, therefore, whether centriolar building blocks might be locally translated at the centrosome. Several mRNAs are concentrated around the centrosomes and/or spindle poles in these embryos (Lécuyer *et al.*, 2007), and such a local translation mechanism has previously been reported for the PCM protein PCNT (pericentrin) in the zebrafish embryo (Sepulveda *et al.*, 2018). In order to address this question, I designed smFISH probes against the mRNA sequences of the centriole proteins Plk4, Sas-6, and Ana2, but did not observe an accumulation of mRNA molecules around the centrosome (**Appendix E**).

Whilst protein translation might replenish the depleted cytoplasmic pool, targeted degradation might allow the embryo to limit the total amount of protein that is present in the cell, which—alternatively or additionally to the sequestration to the centriole/ centrosome—could explain the stepwise drop in Plk4, Cnn, and Spd-2 levels. Intriguingly, the increased sequestration and/or degradation of cytoplasmic material to the exponentially growing number of centrioles and centrosomes could allow the embryo to "count" the number of these organelles. Through the depletion of the cytoplasmic levels of one or multiple growth-limiting building blocks, the embryo can then adapt the

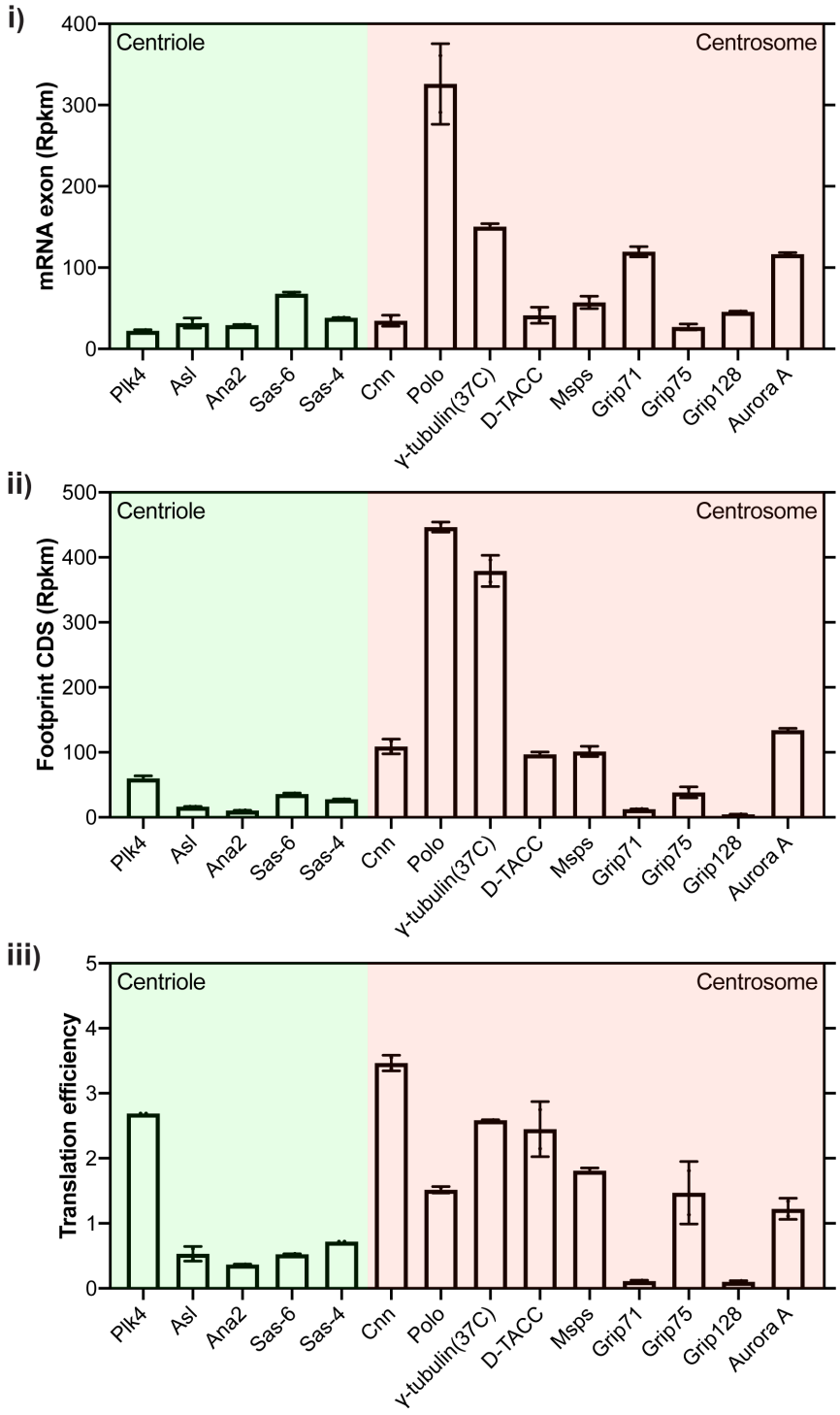


Figure 7-1: Most core centriole and centrosome proteins are actively translated during the early *Drosophila* development

Data mining from mRNA-Seq and ribosome-footprint profiling experiments of 0-2 hour-old *Drosophila* embryos (Kronja *et al.*, 2014) allowed the characterisation of the translation control of the core centriole and centrosome proteins. Graphs show the normalised mRNA CDS (coding sequence) reads **(i)**, normalised footprint density (across the entire locus) **(ii)**, and the translation efficiency (calculated as a ratio of the footprint reads to the mRNA reads) **(iii)** from two biological repeats (mean±SD). All reads were normalised to the reads per kilobase of feature length per million reads (RPKM).

growth parameters accordingly. I made several observations that support the hypothesis that those proteins that decline over cycles, might be targeted for degradation: (1) For Plk4 I showed that—although its core promoter leads to higher cytoplasmic expression levels compared to the core promoter of the cartwheel protein Sas-6 (~31 nM for p(Plk4)-mNG compared to ~15 nM for p(Sas-6)-mNG; **Figure 3-8B**)—its cytoplasmic abundance is so low that it cannot be measured with FCS. Plk4 is a suicide kinase that triggers its own degradation upon auto-activation (Guderian *et al.*, 2010; Sillibourne *et al.*, 2010; Holland *et al.*, 2012; Cunha-Ferreira *et al.*, 2013), and in collaboration with Mustafa Aydogan I identified that ePlk4-mNG is stabilised both at the centriole and in the cytoplasm if its kinase activity is reduced (**Figure 5-5**). (2) For Cnn and Spd-2, I observed a sudden drop in cytoplasmic levels between the end of mitosis and the beginning of the following S-phase (**Figure 6-10ii+iii**). As both proteins exhibit a slight lag-phase at the beginning of S-phase before their incorporation at the centrosome is initiated (**Figure 6-4**), it seems unlikely that the cytoplasmic concentration drop is exclusively generated by the sequestration to the centrosomes. (3) I identified that the cytoplasmic concentration of truncated versions of Cnn and Spd-2 does not decrease between cycles 11-14 if they cannot be recruited to the centrosome (**Figure 6-11**). In addition, both mutant forms of Cnn showed significantly higher expression levels compared to WT Ubq-GFP-Cnn. This is consistent with the possibility that only those molecules that have been incorporated into the PCM might be modified and marked for subsequent degradation.

Further experiments will be necessary to test these ideas and to understand why some proteins exhibit a cytoplasmic depletion between nuclear cycles 11-14 while others remain at relatively constant levels. Unfortunately, drug injections to inhibit either

translation or degradation do not allow measurements between multiple cycles as both alterations would lead to cell cycle arrest (Edgar, Kiehle and Schubiger, 1986; Su *et al.*, 1998). In collaboration with Siu-Shing Wong and Saroj Saurya, we are currently generating mutant forms of Plk4, Cnn, and Spd-2, where known degron motifs (Destruction and KEN boxes) are mutated so that they can no longer be targeted for degradation by the anaphase-promoting complex (APC).

7.2 Centriole duplication and centrosome maturation do not seem to be influenced by a cytoplasmic pool limitation in the *Drosophila* embryo

A powerful mechanism that was proposed for the regulation of centriole number and centrosome size is the concept of cytoplasmic pool limitation, where the cytoplasmic pool of a limiting component is gradually depleted during organelle assembly until the cytoplasmic concentration of the building block is too low to promote further growth (Goehring and Hyman, 2012). However, there is very little evidence to support this hypothesis. In human cell lines this question is especially hard to address due to the long cell cycle length and imaging limitations caused by bleaching and phototoxicity, which occur when cells are exposed to long durations of laser exposure (Douthwright and Sluder, 2017). Therefore, the *Drosophila* embryo with its short nuclear cycle length is an excellent system which allowed me to determine the cytoplasmic concentration of the core centriole and centrosome proteins during an entire nuclear cycle with high temporal resolution. Importantly, I have identified that none of the core proteins exhibit a drastic cytoplasmic drop in concentration throughout interphase when centrioles/centrosomes are being assembled. Only [Cnn] showed a more dramatic but only partial depletion of ~25% during S-phase. The common assumption in the field is that a cytoplasmic pool

limitation describes the process of a protein's cytoplasmic building blocks being "used up" to restrict organelle size. Therefore, my measurements suggest that both processes, centriole assembly and mitotic PCM expansion, are not influenced by the cytoplasmic pool limitation of one of their core building blocks. I would, however, argue that the definition of the cytoplasmic pool limitation should be amended as I have shown that the cytoplasmic concentration of a protein (Plk4, Cnn, and Spd-2) can be limiting for the growth dynamics of an organelle even if its cytoplasmic building blocks are not "used up" during the assembly process within the cycle.

It needs to be highlighted that the *Drosophila* embryo progresses through its nuclear divisions incredibly fast and needs to double its number of centrioles/centrosomes every 10-15 minutes (Foe and Alberts, 1983). Vertebrate cells, in comparison, divide significantly slower and centriole duplication takes ~10 hours (Takao *et al.*, 2019). This provides the vertebrate cell with sufficient time to influence the organelle's growth dynamics through changes in the cytoplasmic abundance of its centriolar proteins during the assembly process. It has in fact been shown that the levels of most core centriole proteins change throughout the cell cycle (Strnad *et al.*, 2007; Tang *et al.*, 2009; Guderian *et al.*, 2010; Sillibourne *et al.*, 2010; Arquint *et al.*, 2012). The fast cell cycle progression in the *Drosophila* embryo might not allow for enough time to control the cytoplasmic protein abundance within a cycle, which might be the reason for the presumably constantly elevated cytoplasmic protein concentrations throughout the early development (**Figure 4-4**). Therefore, other mechanisms must be in place to ensure that centrioles only duplicate once every nuclear division and grow to a similar size in every cycle. One such mechanism to control the timing of centriole growth might be the potential cytoplasmic

phosphorylation of Ana2 by the cell cycle regulator Cdk1 in late S-phase/mitosis to inhibit its recruitment to the centriole that I described in **Chapter 4**. Another mechanism that might restrict centriole duplication to the existing mother centriole is that both core cartwheel proteins, Sas-6 and Ana2, are kept in a lower oligomeric state in the cytoplasm (see **Chapter 5**). My stoichiometry measurements obtained by cytoplasmic FCS recordings indicate that Sas-6 is mostly monomeric and Ana2 on average dimeric in the cytoplasm whilst they require homo-dimerisation and homo-tetramerisation, respectively, for cartwheel assembly. Interestingly, my CPM measurements indicate that this might also be the case for Cnn, which is predicted to be dimeric at the centrosome (Feng *et al.*, 2017), but which appears to be mostly monomeric in the cytoplasm according to my FCS measurements (see **Appendix F**). Due to the presence of small cytoplasmic Cnn aggregates, which probably originate from the outwards fluxing of the Cnn scaffold, the measurement of Cnn's molecular brightness is not as reliable as for the other characterised proteins Sas-6 and Ana2. However, a similar observation was made for the Cnn homologue SPD-5 in *C. elegans* embryos (Wueseke *et al.*, 2014).

My findings suggest that these large embryo systems can store large amounts of their key building blocks at a relatively low concentration— as assembly is not limited by diffusion— to avoid unwanted organelle biogenesis. Thereby, proteins that require a certain concentration threshold to oligomerise and initiate organelle assembly, are kept in a lower oligomeric state in the cytoplasm. It will be interesting to test if this might also be true in normal cells, or only in these large eggs which exhibit a significantly faster cell cycle speed.

8 References

Alvarez-Rodrigo, I. *et al.* (2019) 'Evidence that a positive feedback loop drives centrosome maturation in fly embryos', *eLife*, 8, pp. 1–31. doi: 10.7554/eLife.50130.

Alvarez-Rodrigo, I. *et al.* (2021) 'Ana1 helps recruit Polo to centrioles to promote mitotic PCM assembly and centriole elongation', *Journal of Cell Science*, 134(14). doi: 10.1242/jcs.258987.

Alves-Cruzeiro, J. M. D. C., Nogales-Cadenas, R. and Pascual-Montano, A. D. (2014) 'CentrosomeDB: A new generation of the centrosomal proteins database for Human and Drosophila melanogaster', *Nucleic Acids Research*, 42(D1), pp. 430–436. doi: 10.1093/nar/gkt1126.

Arquint, C. *et al.* (2012) 'Cell-cycle-regulated expression of STIL controls centriole number in human cells', *Journal of Cell Science*, 125(5), pp. 1342–1352. doi: 10.1242/jcs.099887.

Arquint, C., Gabryjonczyk, A. M. and Nigg, E. A. (2014) 'Centrosomes as signalling centres', *Philosophical Transactions of the Royal Society B: Biological Sciences*, 369(1650). doi: 10.1098/rstb.2013.0464.

Arquint, C. and Nigg, E. A. (2014) 'STIL microcephaly mutations interfere with APC/C-mediated degradation and cause centriole amplification', *Current Biology*, 24(4), pp. 351–360. doi: 10.1016/j.cub.2013.12.016.

Arquint, C. and Nigg, E. A. (2016) 'The PLK4-STIL-SAS-6 module at the core of centriole duplication', *Biochemical Society Transactions*, 44(5), pp. 1253–1263. doi: 10.1042/BST20160116.

Avidor-Reiss, T. *et al.* (2004) 'Decoding cilia function: Defining specialized genes required for compartmentalized cilia biogenesis', *Cell*, 117(4), pp. 527–539. doi: 10.1016/S0092-8674(04)00412-X.

Aydogan, M. G. *et al.* (2018) 'A homeostatic clock sets daughter centriole size in flies', *Journal of Cell Biology*, 217(4), pp. 1233–1248. doi: 10.1083/jcb.201801014.

Aydogan, M. G. *et al.* (2020) 'An Autonomous Oscillation Times and Executes Centriole Biogenesis', *Cell*, 181(7), pp. 1566-1581.e27. doi: 10.1016/j.cell.2020.05.018.

Bacia, K. and Schwille, P. (2007) 'Practical guidelines for dual-color fluorescence cross-correlation spectroscopy', *Nature Protocols*, 2(11), pp. 2842–2856. doi: 10.1038/nprot.2007.410.

Balestra, F. R. *et al.* (2013) 'Discovering regulators of centriole biogenesis through siRNA-based functional genomics in human cells', *Developmental Cell*, 25(6), pp. 555–571. doi: 10.1016/j.devcel.2013.05.016.

Banani, S. F. *et al.* (2017) 'Biomolecular condensates: Organizers of cellular biochemistry', *Nature Reviews Molecular Cell Biology*, 18(5), pp. 285–298. doi: 10.1038/nrm.2017.7.

Barr, A. R., Kilmartin, J. V. and Gergely, F. (2010) 'CDK5RAP2 functions in centrosome to spindle pole attachment and DNA damage response', *Journal of Cell Biology*, 189(1), pp. 23–39. doi: 10.1083/jcb.200912163.

Barros, T. P. *et al.* (2005) 'Aurora A activates D-TACC-Msps complexes exclusively at centrosomes to stabilize centrosomal microtubules', *Journal of Cell Biology*, 170(7), pp. 1039–1046. doi: 10.1083/jcb.200504097.

Basto, R. *et al.* (2006) 'Flies without Centrioles', *Cell*, 125(7), pp. 1375–1386. doi: 10.1016/j.cell.2006.05.025.

Basto, R. *et al.* (2008) 'Centrosome Amplification Can Initiate Tumorigenesis in Flies', *Cell*, 133(6), pp. 1032–1042. doi: 10.1016/j.cell.2008.05.039.

Bate, M. (1993) *The Development of Drosophila melanogaster*. Woodbury, NY: Cold Spring Harbor Laboratory Press.

Bauer, M. *et al.* (2016) 'Quantitative analysis of human centrosome architecture by targeted proteomics and fluorescence imaging', *The EMBO Journal*, 35(19), pp. 2152–2166. doi: 10.15252/embj.201694462.

Baumbach, J. *et al.* (2015) 'Dissecting the Function and Assembly of Acentriolar

Microtubule Organizing Centers in Drosophila Cells In Vivo', *PLoS Genetics*, 11(5), pp. 1–22. doi: 10.1371/journal.pgen.1005261.

Bazzi, H. and Anderson, K. V. (2014) 'Acentriolar mitosis activates a p53-dependent apoptosis pathway in the mouse embryo', *Proceedings of the National Academy of Sciences of the United States of America*, 111(15). doi: 10.1073/pnas.1400568111.

Bettencourt-Dias, M. *et al.* (2005) 'SAK/PLK4 is required for centriole duplication and flagella development', *Current Biology*, 15(24), pp. 2199–2207. doi: 10.1016/j.cub.2005.11.042.

Bettencourt-Dias, M. *et al.* (2011) 'Centrosomes and cilia in human disease', *Trends in Genetics*, 27(8), pp. 307–315. doi: 10.1016/j.tig.2011.05.004.

Bicknell, L. S. *et al.* (2011) 'Mutations in ORC1, encoding the largest subunit of the origin recognition complex, cause microcephalic primordial dwarfism resembling Meier-Gorlin syndrome', *Nature Genetics*, 43(4), pp. 350–356. doi: 10.1038/ng.776.

Bindels, D. S. *et al.* (2016) 'MScarlet: A bright monomeric red fluorescent protein for cellular imaging', *Nature Methods*, 14(1), pp. 53–56. doi: 10.1038/nmeth.4074.

Bisgrove, B. W. and Yost, H. J. (2006) 'The roles of cilia in developmental disorders and disease', *Development*, 133(21), pp. 4131–4143. doi: 10.1242/dev.02595.

Bishop, A. C. *et al.* (2000) 'A chemical switch for inhibitor-sensitive alleles', *Nature*, 408(December), pp. 961–964. Available at: www.nature.com.

Blachon, S. *et al.* (2008) 'Drosophila asterless and vertebrate Cep152 are orthologs essential for centriole duplication', *Genetics*, 180(4), pp. 2081–2094. doi: 10.1534/genetics.108.095141.

Bobinnec, Y. *et al.* (1998) 'Centriole disassembly in vivo and its effect on centrosome structure and function in vertebrate cells', *Journal of Cell Biology*, 143(6), pp. 1575–1589. doi: 10.1083/jcb.143.6.1575.

Boese, C. J. *et al.* (2018) 'Asterless is a Polo-like kinase 4 substrate that both activates and

inhibits kinase activity depending on its phosphorylation state', *Molecular Biology of the Cell*, 29(23), pp. 2874–2886. doi: 10.1091/mbc.E18-07-0445.

van Breugel, M. *et al.* (2014) 'Structure of the SAS-6 cartwheel hub from Leishmania major', *eLife*, 2014(3), pp. 1–16. doi: 10.7554/eLife.01812.

Van Breugel, M. *et al.* (2011) 'Structures of SAS-6 suggest its organization in centrioles', *Science*, 331(6021), pp. 1196–1199. doi: 10.1126/science.1199325.

Brouhard, G. J. and Rice, L. M. (2018) 'Microtubule dynamics: An interplay of biochemistry and mechanics', *Nature Reviews Molecular Cell Biology*, 19(7), pp. 451–463. doi: 10.1038/s41580-018-0009-y.

Buszczak, M. *et al.* (2007) 'The carnegie protein trap library: A versatile tool for drosophila developmental studies', *Genetics*, 175(3), pp. 1505–1531. doi: 10.1534/genetics.106.065961.

Cabral, G. *et al.* (2019) 'Differential Requirements for Centrioles in Mitotic Centrosome Growth and Maintenance', *Developmental Cell*, 50(3), pp. 355-366.e6. doi: 10.1016/j.devcel.2019.06.004.

Callaini, G., Whitfield, W. G. F. and Riparbelli, M. G. (1997) 'Centriole and centrosome dynamics during the embryonic cell cycles that follow the formation of the cellular blastoderm in Drosophila', *Experimental Cell Research*, 234(1), pp. 183–190. doi: 10.1006/excr.1997.3618.

Carvalho-Santos, Z. *et al.* (2010) 'Stepwise evolution of the centriole-assembly pathway', *Journal of Cell Science*, 123(9), pp. 1414–1426. doi: 10.1242/jcs.064931.

Carvalho-Santos, Z. *et al.* (2011) 'Tracing the origins of centrioles, cilia, and flagella', *Journal of Cell Biology*, 194(2), pp. 165–175. doi: 10.1083/jcb.201011152.

Carvalho-Santos, Z. *et al.* (2012) 'BLD10/CEP135 Is a Microtubule-Associated Protein that Controls the Formation of the Flagellum Central Microtubule Pair', *Developmental Cell*, 23(2), pp. 412–424. doi: 10.1016/j.devcel.2012.06.001.

Cavalier-Smith, T. (2002) 'The phagotrophic origin of eukaryotes and phylogenetic classification on protozoa', *International Journal of Systematic and Evolutionary Microbiology*, 52(2), pp. 297–354. doi: 10.1099/00207713-52-2-297.

Chan, J. Y. (2011) 'A Clinical Overview of Centrosome Amplification in Human Cancers', *International Journal of Biological Sciences*, 7(8), pp. 1122–1144. doi: 10.7150/ijbs.7.1122.

Chan, Y. H. M. and Marshall, W. F. (2010) 'Scaling properties of cell and organelle size', *Organogenesis*, 6(2), pp. 88–96. doi: 10.4161/org.6.2.11464.

Chavali, P. L., Pütz, M. and Gergely, F. (2014) 'Small organelle, big responsibility: The role of centrosomes in development and disease', *Philosophical Transactions of the Royal Society B: Biological Sciences*, 369(1650). doi: 10.1098/rstb.2013.0468.

Chen, H. Y. *et al.* (2017) 'Human microcephaly protein RTTN interacts with STIL and is required to build full-length centrioles', *Nature Communications*, 8(1). doi: 10.1038/s41467-017-00305-0.

Choi, Y. K. *et al.* (2010) 'CDK5RAP2 stimulates microtubule nucleation by the γ-tubulin ring complex', *Journal of Cell Biology*, 191(6), pp. 1089–1095. doi: 10.1083/jcb.201007030.

Chu, J. *et al.* (2014) 'Non-invasive intravital imaging of cellular differentiation with a bright red-excitable fluorescent protein', *Nature Methods*, 11(5), pp. 572–578. doi: 10.1038/nmeth.2888.

Cizmecioglu, O. *et al.* (2010) 'Cep152 acts as a scaffold for recruitment of Plk4 and CPAP to the centrosome', *Journal of Cell Biology*, 191(4), pp. 731–739. doi: 10.1083/jcb.201007107.

Coelho, P. A. *et al.* (2015) 'Over-expression of Plk4 induces centrosome amplification, loss of primary cilia and associated tissue hyperplasia in the mouse', *Open Biology*, 5(12). doi: 10.1098/rsob.150209.

Conduit, P. T. *et al.* (2010) 'Centrioles regulate centrosome size by controlling the rate of Cnn incorporation into the PCM', *Current Biology*, 20(24), pp. 2178–2186. doi: 10.1016/j.cub.2010.11.011.

Conduit, P. T., Richens, J. H., *et al.* (2014) 'A molecular mechanism of mitotic centrosome assembly in Drosophila', *eLife*, 3(August2014), pp. 1–23. doi: 10.7554/eLife.03399.

Conduit, P. T., Feng, Z., *et al.* (2014) 'The centrosome-specific phosphorylation of Cnn by Polo/Plk1 drives Cnn scaffold assembly and centrosome maturation', *Developmental Cell*, 28(6), pp. 659–669. doi: 10.1016/j.devcel.2014.02.013.

Conduit, P. T., Wainman, A. and Raff, J. W. (2015) 'Centrosome function and assembly in animal cells', *Nature Reviews Molecular Cell Biology*, 16(10), pp. 611–624. doi: 10.1038/nrm4062.

Cottee, M. A. *et al.* (2013) 'Crystal structures of the CPAP/STIL complex reveal its role in centriole assembly and human microcephaly', *eLife*, 2013(2), pp. 1–23. doi: 10.7554/eLife.01071.

Cottee, M. A. *et al.* (2015) 'The homo-oligomerisation of both Sas-6 and Ana2 is required for efficient centriole assembly in flies', *eLife*, 4(MAY), pp. 1–65. doi: 10.7554/eLife.07236.

Cottee, M. A. *et al.* (2017) 'A key centriole assembly interaction interface between human PLK4 and STIL appears to not be conserved in flies', *Biology Open*, 6(3), pp. 381–389. doi: 10.1242/bio.024661.

Cowan, C. R. and Hyman, A. A. (2004) 'Centrosomes direct cell polarity independently of microtubule assembly in C. elegans embryos', *Nature*, 431(7004), pp. 92–96. doi: 10.1038/nature02825.

Craige, B. *et al.* (2010) 'CEP290 tethers flagellar transition zone microtubules to the membrane and regulates flagellar protein content', *Journal of Cell Biology*, 190(5), pp. 927–940. doi: 10.1083/jcb.201006105.

Cunha-Ferreira, I. *et al.* (2013) 'Regulation of autophosphorylation controls PLK4 self-destruction and centriole number', *Current Biology*, 23(22), pp. 2245–2254. doi: 10.1016/j.cub.2013.09.037.

Dammermann, A. *et al.* (2008) 'SAS-4 is recruited to a dynamic structure in newly forming centrioles that is stabilized by the γ-tubulin-mediated addition of centriolar microtubules',

Journal of Cell Biology, 180(4), pp. 771–785. doi: 10.1083/jcb.200709102.

David, A. *et al.* (2014) ' Lack of centrioles and primary cilia in STIL −/− mouse embryos ', *Cell Cycle*, 13(18), pp. 2859–2868. doi: 10.4161/15384101.2014.946830.

David, A. *et al.* (2016) 'Molecular basis of the STIL coiled coil oligomerization explains its requirement for de-novo formation of centrosomes in mammalian cells', *Scientific Reports*, 6(March), pp. 1–10. doi: 10.1038/srep24296.

Debec, A. *et al.* (1999) 'The centrosome cycle in syncytial Drosophila embryos analyzed by energy filtering transmission electron microscopy', *Biology of the Cell*, 91(4–5), pp. 379–391. doi: 10.1111/j.1768-322X.1999.tb01095.x.

Decker, M. *et al.* (2011) 'Limiting amounts of centrosome material set centrosome size in C. elegans embryos', *Current Biology*, 21(15), pp. 1259–1267. doi: 10.1016/j.cub.2011.06.002.

Delattre, M., Canard, C. and Gönczy, P. (2006) 'Sequential Protein Recruitment in C. elegans Centriole Formation', *Current Biology*, 16(18), pp. 1844–1849. doi: 10.1016/j.cub.2006.07.059.

Delattre, M. and Gönczy, P. (2004) 'The arithmetic of centrosome biogenesis', *Journal of Cell Science*, 117(9), pp. 1619–1629. doi: 10.1242/jcs.01128.

Deneke, V. E. *et al.* (2016) 'Waves of Cdk1 Activity in S Phase Synchronize the Cell Cycle in Drosophila Embryos', *Developmental Cell*, 38(4), pp. 399–412. doi: 10.1016/j.devcel.2016.07.023.

Dix, C. I. and Raff, J. W. (2007) 'Drosophila Spd-2 Recruits PCM to the Sperm Centriole, but Is Dispensable for Centriole Duplication', *Current Biology*, 17(20), pp. 1759–1764. doi: 10.1016/j.cub.2007.08.065.

Dobbelaere, J. *et al.* (2008) 'A genome-wide RNAi screen to dissect centriole duplication and centrosome maturation in Drosophila', *PLoS Biology*, 6(9), pp. 1975–1990. doi: 10.1371/journal.pbio.0060224.

Douthwright, S. and Sluder, G. (2017) 'Live Cell Imaging: Assessing the Phototoxicity of 488 and 546 nm Light and Methods to Alleviate it', *Journal of Cellular Physiology*, 232(9), pp. 2461–2468. doi: 10.1002/jcp.25588.

Dumont, J. and Desai, A. (2012) 'Acentrosomal spindle assembly and chromosome segregation during oocyte meiosis', *Trends in Cell Biology*, 22(5), pp. 241–249. doi: 10.1016/j.tcb.2012.02.007.

Dunsing, V. *et al.* (2018) 'Optimal fluorescent protein tags for quantifying protein oligomerization in living cells', *Scientific Reports*, 8(1), pp. 1–12. doi: 10.1038/s41598-018-28858-0.

Dunst, S. and Tomancak, P. (2019) 'Imaging flies by fluorescence microscopy: Principles, technologies, and applications', *Genetics*, 211(1), pp. 15–34. doi: 10.1534/genetics.118.300227.

Dzhindzhev, N. S. *et al.* (2010) 'Asterless is a scaffold for the onset of centriole assembly', *Nature*, 467(7316), pp. 714–718. doi: 10.1038/nature09445.

Dzhindzhev, N. S. *et al.* (2014) 'Plk4 Phosphorylates Ana2 to Trigger Sas6 Recruitment and Procentriole Formation', *Current Biology*, 24(21), pp. 2526–2532. doi: 10.1016/j.cub.2014.08.061.

Dzhindzhev, N. S. *et al.* (2017) 'Two-step phosphorylation of Ana2 by Plk4 is required for the sequential loading of Ana2 and Sas6 to initiate procentriole formation', *Open Biology*, 7(12). doi: 10.1098/rsob.170247.

Edgar, B. A., Kiehle, C. P. and Schubiger, G. (1986) 'Cell cycle control by the nucleo-cytoplasmic ratio in early Drosophila development', *Cell*, 44(2), pp. 365–372. doi: 10.1016/0092-8674(86)90771-3.

Eigen, M. and Rigler, R. (1994) 'Sorting single molecules: Application to diagnostics and evolutionary biotechnology', *Proceedings of the National Academy of Sciences of the United States of America*, 91(13), pp. 5740–5747. doi: 10.1073/pnas.91.13.5740.

Farrell, J. A. and O'Farrell, P. H. (2014) 'From Egg to Gastrula: How the Cell Cycle Is

Remodeled During the Drosophila Mid-Blastula Transition', *Annual Review of Genetics*, 48(1), pp. 269–294. doi: 10.1146/annurev-genet-111212-133531.

Fatalska, A. *et al.* (2020) 'Interaction interface in the C-terminal parts of centriole proteins Sas6 and Ana2: Interaction interface of Sas6-Ana2', *Open Biology*, 10(11). doi: 10.1098/rsob.200221.

Feng, Z. *et al.* (2017) 'Structural Basis for Mitotic Centrosome Assembly in Flies', *Cell*, 169(6), pp. 1078-1089.e13. doi: 10.1016/j.cell.2017.05.030.

Foe, V. E. and Alberts, B. M. (1983) 'Studies of nuclear and cytoplasmic behavior during the five mitotic cycles that precede gastrulation in Drosophila embryogenesis', *Journal of Cell Science*, Vol. 61, pp. 31–70.

Fogarty, P. *et al.* (1997) 'The Drosophila grapes gene is related to checkpoint gene chk1/rad27 and is required for late syncytial division fidelity', *Current Biology*, 7(6), pp. 418–426. doi: 10.1016/S0960-9822(06)00189-8.

Fu, J. *et al.* (2016) 'Conserved molecular interactions in centriole-to-centrosome conversion', *Nature Cell Biology*, 18(1), pp. 87–99. doi: 10.1038/ncb3274.

Fu, J. and Glover, D. M. (2012) 'Structured illumination of the interface between centriole and peri-centriolar material', *Open Biology*, 2(AUG). doi: 10.1098/rsob.120104.

Fu, J., Hagan, I. M. and Glover, D. M. (2015) 'The centrosome and its duplication cycle', *Cold Spring Harbor Perspectives in Medicine*, 5(1), pp. 1–36. doi: 10.1101/cshperspect.a015800.

Galletta, B. J. *et al.* (2016) 'A centrosome interactome provides insight into organelle assembly and reveals a non-duplication role for Plk4', *Nature Communications*, 7. doi: 10.1038/ncomms12476.

Ganem, N. J., Godinho, S. A. and Pellman, D. (2009) 'A mechanism linking extra centrosomes to chromosomal instability', *Nature*, 460(7252), pp. 278–282. doi: 10.1038/nature08136.

Garcia, G., Raleigh, D. R. and Reiter, J. F. (2018) 'How the Ciliary Membrane Is Organized Inside-Out to Communicate Outside-In', *Current Biology*, 28(8), pp. R421–R434. doi: 10.1016/j.cub.2018.03.010.

Gartenmann, L. *et al.* (2017) 'A combined 3D-SIM/SMLM approach allows centriole proteins to be localized with a precision of ∼4–5 nm', *Current Biology*, 27(19), pp. R1054–R1055. doi: 10.1016/j.cub.2017.08.009.

Gartenmann, L. *et al.* (2020) 'Sas-6, Ana2 and Sas-4 self-organise into macromolecular structures that can be used to probe centriole/centrosome assembly', *Journal of Cell Science*, 133(12), pp. 1–13. doi: 10.1242/JCS.244574.

Giansanti, M. G. *et al.* (2008) 'Drosophila SPD-2 Is an Essential Centriole Component Required for PCM Recruitment and Astral-Microtubule Nucleation', *Current Biology*, 18(4), pp. 303–309. doi: 10.1016/j.cub.2008.01.058.

Gilmore, E. C. and Walsh, C. A. (2013) 'Genetic causes of microcephaly and lessons for neuronal development', *Wiley Interdisciplinary Reviews: Developmental Biology*, pp. 461–478. doi: 10.1002/wdev.89.

Gilpin, W., Bull, M. S. and Prakash, M. (2020) 'The multiscale physics of cilia and flagella', *Nature Reviews Physics*, 2(2), pp. 74–88. doi: 10.1038/s42254-019-0129-0.

Godinho, S. A. *et al.* (2014) 'Oncogene-like induction of cellular invasion from centrosome amplification', *Nature*, 510(7503), pp. 167–171. doi: 10.1038/nature13277.

Godinho, S. A. and Pellman, D. (2014) 'Causes and consequences of centrosome abnormalities in cancer', *Philosophical Transactions of the Royal Society B: Biological Sciences*, 369(1650). doi: 10.1098/rstb.2013.0467.

Goehring, N. W. and Hyman, A. A. (2012) 'Organelle growth control through limiting pools of cytoplasmic components', *Current Biology*, 22(9), pp. R330–R339. doi: 10.1016/j.cub.2012.03.046.

Gomez-Ferreria, M. A. *et al.* (2007) 'Human Cep192 Is Required for Mitotic Centrosome and Spindle Assembly', *Current Biology*, 17(22), pp. 1960–1966. doi:

10.1016/j.cub.2007.10.019.

Gonçalves, J. and Pelletier, L. (2017) 'The ciliary transition zone: Finding the pieces and assembling the gate', *Molecules and Cells*, 40(4), pp. 243–253. doi: 10.14348/molcells.2017.0054.

Gonzalez, C., Tavosanis, G. and Mollinari, C. (1998) 'Centrosomes and microtubule organisation during Drosophila development', *Journal of Cell Science*, 111(18), pp. 2697–2706.

Goshima, G. *et al.* (2007) 'Genes required for mitotic spindle assembly in Drosophila S2 cells', *Science*, 316(5823), pp. 417–421. doi: 10.1126/science.1141314.

Gratz, S. J. *et al.* (2014) 'Highly specific and efficient CRISPR/Cas9-catalyzed homology-directed repair in Drosophila', *Genetics*, 196(4), pp. 961–971. doi: 10.1534/genetics.113.160713.

Greenan, G. A. *et al.* (2018) 'Insights into centriole geometry revealed by cryotomography of doublet and triplet centrioles', pp. 1–18.

Guderian, G. *et al.* (2010) 'Plk4 trans-autophosphorylation regulates centriole number by controlling βTrCP-mediated degradation', *Journal of Cell Science*, 123(13), pp. 2163–2169. doi: 10.1242/jcs.068502.

Guichard, P. *et al.* (2010) 'Procentriole assembly revealed by cryo-electron tomography', *EMBO Journal*, 29(9), pp. 1565–1572. doi: 10.1038/emboj.2010.45.

Guichard, P. *et al.* (2013) 'Native architecture of the centriole proximal region reveals features underlying its 9-fold radial symmetry', *Current Biology*, 23(17), pp. 1620–1628. doi: 10.1016/j.cub.2013.06.061.

Guichard, P. *et al.* (2017) 'Cell-free reconstitution reveals centriole cartwheel assembly mechanisms', *Nature Communications*, 8, pp. 1–9. doi: 10.1038/ncomms14813.

Gupta, A. and Kitagawa, D. (2018) 'Ultrastructural diversity between centrioles of eukaryotes', *Journal of Biochemistry*, 164(1), pp. 1–8. doi: 10.1093/jb/mvy031.

Habedanck, R. *et al.* (2005) 'The Polo kinase Plk4 functions in centriole duplication', *Nature Cell Biology*, 7(11), pp. 1140–1146. doi: 10.1038/ncb1320.

Hallen, M. A. *et al.* (2008) 'Fluorescence recovery kinetic analysis of γ-tubulin binding to the mitotic spindle', *Biophysical Journal*, 95(6), pp. 3048–3058. doi: 10.1529/biophysj.108.134593.

Haren, L., Stearns, T. and Lüders, J. (2009) 'Plk1-dependent recruitment of γ-tubulin complexes to mitotic centrosomes involves multiple PCM components', *PLoS ONE*, 4(6). doi: 10.1371/journal.pone.0005976.

Hatch, E. M. *et al.* (2010) 'Cep152 interacts with Plk4 and is required for centriole duplication', *Journal of Cell Biology*, 191(4), pp. 721–729. doi: 10.1083/jcb.201006049.

Hatzopoulos, G. N. *et al.* (2013) 'Structural analysis of the G-box domain of the microcephaly protein CPAP suggests a role in centriole architecture', *Structure*, 21(11), pp. 2069–2077. doi: 10.1016/j.str.2013.08.019.

Heald, R. *et al.* (1996) 'Self-organization of microtubules into bipolar spindles around artificial chromosomes in Xenopus egg extracts', *Nature*, 382(6590), pp. 420–425. doi: 10.1038/382420a0.

Hilbert, M. *et al.* (2013) 'Caenorhabditis elegans centriolar protein SAS-6 forms a spiral that is consistent with imparting a ninefold symmetry', *Proceedings of the National Academy of Sciences of the United States of America*, 110(28), pp. 11373–11378. doi: 10.1073/pnas.1302721110.

Hinchcliffe, E. H. *et al.* (1999) 'Requirement of Cdk2-cyclin E activity for repeated centrosome reproduction in xenopus egg extracts', *Science*, 283(5403), pp. 851–854. doi: 10.1126/science.283.5403.851.

Hiraki, M. *et al.* (2007) 'Bld10p Constitutes the Cartwheel-Spoke Tip and Stabilizes the 9-Fold Symmetry of the Centriole', *Current Biology*, 17(20), pp. 1778–1783. doi: 10.1016/j.cub.2007.09.021.

Hirokawa, N. *et al.* (2006) 'Nodal Flow and the Generation of Left-Right Asymmetry', *Cell*,

125(1), pp. 33–45. doi: 10.1016/j.cell.2006.03.002.

Hirono, M. (2014) 'Cartwheel assembly', *Philosophical Transactions of the Royal Society B: Biological Sciences*, 369(1650). doi: 10.1098/rstb.2013.0458.

Holland, A. J. *et al.* (2010) 'Polo-like kinase 4 kinase activity limits centrosome overduplication by autoregulating its own stability', *Journal of Cell Biology*, 188(2), pp. 191–198. doi: 10.1083/jcb.200911102.

Holland, A. J. *et al.* (2012) 'The autoregulated instability of Polo-like kinase 4 limits centrosome duplication to once per cell cycle', *Genes and Development*, 26(24), pp. 2684–2689. doi: 10.1101/gad.207027.112.

Hsu, W. Bin *et al.* (2008) 'Functional characterization of the microtubule-binding and -destabilizing domains of CPAP and d-SAS-4', *Experimental Cell Research*, 314(14), pp. 2591–2602. doi: 10.1016/j.yexcr.2008.05.012.

Huangfu, D. *et al.* (2003) 'Hedgehog signalling in the mouse requires intraflagellar transport proteins', *Nature*, 426(6962), pp. 83–87. doi: 10.1038/nature02061.

Hung, L.-Y. *et al.* (2004) 'Identification of a Novel Microtubule-destabilizing Motif in CPAP That Binds to Tubulin Heterodimers and Inhibits Microtubule Assembly', *Molecular Biology of the Cell*, 15(6), pp. 2697–2706. doi: 10.1091/mbc.e04-02-0121.

Hung, L.-Y., Tang, C.-J. C. and Tang, T. K. (2000) 'Protein 4.1 R-135 Interacts with a Novel Centrosomal Protein (CPAP) Which Is Associated with the γ-Tubulin Complex', *Molecular and Cellular Biology*, 20(20), pp. 7813–7825. doi: 10.1128/mcb.20.20.7813-7825.2000.

Insinna, C. and Besharse, J. C. (2008) 'Intraflagellar transport and the sensory outer segment of vertebrate photoreceptors', *Developmental Dynamics*, 237(8), pp. 1982–1992. doi: 10.1002/dvdy.21554.

Ishikawa, H. and Marshall, W. F. (2011) 'Ciliogenesis: Building the cell's antenna', *Nature Reviews Molecular Cell Biology*, 12(4), pp. 222–234. doi: 10.1038/nrm3085.

Ishikawa, T. (2017) 'Axoneme structure from motile cilia', *Cold Spring Harbor Perspectives*

in Biology, 9(1). doi: 10.1101/cshperspect.a028076.

Izquierdo, D. *et al.* (2014) 'Stabilization of cartwheel-less centrioles for duplication requires CEP295-mediated centriole-to-centrosome conversion', *Cell Reports*, 8(4), pp. 957–965. doi: 10.1016/j.celrep.2014.07.022.

Jacob, L. S. *et al.* (2011) 'Genome-wide RNAi screen reveals disease-associated genes that are common to Hedgehog and Wnt signaling', *Science Signaling*, 4(157). doi: 10.1126/scisignal.2001225.

Jerka-Dziadosz, M. *et al.* (2010) 'Basal body duplication in paramecium: The key role of Bld10 in assembly and stability of the Cartwheel', *Cytoskeleton*, 67(3), pp. 161–171. doi: 10.1002/cm.20433.

Karr, T. L. and Alberts, B. M. (1986) 'Organization of the cytoskeleton in early Drosophila embryos', *Journal of Cell Biology*, 102(4), pp. 1494–1509. doi: 10.1083/jcb.102.4.1494.

Keller, D. *et al.* (2014) 'Mechanisms of HsSAS-6 assembly promoting centriole formation in human cells', *Journal of Cell Biology*, 204(5), pp. 697–712. doi: 10.1083/jcb.201307049.

Khodjakov, A. *et al.* (2000) 'Centrosome-independent mitotic spindle formation in vertebrates', *Current Biology*, 10(2), pp. 59–67. doi: 10.1016/S0960-9822(99)00276-6.

Kim, S. A., Heinze, K. G. and Schwille, P. (2007) 'Fluorescence correlation spectroscopy in living cells', *Nature Methods*, 4(11), pp. 963–973. doi: 10.1038/nmeth1104.

Kirkham, M. *et al.* (2003) 'SAS-4 is a C. elegans centriolar protein that controls centrosome size', *Cell*, 112(4), pp. 575–587. doi: 10.1016/S0092-8674(03)00117-X.

Kitagawa, D., Kohlmaier, G., *et al.* (2011) 'Spindle positioning in human cells relies on proper centriole formation and on the microcephaly proteins CPAP and STIL', *Journal of Cell Science*, 124(22), pp. 3884–3893. doi: 10.1242/jcs.089888.

Kitagawa, D., Vakonakis, I., *et al.* (2011) 'Structural basis of the 9-fold symmetry of centrioles', *Cell*, 144(3), pp. 364–375. doi: 10.1016/j.cell.2011.01.008.

Klebba, J. E. *et al.* (2015) 'Two Polo-like kinase 4 binding domains in Asterless perform

distinct roles in regulating kinase stability', *Journal of Cell Biology*, 208(4), pp. 401–414. doi: 10.1083/jcb.201410105.

Klena, N. *et al.* (2020) 'Architecture of the centriole cartwheel-containing region revealed by cryo-electron tomography', *The EMBO Journal*, 39(22), pp. 1–17. doi: 10.15252/embj.2020106246.

Kleylein-Sohn, J. *et al.* (2007) 'Plk4-Induced Centriole Biogenesis in Human Cells', *Developmental Cell*, 13(2), pp. 190–202. doi: 10.1016/j.devcel.2007.07.002.

Klingseisen, A. and Jackson, A. P. (2011) 'Mechanisms and pathways of growth failure in primordial dwarfism', *Genes and Development*, 25(19), pp. 2011–2024. doi: 10.1101/gad.169037.

Knoblich, J. A. (2010) 'Asymmetric cell division: Recent developments and their implications for tumour biology', *Nature Reviews Molecular Cell Biology*, 11(12), pp. 849–860. doi: 10.1038/nrm3010.

Kohlmaier, G. *et al.* (2009) 'Overly Long Centrioles and Defective Cell Division upon Excess of the SAS-4-Related Protein CPAP', *Current Biology*, 19(12), pp. 1012–1018. doi: 10.1016/j.cub.2009.05.018.

Koppel, D. E. (1974) 'Statistical accuracy in fluorescence correlation spectroscopy', *Physical Review A*, 10(6), pp. 1938–1945. doi: 10.1103/PhysRevA.10.1938.

Kratz, A. S. *et al.* (2015) 'Plk4-dependent phosphorylation of STIL is required for centriole duplication', *Biology Open*, 4(3), pp. 370–377. doi: 10.1242/bio.201411023.

Kronja, I. *et al.* (2014) 'Widespread changes in the posttranscriptional landscape at the Drosophila oocyte-to-embryo transition', *Cell Reports*, 7(5), pp. 1495–1508. doi: 10.1016/j.celrep.2014.05.002.

Kuhara, A. *et al.* (2008) 'Temperature Sensing by an Olfactory Neuron in a Circuit Controlling Behavior of C. elegans', *Science*, 320(5877), pp. 803–807. doi: 10.1126/science.1148922.

Lacey, K. R., Jackson, P. K. and Stearns, T. (1999) 'Cyclin-dependent kinase control of centrosome duplication', *Proceedings of the National Academy of Sciences of the United States of America*, 96(6), pp. 2817–2822. doi: 10.1073/pnas.96.6.2817.

Lambert, T. J. (2019) 'FPbase: a community-editable fluorescent protein database', *Nature Methods*, 16(4), pp. 277–278. doi: 10.1038/s41592-019-0352-8.

Lane, H. A. and Nigg, E. A. (1996) 'Antibody microinjection reveals an essential role for human polo-like kinase 1 (Plk1) in the functional maturation of mitotic centrosomes', *Journal of Cell Biology*, 135(6 II), pp. 1701–1713. doi: 10.1083/jcb.135.6.1701.

Lattao, R., Kovács, L. and Glover, D. M. (2017) 'The centrioles, centrosomes, basal bodies, and cilia of Drosophila melanogaster', *Genetics*, 206(1), pp. 33–53. doi: 10.1534/genetics.116.198168.

Lawo, S. *et al.* (2012) 'Subdiffraction imaging of centrosomes reveals higher-order organizational features of pericentriolar material', *Nature Cell Biology*, 14(11), pp. 1148–1158. doi: 10.1038/ncb2591.

Lécuyer, E. *et al.* (2007) 'Global Analysis of mRNA Localization Reveals a Prominent Role in Organizing Cellular Architecture and Function', *Cell*, 131(1), pp. 174–187. doi: 10.1016/j.cell.2007.08.003.

Leda, M., Holland, A. J. and Goryachev, A. B. (2018) 'Autoamplification and Competition Drive Symmetry Breaking: Initiation of Centriole Duplication by the PLK4-STIL Network', *iScience*, 8, pp. 222–235. doi: 10.1016/j.isci.2018.10.003.

Lee, H. S., Simon, J. A. and Lis, J. T. (1988) 'Structure and expression of ubiquitin genes of Drosophila melanogaster', *Molecular and Cellular Biology*, 8(11), pp. 4727–4735. doi: 10.1128/mcb.8.11.4727-4735.1988.

Lee, M. J. *et al.* (2001) 'Msps/XMAP215 interacts with the centrosomal protein D-TACC to regulate microtubule behaviour', *Nature Cell Biology*, 3(7), pp. 643–649. doi: 10.1038/35083033.

Lee, S.-Y., Jang, C. and Lee, K.-A. (2014) 'Polo-Like Kinases (Plks), a Key Regulator of Cell

Cycle and New Potential Target for Cancer Therapy', *Development & Reproduciton*, 18(1), pp. 65–71. doi: 10.12717/dr.2014.18.1.065.

Leidel, S. *et al.* (2005) 'SAS-6 defines a protein family required for centrosome duplication in C. elegans and in human cells', *Nature Cell Biology*, 7(2), pp. 115–125. doi: 10.1038/ncb1220.

Leidel, S. and Gönczy, P. (2003) 'SAS-4 is essential for centrosome duplication in C. elegans and is recruited to daughter centrioles once per cell cycle', *Developmental Cell*, 4(3), pp. 431–439. doi: 10.1016/S1534-5807(03)00062-5.

Leung, G. C. *et al.* (2002) 'The sak polo-box comprises a structural domain sufficient for mitotic subcellular localization', *Nature Structural Biology*, 9(10), pp. 719–724. doi: 10.1038/nsb848.

Levine, M. S. *et al.* (2017) 'Centrosome Amplification Is Sufficient to Promote Spontaneous Tumorigenesis in Mammals', *Developmental Cell*, 40(3), pp. 313-322.e5. doi: 10.1016/j.devcel.2016.12.022.

Lin, Y. C. *et al.* (2013) 'Human microcephaly protein CEP135 binds to hSAS-6 and CPAP, and is required for centriole assembly', *EMBO Journal*, 32(8), pp. 1141–1154. doi: 10.1038/emboj.2013.56.

Lindsley, D. L. and Zimm, G. G. (1992) *The Genome of Drosophila melanogaster.*

Loncarek, J. *et al.* (2008) 'Control of daughter centriole formation by the pericentriolar material', *Nature Cell Biology*, 10(3), pp. 322–328. doi: 10.1038/ncb1694.

Loncarek, J. and Bettencourt-Dias, M. (2018) 'Building the right centriole for each cell type', *Journal of Cell Biology*, 217(3), pp. 823–835. doi: 10.1083/jcb.201704093.

Loncarek, J. and Khodjakov, A. (2009) 'Ab ovo or de novo? Mechanisms of centriole duplication', *Molecules and Cells*, 27(2), pp. 135–142. doi: 10.1007/s10059-009-0017-z.

Lopes, C. A. M. *et al.* (2015) 'PLK4 trans-Autoactivation Controls Centriole Biogenesis in Space', *Developmental Cell*, 35(2), pp. 222–235. doi: 10.1016/j.devcel.2015.09.020.

Lowery, D. M., Lim, D. and Yaffe, M. B. (2005) 'Structure and function of Polo-like kinases', *Oncogene*, 24(2), pp. 248–259. doi: 10.1038/sj.onc.1208280.

Lucas, E. P. and Raff, J. W. (2007) 'Maintaining the proper connection between the centrioles and the pericentriolar matrix requires Drosophila Centrosomin', *Journal of Cell Biology*, 178(5), pp. 725–732. doi: 10.1083/jcb.200704081.

Magde, D., Elson, E. and Webb, W. W. (1972) 'Thermodynamic Fluctuations in a Reacting System—Measurement by Fluorescence Correlation Spectroscopy', *Physical Review Letters*, 29(11), pp. 705–708. doi: 10.1103/PhysRevLett.29.705.

Mahen, R. *et al.* (2011) 'Continuous polo-like kinase 1 activity regulates diffusion to maintain centrosome self-organization during mitosis', *Proceedings of the National Academy of Sciences of the United States of America*, 108(22), pp. 9310–9315. doi: 10.1073/pnas.1101112108.

Mahmood, S., Ahmad, W. and Hassan, M. J. (2011) 'Autosomal recessive primary microcephaly (MCPH): clinical manifestations, genetic heterogeneity and mutation continuum', *Orphanet Journal of Rare Diseases*, 6(1), p. 39. doi: 10.1186/1750-1172-6-39.

Markow, T. A., Beall, S. and Matzkin, L. M. (2009) 'Egg size, embryonic development time and ovoviviparity in Drosophila species', *Journal of Evolutionary Biology*, 22(2), pp. 430–434. doi: 10.1111/j.1420-9101.2008.01649.x.

Marsh, B. J. *et al.* (2001) 'Organellar relationships in the Golgi region of the pancreatic beta cell line, HIT-T15, visualized by high resolution electron tomography', *Proceedings of the National Academy of Sciences of the United States of America*, 98(5), pp. 2399–2406. doi: 10.1073/pnas.051631998.

Marshall, W. F. (2016) 'Cell Geometry: How Cells Count and Measure Size', *Annual Review of Biophysics*, 45, pp. 49–64. doi: 10.1146/annurev-biophys-062215-010905.

Matsumoto, Y., Hayashi, K. and Nishida, E. (1999) 'Cyclin-dependent kinase 2 (Cdk2) is required for centrosome duplication in mammalian cells', *Current Biology*, 9(8), pp. 429–432. doi: 10.1016/S0960-9822(99)80191-2.

McLamarrah, T. A. *et al.* (2017) 'An Ordered Pattern of Ana2 Phosphorylation by Plk4 is Required for Centriole Assembly', *bioRxiv*, 217(4), pp. 1217–1231. doi: 10.1101/240374.

Megraw, T. L. *et al.* (1999) 'The Centrosomin protein is required for centrosome assembly and function during cleavage in Drosophila', *Development*, 126(13), pp. 2829–2839. doi: 10.1242/dev.126.13.2829.

Mennella, V. *et al.* (2012) 'Subdiffraction-resolution fluorescence microscopy reveals a domain of the centrosome critical for pericentriolar material organization', *Nature Cell Biology*, 14(11), pp. 1159–1168. doi: 10.1038/ncb2597.

Meraldi, P. *et al.* (1999) 'Centrosome duplication in mammalian somatic cells requires E2F and Cdk2-Cyclin A', *Nature Cell Biology*, 1(2), pp. 88–93. doi: 10.1038/10054.

Meraldi, P. (2016) 'Centrosomes in spindle organization and chromosome segregation: a mechanistic view', *Chromosome Research*, 24(1), pp. 19–34. doi: 10.1007/s10577-015-9508-2.

Moorman, S. J. and Shorr, A. Z. (2008) 'The primary cilium as a gravitational force transducer and a regulator of transcriptional noise', *Developmental Dynamics*, 237(8), pp. 1955–1959. doi: 10.1002/dvdy.21493.

Moritz, M. *et al.* (1995) 'Microtubule nucleation by gamma-tubulin rings in the centrosome', *Nature*, 378(7 December 1995), pp. 638–640.

Motulsky, H. J. and Brown, R. E. (2006) 'Detecting outliers when fitting data with nonlinear regression - A new method based on robust nonlinear regression and the false discovery rate', *BMC Bioinformatics*, 7, pp. 1–20. doi: 10.1186/1471-2105-7-123.

Moyer, T. C. *et al.* (2015) 'Binding of STIL to Plk4 activates kinase activity to promote centriole assembly', *Journal of Cell Biology*, 209(6), pp. 863–878. doi: 10.1083/jcb.201502088.

Nabais, C. *et al.* (2021) 'Plk4 triggers autonomous de novo centriole biogenesis and maturation', *Journal of Cell Biology*, 220(5), pp. 9310–9315. doi: 10.1083/jcb.202008090.

Nano, M. and Basto, R. (2017) 'Consequences of Centrosome Dysfunction During Brain Development', in, pp. 19–45. doi: 10.1007/978-3-319-57127-0_2.

Nigg, E. A. and Holland, A. J. (2018) 'Once and only once: Mechanisms of centriole duplication and their deregulation in diseases', *Nature Reviews Molecular Cell Biology*, 19(5), pp. 297–312. doi: 10.1038/nrm.2017.127.

Nigg, E. A. and Raff, J. W. (2009) 'Centrioles, Centrosomes, and Cilia in Health and Disease', *Cell*, 139(4), pp. 663–678. doi: 10.1016/j.cell.2009.10.036.

Nigg, E. A. and Stearns, T. (2011) 'The centrosome cycle: Centriole biogenesis, duplication and inherent asymmetries', *Nature Cell Biology*, 13(10), pp. 1154–1160. doi: 10.1038/ncb2345.

Novak, Z. A. *et al.* (2014) 'Asterless licenses daughter centrioles to duplicate for the first time in Drosophila embryos', *Current Biology*, 24(11), pp. 1276–1282. doi: 10.1016/j.cub.2014.04.023.

Novak, Z. A. A. *et al.* (2016) 'Cdk1 Phosphorylates Drosophila Sas-4 to Recruit Polo to Daughter Centrioles and Convert Them to Centrosomes', *Developmental Cell*, 37(6), pp. 545–557. doi: 10.1016/j.devcel.2016.05.022.

O'Connell, K. F. *et al.* (2001) 'The C. elegans zyg-1 gene encodes a regulator of centrosome duplication with distinct maternal and paternal roles in the embryo', *Cell*, 105(4), pp. 547–558. doi: 10.1016/S0092-8674(01)00338-5.

O'Connell, K. F., Maxwell, K. N. and White, J. G. (2000) 'The spd-2 gene is required for polarization of the anteroposterior axis and formation of the sperm asters in the Caenorhabditis elegans zygote', *Developmental Biology*, 222(1), pp. 55–70. doi: 10.1006/dbio.2000.9714.

Ohta, M. *et al.* (2014) 'Direct interaction of Plk4 with STIL ensures formation of a single procentriole per parental centriole', *Nature communications*, 5, p. 5267. doi: 10.1038/ncomms6267.

Ohta, M. *et al.* (2018) 'Bimodal Binding of STIL to Plk4 Controls Proper Centriole Copy

Number', *Cell Reports*, 23(11), pp. 3160-3169.e4. doi: 10.1016/j.celrep.2018.05.030.

Oliveira, R. A. *et al.* (2010) 'Cohesin cleavage and Cdk inhibition trigger formation of daughter nuclei', *Nature Cell Biology*, 12(2), pp. 185–192. doi: 10.1038/ncb2018.

Paintrand, M. *et al.* (1992) 'Centrosome organization and centriole architecture: Their sensitivity to divalent cations', *Journal of Structural Biology*, 108(2), pp. 107–128. doi: 10.1016/1047-8477(92)90011-X.

Palazzo, R. E. *et al.* (1999) 'Centrosome maturation', in, pp. 449–470. doi: 10.1016/S0070-2153(99)49021-0.

Panda, P. *et al.* (2020) 'Tissue specific requirement of Drosophila Rcd4 for centriole duplication and ciliogenesis', *Journal of Cell Biology*, 219(8). doi: 10.1083/jcb.201912154.

Peel, N. *et al.* (2007) 'Overexpressing Centriole-Replication Proteins In Vivo Induces Centriole Overduplication and De Novo Formation', *Current Biology*, 17(10), pp. 834–843. doi: 10.1016/j.cub.2007.04.036.

Pelletier, L. *et al.* (2006) 'Centriole assembly in Caenorhabditis elegans', *Nature*, 444(7119), pp. 619–623. doi: 10.1038/nature05318.

Petrášek, Z. and Schwille, P. (2008) 'Precise measurement of diffusion coefficients using scanning fluorescence correlation spectroscopy', *Biophysical Journal*, 94(4), pp. 1437–1448. doi: 10.1529/biophysj.107.108811.

Port, F. *et al.* (2014) 'Optimized CRISPR/Cas tools for efficient germline and somatic genome engineering in Drosophila', *Proceedings of the National Academy of Sciences of the United States of America*, 111(29). doi: 10.1073/pnas.1405500111.

Port, F., Muschalik, N. and Bullock, S. L. (2015) 'Systematic evaluation of Drosophila CRISPR tools reveals safe and robust alternatives to autonomous gene drives in basic research', *G3: Genes, Genomes, Genetics*, 5(7), pp. 1493–1502. doi: 10.1534/g3.115.019083.

Prosser, S. L. and Pelletier, L. (2017) 'Mitotic spindle assembly in animal cells: A fine

balancing act', *Nature Reviews Molecular Cell Biology*, 18(3), pp. 187–201. doi: 10.1038/nrm.2016.162.

Raff, J. W. (2019) 'Phase Separation and the Centrosome: A Fait Accompli?', *Trends in Cell Biology*, 29(8), pp. 612–622. doi: 10.1016/j.tcb.2019.04.001.

Rauch, A. *et al.* (2008) 'Mutations in the Pericentrin (PCNT) Gene Cause Primordial Dwarfism', *Science*, 319(5864), pp. 816–819. doi: 10.1126/science.1151174.

Reiter, J. F. and Leroux, M. R. (2017) 'Genes and molecular pathways underpinning ciliopathies', *Nature Reviews Molecular Cell Biology*, 18(9), pp. 533–547. doi: 10.1038/nrm.2017.60.

Rigler, R. *et al.* (1993) 'Fluorescence correlation spectroscopy with high count rate and low background: analysis of translational diffusion', *European Biophysics Journal*, 22(3), pp. 169–175. doi: 10.1007/BF00185777.

Roberts, D. B. (1986) 'Drosophila — A Practical Approach', *Biochemical Education*, 15(3), p. 162. doi: 10.1016/0307-4412(87)90074-4.

Rodrigues-Martins, A. *et al.* (2007) 'Revisiting the Role of the Mother Centriole in Centriole Biogenesis', *Science*, 316(5827), pp. 1046–1050. doi: 10.1126/science.1142950.

Rogala, K. B. *et al.* (2015) 'The Caenorhabditis elegans protein SAS-5 forms large oligomeric assemblies critical for centriole formation', *eLife*, 4(MAY), pp. 1–51. doi: 10.7554/eLife.07410.

Roque, H. *et al.* (2012) 'Drosophila Cep135/Bld10 maintains proper centriole structure but is dispensable for cartwheel formation', *Journal of Cell Science*, 125(23), pp. 5881–5886. doi: 10.1242/jcs.113506.

Ruettinger, S. *et al.* (2008) 'Comparison and accuracy of methods to determine the confocal volume for quantitative fluorescence correlation spectroscopy', *Journal of Microscopy*, 232(2), pp. 343–352. doi: 10.1111/j.1365-2818.2008.02105.x.

Sabat-Pospiech, D. *et al.* (2019) 'Targeting centrosome amplification, an Achilles' heel of

cancer', *Biochemical Society Transactions*, 47(5), pp. 1209–1222. doi: 10.1042/BST20190034.

Saurya, S. *et al.* (2016) 'Drosophila Ana1 is required for centrosome assembly and centriole elongation', *Journal of Cell Science*, 129(13), pp. 2514–2525. doi: 10.1242/jcs.186460.

Schmidt, T. I. *et al.* (2009) 'Control of Centriole Length by CPAP and CP110', *Current Biology*, 19(12), pp. 1005–1011. doi: 10.1016/j.cub.2009.05.016.

Schonle, A. *et al.* (2014) 'Monitoring triplet state dynamics with fluorescence correlation spectroscopy: bias and correction.', *Microscopy research and technique*, 77(7), pp. 528–536. doi: 10.1002/jemt.22368.

Schwarz, G. (1978) 'Estimating the Dimension of a Model', *The Annals of Statistics*, 6(2), pp. 461–464. doi: 10.1214/aos/1176344136.

Schwille, P., Meyer-Almes, F. J. and Rigler, R. (1997) 'Dual-color fluorescence cross-correlation spectroscopy for multicomponent diffusional analysis in solution', *Biophysical Journal*, 72(4), pp. 1878–1886. doi: 10.1016/s0006-3495(97)78833-7.

Sepulveda, G. *et al.* (2018) 'Co-translational protein targeting facilitates centrosomal recruitment of PCNT during centrosome maturation in vertebrates', *eLife*, 7, pp. 1–28. doi: 10.7554/eLife.34959.

Shaner, N. C. *et al.* (2013) 'A bright monomeric green fluorescent protein derived from Branchiostoma lanceolatum', *Nature Methods*, 10(5), pp. 407–409. doi: 10.1038/nmeth.2413.

Sharma, A. *et al.* (2016) 'Centriolar CPAP/SAS-4 Imparts Slow Processive Microtubule Growth', *Developmental Cell*, 37(4), pp. 362–376. doi: 10.1016/j.devcel.2016.04.024.

Shcherbo, D. *et al.* (2009) 'Far-red fluorescent tags for protein imaging in living tissues', *Biochemical Journal*, 418(3), pp. 567–574. doi: 10.1042/BJ20081949.

Shermoen, A. W., McCleland, M. L. and O'Farrell, P. H. (2010) 'Developmental control of

late replication and s phase length', *Current Biology*, 20(23), pp. 2067–2077. doi: 10.1016/j.cub.2010.10.021.

Sievers, F. *et al.* (2011) 'Fast, scalable generation of high-quality protein multiple sequence alignments using Clustal Omega', *Molecular Systems Biology*, 7(539). doi: 10.1038/msb.2011.75.

Sillibourne, J. E. *et al.* (2010) 'Autophosphorylation of Polo-like Kinase 4 and Its Role in Centriole Duplication', *Molecular Biology of the Cell*. Edited by T. Stearns, 21(4), pp. 547–561. doi: 10.1091/mbc.e09-06-0505.

Singla, V. and Reiter, J. F. (2006) 'The primary cilium as the cell's antenna: Signaling at a sensory organelle', *Science*, 313(5787), pp. 629–633. doi: 10.1126/science.1124534.

Sir, J. H. *et al.* (2013) 'Loss of centrioles causes chromosomal instability in vertebrate somatic cells', *Journal of Cell Biology*, 203(5), pp. 747–756. doi: 10.1083/jcb.201309038.

Slevin, L. K. *et al.* (2012) 'The structure of the Plk4 cryptic polo box reveals two tandem polo boxes required for centriole duplication', *Structure*, 20(11), pp. 1905–1917. doi: 10.1016/j.str.2012.08.025.

Sonnen, K. F. *et al.* (2012) '3D-structured illumination microscopy provides novel insight into architecture of human centrosomes', *Biology Open*, 1(10), pp. 965–976. doi: 10.1242/bio.20122337.

Sonnen, K. F. *et al.* (2013) 'Human Cep192 and Cep152 cooperate in Plk4 recruitment and centriole duplication', *Journal of Cell Science*, 126(14), pp. 3223–3233. doi: 10.1242/jcs.129502.

Spasic, M. and Jacobs, C. R. (2018) 'Whole Tissue Function', pp. 42–52. doi: 10.1016/j.semcdb.2017.08.036.Primary.

Steere, N. *et al.* (2011) 'Centrosome amplification in CHO and DT40 cells by inactivation of cyclin-dependent kinases', *Cytoskeleton*, 68(8), pp. 446–458. doi: 10.1002/cm.20523.

Steiert, F. (2016) 'Photophysical Characterization of GFP Variants by Single-Molecule

Spectroscopy and Microscopy', *Technische Universität München*, (December).

Stevens, N. R. *et al.* (2009) 'Ana3 is a conserved protein required for the structural integrity of centrioles and basal bodies', *Journal of Cell Biology*, 187(3), pp. 355–363. doi: 10.1083/jcb.200905031.

Stevens, N. R. *et al.* (2010) 'Drosophila Ana2 is a conserved centriole duplication factor', *Journal of Cell Biology*, 188(3), pp. 313–323. doi: 10.1083/jcb.200910016.

Stevens, N. R., Roque, H. and Raff, J. W. (2010) 'DSas-6 and Ana2 Coassemble into Tubules to Promote Centriole Duplication and Engagement', *Developmental Cell*, 19(6), pp. 913–919. doi: 10.1016/j.devcel.2010.11.010.

Strnad, P. *et al.* (2007) 'Regulated HsSAS-6 Levels Ensure Formation of a Single Procentriole per Centriole during the Centrosome Duplication Cycle', *Developmental Cell*, 13(2), pp. 203–213. doi: 10.1016/j.devcel.2007.07.004.

Su, T. T. *et al.* (1998) 'Exit from mitosis in Drosophila syncytial embryos requires proteolysis and cychn degradation, and is associated with localized dephosphorylation', *Genes and Development*, 12(10), pp. 1495–1503. doi: 10.1101/gad.12.10.1495.

Szollosi, D., Calarco, P. and Donahue, R. P. (1972) 'Absence of centrioles in the first and second meiotic spindles of mouse oocytes.', *Journal of Cell Science*, 11(2), pp. 521–541.

Takao, D. *et al.* (2019) 'Feedback loops in the Plk4–STIL–HsSAS6 network coordinate site selection for procentriole formation', *Biology Open*, 8(9), pp. 1–9. doi: 10.1242/bio.047175.

Tang, C. J. C. *et al.* (2009) 'CPAP is a cell-cycle regulated protein that controls centriole length', *Nature Cell Biology*, 11(7), pp. 825–831. doi: 10.1038/ncb1889.

Tang, C. J. C. *et al.* (2011) 'The human microcephaly protein STIL interacts with CPAP and is required for procentriole formation', *EMBO Journal*, 30(23), pp. 4790–4804. doi: 10.1038/emboj.2011.378.

Tanos, B. E. *et al.* (2013) 'Centriole distal appendages promote membrane docking,

leading to cilia initiation', *Genes and Development*, 27(2), pp. 163–168. doi: 10.1101/gad.207043.112.

La Terra, S. *et al.* (2005) 'The de novo centriole assembly pathway in HeLa cells: Cell cycle progression and centriole assembly/maturation', *Journal of Cell Biology*, 168(5), pp. 713–722. doi: 10.1083/jcb.200411126.

Tinevez, J. Y. *et al.* (2017) 'TrackMate: An open and extensible platform for single-particle tracking', *Methods*, 115, pp. 80–90. doi: 10.1016/j.ymeth.2016.09.016.

Tolwinski, N. S. (2017) 'Introduction: Drosophila-A model system for developmental biology', *Journal of Developmental Biology*, 5(3), pp. 10–11. doi: 10.3390/jdb5030009.

Tovey, C. A. *et al.* (2021) 'Autoinhibition of Cnn binding to γ-TuRCs prevents ectopic microtubule nucleation and cell division defects', *The Journal of cell biology*, 220(8). doi: 10.1083/jcb.202010020.

Tsou, M. F. B. and Stearns, T. (2006) 'Mechanism limiting centrosome duplication to once per cell cycle', *Nature*, 442(7105), pp. 947–951. doi: 10.1038/nature04985.

Ulbrich, M. H. and Isacoff, E. Y. (2007) 'Subunit counting in membrane-bound proteins', *Nature Methods*, 4(4), pp. 319–321. doi: 10.1038/nmeth1024.

Vaizel-Ohayon, D. and Schejter, E. D. (1999) 'Mutations in centrosomin reveal requirements for centrosomal function during early Drosophila embryogenesis', *Current Biology*, 9(16), pp. 889–898. doi: 10.1016/S0960-9822(99)80393-5.

Varmark, H. *et al.* (2007) 'Asterless Is a Centriolar Protein Required for Centrosome Function and Embryo Development in Drosophila', *Current Biology*, 17(20), pp. 1735–1745. doi: 10.1016/j.cub.2007.09.031.

Vidwans, S. J., Wong, M. L. and O'Farrell, P. H. (1999) 'Mitotic regulators govern progress through steps in the centrosome duplication cycle', *Journal of Cell Biology*, 147(7), pp. 1371–1377. doi: 10.1083/jcb.147.7.1371.

Vidwans, S. J., Wong, M. L. and O'Farrell, P. H. (2003) 'Anomalous centriole configurations

are detected in Drosophila wing disc cells upon Cdk1 inactivation', *Journal of Cell Science*, 116(1), pp. 137–143. doi: 10.1242/jcs.00204.

Waithe, D. *et al.* (2016) 'FoCuS-point: Software for STED fluorescence correlation and time-gated single photon counting', *Bioinformatics*, 32(6), pp. 958–960. doi: 10.1093/bioinformatics/btv687.

Wang, W. J. *et al.* (2011) 'The conversion of centrioles to centrosomes: Essential coupling of duplication with segregation', *Journal of Cell Biology*, 193(4), pp. 727–739. doi: 10.1083/jcb.201101109.

Wang, X. *et al.* (2009) 'Asymmetric centrosome inheritance maintains neural progenitors in the neocortex', *Nature*, 461(7266), pp. 947–955. doi: 10.1038/nature08435.

Warn, R. M. (1986) 'The Cytoskeleton of the Early Drosophila Embryo', *Journal of Cell Science*, 1986(Supplement 5), pp. 311–328. doi: 10.1242/jcs.1986.Supplement_5.20.

Waters, A. M. and Beales, P. L. (2011) 'Ciliopathies: An expanding disease spectrum', *Pediatric Nephrology*, 26(7), pp. 1039–1056. doi: 10.1007/s00467-010-1731-7.

Wessel, A. D. *et al.* (2015) 'The mechanical properties of early drosophila embryos measured by high-speed video microrheology', *Biophysical Journal*, 108(8), pp. 1899–1907. doi: 10.1016/j.bpj.2015.02.032.

Winey, M. and O'Toole, E. (2014) 'Centriole structure', *Philosophical Transactions of the Royal Society B: Biological Sciences*, 369(1650). doi: 10.1098/rstb.2013.0457.

Wong, C. and Stearns, T. (2003) 'Centrosome number is controlled by a centrosome-intrinsic block to reduplication', *Nature Cell Biology*, 5(6), pp. 539–544. doi: 10.1038/ncb993.

Wong, Y. L. *et al.* (2015) 'Reversible centriole depletion with an inhibitor of Polo-like kinase 4', *Science*, 348(6239), pp. 1155–1160. doi: 10.1126/science.aaa5111.

Woodruff, J. B. *et al.* (2015) 'Regulated assembly of a supramolecular centrosome scaffold in vitro', *Science*, 348(6236), pp. 808–812. doi: 10.1126/science.aaa3923.

Woodruff, J. B. *et al.* (2017) 'The Centrosome Is a Selective Condensate that Nucleates Microtubules by Concentrating Tubulin', *Cell*, 169(6), pp. 1066-1077.e10. doi: 10.1016/j.cell.2017.05.028.

Wueseke, O. *et al.* (2014) 'The Caenorhabditis elegans pericentriolar material components SPD-2 and SPD-5 are monomeric in the cytoplasm before incorporation into the PCM matrix', *Molecular Biology of the Cell*, 25(19), pp. 2984–2992. doi: 10.1091/mbc.E13-09-0514.

Wueseke, O. *et al.* (2016) 'Polo-like kinase phosphorylation determines Caenorhabditis elegans centrosome size and density by biasing SPD-5 toward an assembly-competent conformation', *Biology Open*, 5(10), pp. 1431–1440. doi: 10.1242/bio.020990.

Yamamoto, S. and Kitagawa, D. (2019) 'Self-organization of Plk4 regulates symmetry breaking in centriole duplication', *Nature Communications*, 10(1), pp. 1–12. doi: 10.1038/s41467-019-09847-x.

Yoshiba, S. *et al.* (2019) 'HsSAS-6-dependent cartwheel assembly ensures stabilization of centriole intermediates', *Journal of Cell Science*, 132(12). doi: 10.1242/jcs.217521.

Zalokar, M. and Erk, I. (1976) 'Division and migration of nuclei during early embryogenesis of Drosophila melanogaster', *Journal de microscopie et de biologie cellulaire*.

Zitouni, S. *et al.* (2016) 'CDK1 Prevents Unscheduled PLK4-STIL Complex Assembly in Centriole Biogenesis', *Current Biology*, 26(9), pp. 1127–1137. doi: 10.1016/j.cub.2016.03.055.

Zwicker, D. *et al.* (2014) 'Centrosomes are autocatalytic droplets of pericentriolar material organized by centrioles', *Proceedings of the National Academy of Sciences of the United States of America*, 111(26). doi: 10.1073/pnas.1404855111.

9 Appendices

9.1 Appendix A

Table 9: Fly genotypes used in this thesis

Fly genotypes used in this thesis	Figure
w; eSas-6-GFP#6/+ ; Sas-6^{c02901}/Sas-6^{c02901}	3.4
w; eSas-6-GFP#6/eSas-6-GFP#6 ; Sas-6^{c02901}/Sas-6^{c02901}	3.4
w; eSas-6-GFP#6/+ ; Sas-6^{c02901}, eSas-6-GFP#1/+	3.4
w; eSas-6-GFP#6/eSas-6-GFP#6 ; Sas-6^{c02901}, eSas-6-GFP#1/Sas-6^{c02901}, eSas-6-GFP#1	3.4
w;; p(Sas-6)-mNG#2/eAsl-mKate2(14-10), asl^{B46}	3.4 3.8 3.9 5.7 8.5
w;; p(Plk4)-mNG#6/eAsl-mKate2(14-10), asl^{B46}	3.4 3.8 3.9 5.7 8.5
w;; p(Sas-6)-dNG#10/eAsl-mKate2(14-10), asl^{B46}	3.4 3.8 3.9 5.7 8.5
w;; p(Sas-6)-mNG#2/p(Sas-6)-mScarlet-I#1	3.5
w;; p(Sas-6)-mScarlet-I+mNG#5/+	3.5
w;; eAsl-mKate2(14-10), asl^{B46}/+	3.6 3.7
w;; ePlk4-mNG, Plk4^{Aa74} (C4)/Plk4^{Aa74}	3.6
w;; ePlk4-mNG, Plk4^{Aa74} (C4)/ePlk4-mNG, Plk4^{Aa74} (C4)	3.6 4.2 4.4 5.4 8.4
w; mNG-eAna2 (#2)/mNG-eAna2 (#2)	4.2 4.3 4.4

	4.5 5.6 5.7
w; eAna2-mNG (3.72)/eAna2-mNG (3.72)	4.2 4.3 4.4 4.5 4.8 4.10 5.6 5.7 8.2 8.4
w;; mNG-eSas-6 (2.37)/mNG-eSas-6 (2.37)	4.2 4.3 4.4 4.5 5.6 5.7
w;; eSas-6-mNG (#47)/eSas-6-mNG (#47)	4.1 4.2 4.3 4.4 4.5 5.6 5.7
w;; mNG-eAsl (40.6)/+	4.2 4.3
w;; eAsl-mNG (#74)/eAsl-mNG (#74)	4.2 4.3 4.4 4.5 5.4
w;; eSas-4-mNG (#47)/eSas-4-mNG (#47)	4.2 4.3 4.4 4.5

	5.6
w;; mNG-ePlk4 (PN36f)/mNG-ePlk4 (PN36f)	4.2 4.3
w; ana2$^{\Delta a}$/+ ; eAna2(WT)-mNG#1/eAsl-mKate2(14-10), asl^{B46}	4.6 8.3
w; ana2$^{\Delta a}$/+ ; eAna2(ΔCC)-mNG#4/eAsl-mKate2(14-10), asl^{B46}	4.6 8.3
w; ana2$^{\Delta a}$/+ ; eAna2(ΔSTAN)-mNG#2/eAsl-mKate2(14-10), asl^{B46}	4.6 8.3
w; ana2$^{\Delta a}$/ana2$^{\Delta a}$; eAna2(WT)-mNG#1/eAna2(WT)-mNG#1	4.7 8.3
w; ana2$^{\Delta b}$, eAna2(12A)-mNG(9-15)/ana2$^{\Delta b}$, eAna2(12A)-mNG(9-15)	4.7 4.8 8.3
w;; eSas-6-mNG (#47)/+	4.9
w; ana2$^{\Delta a}$, eAna2(12A)#1(Rec6)/ana2$^{\Delta a}$, eAna2(12A)#1(Rec6) ; eSas-6-mNG (#47)/+	4.9
w; ana2$^{\Delta a}$/ana2$^{\Delta a}$; eAna2(S284A T301A)-mNG#3/eAna2(S284A T301A)-mNG#3	4.10 8.3
w; ana2$^{\Delta a}$/ana2$^{\Delta a}$; eAna2(S284E T301E)-mNG#9/eAna2(S284E T301E)-mNG#9	4.10 8.3
w; eAsl-GFP/eAsl-GFP ; asl^{B46}/ asl^{B46}	5.4
w; ePlk4(WT)-mNG#20/+	5.5
w;; ePlk4(SK1)-mNG/+	5.5
w; ePlk4(KD)-mNG/+	5.5
w; mNG-eAna2 (#2)/+	5.7
w; eAna2-mNG (3.72)/+	5.7
w;; mNG-eSas-6 (2.37)/+	5.7
w;; eSas-6-mNG (#47) /+	5.7
w; ana2$^{\Delta a}$/eAna2-mNG (3.72) ; eAna2-mScarlet-I#12/+	5.8
w; eSas-6-mScarlet-I#5/+ ; sas-6$^{\Delta a}$/eSas-6-mNG (#47)	5.8
w; eGrip75-GFP/eGrip75-GFP	6.3
eGrip128-GFP/eGrip128-GFP	6.3
w;; ncd-γ-tubulin-GFP/ncd-γ-tubulin-GFP	6.3
w;; Ubq-Aurora A-GFP/Ubq-Aurora A-GFP	6.3
w; Ubq-GFP-D-TACC/Ubq-GFP-D-TACC ; stella^{592}/stella^{592}	6.3
Ubq-Grip71-GFP/Ubq-Grip71-GFP	6.3
w;; Ubq-MSPS-GFP/Ubq-MSPS-GFP	6.3

w;; ePolo-TRAP-GFP/+	6.5 6.10
w;; mNG-eCnn (38c)/mNG-eCnn (38c)	6.5 6.6 6.7 6.10 8.5
w;; eSpd-2-mNG (S2C)/eSpd-2-mNG (S2C)	6.5 6.8 6.9 6.10
w; mNG-eCnn (38c)/cnn^{f04547}	6.6 6.7
w; Ubq-mNG-Cnn, cnn^{f04547}/cnn^{HK21}	6.6
w; cnn^{f04547}, Ubq-GFP-Cnn/cnn^{f04547}	6.7
w; cnn^{f04547}, Ubq-GFP-Cnn/cnn^{f04547}, Ubq-GFP-Cnn	6.7
w; cnn^{f04547}, Ubq-GFP-Cnn/cnn^{f04547}, Ubq-GFP-Cnn ; Ubq-GFP-Cnn/Ubq-GFP-Cnn	6.7
w;; eSpd-2-mNG (S2C)/$spd\text{-}2^{z35711}$	6.8 6.9
w; Ubq-Spd-2-mNG/+ ; eSpd-2-mNG (S2C)/eSpd-2-mNG (S2C)	6.8 6.9
w; Ubq-Spd-2-mNG/Ubq-Spd-2-mNG ; eSpd-2-mNG (S2C)/eSpd-2-mNG (S2C)	6.8 6.9
w; Ubq-GFP-Cnn, cnn^{f04547}/+	6.11
w; Ubq-GFP-Cnn(ΔLZ)#4, cnn^{f04547}/+	6.11
w; Ubq-GFP-Cnn(ΔCM2), cnn^{f04547}/+	6.11
w; Ubq-Spd-2-GFP/+ ; $spd\text{-}2^{G20143}$/+	6.11
w;; Ubq-Spd-2-GFP(ΔAsh1), $spd\text{-}2^{G20143}$/+	6.11
Ubq-Ana1-GFP/Ubq-Ana1-GFP ; $ana1^{mecB}$	8.1
Ubq-Ana1-GFP/+ ; $ana1^{mecB}$/$ana1^{mecB}$	8.1
w; eAna2-mNG (3.72)/$ana2^{\Delta a}$	8.2
w; eAna2-mNG (3.72)/eAna2-mNG (3.72) ; Ubq-Ana2/+	8.2
w; eAna2-mNG (3.72)/eAna2-mNG (3.72) ; $asl^{\Delta b}$/+	8.2
Ubq-Asl#8/+ ; eAna2-mNG (3.72)/eAna2-mNG (3.72)	8.2
w; eAna2-mNG/eAna2-mNG (3.72) ; $sas\text{-}4^{\Delta b}$/+	8.2
w; eAna2-mNG/eAna2-mNG (3.72) ; Ubq-Sas-4#5/+	8.2
w; eAna2-mNG (3.72)/eAna2-mNG (3.72) ; $sas\text{-}6^{\Delta a}$/+	8.2

w; eAna2-mNG (3.72)/eAna2-mNG (3.72) ; Ubq-Sas-6/+	8.2
w; eAna2-mNG (3.72)/eAna2-mNG (3.72) ; $sak^{\Delta a}$/+	8.2
w; Ubq-Plk4#1, eAna2-mNG (3.72) (Rec.1)/eAna2-mNG (3.72)	8.2
w; $ana2^{\Delta a}$/+ ; eAna2(S318A S373A)-mNG#1/eAsl-mKate2(14-10), asl^{B46}	8.3
w; $ana2^{\Delta a}$/+ ; eAna2(S318E S373E)-mNG#1/eAsl-mKate2(14-10), asl^{B46}	8.3
w; mNG-eCnn (38c)/+	8.5

Table 10: Primers designed for mNG knock-in screening

ID_Name	Sequence (5'-)	Used for:
15_sas-6 nterm scr up out for	CTCCCCTATATCCGCTGGTTGGA	Screening primers for mNG knock-in event
16_NeonGreen scr up ins rev	CCCGTCAGGGTAGGGCAGGTAC	
17_NeonGreen scr down ins for	GAAGACCGAGCTGAAGCACTCCA	
18_sas-6 nterm scr down out rev	CACATACCTTCTCTTTGTTTCCCT	
27_sas-6 cterm scr up out for	CAGCATGCTGGAAGCCTCCCAC	
28_sas-6 cterm scr down out rev	CAGCAGATTTCCGATTTCCACCC	
41_ana2 nterm scr up out for	CGCCGAGGAAGAGCTGCAGCTG	
42_ana2 nterm scr down out rev	CGCCCCCAGGCGCATATCCTTC	
51_ana2 cterm scr up out for	CCTCGTGCTGCACCCACCTTCG	
52_ana2 cterm scr down out rev	CCATCCCCTGTTCCCAGTCGAC	
141_Asl_nt_scr_up_out_for	CTTTGATGCGCAAAGTTGGAAACG	
142_Asl_nt_scr_down_out_rev	CGAAGCGACTGTTTGCTCCAAATA	
107_Asl_ct_scr_up_out_for	GCGATAACCTTTCAGACATGCTAG	
108_Asl_ct_scr_down_out_rev	GGAGAGTCCCTGAACACGAACGT	
117_Sas4_ct_scr_up_out_for	GCAGGCGCATGTCTCGGCACAG	
118_Sas4_ct_scr_down_out_rev	CTCTGATCTGGCAACGCCAGGC	
149_Plk4_nt_scr_up_out_for	TCATTGACGTGTGTGAGAGTCCAA	
150_Plk4_nt_scr_down_out_rev	CAAATGTACATTGTAAATTCCTGAAT	
95_plk4_ct_scr_up_out_for	CAGTGGCTTACCAGTGAGAGAGC	
96_plk4_ct_scr_down_out_rev	GAGCGATTTACGCACAATACAACG	
121_NG_screen_for	CGAGGAGGATAACATGGCCTCTC	
122_NG_screen_rev	CGGTAAAGGCCTTCTGCCACTCC	

Table 11: Primers designed for sgRNA and HDR donor plasmid generation

ID_Name	Sequence (5'-)	Used for:
3_sas-6_gRNA_nterm_for	GTCGAGTAGCTATCCTCGCTCCC	Primers to introduce gRNA sequence into the pCFD3 plasmic
4_sas-6_gRNA_nterm_rev	AAACGGGAGCGAGGATAGCTACT	
5_sas-6_gRNA_cterm_for	GTCGAGAACGGCTTGCAATACCCA	
6_sas-6_gRNA_cterm_rev	AAACTGGGTATTGCAAGCCGTTCT	
29_ana2_gRNA_nterm_for	GTCGGCAGCATATCCTCCGTTTC	
30_ana2_gRNA_nterm_rev	AAACGAAACGGAGGATATGCTGC	
31_ana2_gRNA_cterm_for	GTCGCTTTCACAACAGCTTCGGC	
32_ana2_gRNA_cterm_rev	AAACGCCGAAGCTGTTGTGAAAG	
145_Asl_gRNA_nt_for	GTCGATACCTGGCGTGTTCATATT	
146_Asl_gRNA_nt_rev	AAACAATATGAACACGCCAGGTAT	
97_asl_gRNA_ct_for	GTCGTTAGCTGTGACCATTGCCTT	
98_asl_gRNA_ct_rev	AAACAAGGCAATGGTCACAGCTAA	
119_Sas4_gRNA_ct_for	GTCGAGAGACCCGACTCTAATACT	
120_Sas4_gRNA_ct_rev	AAACAGTATTAGAGTCGGGTCTCT	
147_Plk4_gRNA_nt_for	GTCGCTAGCTATGTTATCCAATC	
148_Plk4_gRNA_nt_rev	AAACGATTGGATAACATAGCTAG	
93_Plk4_gRNA_ct_for	GTCGATAATAAGGCGTTGTCGTTT	
94_Plk4_gRNA_ct_rev	AAACAAACGACAACGCCTTATTAT	
57_pCFD3_for_57	GGTTAGCTCGCCAAGCAGAGAG	Screening primers for guides
58_pCFD3_rev_57	CAACTCTCAGGCTCCAGGTAGG	
7_pBs SK- sas-6 N up rev	GGGAGCGAGGATAGCTACTCGAATTCGATATCAAG CTTATCGATA	Primers (with overlap for NEBuilder assembly) to generate the HDR template
8_pBs SK- sas-6 N down for	GGGAGCGAGGATAGCTACTCACTAGTTCTAGAGCG GCCGCCA	
9_sas-6 nterm rep up for	GAGTAGCTATCCTCGCTCCCTGGGTGGTCCACTGTT GTCCCGCTG	
10_sas-6 nterm rep up rev	TGCTCACCATGATAGATCAGGCTCGTGAGAAAC	
11_sas-6 nterm rep NGreen for	CTGATCTATCATGGTGAGCAAGGGCGAGGAGG	
12_sas-6 nterm rep NGreen rev	ACTATACGAGTCTTCTGATCCTGGAGGCCACATGAA GCCTGCTTTTTTGTACAAACT	
13_sas-6 nterm rep down for	GATCAGAAGACTCGTATAGTGCCAAAATGGACTAT GGCAAGAG	
14_sas-6 nterm rep down rev	GAGTAGCTATCCTCGCTCCCTGGCAGTGTGCTGCTT GAGGTCCTC	

19_pBS SK- sas-6 C up rev	TGGGTATTGCAAGCCGTTCTGAATTCGATATCAAGCTTATCGATA	
20_pBS SK- sas-6 C down for	TGGGTATTGCAAGCCGTTCTACTAGTTCTAGAGCGGCCGCCA	
21_sas-6 cterm rep up for	AGAACGGCTTGCAATACCCACGGCAACGCACAACGCGCGCATGCG	
22_sas-6 cterm rep up rev	TAGGGATGGCCAATCTCTCCTTTAGAATGAGGATTTCTGAAAAGAG	
23_sas-6 cterm rep NGreen for	GGAGAGATTGGCCATCCCTACTGGCAAAGAAAATCGGCGAGACCCAGCTTTCTTGTACAAAGTG	
24_sas-6 cterm rep NGreen rev	ATAAGTAAAATTACTTGTACAGCTCGTCCATGC	
25_sas-6 cterm rep down for	GTACAAGTAATTTTACTTATTGTTAATGCATTTTTTC	
26_sas-6 cterm rep down rev	AGAACGGCTTGCAATACCCACGGCGCTGTGTATCCATCTTGGCCGC	
33_pBs SK- ana2 N up rev	GAAACGGAGGATATGCTGCCGAATTCGATATCAAGCTTATCGATA	
34_pBs SK- ana2 N down for	GAAACGGAGGATATGCTGCCACTAGTTCTAGAGCGGCCGCCA	
35_ana2 nterm rep up for	GGCAGCATATCCTCCGTTTCGGGCCGTGAAATGCCCAGCGAGCTG	
36_ana2 nterm rep up rev	TGCTCACCATTTGGAGCGTATTTGTTTATATTTGC	
37_ana2 nterm rep NGreen for	TACGCTCCAAATGGTGAGCAAGGGCGAGGAGG	
38_ana2 nterm rep NGreen rev	GGTAACATGTCTTCAGTCTCGGGAACAAACATGAAGCCTGCTTTTTTGTACAAACT	
39_ana2 nterm rep down for	GAGACTGAAGACATGTTACCCAGACTAGCGCCCAGGCCGAGT	
40_ana2 nterm rep down for	GGCAGCATATCCTCCGTTTCGGGGCAAGTATTTCAGCGCCAGCTCG	
43_pBs SK- ana2 C up rev	GCCGAAGCTGTTGTGAAAGCGAATTCGATATCAAGCTTATCGATA	
44_pBs SK- ana2 C down for	GCCGAAGCTGTTGTGAAAGCACTAGTTCTAGAGCGGCCGCCA	
45_ana2 cterm rep up for	GCTTTCACAACAGCTTCGGCTGGGGCCACAGAACTGGGTCCTCGC	
46_ana2 cterm rep up rev	TAGTAATTTAGGTTGATTCCTGATATTCTCCAAGTCCAGT	

47_ana2 cterm rep NGreen for	GGAATCAACCTAAATTACTAGACCCAGCTTTCTTGTACAAAGTG	
48_ana2 cterm rep NGreen rev	GTACATGCTTTTACTTGTACAGCTCGTCCATGC	
49_ana2 cterm rep down for	GTACAAGTAAAAGCATGTACAATGTTCGTTTTGTT	
50_ana2 cterm rep down rev	GCTTTCACAACAGCTTCGGCTGGGGACCCCTCTCAATATCAGGTGG	
133_Asl_nt_rep_bb_for	CCGAATATGAACACGCCAGGTATACTAGTTCTAGAGCGGCCGCCA	
134_Asl_nt_rep_bb_rev	CCGAATATGAACACGCCAGGTATGAATTCGATATCAAGCTTATCGATA	
135_Asl_nt_rep_up_for	CCTGGCGTGTTCATATTCGGCCAAGGTTTTCCAAATAGATCCCG	
136_Asl_nt_rep_up_rev	TGCTCACCATATTCaGCTAAGGGGACGCCACAAGCAT	
137_Asl_nt_rep_NG_for	TTAGCtGAATATGGTGAGCAAGGGCGAGGAGG	
138_Asl_nt_rep_NG rev	TTATcCCgGGaGTaTTCATGAAGCCTGCTTTTTTGTACAAACT	
139_Asl_nt_rep_down_for	CATGAAtACtCCcGGgATAAGCCTCTTTCAGGGGGCGGA	
140_Asl_nt_rep_down_rev	CCTGGCGTGTTCATATTCGGCAATGCGGGCTTTCAAGTCAACG	
99_Asl_ct_rep_bb_for	CCAAAGGCAATGGTCACAGCTAAACTAGTTCTAGAGCGGCCGCCA	
100_Asl_ct_rep_bb_rev	CCAAAGGCAATGGTCACAGCTAAGAATTCGATATCAAGCTTATCGATA	
101_Asl_ct_rep_up_for	GCTGTGACCATTGCCTTTGGGGAAATTCAGTTGTTGAAACTCCA	
102_Asl_ct_rep_up_rev	agaaTGgCCgTTgCCcTTaGGCTTTCTATTTGAGTTGGTGATTG	
103_Asl_ct_rep_NG_for	CtAAgGGcAAcGGcCAttctGACCCAGCTTTCTTGTACAAAGTG	
104_Asl_ct_rep_NG rev	TTCCTAAGTCTTACTTGTACAGCTCGTCCATGC	
105_Asl_ct_rep_down_for	GTACAAGTAAGACTTAGGAAAATATATATATGTATAT	
106_Asl_ct_rep_down_rev	GCTGTGACCATTGCCTTTGGGAGTGGATAGCATCCTCTGCCTG	

109_Sas4_ct_rep_bb_for	CCAAGTATTAGAGTCGGGTCTCTACTAGTTCTAGAGCGGCCGCCA	
110_Sas4_ct_rep_bb_rev	CCAAGTATTAGAGTCGGGTCTCTGAATTCGATATCAAGCTTATCGATA	
111_Sas4_ct_rep_up_for	GACCCGACTCTAATACTTGGCAGTGAGAAGGAGCAGCGAAACT	
112_Sas4_ct_rep_up_rev	TGGGTCgTAtTTaGCATAGTCTGTGTCCATTATGAGCT	
113_Sas4_ct_rep_NG_for	ACTATGCtAAaTAcGACCCAGCTTTCTTGTACAAAGTG	
114_Sas4_ct_rep_NG rev	AGACCCGACTTTACTTGTACAGCTCGTCCATGC	
115_Sas4_ct_rep_down_for	GTACAAGTAAAGTCGGGTCTCTGCTTCCGTTG	
116_Sas4_ct_rep_down_rev	GACCCGACTCTAATACTTGGTGTTCGCTGCATTCTTGTTGAGTT	
151_Plk4_nt_rep_bb_for	CCCGATTGGATAACATAGCTAGCACTAGTTCTAGAGCGGCCGCCA	
152_Plk4_nt_rep_bb_rev	CCCGATTGGATAACATAGCTAGCGAATTCGATATCAAGCTTATCGATA	
159_Plk4_nt_rep_up_for_new	AGCTATGTTATCCAATCGGGGTGTGAGAGTCCAAGGTTGTCTG	
160_Plk4_nt_rep_up_rev_new	TGCTCACCATAGCTAGCCTTTTTTCTGTAGACTTAC	
155_Plk4_nt_rep_NG_for	AAGGCTAGCTATGGTGAGCAAGGGCGAGGAGG	
156_Plk4_nt_rep_NG rev	AACGCtCtgTTactgAgCATGAAGCCTGCTTTTTTGTACAAACTT	
157_Plk4_nt_rep_down_for	ATGcTcagtAAcaGaGCGTTTGGAGAAACAATTGAGGTG	
158_Plk4_nt_rep_down_rev	AGCTATGTTATCCAATCGGGTACTGCTAGCAAATGTTATGATTCC	
85_Plk4_ct_rep_bb_for	CCAAAACGACAACGCCTTATTATACTAGTTCTAGAGCGGCCGCCA	
86_Plk4_ct_rep_bb_rev	CCAAAACGACAACGCCTTATTATGAATTCGATATCAAGCTTATCGATA	
87_Plk4_ct_rep_up_for	ATAAGGCGTTGTCGTTTTGGGCCACCAGATCTTCAAATACCAAG	
88_Plk4_ct_rep_up_rev	GCGATTgTAgTAtGGgGTaGTgGTcTTaGGAGTCATTGCATTGTTGTAGTCAG	

89_Plk4_ct_rep_NG_for	CtACcCCaTAcTAcAATCGCATGCTTCTTGACCCAGCTTTCTTGTACAAAGTG	
90_Plk4_ct_rep_NG_rev	TTTGATTCAATTACTTGTACAGCTCGTCCATGC	
91_Plk4_ct_rep_down_for	GTACAAGTAATTGAATCAAAACTTAATTCCAAAATA	
92_Plk4_ct_rep_down_rev	ATAAGGCGTTGTCGTTTTGGCCACCTTCCAACGAAACCCAACA	

Table 12: Primers designed for transformation plasmid generation

ID_Name	Sequence (5'-)	Used for:
67_pSas6NG_pl_for	GATACACAGCGACCCAGCTTTCTTGTACAAAGTT	Primers to generate untagged mNG FCS control lines
68_pSas6NG_pl_rev	GGTTGGGGACGAAGCCTGCTTTTTTGTACAAAGT	
69_pSas6NG_prom_for	AGCAGGCTTCGTCCCCAACCAACCCTAGACCC	
70_pSas6NG_prom_rev	TGCTCACCATGACAGATCAGGCTCGTAAGAAAC	
71_pSas6NG_NG_for	CTGATCTGTCATGGTGAGCAAGGGCGAGGAGG	
72_pSas6NG_NG_rev	ATAAGTAAAATTACTTGTACAGCTCGTCCATGC	
73_pSas6NG_UTR_for	GTACAAGTAATTTTACTTATTGTTAATGCATTTTTTC	
74_pSas6NG_UTR_rev	AAGCTGGGTCGCTGTGTATCCATCTTGGCCGC	
75_pSas6NGNG_NG1_rev	GCGGCCGCCACTTGTACAGCTCGTCCATGCCC	
76_pSas6NGNG_NG2_for	GCTGTACAAGTGGCGGCCGCTCGAGATGGTGA	
77_pSakNG_pl_for	GTATTGTGCGGACCCAGCTTTCTTGTACAAAGTT	
78_pSakNG_pl_rev	GGCGGAAGACGAAGCCTGCTTTTTTGTACAAAGT	
79_pSakNG_prom_for	AGCAGGCTTCGTCTTCCGCCCTTCTACTTCTGC	
80_pSakNG_prom_rev	TGCTCACCATAGCTAGCCTTTTTTCTGTAGACTTA	
81_pSakNG_NG_for	AAGGCTAGCTATGGTGAGCAAGGGCGAGGAGG	
82_pSakNG_NG_rev	TTTGATTCAATTACTTGTACAGCTCGTCCATGC	
83_pSakNG_UTR_for	GTACAAGTAATTGAATCAAAACTTAATTCCAAAATA	
84_pSakNG_UTR_rev	AAGCTGGGTCCGCACAATACAACGAACAGTGAAC	
165_eAna2-mNG(X)_pl_for	GAAGCTGTTGGACCCAGCTTTCTTGTACAAAGTG	Primers to generate mutant forms of eAna2-mNG
166_eAna2-mNG(X)_pl_rev	GAACAAACATTTGGAGCGTATTTGTTTATATTTGCC	
167_eAna2-mNG(X)_ins_for	TACGCTCCAAATGTTTGTTCCCGAAACGGAGGAT	
168_eAna2-mNG(X)_ins_rev	AAGCTGGGTCCAACAGCTTCGGCTGGTTCCTGA	
173_A2-NG_ins_for	tgtatgaaaagaatccaataaaacatccttcctagcaggtagacgcttgtctcccatt	

174_A2-NG_ins_rev	attggattcttttcatacagattcaacgtacgcaccttgattggtggtcagaatatcgc	
175_mCardinal_for	CTGATCTGTCATGGTGAGCAAGGGCGAGGAGC	Primers to generate untagged FCCS control lines
176_mCardinal_rev	AGTAAAATTACTTGTACAGCTCGTCCATGCCAT	
177_mCardinal_bb_for	GCTGTACAAGTAATTTTACTTATTGTTAATGCATTTT	
178_mCardinal_bb_rev	TGCTCACCATGACAGATCAGGCTCGTAAGAAAC	
179_mKate2_for	CTGATCTGTCATGGTGAGCGAGCTGATTAAGGA	
180_mKate2_rev	AGTAAAATTATCTGTGCCCCAGTTTGCTAGGG	
181_mKate2_bb_for	GGGGCACAGATAATTTTACTTATTGTTAATGCATTTT	
182_mKate2_bb_rev	CGCTCACCATGACAGATCAGGCTCGTAAGAAAC	
183_mScarlet_for	CTGATCTGTCATGGTGAGTAAAGGAGAAGCTGTG	
184_mScarlet_rev	AGTAAAATTATTTGTATAGTTCATCCATGCCACC	
185_mScarlet_bb_for	ACTATACAAATAATTTTACTTATTGTTAATGCATTTT	
186_mScarlet_bb_rev	TACTCACCATGACAGATCAGGCTCGTAAGAAAC	
187_dCardinal_rev	GCGGCCGCCACTTGTACAGCTCGTCCATGCCAT	
188_dCardinal_bb_for	GCTGTACAAGTGGCGGCCGCTCGAGATGGTGA	
189_dKate2_rev	GCGGCCGCCATCTGTGCCCCAGTTTGCTAGGG	
190_dKate2_bb_for	GGGGCACAGATGGCGGCCGCTCGAGATGGTGA	
191_dScarlet_rev	GCGGCCGCCATTTGTATAGTTCATCCATGCCACC	
192_dScarlet_bb_for	ACTATACAAATGGCGGCCGCTCGAGATGGTGA	
221_A2Ct_XSTOP_for	GAAGCTGTTGGACCCAGCTTTCTTGTACAAAGTG	Deletion of the stop codon in pTS33+34
222_A2Ct_XSTOP_rev	AAGCTGGGTCCAACAGCTTCGGCTGGTTCCTGA	
223_S6Ct_XSTOP_for	AAATCGGCGAGACCCAGCTTTCTTGTACAAAGTG	
224_S6Ct_XSTOP_rev	AAGCTGGGTCTCGCCGATTTTCTTTGCCCGTGG	

9.2 Appendix B

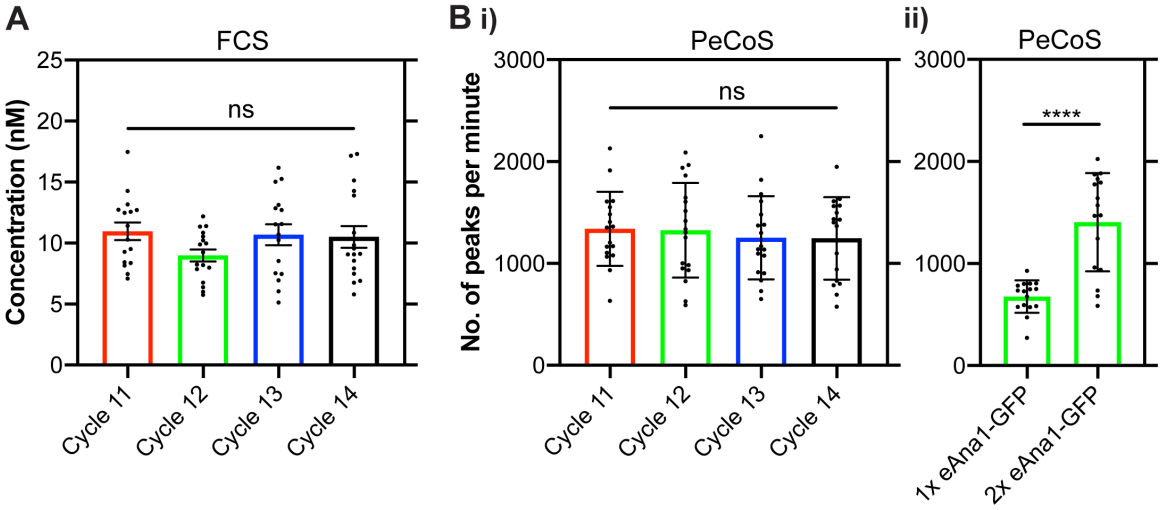


Figure 9-1: PeCoS allows the quantification of eAna1-GFP's relative cytoplasmic concentration
(A) Bar graph quantifies the relative cytoplasmic concentration (mean±SEM) of eAna1-GFP measured with FCS at the beginning of S-phase. **(B) (i)** Bar graph depicts the relative cytoplasmic concentration (mean±SD) of eAna1-GFP measured with PeCoS at the beginning of S-phase. **(ii)** Bar graph quantifies the relative cytoplasmic concentration (mean±SD) of embryos expressing either 1x or 2x copies of eAna1-GFP, which were measured at the beginning of S-phase in nuclear cycle 12.

For FCS measurements, each data point represents the average of 4-6x 10-second-long recordings. For PeCoS measurements, each data point represents an individual 180-second-long recording. Statistical significance was assessed using an ordinary one-way ANOVA test (ns, not significant) for measurements between cycles 11-14, or an ordinary unpaired t-test with Welch's correction (****, $P<0.0001$) for the comparison between 1x and 2x embryos in cycle 12.

9.3 Appendix C

Ana2's cytoplasmic oligomerisation is insensitive to the expression level changes of the other core centriole duplication proteins

As Ana2 is present in a higher—on average dimeric—oligomeric state in the cytoplasm, I set out to further characterise how its cytoplasmic stoichiometry can be influenced. First, I wanted to determine if Ana2 might be sensitive to the presence or absence of one of the other core centriole duplication proteins, which include Asl, Plk4, Sas-6, and Sas-4. In order to test if any of these centriolar proteins can affect Ana2's cytoplasmic stoichiometry, I measured embryos from mothers expressing endogenously tagged eAna2-mNG at the beginning of nuclear cycle 12 in a variety of genetic backgrounds. Unfortunately, it was not possible to completely deplete any of the five core centriole duplication proteins as they are essential for centriole duplication and their absence would lead to developmental arrest. I therefore genetically halved their dose by deleting one of the two endogenous alleles of each protein (referred to as gene$^{+/-}$). In addition, I also wanted to assess how Ana2 responds to the overabundance of any of the core centriole duplication proteins, which was achieved through the overexpression of the proteins from the Ubiquitin (Ubq) promoter (Lee, Simon and Lis, 1988). Interestingly, Ana2's stoichiometry was insensitive to the alteration of any of the core centriole duplication proteins, both their reduction and overexpression (**Figure 9-2A**). Only the overexpression of untagged Ana2 led to a decrease in CPM which can be explained by the formation of heterooligomers (as previously shown in embryos from mothers heterozygous for tagged and untagged Ana2). Genetically halving the dose of eAna2-mNG did not affect its molecular brightness/stoichiometry, suggesting that Ana2's dimerisation

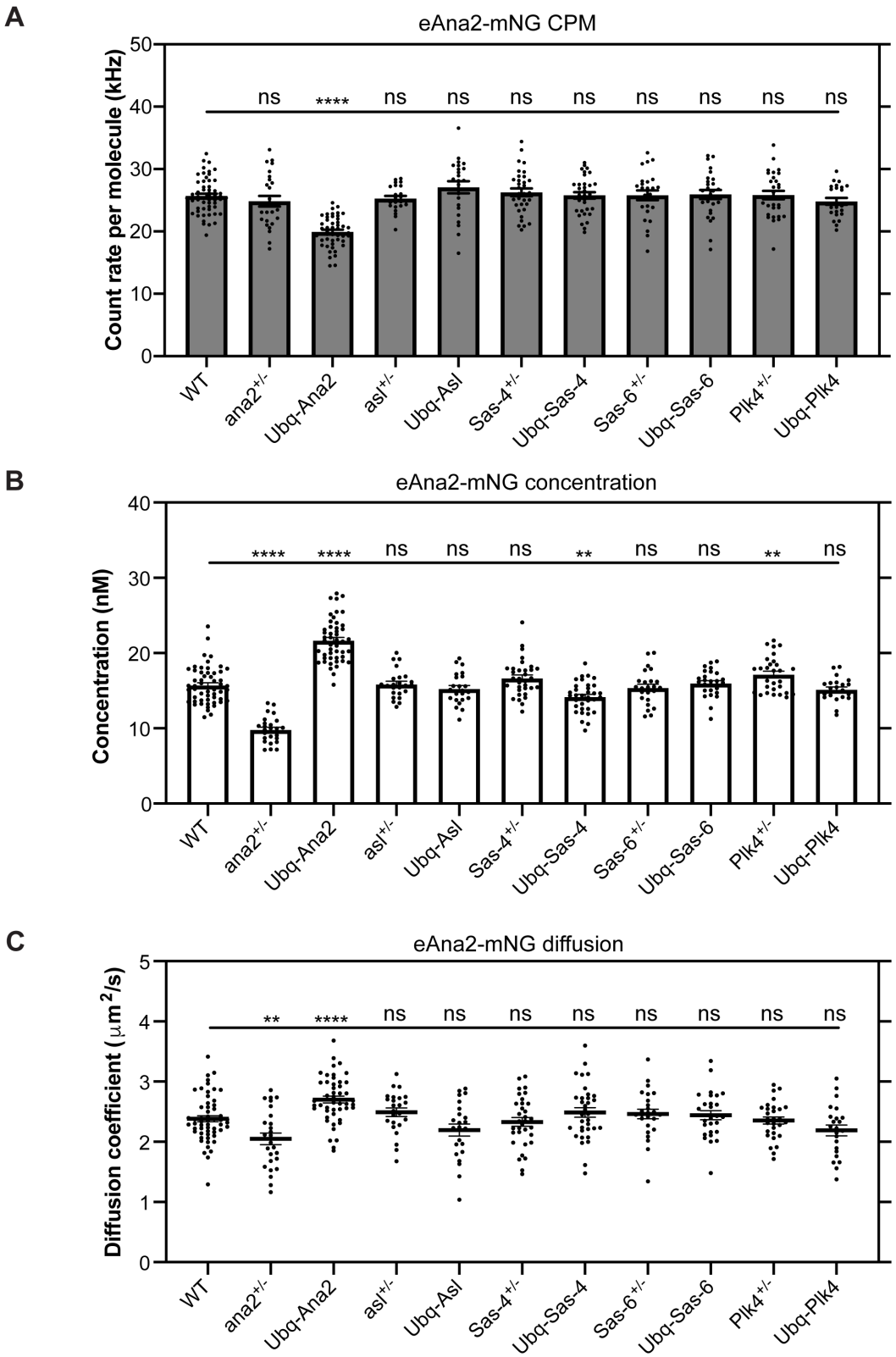


Figure 9-2: Ana2's cytoplasmic oligomerisation state is insensitive to the expression levels of the other core centriole duplication proteins

Bar graphs quantify the average molecular brightness **(A)**, cytoplasmic concentration **(B)**, and diffusion coefficient **(C)** of eAna2-mNG in various genetic halve dose (+/-) and overexpression (Ubq) backgrounds measured with FCS at the beginning of S-phase in nuclear cycle 12. Each data point represents the average of 4-6x 10-second-long recordings. Data are presented as Mean±SEM. Statistical significance was assessed using an ordinary unpaired t-test with Welch's correction (****, P<0.0001; **, P<0.01; ns, not significant).

capability is not particularly concentration sensitive. Interestingly, I observed a minor, but statistically significant, change in Ana2's cytoplasmic concentration in embryos where Sas-4 was overexpressed (Ubq-Sas-4) or the concentration of Plk4 was halved (*Plk4*$^{+/-}$) (**Figure 9-2B**). Ana2 can interact with both proteins at the centriole (see **Chapter 1, Section 1.2.3**), and the changes in Ana2's cytoplasmic concentration might be caused by it increased/decreased recruitment to the centriole. To summarise, this data indicates that Ana2's cytoplasmic stoichiometry is not influenced by any other core centriole duplication proteins, although it is possible that only halving the dose of another protein is not sufficient to abolish its contribution to Ana2's homo-oligomerisation if the protein is present in high abundance.

Generating mutant forms of Ana2 to test how individual domains affect its cytoplasmic stoichiometry

Given Ana2's insensitivity to concentration changes of the other core centriole duplication proteins, I aimed to generate mutant forms of eAna2-mNG where either entire interaction domains or specific phosphorylation sites were mutated. All mutant forms of Ana2 could be divided into three categories: (1) Mutations affecting Ana2's potential Cdk phosphorylation sites (all 12 sites mutated to an alanine (A) (phosphonull), or only two highly conserved sites mutated to either S283A T301A (phosphonull) or S283E T301E (phosphomimetic)); (2) Deletion of the central CC domain (ΔCC); (3) Mutation/deletion of the C-terminal STAN domain (the two key Plk4-phosphorylation sites mutated to either S318A S373A (phosphonull) or S318E S373E (phosphomimetic), or complete deletion of the STAN domain (ΔSTAN)). Once again, eAna2-mNG's average cytoplasmic stoichiometry was assessed at the beginning of nuclear cycle 12. While all mutant forms affecting the

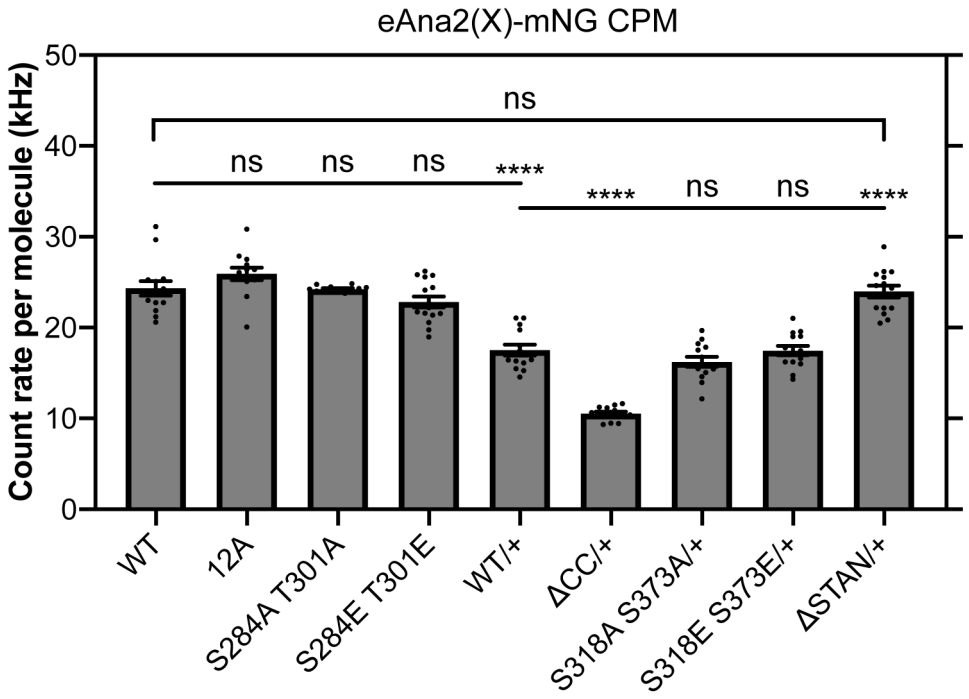


Figure 9-3: Ana2 needs its CC domain for dimerisation, and the deletion of its STAN domain might allow Ana2 to form higher oligomeric structures in the cytoplasm

Bar graph depicts the average cytoplasmic molecular brightness (mean±SEM) of mutant forms of eAna2-mNG, either from mothers homozygously expressing the transgene or—if the transgene did not rescue the mutant phenotype—heterozygously in the presence of an untagged WT Ana2 allele (/+). Each data point represents the average of 4-6x 10-second-long recordings. Statistical significance was assessed using an unpaired t-test with Welch's correction (for Gaussian-distributed data) or a Mann-Whitney test (****, P<0.0001; ns, not significant).

potential Cdk phosphorylation of Ana2 rescued the *ana2*$^{-/-}$ mutant phenotype and could be measured as homozygotes, all mutations of the CC and STAN domain did not and had to be assessed in the presence of WT untagged Ana2 (heterozygous for fluorescently tagged mutant Ana2). As Ana2 on average dimerises in the cytoplasm, a significant difference in CPM was observed between embryos from mothers homozygous and heterozygous for WT eAna2-mNG, and, depending on whether the mutation of interest was measured in the presence of untagged Ana2, the homozygous or heterozygous control was used for statistical comparison (**Figure 9-3**).

Mutations of Ana2's potential Cdk phosphorylation sites do not affect its cytoplasmic stoichiometry, but the deletion of its CC domain forces Ana2 into a monomeric state

The phosphonull mutation of all 12 potential Cdk phosphorylation sites and the phosphonull/phosphomimetic mutation of the two highly conserved potential Cdk phosphorylation sites (S283 T301) did not affect Ana2's average stoichiometry (**Figure 9-3**). As expected, the deletion of the central CC domain led to a lower molecular brightness than the heterozygous control. Its molecular brightness was about half of homozygous WT eAna2-mNG, which suggests that it is present as a monomer. Structural studies have shown that the CC domain is required for Ana2's homo-oligomerisation (Cottee *et al.*, 2015), and this result confirms that Ana2 needs its central CC region to form homo-oligomers in the cytoplasm (**Figure 9-3**). As previously reported, I observed that eAna2(ΔCC)-mNG did not localise to the centriole, which highlights the importance of Ana2's oligomerisation capability for its protein function.

The deletion of the STAN domain might allow Ana2 to form higher oligomeric structures in the cytoplasm

The most unexpected behaviour was observed for mutations affecting Ana2's STAN domain. The C-terminally located STAN domain is crucial for the initial steps of centriole assembly, and it was shown that Ana2/STIL is phosphorylated by Plk4/PLK4 in its STAN domain to promote the interaction with Sas-6/SAS-6 and initiate cartwheel assembly (Dzhindzhev *et al.*, 2014; Ohta *et al.*, 2014; Fatalska *et al.*, 2020). A previous RNA-injection experiment in the lab testing Ana2's centriolar localisation of various STAN-domain point mutants highlighted the importance of two conserved phosphorylation sites within the STAN domain, S318 and S373, for its centriolar localisation (Boris Sieber thesis (2015)).

When either of the two residues was mutated to an alanine to inhibit the phosphorylation by Plk4, Ana2-GFP hardly localised to the centriole. Similar results were obtained when the entire STAN domain was deleted. In contrast, the mutation of S318 and S373 to glutamic acid to mimic the phosphorylation by Plk4 restored Ana2's localisation. It was suggested that Plk4's phosphorylation of Ana2 allows it to fold back on itself to promote its interaction with Sas-6 and initiate cartwheel assembly (McLamarrah *et al.*, 2017). Given Ana2's dimeric cytoplasmic stoichiometry, I wondered if Plk4's phosphorylation of the STAN domain might also be responsible for Ana2's centriolar tetramerisation. The phosphonull (S318E S373E) or phosphomimetic (S318E and S373E) mutation of both crucial Plk4 phosphorylation sites, however, did not affect Ana2's stoichiometry (**Figure 9-3**). Surprisingly, the deletion of the entire STAN domain led to a significant increase in CPM compared to the heterozygous WT control (**Figure 9-3**), and eAna2(ΔSTAN)-mNG's molecular brightness was not statistically significantly different to the homozygous WT eAna2-mNG control. If ~50% of Ana2 is fluorescently tagged in the heterozygous eAna2(ΔSTAN)-mNG/+ measurements compared to 100% in the homozygous control, a similar CPM between the two indicates that eAna2(ΔSTAN)-mNG forms cytoplasmic tetramers (with—on average—two tagged and two untagged Ana2 molecules). This result suggests that the STAN domain might lock Ana2 in an inhibited state that does not allow its tetramerisation in the cytoplasm, and Ana2 needs to be modified, presumably at the centriole, to release the inhibition of the STAN domain and allow for the assembly of higher oligomeric structures.

9.4 Appendix D

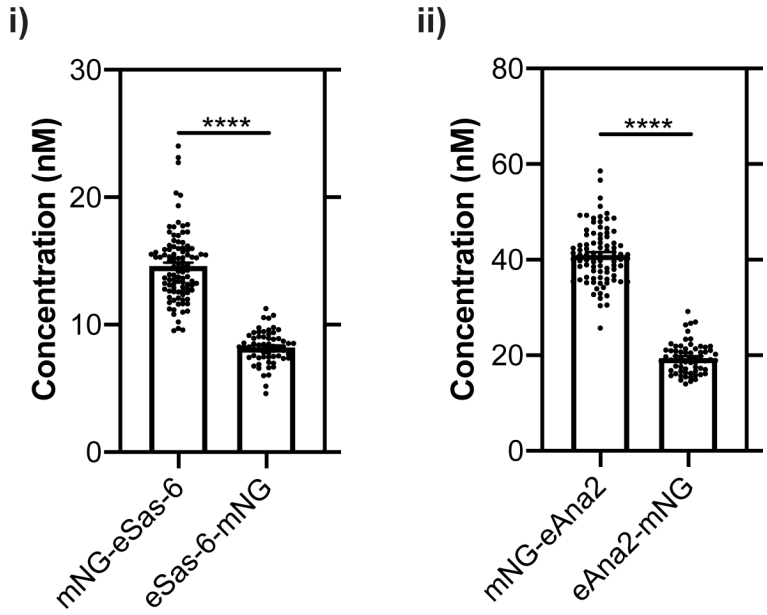


Figure 9-4: N-terminally tagged Sas-6 and Ana2 show an increased cytoplasmic concentration compared to their C-terminal proteins when measured by FCS

Bar graphs quantify the cytoplasmic concentration (mean±SEM) of Sas-6 **(i)** and Ana2 **(ii)** endogenously tagged on both their N- and C-termini measured by FCS in cycles 11-14. Each data point represents the average of 4-6x 10-second-long recordings. Statistical significance was assessed using an unpaired t-test with Welch's correction (****, P<0.0001).

9.5 Appendix E

smFISH (single molecule fluorescence in situ hybridization) protocol

smFISH probe sets were designed complementary to the mRNA sequence of the three core centriole proteins Ana2, Sas-6, and Plk4 to identify the localisation of their mRNA in the *Drosophila* syncytium, and to test whether they accumulate around the centriole for localised translation. Before the design of the smFISH probes, all genes were sequenced to obtain the correct nucleotide sequence. In addition, I also designed a probe set complementary to the mRNA sequence of mNeonGreen (mNG) labelled with a different fluorescent dye to identify co-localisation of the two fluorophores and therefore the staining efficiency.

Table 13: Parameters and target sequence which were used for the smFISH probe design

Gene	Exon	Masking level	Min. spacing	No. of probes	Fluorophore
Ana2	1+2	5	2	47	Quasar670
Sas-6	2+3	5	2	48	Quasar670
Plk4	4+5	5	2	47	Quasar670
mNG	all	5	1	31	Quasar570

The staining protocol was optimised from a previous protocol "Stellaris® RNA FISH Probes – Protocol for *Drosophila* Embryo" and combined with an immunofluorescence staining of Asl to identify the localisation of the centrioles. The entire staining was performed under RNAse-free conditions and is described below:

Embryos were collected for 3 hours on fruit juice agar plates in egg-laying cages and then transferred into a mesh basket using an embryo wash solution (0.6% NaCl, 0.04% TritonX). Afterwards, the embryos were devitellinized in a 50% bleach solution for 2 minutes, and thoroughly washed 3x alternating between wash buffer and water. Using a brush, the

embryos were transferred into a 20 mL scintillation vial containing 10 mL of embryo fixation solution (0.5% Phosphate buffered saline, 40% Ultra-pure formaldehyde, 50% Heptane) and shaken on an orbital shaker for 30 minutes at 220 rpm. Then, the aqueous phase was completely removed and replaced by 8 mL methanol, and the vial was vigorously shaken for 30 seconds. After the fixed embryos subsided to the bottom of the vial, the entire heptane phase and most of the methanol phase were removed, and the embryos washed in 4x 1mL methanol and transferred into a 1.5 mL Eppendorf tube. The fixed embryos were then stored for at least 1 day at -20 °C.

For the staining, an aliquot of fixed embryos was transferred into a Wheaton glass and transitioned from methanol to PBT (0.1% Tween-20 in 1xPBS) with 25%, 50%, and 100% ratios (rocking on a roller platform at room temperature (RT) for 5 minutes each). Then, the embryos were rocked 3x for 10 minutes with PBT, followed by a blocking step for 1 hour using a blocking buffer (0.1% goat serum, 1% glycine, 1x PBS, 0.3% TritonX), 1x for 10 minutes in a 50:50 PBT/Wash buffer A (10% deionized formamide, 2% SSC solution) mix, and 2x for 5 minutes in Wash buffer A all at RT. After the removal of the Wash buffer A, the embryos were incubated in 0.5 mL Hybridization buffer (10% Deionized formamide, 5% Dextran sulphate solution, 2% SSC) for 5 minutes at RT. The Hybridization buffer was replaced with 1 mL of fresh Hybridization buffer and incubated in a 37 °C water bath for 2 hours. Afterwards, the embryos were incubated in 0.25 mL of Hybridization buffer containing both smFISH probes (diluted to 50 nM) and the primary antibody (α-Asl NT #11 Rabbit 1:500) for 14-15 hours in the dark at 37 °C. On the next day, the Hybridization buffer containing the fluorophores and primary antibody was removed and the embryos were washed 1x with 0.5 mL pre-warmed Wash Buffer A in the dark at 37 °C, followed by

2x with 0.5 mL pre-warmed Wash Buffer A for 15 minutes in the dark at 37 °C, 1x with 0.5 mL Wash Buffer A containing the secondary antibody (Alexa 488 #22, 1:1000) for 45 minutes in the dark at RT, 1x with 0.5 mL Wash Buffer A for 15 minutes in the dark at RT, and 3-12x with 1mL PBT for 10 minutes in the dark at RT. The embryos were then placed on imaging slides, the excess liquid thoroughly removed, and the embryos mounted under a cover glass using Prolong Diamond Antifade with DAPI (P36966, Invitrogen) and the cover glass sealed. The slides were dried in the dark at RT for ~24 hours, then stored at -20 °C for at least one day and imaged on a PerkinElmer ERS spinning-disk confocal system mounted on a Zeiss Axiovet 200M microscope with an Orca ER CCD camera (Hamamatsu Photonics, Japan). A 63x, 1.4 NA objective and laser excitations at 405nm (DAPI), 488nm (Alexa488/centriole), 561nm (Quasar570), and 640nm (Quasar670) were used. For each embryo a stack of 17 slices with 0.5 μm step-size was taken, and the pixel size in xy was determined to be ~0.11 nm.

For the analysis, maximum intensity stacks were first analysed with the Fiji plugin Coloc 2 for the spot detection of both channels, and in collaboration with Felix Zhou (Ludwig Institute for Cancer Research, Oxford) a customised python script was written that allowed the quantification of the colocalised signal from both channels. Colocalisation was hereby defined as any signal that exhibited a maximum shift of 2 pixels.

<u>smFISH experiments of Plk4, Sas-6, and Ana2 reveal that their mRNA molecules do not accumulate at the centriole</u>

In order to assess the staining efficiency of my smFISH procedure, I stained eAna2-mNG (=positive control) and untagged eAna2 (=negative control) embryos with the smFISH probes targeting the mRNA sequence of Ana2 and mNG and compared the fraction of

colocalised signal. Unfortunately, the smFISH staining for the mRNA of mNG had a very low SNR, presumably caused by the low number and close spacing of the probes due to the short nucleotide sequence of the fluorophore sequence. In an attempt to reduce the background noise of the mNG staining, I tested the staining protocol with a varying number of final PBT washes and observed the best colocalization (~20% of Ana2's signal colocalised with mNG's signal) when I washed the embryos 9x for 10 minutes (**Figure 9-5A**). Despite the low signal of mNG, I still observed a significant discrepancy in colocalisation of the two probes between embryos expressing tagged and untagged Ana2, indicating that I can indeed detect mRNA molecules in the embryo (**Figure 9-5A**). Although this control suggests a very low staining efficiency, I believe that the low SNR of the mNG smFISH staining is responsible for the low colocalisation. For all probes targeting the mRNA of a gene (Ana2, Sas-6, Plk4) I obtained very clear intensity signals with a low background fluorescence, and I therefore believe that the staining efficiency of those probes is much higher (**Figure 9-5B**). In an initial staining, I imaged ~40-60 embryos in various nuclear cycles and cell-cycle stages for each gene. By eye, I looked for the localisation of the gene-specific mRNA probe signal in relation to the centriole (Asl staining), but for none of the three proteins I observed a high mRNA abundance around the centriole. Some images for the smFISH staining of Plk4 are depicted in **Figure 9-5B**.

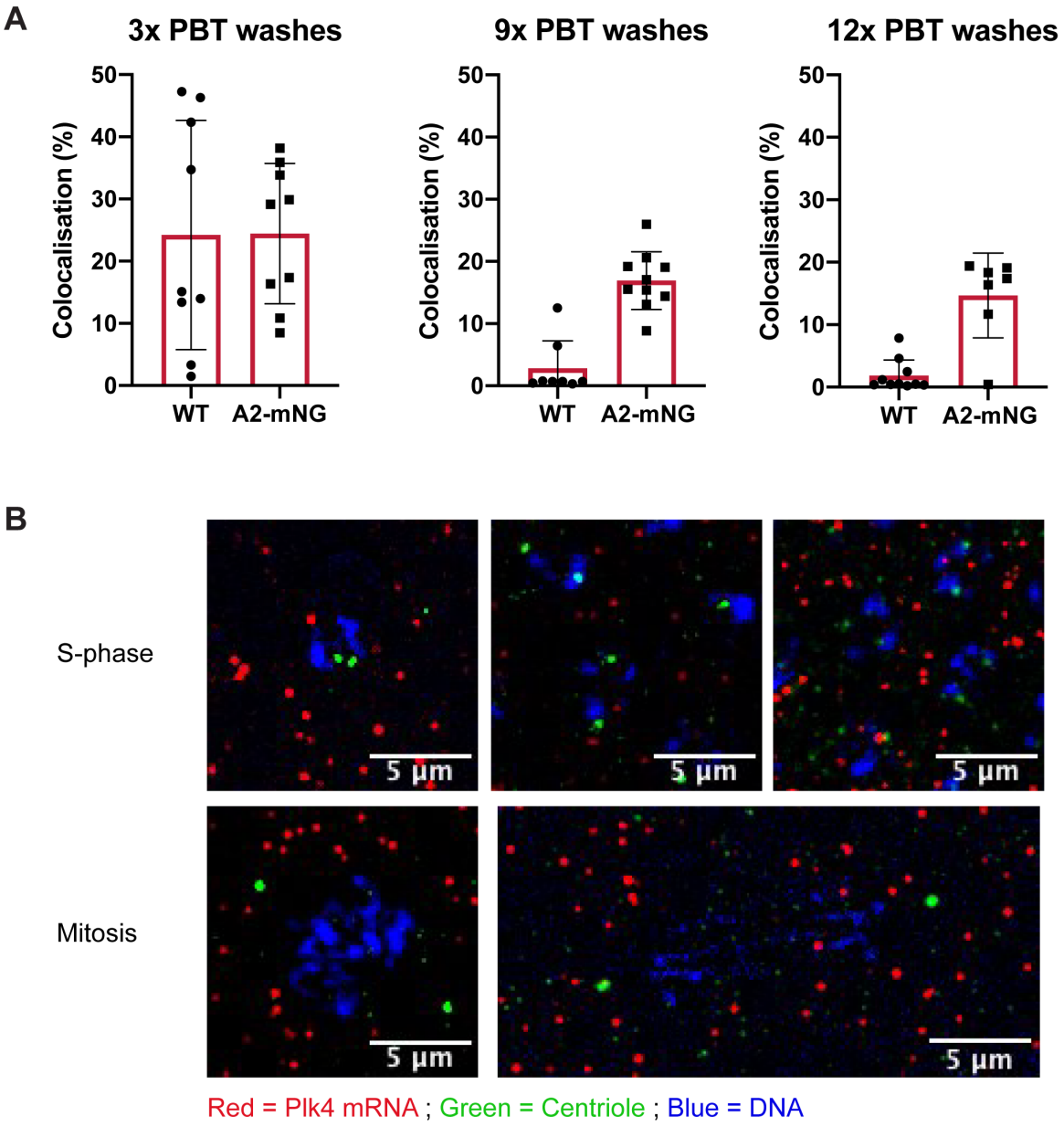


Figure 9-5: The smFISH staining of Ana2, Sas-6, and Plk4 does not show an accumulation of their mRNA around the centriole

(A) Bar graphs quantify the fraction of colocalisation (mean±SD) between smFISH staining of Ana2 and mNG in a positive and negative control with a varying number of final washes. Each data point represents the colocalisation within an individual embryo. **(B)** Pictures show the localisation of Plk4 mRNA molecules (*red*) and of centrioles (*green*) at different cell-cycle stages.

9.6 Appendix F

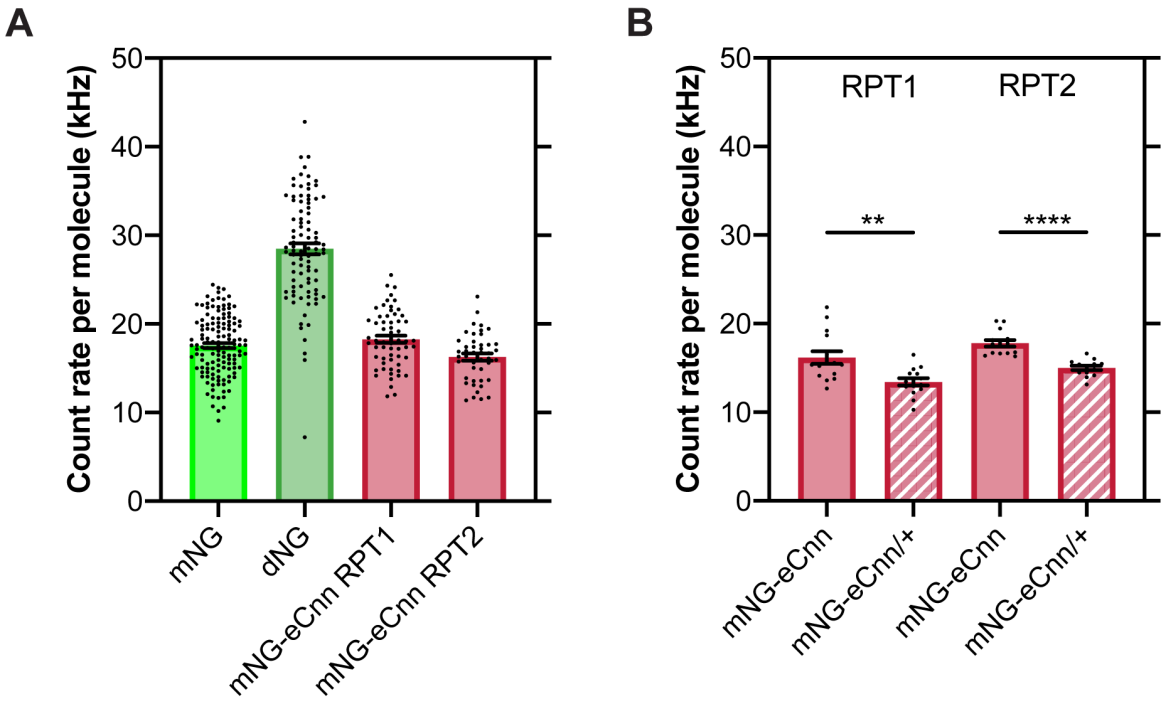


Figure 9-6: Cnn seems to be mainly monomeric in the cytoplasm
(A) Bar graph quantifies cytoplasmic CPM measurements (mean±SEM) of mNG-tagged Cnn (two biological repeats) in comparison to untagged monomeric and dimeric NeonGreen (mNG/dNG) control measurements. As there was a long time gap of ~1 year in-between control and mNG-eCnn measurements, the stoichiometry comparison might be inaccurate due to performance variability of the microscope over time. **(B)** Bar graph quantifies the average cytoplasmic molecular brightness (mean±SEM) of mNG-tagged Cnn in embryos from mothers heterozygous or homozygous for the fluorescently tagged protein of interest (for each repeat, both genotypes were measured side by side). Each data point represents the average of 4-6x 10-second-long recordings. Statistical significance was assessed using an ordinary unpaired t-test with Welch's correction (****, P<0.0001; **, P<0.01).